

UC Riverside

UC Riverside Electronic Theses and Dissertations

Title

Dynamic High Pressure Measurements and Molecular Dynamics Simulations of Phase Changes and Vibrational Dynamics in Molecular Solids

Permalink

<https://escholarship.org/uc/item/4bz877qx>

Author

Rice, Andrew Patrick

Publication Date

2011

Peer reviewed|Thesis/dissertation

UNIVERSITY OF CALIFORNIA
RIVERSIDE

Dynamic High Pressure Measurements and Molecular Dynamics Simulations of Phase
Changes and Vibrational Dynamics in Molecular Solids

A Dissertation submitted in partial satisfaction
of the requirements for the degree of

Doctor of Philosophy

in

Chemistry

by

Andrew Patrick Rice

June 2011

Dissertation Committee:

Dr. Eric Chronister, Chairperson

Dr. Christopher J. Bardeen

Dr. Leonard Mueller

Copyright by
Andrew Patrick Rice
2011

The Dissertation of Andrew Patrick Rice is approved:

Committee Chairperson

University of California, Riverside

ACKNOWLEDGEMENTS

(in no particular order)

It is hard to imagine how many years have gone by since I began this doctoral program here at the University of California, Riverside. So many things have changed from politics to the internet, but what has not changed is the need to give thanks where it is deserved.

I would like to thank my advisor, Dr. Eric Chronister, for giving me the opportunity to learn and develop as a physical chemist, and especially his encouragement for me to have a positive outlook on my own research.

I would like to thank those who have provided me with help in my research projects. Thanks goes to Dr. Fook Tham, our department crystallographer, for performing the single crystal X-ray diffraction on p-terphenyl and to Dr. Dan Borchardt, for his assistance with the many departmental optical instruments, especially the Raman spectrometer. I also would like to thank the entire CNAS Machine Shop, particularly Daniel Adams for his work and advice on the development of our Dynamic Diamond Anvil Cell. I would like to acknowledge Dr. Morton's group for their work on the synthesis of their cyclic diamine compounds seen in Chapter Three, and for providing me the opportunity to provide my own analysis of such interesting compounds. Also, a special thanks to Dr. Bohdan Schatschneider for performing additional calculations at 298 K for statistical analysis in Chapter Five.

Special thanks to my lab mates and friends: my friends and labmates Dr. Marta Fellows Olteanu and Sebastian Jezowski who were always there to help and listen; Dr. Arun Agarwal and David Medina for their friendship, support, and the many, many

lunches where we vented our frustrations and cheered ourselves up; Dr. Bohdan Schatschneider, with whom I am glad to be acquainted in spite of our complete opposite personalities; and Dr. Michael McIntire whom I knew for only a year and a half, but they were a fun and crazy year of moving an entire lab halfway across campus and eating Wendy's spicy chicken sandwiches and Frostys.

Thanks to all the professors I have taught for, especially Dr. Richard Debus and Dr. Ludwig Bartels for their insightful advice and examples of teaching physical chemistry. I would like to thank my RCCD Faculty Internship mentor Dr. Diane Marsh from Moreno Valley College for her current mentorship.

My parents were a constant in their loving support and encouragement. I would also like to thank my friends in Bible study and church, who helped provide balance in my life and spiritual support.

Thanks and praise to God, without whom none of this would be possible.

FORMAL ACKNOWLEDGEMENTS

Computational results obtained using software programs from Accelrys Software Inc. Dynamics calculations performed with the Discover program using a Custom forcefield, and graphical displays generated with Materials Studio 4.4.

Some images were prepared using GIMP 2.6.8, open source image manipulation software.

Chemical structures drawn using ACD/ChemSketch 12.0 freeware.

Discrete Fourier Transformations performed using Mathematica 7.0.

Figure 5.2 reprinted with permission from Baer, B. J.; Chronister, E. L., Pressure induced phase transitions in pentacene doped para-terphenyl probed by changes in the impurity absorption spectrum. *The Journal of Chemical Physics* **1993**, *99* (4), 3137-3138..

Copyright 1993, American Institute of Physics.

Figure 5.3 reprinted with permission from Baer, B. J.; Chronister, E. L., Temperature and pressure dependent optical dephasing of pentacene in triclinic and monoclinic p-terphenyl. *The Journal of Physical Chemistry* **1995**, *99* (19), 7324-7329. Copyright 1995,

American Chemical Society.

ABSTRACT OF THE DISSERTATION

Dynamic High Pressure Measurements and Molecular Dynamics Simulations of Phase Changes and Vibrational Dynamics in Molecular Solids

by

Andrew Patrick Rice

Doctor of Philosophy, Graduate Program in Chemistry
University of California, Riverside, June 2011
Dr. Eric Chronister, Chairperson

The parameters of temperature and, particularly, pressure are useful tools for the investigation of the phase transitions and vibrational dynamics of condensed matter, such as molecular crystals. Building upon the design of the Merrill-Bassett Diamond Anvil Cell (DAC), a Dynamic DAC was developed and shown to be able to dynamically control the pressure of the sample. Also, the dynamic phase changes of water to solid Ice VI and VII were imaged using the Dynamic DAC.

Using a standard DAC, the hydrogen bonding of both N¹,N¹,N⁵,N⁵,3,3-hexamethylcadaverine HBr (33HMCHBr) and N,N,N',N'-tetramethylputrescine HI (TMPHI) were explored using high pressure Raman spectroscopy. Evidence of a possible phase transition for 33HMCHBr is shown along with the likely vibrational mode of the low barrier hydrogen bond in TMPHI.

New single crystal x-ray crystallographic evidence is shown regarding a new crystal structure of p-terphenyl involving twinning at low temperature as well as x-ray diffraction evidence of the temperature induced phase transition in p-terphenyl.

Lastly, the results of computational studies, using a previously developed forcefield, of the pentacene in p-terphenyl mixed molecular crystal are shown. The polarizations of the calculated modes of the hindered translations of pentacene along the molecular and crystallographic axes and the anharmonicity of the modes are investigated. Also, a discussion on the identification and separation of the intramolecular motions from the calculated hindered rotations spectrum is presented.

Table of Contents

Chapter 1: An Introduction to High Pressure Experimental and Computational Studies.....	1
1.1 Background to the Field of High Pressure Experimental Techniques	1
1.2 Determining Pressure with the Ruby Florescence Pressure Scale	3
1.3 High Pressure Raman Spectroscopy	4
1.4 Computational Studies of Temperature and Pressure Effects on Mixed Crystals	5
1.5 Single Crystal X-ray Diffraction Studies of Temperature Effects on Molecular Crystals.....	5
Chapter 2: Development and Characterization of a Dynamic Diamond Anvil Cell (DDAC).....	8
2.1 The Interesting Uses of the DDAC	8
2.2 Development of The DDAC	10
2.3 Characterization of the Dynamic Pressure Capability of the DDAC.....	16
2.3.1 Characterization of the Pressure Range of the DDAC.....	16
2.3.2 Pressure Change Reproducibility of the DDAC Using an Inconel Gasket.....	17
2.3.3 Time Response of the DDAC Pressure Change	23
2.4 Visualizing Dynamic Phase Transitions Using the DDAC.....	29
2.4 Conclusion	43
Chapter 3: High Pressure Raman Spectroscopy of Protonated and Deuterated Cyclic Aliphatic Tertiary Diamines	47
3.1 Low Barrier Hydrogen Bonds.....	47
3.2 Raman Spectroscopy in a Diamond Anvil Cell	52
3.2.1 Loading the DAC and Obtaining Spectra.....	52
3.2.2 Determining Peak Positions By Fitting A Sum of Gaussian Lineshapes.....	53
3.2.3 Error Analysis of Peak Positions from a Fitted Sum of Gaussian Lineshapes	54
3.3 Results.....	55
3.3.1 33HMCCBr Pressure Dependent Shift in Raman Frequencies	55
3.3.2 TMPHI Pressure Dependent Shift in Raman Frequencies.....	62
3.4 Conclusion	68

Chapter 4 An X-ray Crystallography Study of the Crystal Structure of p-Terphenyl at Varying Temperature.....	71
4.1 The Basics of X-ray Crystallography Structure Determination.....	71
4.2 Optical Studies of p-Terphenyl Crystal Structure Using Pentacene Guest Molecule as Probe	75
4.3 Low and Room Temperature Crystal Structures for PTP	77
4.4 X-ray Diffraction Data Collection for PTP at Varying Temperatures.....	80
4.5 Structure Refinement for PTP at Varying Temperatures	81
4.6 Determining The Phase Transition Temperature From X-ray Diffraction.....	89
4.7 Modeling Disorder in the PTP Crystal Structure	96
4.8 Conclusion	115
Chapter 5: Molecular Dynamics of Mixed Molecular Crystals Under High Pressure and Low Temperature	119
5.1 Introduction.....	119
5.1.1 Experimental Studies of Ideal Mixed Molecular Crystals	119
5.1.2 Refined Classical Forcefield For p-Terphenyl Molecular Dynamics Simulations	120
5.1.3 Fourier Transform Analysis of Molecular Dynamics Trajectories Used For Investigating Molecular Motions.....	121
5.2 Method for Obtaining Hindered Vibrational Modes From Classical Molecular Dynamic Calculation of Pentacene and p-Terphenyl	125
5.2.1 Classical Molecular Dynamics Calculations Settings.....	125
5.2.2 Method for Extracting Translations and Rotation Data for Pentacene from the MD trajectories.....	126
5.2.3 Fourier Transform Analysis of Extracted Translation and Rotation Data	133
5.3 Results of the Hindered Translations and Rotations of Pentacene in p-Terphenyl at 298 K and 50 K.....	134
5.3.1 Improved FT Spectrum Using Additional MD Calculations	134
5.3.2 Effect of Nonbonding Method on the Hindered Translations of Pentacene in p-Terphenyl	135
5.3.3 Determining the Polarization of the Hindered Translation Modes at 298 K and 50 K along Molecular and Crystallographic Axes.....	141
5.3.4 Effect of Pressure on the Frequency of the Calculated Vibrational Modes of the Hindered Translations at 298 K.....	152

5.3.5 Effect of Pressure and a Phase Transition on the Frequency of the Calculated Vibrational Modes of the Hindered Translations at 50 K.....	157
5.3.6 Identification and Removal of Intramolecular Modes from the FT of the Hindered Rotations of the Pentacene in p-Terphenyl at 50 K.....	162
5.4 Conclusions and Future Work.....	166
Appendix	170
A.1 Extraction Scripts.....	170
A.1.1 Center of Mass.....	170
A.1.2 Single Vector Rotations.....	171
A.1.3 Multi Vector Rotations.....	172
A.2 Fourier Transform Mathematica Notebook.....	176

TABLE OF FIGURES

CHAPTER 2:

Figure 2.1 Diagram of the Dynamic DAC Version 1.....	13
Figure 2.2 Diagram of Dynamic DAC V1 Movable Plate.....	14
Figure 2.3 Diagram of the Dynamic DAC Version 2.....	15
Figure 2.4 Pressure Change From PE Actuators Extension versus Varying Initial Pressures Dynamic DAC V.1	19
Figure 2.5 Pressure Change From PE Actuators Extension versus Varying Initial Pressures Dynamic DAC V.2	20
Figure 2.6 Dynamic DAC V.1 Ruby Fluorescence Measurements Before and After Multiple on/off Cycle with PE Actuator	21
Figure 2.7 Dynamic DAC V.2 Ruby Fluorescence Measurements Before and After Multiple on/off Cycle with PE Actuator	22
Figure 2.8 Time Response of Ruby Fluorescence in the Dynamic DAC V.1	24
Figure 2.9 Time Response of Ruby Fluorescence in the Dynamic DAC V.2	25
Figure 2.10 Time Response of the Laser Intensity Blocked by a Moving PE4 Actuator	28
Figure 2.11 Video Images of Water/ Ice VI in Equilibrium in a DDAC Changing as Voltage (150V) Was Instantly Applied to PE Actuators	31
Figure 2.12 Video Images of Water/ Ice VI in Equilibrium in a DDAC Changing as Voltage (150V) Was Instantly Removed to PE Actuators.....	33
Figure 2.13 Video Images of Water/ Ice V1 in Equilibrium in a DDAC Changing as Voltage (150V) Was Instantly Applied to PE Actuators	35
Figure 2.14 Video Images of Water/ Ice VI in Equilibrium in a DDAC Changing as Voltage (150V) Was Instantly Removed to PE Actuators.....	37
Figure 2.15 Video Images of Water/ Ice VI in Equilibrium in a DDAC Changing as a Triangle Wave Was Applied to PE Actuators.....	39

Figure 2.16 Video Images of Ice VI/ Ice VII in Equilibrium in a DDAC Changing as a Triangle Wave Was Applied to PE Actuators.....	41
---	----

CHAPTER 3:

Figure 3.1 Structures for Monoprotonated and Diprotonated Hexamethylcadaverine.....	50
Figure 3.2 Structures for Monoprotonated and Diprotonated Tetramethylputrescine	51
Figure 3.3 Raman Pressure Series (Increasing Pressure) for 33HMCHBrMP	57
Figure 3.4 Raman Pressure Series (Decreasing Pressure) for 33HMCHBrMP.....	58
Figure 3.5 Pressure Induced Shift in Select Peaks for 33HMCHBrMP as Pressure is Increased	59
Figure 3.6 Apparent Hysteresis in Phase Change when Applying Pressure Versus Releasing Pressure	60
Figure 3.7 Raman Spectra of “Monoprotonated” and “Diprotonated” 33HMCHBr.....	61
Figure 3.8 Raman Pressure Studies (Decreasing Pressure) for TMPHIMP	63
Figure 3.9 Raman Pressure Studies (Increasing Pressure) for TMPHIMP.....	64
Figure 3.10 Pressure Induced Shift in the Raman Peak Position for TMPHIMP v1- v4	65
Figure 3.11 Pressure Induced Shift in the Raman Peak Position for TMPHIMP v5- v8	66
Figure 3.12 Evidence of Peak Absence (Shift) due to Deuteration	67

CHAPTER 4:

Figure 4.1 Indexed Reciprocal Lattice Reflections Plots Projected Parallel to the c-Axis.....	91
Figure 4.2 Temperature Dependent Change in Ratio of Grey Reflections to Red Reflections	95
Figure 4.3 PTP Molecule at 298 K with 50% Thermal Ellipsoids Without Modeling Middle Ring Disorder	99
Figure 4.4 PTP Molecule at 298 K with 50%/50% with Middle Ring Disorder	100
Figure 4.5 PTP Molecule at 200 K with 50%/50% with Middle Ring Disorder	101
Figure 4.6 PTP Molecule at 193 K with 50%/50% with Middle Ring Disorder	102

Figure 4.7 Relative Position of Carbon Atoms in with Respect to Each Other in the Disordered Sites	103
Figure 4.8 Four Unique PTP Molecules in the Low Temperature Pseudo Merohedral Triclinic $C\bar{1}$ Space Group (188 K) without Middle Ring Disorder	104
Figure 4.9 Four Unique PTP Molecules in the Low Temperature Pseudo Merohedral Triclinic $C\bar{1}$ Space Group (188 K) with Middle Ring Disorder	105
Figure 4.10 Packing of the PTP Molecules in the $P2_1/a$ Unit Cell at 193 K (ab plane)	108
Figure 4.11 Packing of the PTP Molecules in the $P2_1/a$ Unit Cell at 193 K (001 plane)	109
Figure 4.12 Packing of the PTP Molecules in the $P2_1/a$ Unit Cell at 193 K (along long molecular axis).....	110
Figure 4.13 Packing of the PTP Molecules in the $P2_1/a$ Unit Cell at 193 K (along long molecular axis).....	111
Figure 4.14 Packing of the PTP Molecules in the $P2_1/a$ Unit Cell at 193 K (along b axis).....	112
Figure 4.15 Packing of the PTP Molecules in the Low Temperature Pseudo Merohedral Triclinic $C\bar{1}$ Space Group at 100 K.....	113
Figure 4.16 Packing of the Asymmetrical Unit of PTP Molecules in the Low Temperature Pseudo Merohedral Triclinic $C\bar{1}$ Space Group at 100 K.....	114

CHAPTER 5:

Figure 5.1 Comparison of the Pentacene Molecule and p-Terphenyl Molecule.....	122
Figure 5.2 Phase Diagram of p-Terphenyl Determined From Mixed Crystal Studies.....	123
Figure 5.3 The Effect of the Phase Transition on the Optical Dephasing of Pentacene in p-Terphenyl	124
Figure 5.4 Diagram of the Defined Molecular Axis of Pentacene.....	129
Figure 5.5 Diagram of Molecular Vectors for Rotation Determination.....	131
Figure 5.6 The Effect of Unique and Identical Initial Velocities on MD Calculations.....	137
Figure 5.7 The Effect of Averaging (3 Unique sets) on the Hindered Translation Spectrum	138
Figure 5.8 Successive Averaging On the Hindered Translations For Pentacene in p-Terphenyl at 298 K and 0 kbar.....	139

Figure 5.9 Effect of Atoms Based Versus Ewald Methods For Nonbonding Interactions on the Hindered Translations For Pentacene in p-Terphenyl.....	140
Figure 5.10 Labeled Vibrations from Gaussian Peaks for Hindered Translations For Pentacene in p-Terphenyl at 298 K and 0 kbar	144
Figure 5.11 Polarization of the Hindered Translations For Pentacene in p-Terphenyl at 298 K and 0 kbar along Molecular Axes	145
Figure 5.12 Polarization of the Hindered Translations For Pentacene in p-Terphenyl at 298 K and 0 kbar along Crystal Lattice Axes	146
Figure 5.13 Labeled Vibrations from Gaussian Peaks for Hindered Translations For Pentacene in p-Terphenyl at 50 K.....	147
Figure 5.14 Polarization of the Hindered Translations For Pentacene in p-Terphenyl at 50 K and 0 kbar along Molecular Axes	148
Figure 5.15 Polarization of the Hindered Translations For Pentacene in p-Terphenyl at 50 K and 0 kbar along Crystal Lattice Axes	149
Figure 5.16 Polarization of the Hindered Translations For Pentacene in p-Terphenyl at 50 K and 20 kbar along Molecular Axes (focus on ν_1)	150
Figure 5.17 Polarization of the Hindered Translations For Pentacene in p-Terphenyl at 50 K and 20 kbar along Crystallographic Axes (focus on ν_1).....	151
Figure 5.18 Pressure Induced Shift in the Averaged Hindered Translations Spectra at 298 K.....	154
Figure 5.19 Shift of Vibrational Modes in the Hindered Translations at 298 K.....	155
Figure 5.20 The Mode Grüneisen Parameter Plot for the Hindered Translations of Pentacene in p-Terphenyl at 298 K.....	156
Figure 5.21 Pressure Induced Shift in the Averaged Hindered Translations Spectra at 50 K.....	159
Figure 5.22 Shift of Vibrational Modes in the Hindered Translations at 50 K.....	160
Figure 5.23 The Mode Grüneisen Parameter Plot for the Hindered Translations of Pentacene in p-Terphenyl at 50 K.....	161
Figure 5.24 Reduction of Intramolecular Modes in the Hindered Rotations Spectrum for Pentacene in p-Terphenyl.....	164

Figure 5.25 Pressure Series of the Hindered Rotations of Pentacene in p-Terphenyl at 50 K about Molecular Axes	165
---	-----

TABLE OF TABLES

CHAPTER 4:

Table 4.1 Crystal Data and Structure Refinement for para-Terphenyl at 100 K and 175 K.....	84
Table 4.2 Crystal Data and Structure Refinement for para-Terphenyl at 188 K and 193 K.....	85
Table 4.3 Crystal Data and Structure Refinement for para-Terphenyl at 200 K and 296 K.....	86
Table 4.4 Torsion Angles of PTP Molecules in Monoclinic $P2_1/a$ Space Group at 296 K, 200 K, and 193 K.....	87
Table 4.5 Torsion Angles of PTP Molecules in Triclinic $C\bar{1}$ Space Group at 188 K, 175 K, and 100 K.....	88
Table 4.6 Comparison of Final R1 Values for Crystal Structure at Varying Temperatures with and Without Twinning.....	88
Table 4.7 Total Number of Reflections Harvested from 100 Frames of Partial Data Set and Their Grey/ Red Reflection Ratios at Varying Temperatures.....	94

CHAPTER 5:

Table 5.1 2x2x2 Crystal Lattice Parameters for p-Terphenyl.....	130
Table 5.2 Normalized Crystal Lattice Axes.....	130
Table 5.3 Normalized Molecular Axes of Pentacene.....	130
Table 5.4 Single Vector Definitions of the Rotations of the Pentacene Molecule about Molecular Axes.....	132
Table 5.5 Multivector Definitions of the Rotations of the Pentacene Molecule about Molecular Axes.....	132
Table 5.6 Polarization of the Vibrational Modes of Hindered Translations For Pentacene in p-Terphenyl at 298 K.....	142
Table 5.7 Polarization of the Vibrational Modes of Hindered Translations For Pentacene in p-Terphenyl at 50 K.....	143

Chapter I

An Introduction to High Pressure Experimental and Computational Studies

1.1: Background to the Field of High Pressure Experimental Techniques

The history of high pressure research in the following section has been summarized from more detailed accounts.¹⁻⁷

The work of Percy Bridgman is said to have been a turning point in pressure research and the beginning of the modern era of high pressure research. A major problem preventing higher pressures (>2,000-3,000 atm) being obtained was the leak of the sample from the piston type devices used to obtain pressure. While waiting for replacement parts, Bridgman began tinkering with one of the high pressure presses, modifying the seal to a new design. The new design was geometrically constructed such that a soft solid seal was kept at a pressure slightly larger than the sample under pressure. This prevented leakage from the cell, allowing for initial pressures of up to 7,000 atm to be reached. Bridgman would later reach pressures as high as 20,000 atm.¹

Several attempts by Bridgman and others were made to incorporate glass windows into their piston cells in order to visually and spectroscopically observe samples under pressure; however, many of these attempts failed after, at most, ~12,000 atm.² In 1958, Alvin Van Valkenburg discovered that samples could be placed under pressure and observed when compressed between two diamond anvils. This was the birth of the

diamond anvil cell (DAC).^{3,4} Originally, solid samples were placed between the diamonds and, as force was applied, the sample extruded out from the sides until there was a thin layer of sample that would no longer flow. There was then a pressure gradient on the sample. The use of a gasket for liquid samples, as well as the eventual use of liquid hydrostatic pressure mediums for crystal samples, was developed later, also by Van Valkenburg.³⁻⁵

In 1969, Leo Merrill joined the research group of William Basset at the University of Rochester as a graduate student. For his thesis, Merrill developed a cell able to be mounted to a single-crystal X-ray goniometer for the collection of single-crystal XRD data.³ The Merrill-Basset style DAC consists of the two diamonds attached to metal supports mounted in two steel plates brought together by three screws. A metal gasket is used to contain the sample.

The Merrill-Basset cell, as it has come to be known, has become a popular design,³ and is the design from which the cells used in the Chronister group are based. A recent modification of the Merrill-Basset cell has been developed by the Chronister group which employs piezoelectric actuators to apply the force to the diamonds in a dynamic manner—the Dynamic DAC. This is similar to, but inverse of, the dynamic DAC developed by Evans, *et al.* which uses bolts with spring washers to apply pressure and, using the piezoelectric actuators, dynamically release the pressure.⁸ Our recently developed Dynamic DAC will be discussed in **Chapter 2**.

1.2: Determining Pressure with the Ruby Fluorescence Pressure Scale

In our cells, the typical diamond can have a culet diameter from 1mm to 0.6 mm. Since pressure can be related to force and area by **Equation 1.1**, it can be seen that having a small area allows for large pressures with minimal force. When conducting high pressure experiments, it is useful to know the pressure inside the cell. After developing the new seal for his pressure cell, Bridgman developed a technique for determining the actual pressure inside of the cell. Using a piston with a precisely measured area as well as precise weights for a primary measure of pressure, Bridgman calibrated the change in the electrical resistance of mercury for use as a secondary pressure gauge.^{1,2} DAC experiments often consisted of XRD studies, for which Dan Decker, in 1968, calibrated the compressibility of NaCl to serve as a gauge.³ In 1971, National Bureau of Standards Division Chief Jack Wachtman requested the high pressure group to find a spectroscopic method for measuring pressure in the DAC, suggesting the use of the shift in the ruby fluorescence with pressure.³

$$P = \frac{F}{A} \quad 1.1$$

The use of the shift in the R-lines luminescence of ruby (Cr^{3+} doped Al_2O_3) was first demonstrated up to 22.3 kbar (hydrostatic pressure) and 40kbar (non-hydrostatic pressure) by Forman, et al.⁹ This was followed by calibration up to 195 kbar¹⁰ and then 1 Mbar by 1978¹¹. For the most part, the shift in the R1 fluorescence peak (694.2 nm) is linear ($-0.77 \pm 0.03 \text{ cm}^{-1}$);⁹ However, a more accurate value is obtained from the formula determined by Mao et al, seen in **Equation 1.2** (where $a = 19.04 \text{ Mbar}$, $b=5$, $\lambda_0=6942 \text{ \AA}$

and $\Delta\lambda$ is the shift in the R1 peak maxima).¹¹ The shift of the ruby fluorescence is also temperature dependent and so this must be considered when doing low temperature experiments.⁹ When performing high pressure experiments in a DAC, a small piece of ruby is added to the sample. During the experiment, the pressure in the cell can then be determined at any time by measuring the R1 maximum of the ruby fluorescence peak and determining the shift from its ambient pressure value.

$$P(\text{Mbar}) = \frac{a}{b} \left[\left(1 + \frac{\Delta\lambda}{\lambda_0} \right)^b - 1 \right] \quad 1.2$$

1.3: High Pressure Raman Spectroscopy

The reason the ruby calibration is possible is because the diamonds are relatively clear in the visible (Type I and II) and IR regions (Type II). This property of the diamonds also allows for experimental techniques such as Raman spectroscopy. Raman spectroscopic studies have been performed to study the effects pressure on the vibrational modes, hydrogen bonding and phase transitions of condensed phases.¹²⁻¹⁵ In **Chapter 3**, a DAC has been used to study an interesting class of compounds- cyclic diamines. Effects such as vibrational shifting of hydrogen bonds, low barrier hydrogen bonds, and phase changes will be discussed.

1.4: Computational Studies of Temperature and Pressure Effects on Mixed Crystals

In addition to experimental techniques, computational studies can be performed that look at the effects of parameters such as temperature and pressure.¹⁶⁻²⁰ Studies of p-terphenyl using classical molecular dynamics have led to the development of a forcefield that closely simulates the transition temperature (at ambient pressure) and the transition pressure (at 20 K).^{17,20} Using this forcefield and a modification of a Fourier transform analysis of molecular dynamics trajectories used to study proteins,²¹⁻²³ pentacene in p-terphenyl was studied to investigate the pseudolocal phonon motions of the pentacene for which interesting experimental results exist.²⁴⁻²⁷ This study is described in **Chapter 5**.

1.5: Single Crystal X-ray Diffraction Studies of Temperature Effects on Molecular Crystals

The triclinic low temperature phase of p-terphenyl has been in the literature since the mid 70s.²⁸ However, recent computational studies on the low temperature phase of p-terphenyl^{19,20} has led to further single crystal x-ray studies using modern instrumentation, which has further elucidated the complex nature of the low temperature phase, including single crystal x-ray diffraction evidence of the temperature induced phase change. This study will be discussed in **Chapter 4**.

References

- (1) Hazen, R. M. *The New Alchemists : Breaking Through the Barriers of High Pressure*; 1st ed.; Times Books: New York, 1993.
- (2) Bridgman, P. W. *The Physics of High Pressure*; Dover Publications: New York, 1970.
- (3) Bassett, W. A. *High Pres. Res.* **2009**, *29*, 163
- (4) Benson, W. E.; Sclar, C. B. *Am Mineral* **1995**, *80*, 191.
- (5) Jayaraman, A. *Rev. Mod. Phys.* **1983**, *55*, 65.
- (6) Dunstan, D. J.; Spain, I. L. *J Phys E Sci Instrum* **1989**, *22*, 913.
- (7) Spain, I. L.; Dunstan, D. J. *J Phys E Sci Instrum* **1989**, *22*, 923.
- (8) Evans, W. J.; Yoo, C.-S.; Lee, G. W.; Cynn, H.; Lipp, M. J.; Visbeck, K. *Review of Scientific Instruments* **2007**, *78*, 073904.
- (9) Forman, R. A.; Piermarini, G. J.; Barnett, J. D.; Block, S. *Science* **1972**, *176*, 284.
- (10) Piermarini, G. J.; Block, S.; Barnett, J. D.; Forman, R. A. *J Appl Phys* **1975**, *46*, 2774.
- (11) Mao, H. K.; Bell, P. M.; Shaner, J. W.; Steinberg, D. J. *J Appl Phys* **1978**, *49*, 3276.
- (12) Adams, D. M.; Sharma, S. K. *Journal of the Chemical Society, Faraday Transactions 2: Molecular and Chemical Physics* **1978**, *74*, 1355.
- (13) Mishra, A. K.; Murli, C.; Sharma, S. M. *The Journal of Physical Chemistry B* **2008**, *112*, 15867.
- (14) Shimada, H.; Nibu, Y.; Shimada, R. *J Raman Spectrosc* **2008**, *39*, 32.
- (15) Yoo, C.-S.; Cynn, H. *The Journal of Chemical Physics* **1999**, *111*, 10229.
- (16) Berendsen, H. J. C.; Postma, J. P. M.; van Gunsteren, W. F.; DiNola, A.; Haak, J. R. *The Journal of Chemical Physics* **1984**, *81*, 3684.
- (17) Bordat, P.; Brown, R. *Chem Phys* **1999**, *246*, 323.
- (18) Parrinello, M.; Rahman, A. *J Appl Phys* **1981**, *52*, 7182.

- (19) Schatschneider, B. 3332637, University of California, Riverside, 2008.
- (20) Schatschneider, B.; Chronister, E. L. *Mol Simulat* **2008**, *34*, 1159.
- (21) Dauber-Osguthorpe, P.; Osguthorpe, D. J. *J Am Chem Soc* **1990**, *112*, 7921.
- (22) Dauber-Osguthorpe, P.; Osguthorpe, D. J.; Stern, P. S.; Moulton, J. *Journal of Computational Physics* **1999**, *151*, 169.
- (23) Sessions, R. B.; Dauber-Osguthorpe, P.; Osguthorpe, D. J. *Journal of Molecular Biology* **1989**, *210*, 617.
- (24) Baer, B. J.; Chronister, E. L. *The Journal of Chemical Physics* **1993**, *99*, 3137.
- (25) Baer, B. J.; Chronister, E. L. *Chem Phys* **1994**, *185*, 385.
- (26) Baer, B. J.; Chronister, E. L. *High Pres. Res.* **1994**, *12*, 101
- (27) Baer, B. J.; Chronister, E. L. *The Journal of Physical Chemistry* **1995**, *99*, 7324.
- (28) Baudour, J. L.; Delugeard, Y.; Cailleau, H. *Acta Crystallographica Section B* **1976**, *32*, 150.

Chapter II

Development and Characterization of a Dynamic Diamond Anvil Cell (DDAC)

2.1: The Interesting Uses of the DDAC

The world is dynamic and changing; often new methods are required to study those changes reversibly and on a timescale of interest. Modern interest in dynamics can be seen in the field of biochemistry where protein dynamics are studied. In protein dynamics, scientists are attempting to better their understanding of the kinetics and thermodynamics of the folding of proteins into their native conformations. Common techniques for causing proteins to denature (unfold) are by adding a chemical denaturant,¹ changing the temperature,²⁻⁴ and changing the pressure.³⁻⁸ An advantage of pressure-induced denaturing is its ability to study both the folding and unfolding kinetics.³⁻⁶ It has been shown that pressure-induced denaturing may not under go similar pathways to that of temperature- and chemical-induced denaturing.^{3,6} It has also been shown that the rate of unfolding in several proteins is much slower than that of folding.^{3,5,6}

Pressure-induced denaturation experiments have been performed using high pressure pumps⁵⁻⁹ and valves as well as studies using a standard DAC.^{3,4} In studies by Panick, et al.⁴, staphylococcal nuclease (Snase) was studied using temperature and pressure denaturation by synchrotron X-ray small angle scattering (SAXS) and FT-IR. It

was shown that pressure induced denaturing for Snase begins around 1800 bar for wild type Snase and is reversible.⁴ Upon denaturing, the radius of gyration for Snase increased, but not as much as expected for a completely random coil. Pair-distance distribution functions show a change in the shape from spherical to ellipsoidal.⁴ FT-IR analysis shows that pressure denaturing increases the amount of turn structures and disorder, and decreases the amount of β sheets and α helices; some of the β structure remains in the final denatured state.⁴

A related, interesting field of pressure induced dynamics is phase transitions. Pressure can alter the state of matter for many things, from everyday compounds such as H_2O ¹⁰⁻¹⁴ to chemical explosives such as HMX¹⁵. The kinetics, with respect to the pressure induced phase change, in such materials has sparsely been examined experimentally due to the limitations of dynamic high pressure methods. However, the Dynamic DAC is a useful tool for investigating such phenomena.

The solid phases of water, for example, have been studied by static means using a DAC and the raman spectroscopic changes due to the phase transitions have been examined for both temperature and pressure.¹⁰⁻¹² Recently, a dynamic DAC (dDAC) has been developed¹⁶ by Evans *et al.* and used to examine the effect of the compression rate on the phase transitions of Ice VI^{17,18} and Ice VII.¹⁸

In a study using their dDAC, it was shown that as the compression rates were increased, the crystal growth of Ice VI went from an octahedral facet growth to faceted, concaved shaped, 4-fold symmetric dendritic growth.¹⁷ The rate of and type of (sinusoidal versus step) the compression waveform were contributing factors to the

formation of the 4-fold symmetric dendritic growth. Particularly, the important factor was the sinusoidal compression waveform shape; when a step function of similar compression rate was applied the dendritic type growth did not occur.¹⁷

In another study, their dDAC was used to supercompress water into the stability region of Ice VI followed by a transformation to a metastable Ice VII state.¹⁸ The metastable Ice VII was shown to transition back to Ice VI then water as the compression was removed. It has been suggested that high density water has a similar local structure to Ice VII giving it a smaller interfacial energy; this would give rise to the formation of the metastable Ice VII state.¹⁸

In **Section 2.4**, the capability to induce and observe the phase transitions of water \leftrightarrow Ice VI and Ice VI \leftrightarrow Ice VII is demonstrated for our Dynamic DAC developed in **Section 2.2**.

2.2: Development of the DDAC

In developing a method for fast, high pressure (kbars of pressure) dynamic studies, a modification of the Merrill-Basset DAC was built using PE4 Thorlabs piezoelectric (PE) actuators to apply the pressure to the diamond anvils. The pressure changes would be obtained by using the 4mm manual adjustment to set a starting pressure and the 15 μ m extension of the piezoelectric stack would apply additional pressure. This design is different than the dDAC built by Evans, *et al.*, which uses spring washer loaded screws to apply the initial pressure to the sample, while the PE actuators

are used to release the pressure with applied voltage.¹⁶ This is reverse to that of the cell proposed in the rest of this chapter.

The first version of this cell design consists of a static top plate (part A in **Figure 2.1**) which is bolted to the base plate (Part C in **Figure 2.1**), which also holds the piezoelectric actuators (Part D in **Figure 2.1**). The diamond anvils are attached to backing plates (not shown), which each insert into the static top plate (part A) and the movable plate (Part B in **Figure 2.1**) that glides along the shoulder bolts, and to which the PE actuators apply their force. The pieces are made from Inconel 718 material and the PE actuators are attached to the base plate by use of a spring and clamp that required a modification of the PE4 Thorlabs casing by making a small notch into which the clamps slide.

Initial measurements of the ruby fluorescence indicated ~1 kbar pressure change, when voltage was applied to the PE actuators with a preloaded cell, lower than estimated by the amount of compression that was expected from the 15 μm extension by the actuators upon application of 150 volts. For this reason, physical measurements of the movement in the plates of the cell when 150 volts was applied to the PE actuators were taken using a digital dial indicator. The results of those measurements indicated that the static top plate appeared to be moving by 0.0002 ± 0.0001 in (4.8 μm) and the movable plate (measured at the three “wings” of the plate seen in **Figure 2.2**) was moving 0.0004 ± 0.0001 in (9.6 μm). This suggested that the cell might have bending issues that, due to the scale of the travel of the PE actuators (micrometers), could significantly limit the pressure change.

For this reason, several modifications to the version 1 cell were made including supporting plates of stronger material to prohibit the bending of the plates. These supporting plates were made of tungsten carbide. Results from the use of these plates, both measurements with the dial indicator and ruby fluorescence pressure measurements seemed to indicate no change in the amount of travel and pressure change capable by the cell.

At this point, a new cell with a modified design from the former was designed and constructed to prevent bending. Since guide pins are used in the two plates containing the diamond anvils, it was deemed an unnecessary source of friction to have the movable plate glide along the shoulder bolts that restrict the movement of the static top plate. The second version of the DDAC is shown in **Figure 2.3**. In this version of the cell, the static top plate (part A in **Figure 2.3**) is the same diameter as the base plate (part C in **Figure 2.3**), and much thicker than the top plate of the version 1 cell. The movable plate (part B in **Figure 2.3**) is smaller in diameter so as to not glide along the shoulder bolts. This also allows the PE actuators (part D in **Figure 2.3**) to apply their force closer to the center of the movable plate, where a diamond anvil is located, which limits the amount of bending that can occur. The movable plate is also thicker than that of the version 1 cell. Furthermore, all the plates were made of Inconel 718, as in the previous cell, but the material was commercially hardened to stiffer specifications. Initial ruby fluorescence pressure measurements with application of PE actuators at different initial pressures indicated a ~1 kbar pressure change like that of the version 1 cell. However, further characterization yielded a ~5 kbar pressure change, which is shown in the next section.

Figure 2.1: Diagram of the Dynamic DAC Version 1

A: Static Top Plate

B: Movable plate

C: Base Plate

D Piezoelectric (PE) Actuators

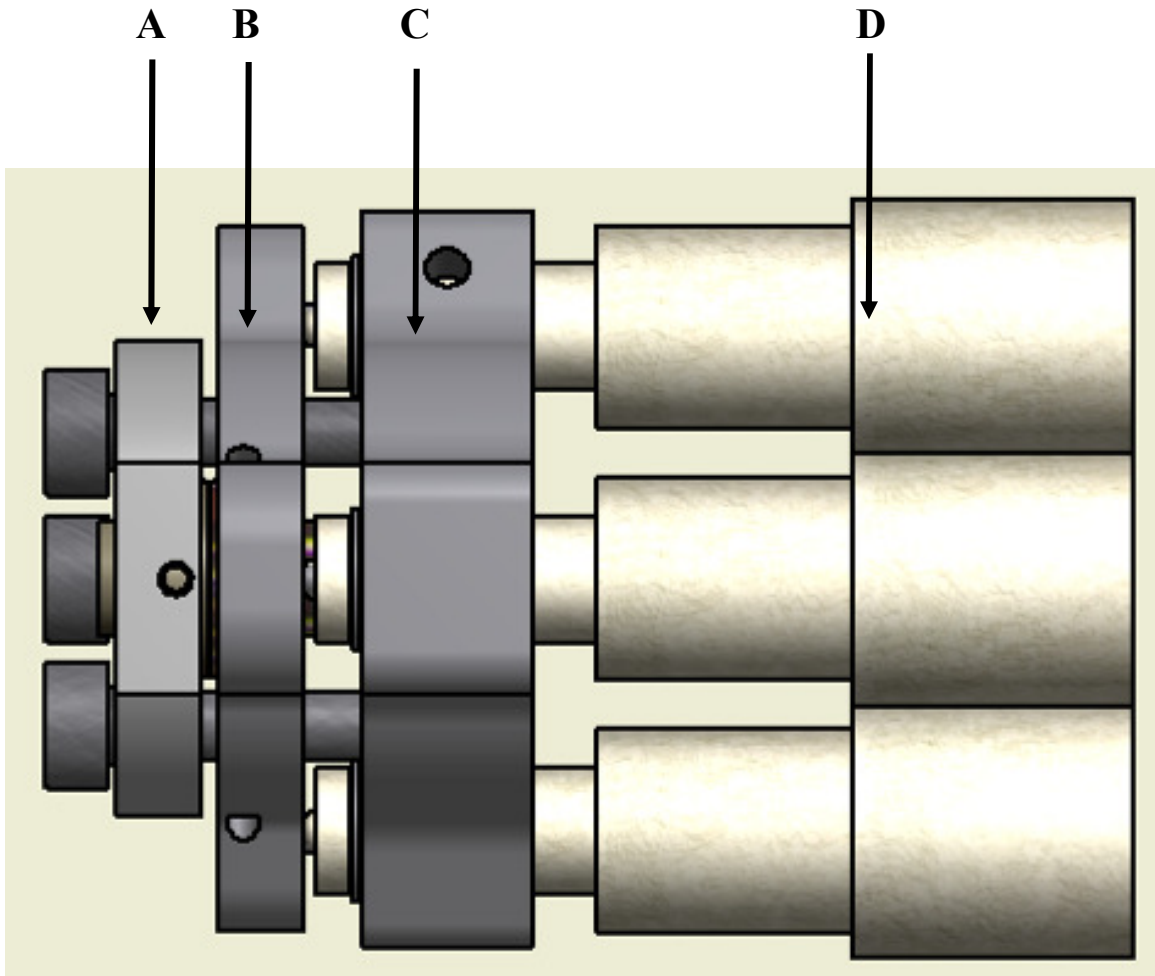


Figure 2.2: Diagram of Dynamic DAC V1 Movable Plate
This demonstrates the “wings” which are labeled with arrows.

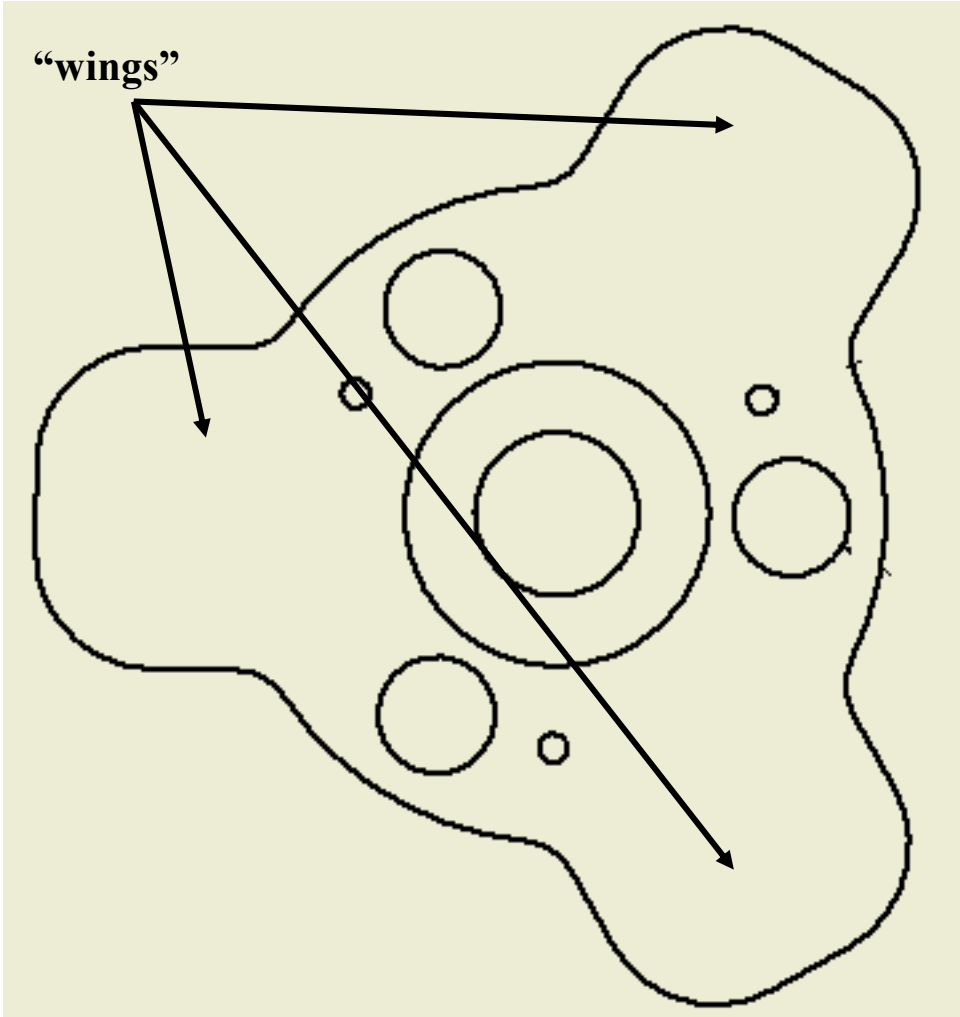


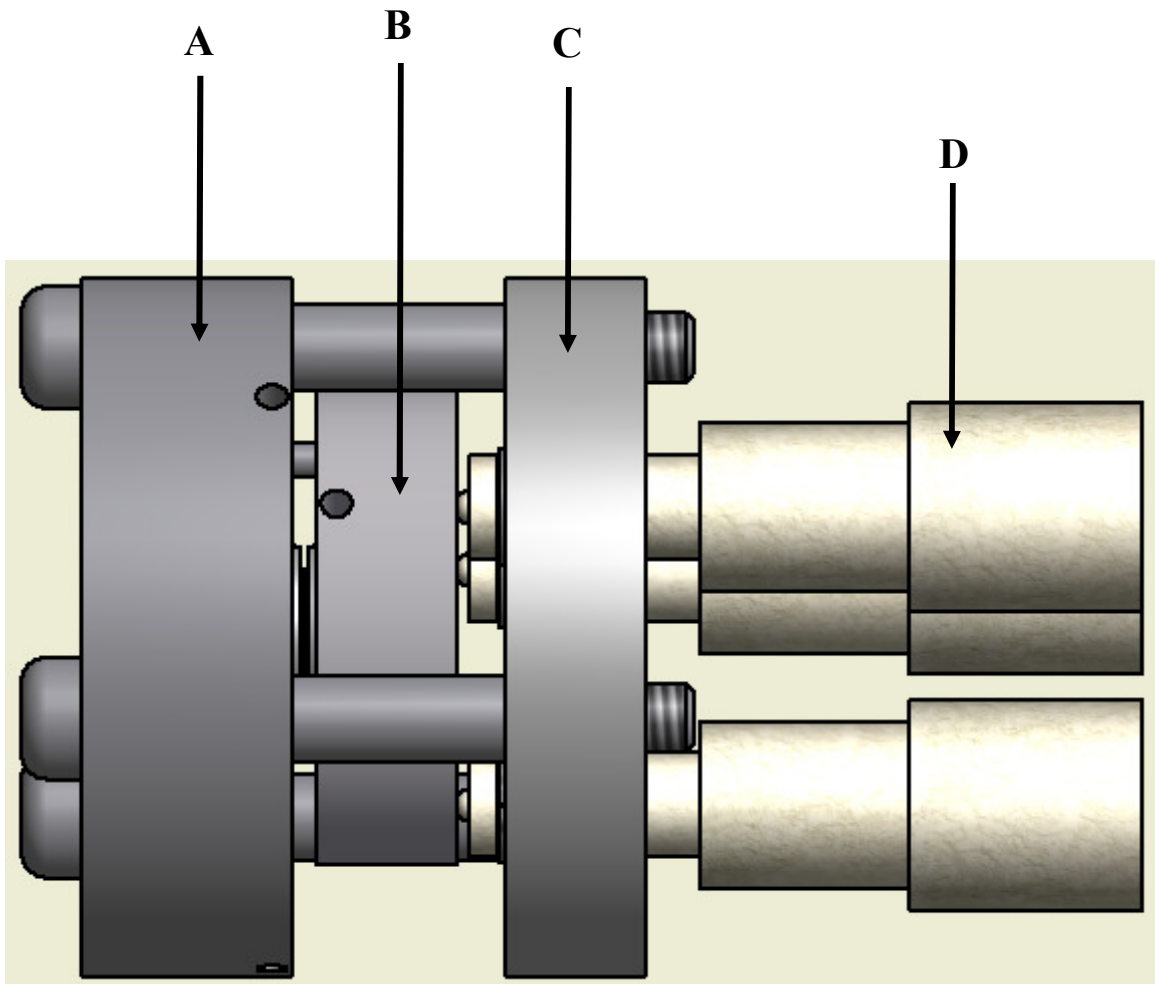
Figure 2.3: Diagram of the Dynamic DAC Version 2

A: Static Top Plate

B: Movable plate

C: Base Plate

D Piezoelectric (PE) Actuators



2.3: Characterization of the Dynamic Pressure Capability of the DDAC

2.3.1 Characterization of the Pressure Range of the DDAC

A Rhodamine 101 in PMMA sample was loaded with a chip of ruby into a small 0.4 mm hole of an Inconel gasket. This was done for both versions of the DDAC. Each cell was then assembled by tightening the shoulder bolts, followed by applying the initial pressure by the manual four millimeter adjustment of the piezoelectric (PE) actuators. This was done in a uniform manner to assure that the backing plates (as well as the diamonds) remained parallel to each other. The pressures in the cell were determined using the Mao *et al.* ruby fluorescence calibration equation¹⁹, previously described in **Chapter 1**. All ruby fluorescence measurements were made using a Dilor XY Laser Raman Spectrometer with a 532 nm DPSS laser with an output of ~200 mW. A 532 nm band pass filter was used to remove any sidebands from the laser, and cut the power by approximately half. Neutral density filters were used as needed.

In order to study the amount of pressure change capable by the cells, an initial pressure was applied using the manual 4 mm adjustment on the PE actuators; this pressure was labeled “0 volts” as ~0 V was applied to the PE actuators. After this measurement, the pressure was measured for the cell when the maximum acceptable voltage (~150 volts) was applied to the PE actuators, labeled “150 volts.” This was done over a range of pressures from about 5 to 50 kbar, making measurements every pressure as the pressure was increased, and then backing off in pressure making the measurements. The results of this experiment show that as the initial pressure is

increased, the change in the pressure also increases (to ~4-5 kbar), which makes sense as the increased initial pressure is due to a compressed sample volume which makes the relative compression from the PE extension greater. Also, as the initial pressure was released back down from ~40 kbar, the change in the pressure when voltage is applied to PE actuators remains around ~4-5 kbar. This hysteresis effect can be seen in **Figures 2.4 and 2.5** and suggests the cells require some sort of pressure annealing to perform the greatest pressure changes at the lower pressures.

2.3.2 Pressure Change Reproducibility of the DDAC Using an Inconel Gasket

Having shown the DDAC could obtain a pressure change of at least ~5 kbar, the reproducibility was tested to see if the elasticity of the Inconel was enough to handle multiple on/off pressure change cycles. Samples loaded in the previous experiment, were used for both of the dynamic DAC cells. The set up used a ~20.4 ms period symmetric square wave to switch the applied voltage on the PE actuators quickly so as to do a large number of cycles in a two hour time frame. Using this method, the dynamic DAC underwent ~353,000 on/off pressure cycles. As can be seen in **Figures 2.6 and 2.7**, there was minimal pressure loss over the period of cycling when using the Inconel gasket material. Although there are small shifts, they do not appear to be a consistent and clear evidence of pressure loss. Although the sample pressure change appears to decrease (from ~ 4kbar to 3 kbar change) after the multiple cycles for dynamic DAC V.1, the overall pressure appears to have increased (from ~6.6 kbar to 7 kbar.) However, in the

dynamic DAC V.2, the both the pressure change and the initial pressures remain close to the same. These are all within an expected error of ~ 1 kbar for the pressure measurements.

Figure 2.4: Pressure Change From PE Actuators Extension Versus Varying Initial Pressures for Dynamic DAC V.1

After increasing the pressure to ~40 kbar (red series), the return measurements (green series) show that the change in pressure caused by voltage on the PE actuators is larger at lower pressures.

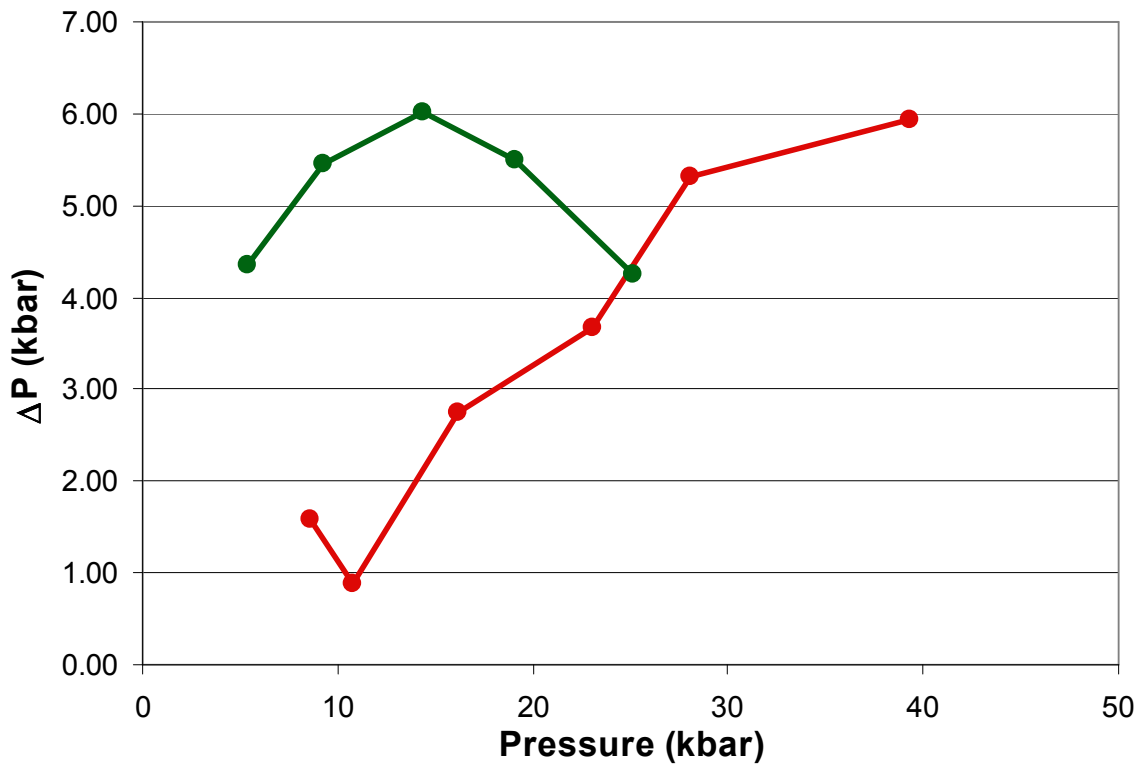


Figure 2.5: Pressure Change From PE Actuators Extension Versus Varying Initial Pressures for Dynamic DAC V.2

After increasing the pressure to ~48 kbar (red series), the return measurements (green series) show that the change in pressure caused by voltage on the PE actuators is larger at lower pressures.

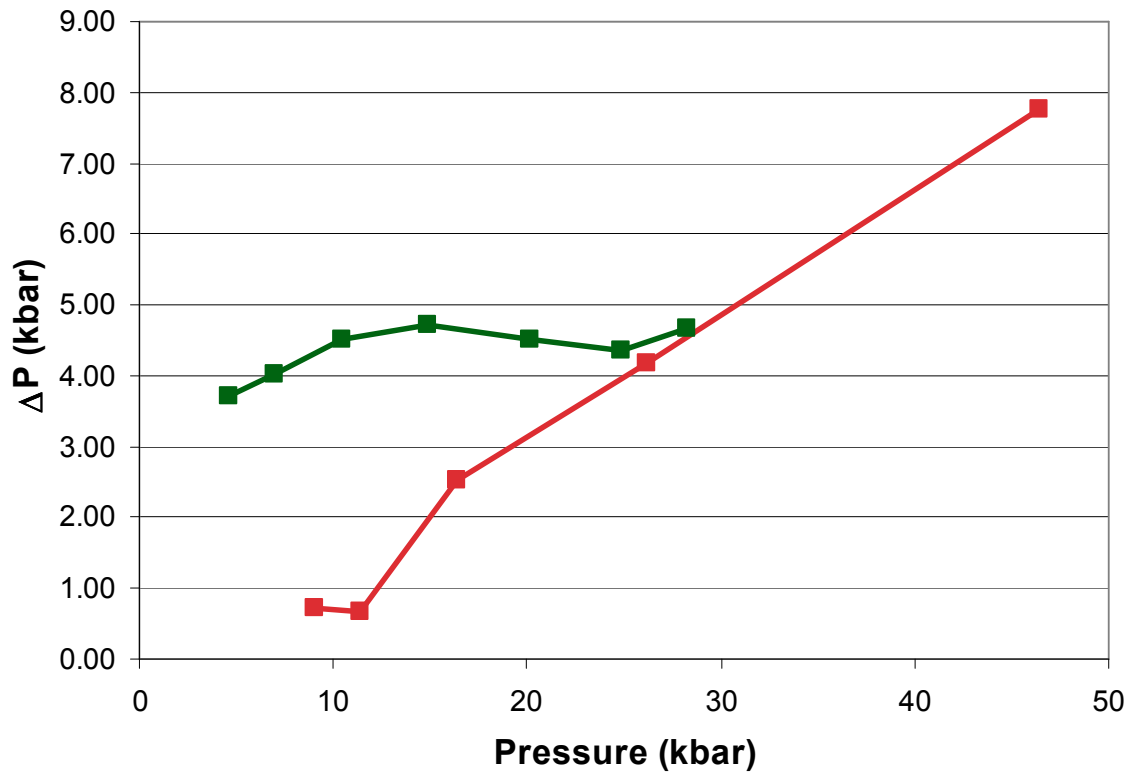


Figure 2.6: Dynamic DAC V.1 Ruby Fluorescence Measurements Before and After Multiple on/off Cycle with PE actuators (Inconel Gaskets)

The ruby fluorescence in the dynamic DAC V.1 with 0 volts (a) and 150 Volts (b) applied to the PE actuators before and after the 353,000 on/off cycles. The blue is the spectra before and the red is the spectra after.

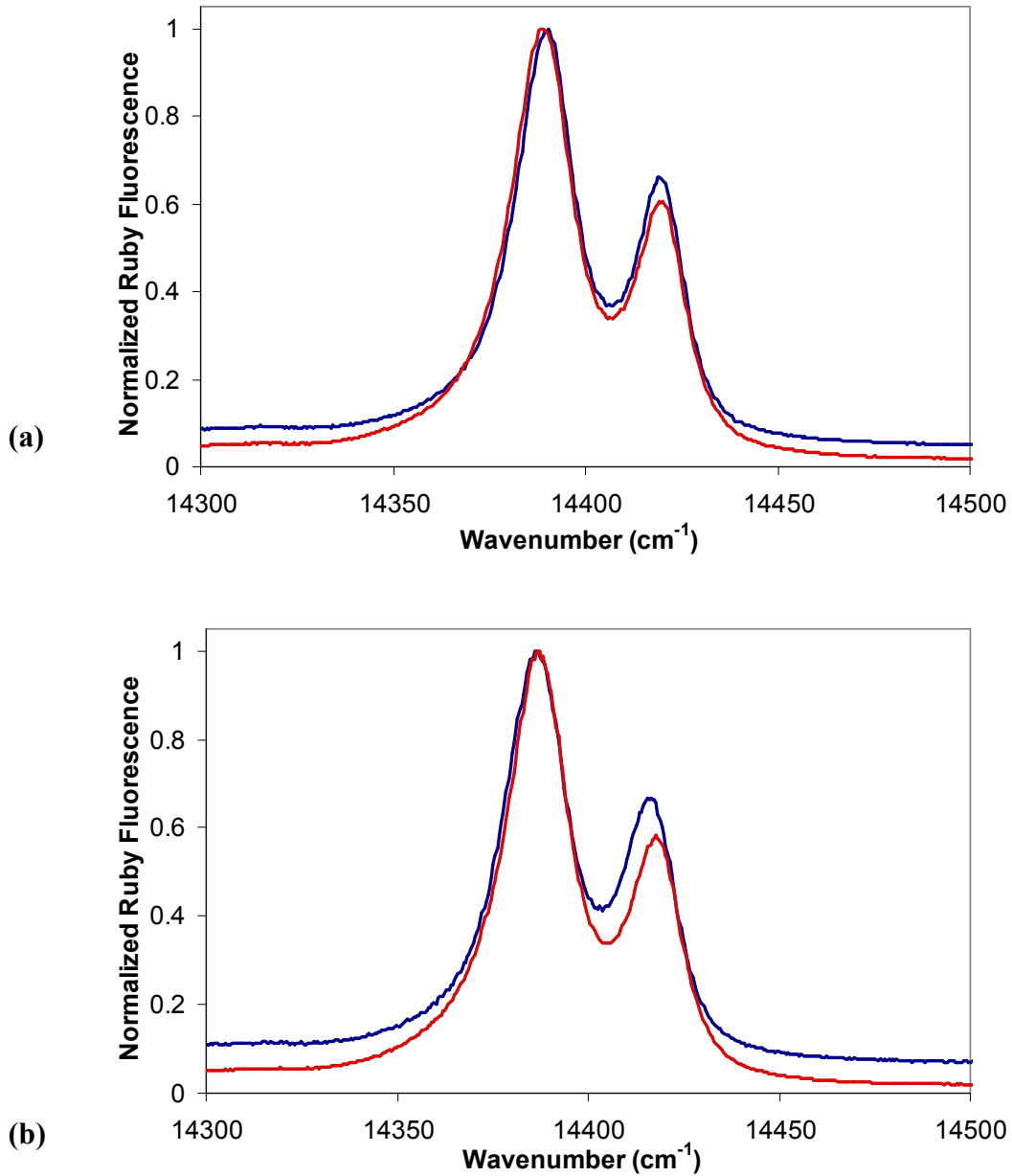
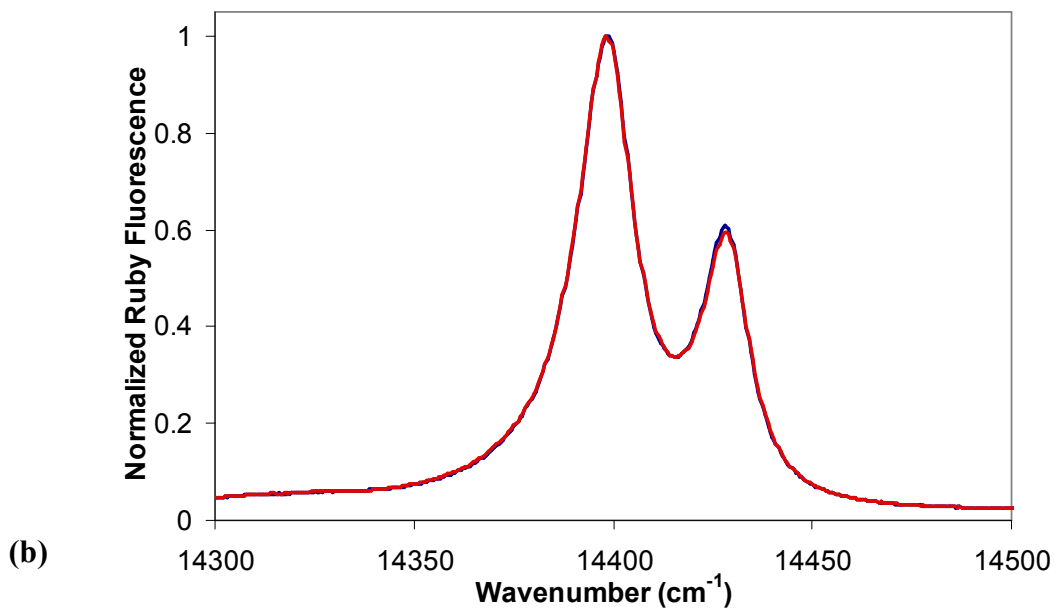
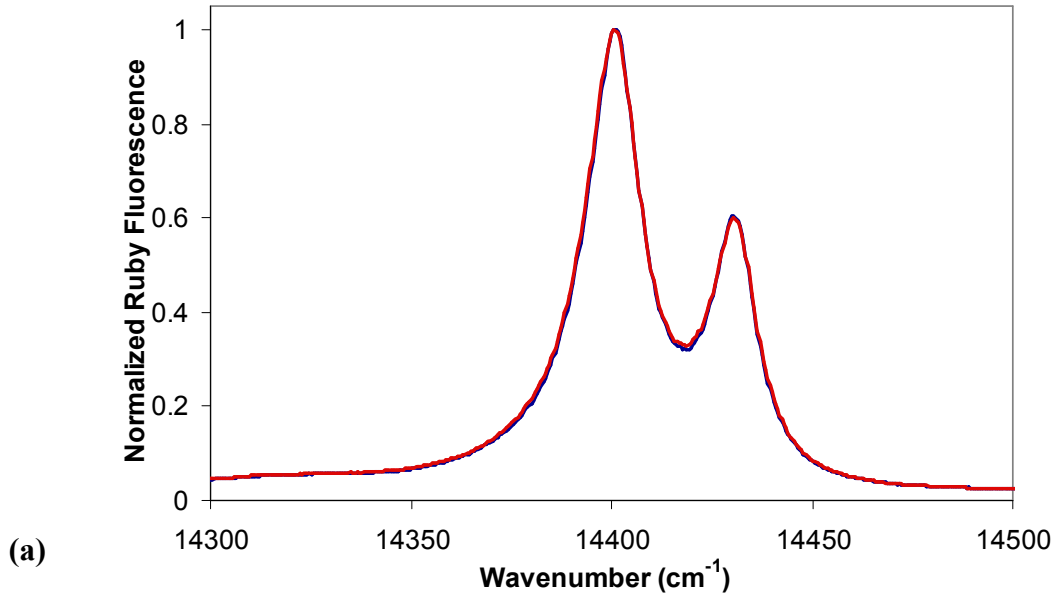


Figure 2.7: Dynamic DAC V.2 Ruby Fluorescence Measurements Before and After Multiple on/off Cycle with PE actuators (Inconel Gaskets)

The ruby fluorescence in the dynamic DAC V.2 with 0 Volts (a) and 150 volts (b) applied to the PE actuators before and after the 353,000 on/off cycles. The blue is the spectra before and the red is the spectra after.



2.3.3 Time Response of the DDAC Pressure Change

In order to determine the time response of the pressure change made in the DDAC, the shift in the ruby fluorescence R1 peak due to the pressure change was measured using the following described set up: A 532 nm DPSS laser was focused into the DDAC with the resulting ruby fluorescence focused into a SPEX double monochromator with an attached peltier cooled PMT detector. The data was collected using a digital oscilloscope by setting the double monochromator to a desired wavenumber (typically, off center from the maxima of the R1 ruby fluorescence peak) and measuring the change in the intensity of the PMT signal due to the pressure induced shift in the R1 peak. The resulting time response in the two DDAC (Versions 1 and 2) can be seen in **Figure 2.8 and 2.9**. It can be seen that for the V.1 cell, there is a 8 ms time response while for the V.2 cell there is a 4 ms time response. This is counter intuitive to expected decrease in the speed of the movable plate in the Version 2 cell due to its increased mass.

Figure 2.8: Time Response of Ruby Fluorescence in the Dynamic DAC V.1
The ruby fluorescence time response of the DDAC V.1 when (a) applying and (b) releasing the pressure using the PE actuators extension. The time response appears to be around 8 ms.

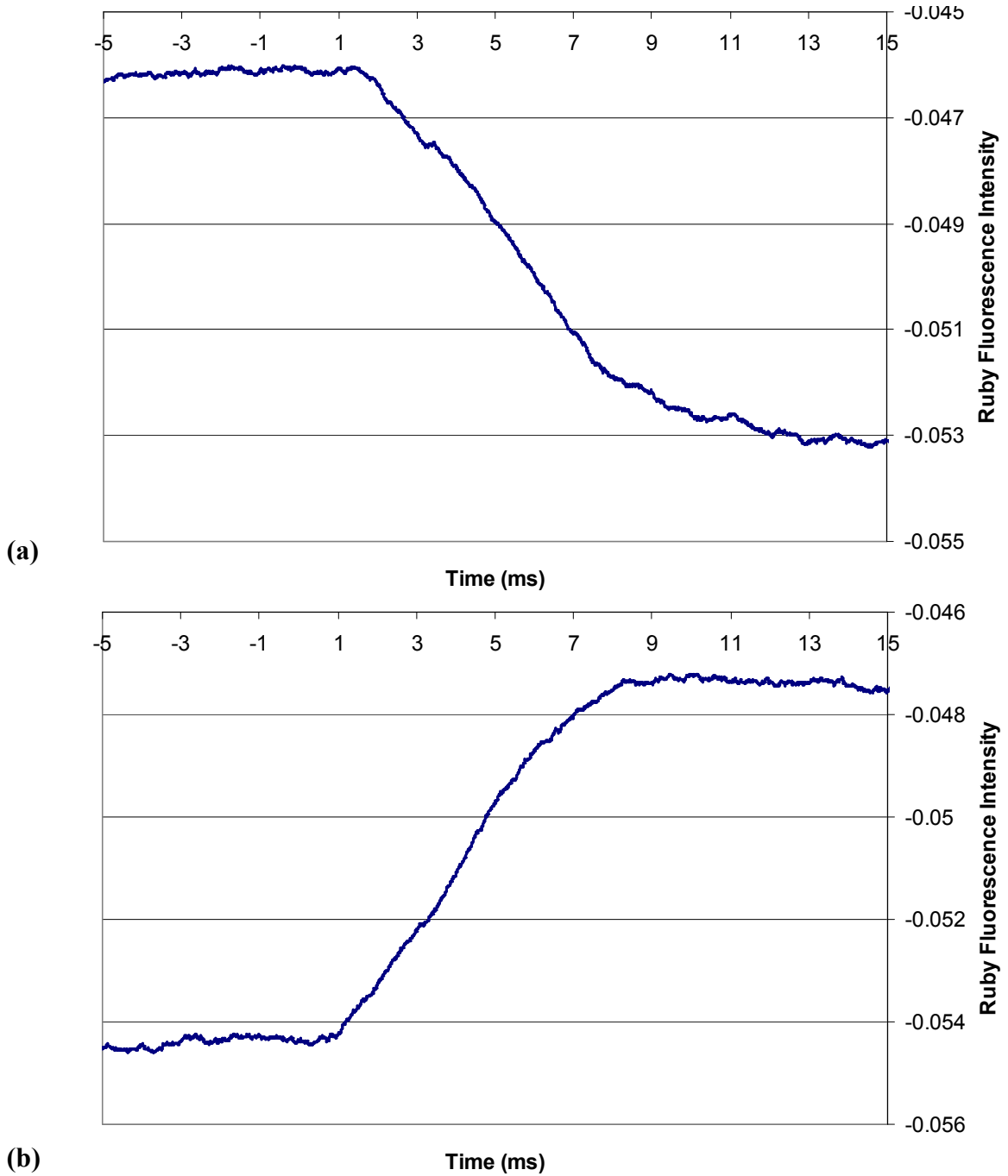
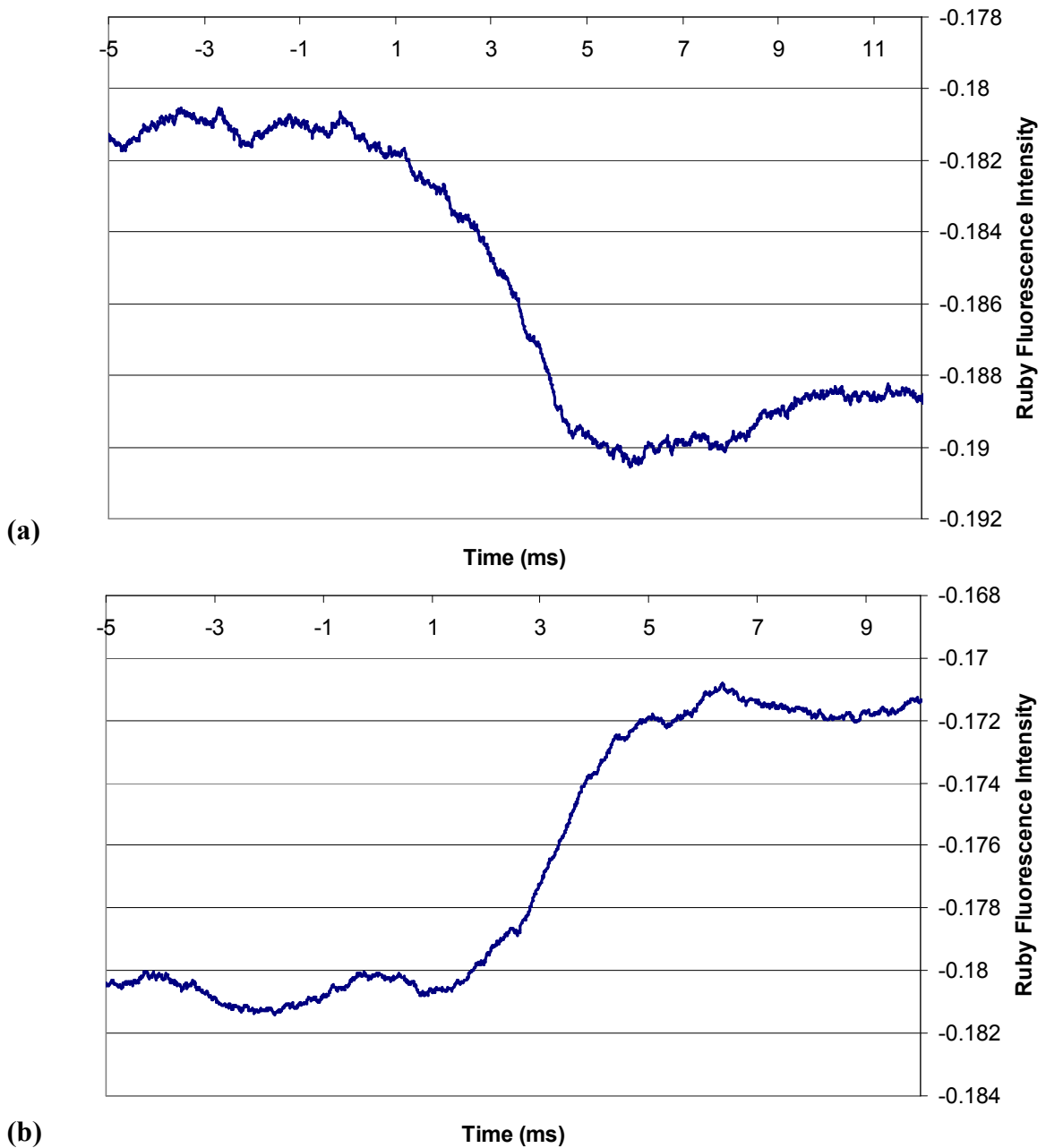


Figure 2.9: Time Response of Ruby Fluorescence in the Dynamic DAC V.2
The ruby fluorescence time response of the DDAC V.2 when (a) applying and (b) releasing the pressure using the PE actuators. The time response appears to be around 4 ms.



In order to understand what is going on, it is necessary to look further into the time response of the whole DDAC set-up. The time response of the high voltage output from the Thorlabs MDT693A PE voltage driver was measured at each port by use of a high voltage oscilloscope probe and a digital oscilloscope. It was shown that with no load attached the voltage takes $\sim 100 \mu\text{s}$ to internally charge and discharge; whereas, with the $1.4 \mu\text{F}$ PE actuator attached, the high voltage took $\sim 4.1 \text{ ms}$ to charge and $\sim 3.6 \text{ ms}$ to discharge. These time scales suggest that the attached PE actuators should not be able to go any faster than $\sim 4 \text{ ms}$, being limited by the rate at which the voltage is able to increase. This leaves the possibility that due to the irregular shape of the moving plate in the DDAC V.1 and the location of the point of contact of the PE actuators that the wings of the plate, which make direct contact with the PE actuators, are moving at the speed of the PE actuators while the center portion of the plate is left to trail behind. Since the shape of the movable plate in the DDAC V.2 cell is circular and the PE actuators make contact closer to the center (where the diamond anvils are located), such bending is less likely to occur.

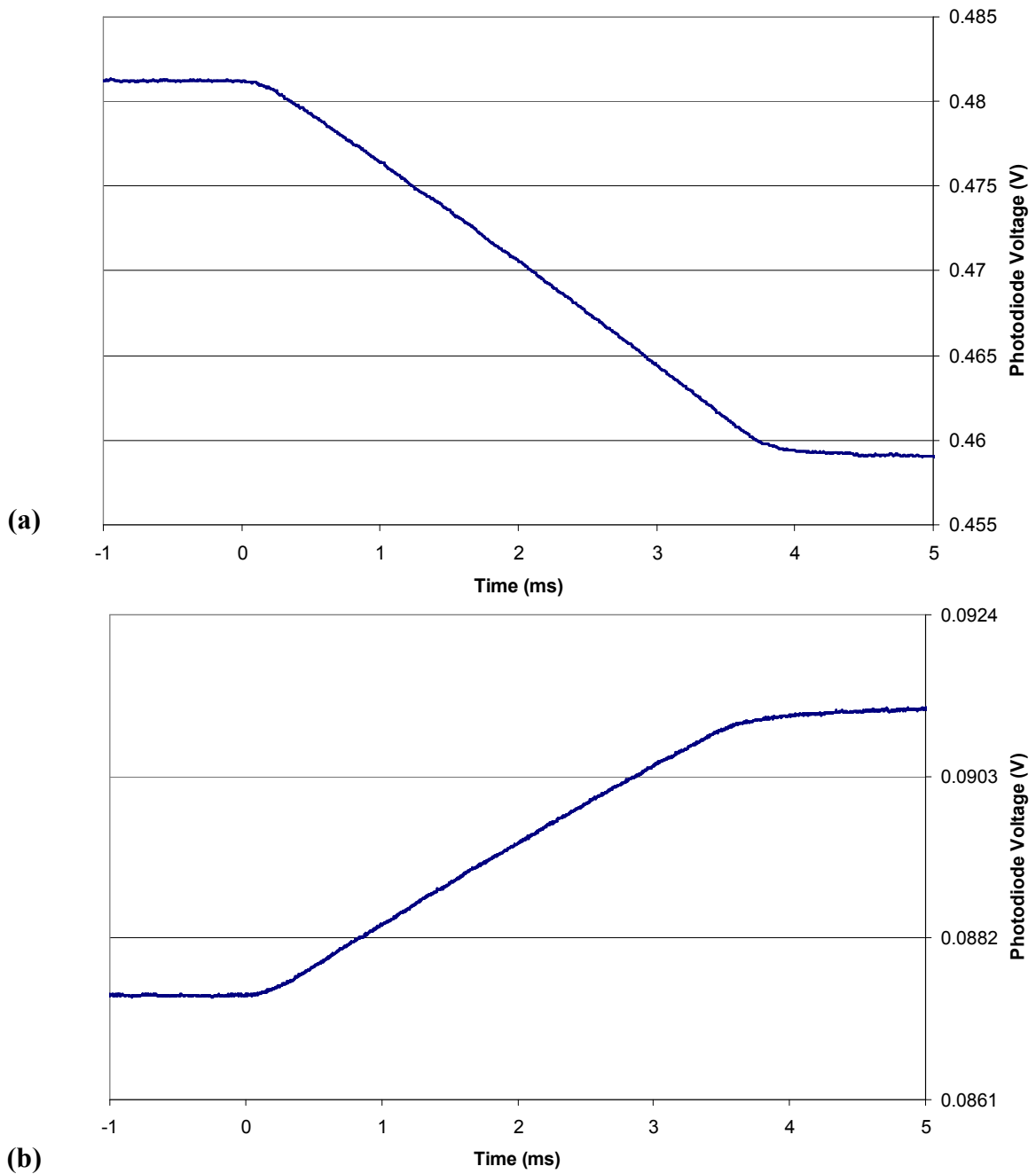
This is further supported by the measurement of the movement of the PE actuators with time. Using a collimated light source (532 nm DPSS laser,) a PE actuator is placed so that the tip blocks the center of the beam, which is being directed into a photodiode connected to a 22 V battery. Neutral density filters are used so as to not overload the photodiode. The signal from the photodiode was averaged using a digital oscilloscope triggered by the same frequency square wave driving the PE voltage driver. While the resulting time response curve from the experiment is affected by the beam

profile of the laser, it is enough to see that there is a ~ 4 ms time scale for the full movement of the PE actuator (**Figure 2.10**).

This evidence demonstrates that the current limit of the time response in the DDACs is due to the voltage driver for the PE actuators. Work on a custom voltage driver is in progress and initial results indicate that a μs time scale is obtainable.

Figure 2.10: Time Response of the Laser Intensity Blocked by a Moving PE4 Actuator

The time response of the **(a)** charging (extending) and **(b)** discharging (contracting) 1.4 μF PE actuator represented by the change in the intensity of laser light collected by a photodiode. The time response appears to be around 4 ms.



2.4: Visualizing Dynamic Phase Transitions Using the DDAC

One of the useful properties of diamond anvil cells is the ability to visualize what is taking place under pressure. The equilibrium between two states of matter in a pressure induced phase transition can be observed using a DAC²⁰. One interesting system that undergoes phase transitions with applied pressure is water. At room temperature, liquid water undergoes a phase change to a form of ice called Ice VI, at ~10 kbar, and then to Ice VII at ~23 kbar¹³. For these reasons, the liquid water/Ice VI and Ice VI/ Ice VII transitions were studied using the DDAC and a home made video microscope.

The video microscope consisted of a white light source focused into the sample hole of the DDAC. The image of the sample was then collected using a 4 cm lens and projected onto the CMOS detector of a Pixelink PL-B742F CMOS video camera. A sample of Millipore filtered water was loaded into the 0.4 mm hole of an Inconel gasket, along with a chip of ruby for pressure determination using ruby fluorescence. In order to view the equilibrium mixture, the manual adjust screws for the PE actuators were used to apply an initial pressure several kbars above the room temperature transition pressure (~10 kbar for Ice VI and ~23 kbar for Ice VII) to insure that the sample underwent the expected phase change. Then, while viewing the sample using the video microscope, the pressure was lowered using the manual adjusting screws of the PE 4 actuators until the equilibrium between two states (either water Ice VI or Ice VI/ Ice VII) could be observed. The videos were captured at 20 fps as .avi and converted to .mov files.

In **Figures 2.11** and **2.12**, the water/ Ice VI ratio was shown to alter as the compression provided by the PE actuators were turned on and off manually. This was done by turning the enable button on and off on the Thorlabs Piezoelectric control box, which controls the voltage applied simultaneously to the separate PE actuator ports labeled X, Y, and Z on the box. Growth of the denser Ice VI can be seen in **Figure 2.11** as the compression is increased. In **Figure 2.12**, melting of the Ice VI crystal to form the less dense liquid water was observed when compression was decreased.

In **Figures 2.13** and **2.14** a similar video was recorded. However, instead of directly turning on and off the voltage, software was used to control the Thorlabs voltage driver and apply an 18 s square wave function to the three separate ports. The change in the water/ Ice VI ratio change was less noticeable. A possible explanation could have been the software was not accurately delivering the 150 V max as in the previous experiment. However, the measured voltage at the port using a high voltage probe was shown to be 150 V. Another explanation is that the DDAC cell used for these experiments had not yet consistently shown the large pressure (compression) change in previous characterizations, as was later demonstrated possible. It is likely that the sample in **Figures 2.11** and **2.12** was experiencing a larger compression change from the applied voltage than in **Figures 2.13-2.16**. Since the changes are more subtle in **Figures 2.13-2.16**, arrows have been drawn to direct attention to areas where change is best observed.

Figure 2.11: Video Images of Water/ Ice VI in Equilibrium in a DDAC Changing as Voltage (150 V) Was Instantly Applied to PE Actuators

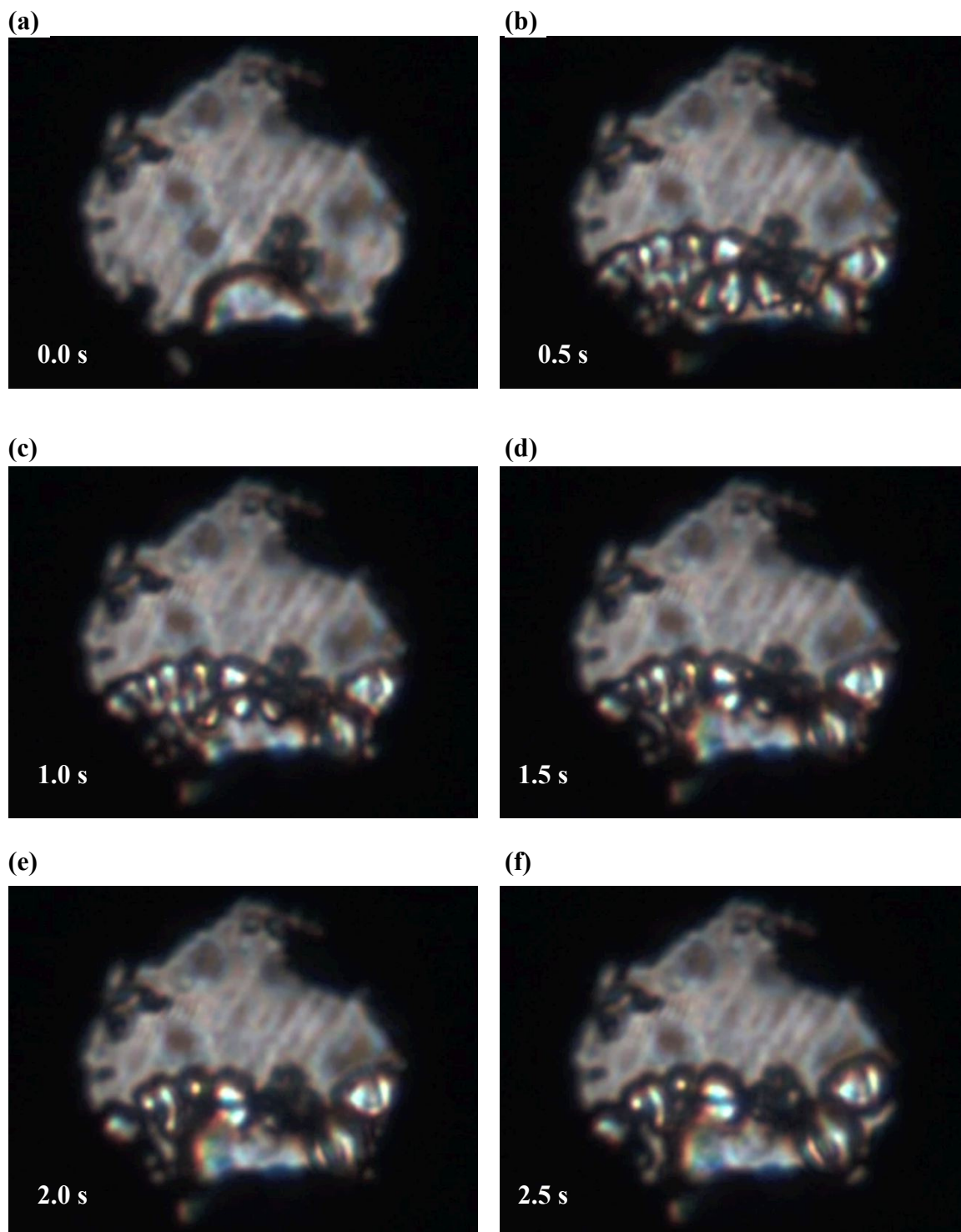
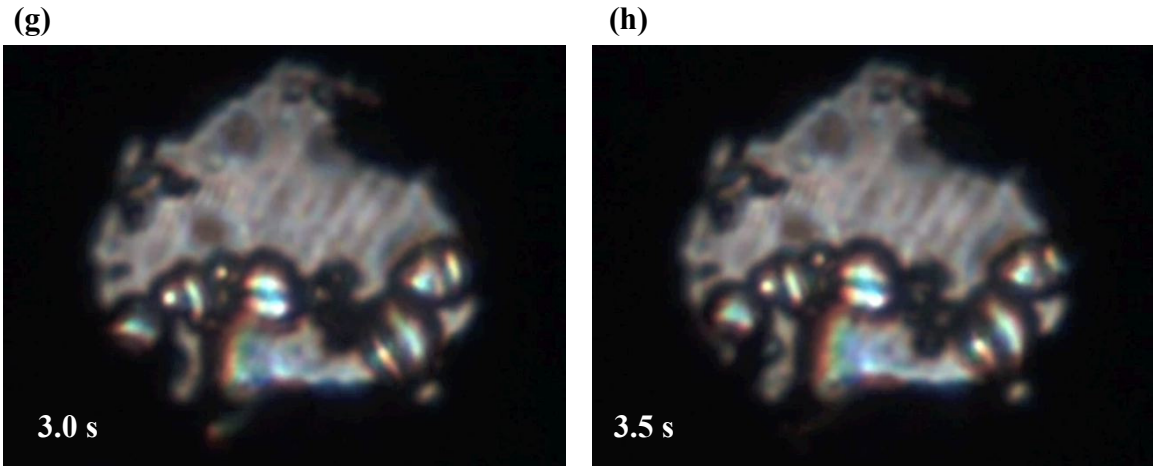


Figure 2.11: Video Images of Water/ Ice VI in Equilibrium in a DDAC Changing as Voltage (150 V) Was Instantly Applied to PE Actuators



Images extracted (at 2 fps) from a section of video showing the change in the water/ Ice VI equilibrium ratio in the DDAC when voltage (150 V) was instantly applied to the PE actuators. The voltage was applied by switching on the enable button on the Thorlabs control box. Original frame rate was 20 fps. The voltage was removed at frame (a). The application of voltage (greater compression) can be shown to favor the formation of Ice VI over liquid water since it greater density.

Figure 2.12: Video Images of Water/ Ice VI in Equilibrium in a DDAC Changing as Voltage (150 V) Was Instantly Removed from PE Actuators

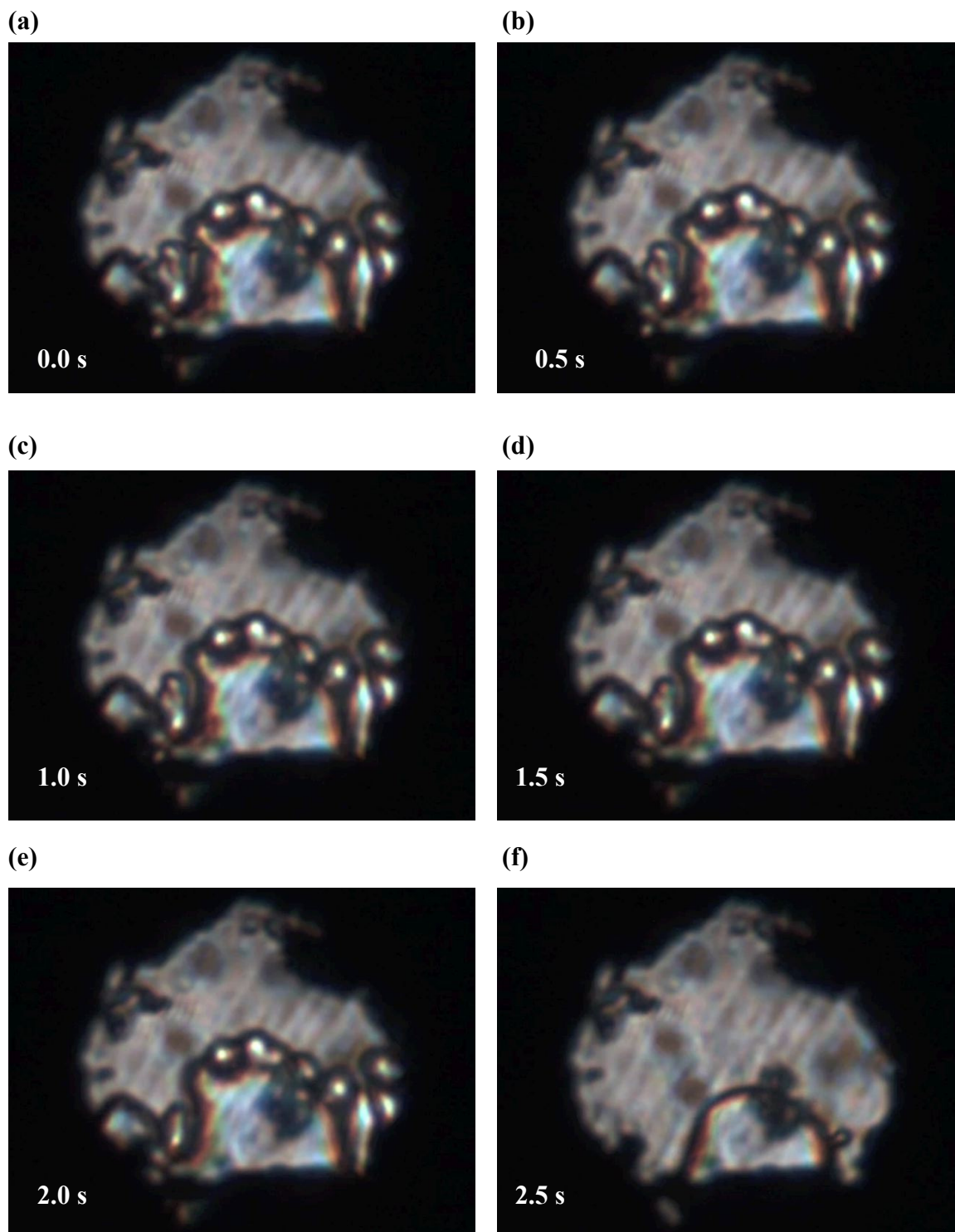
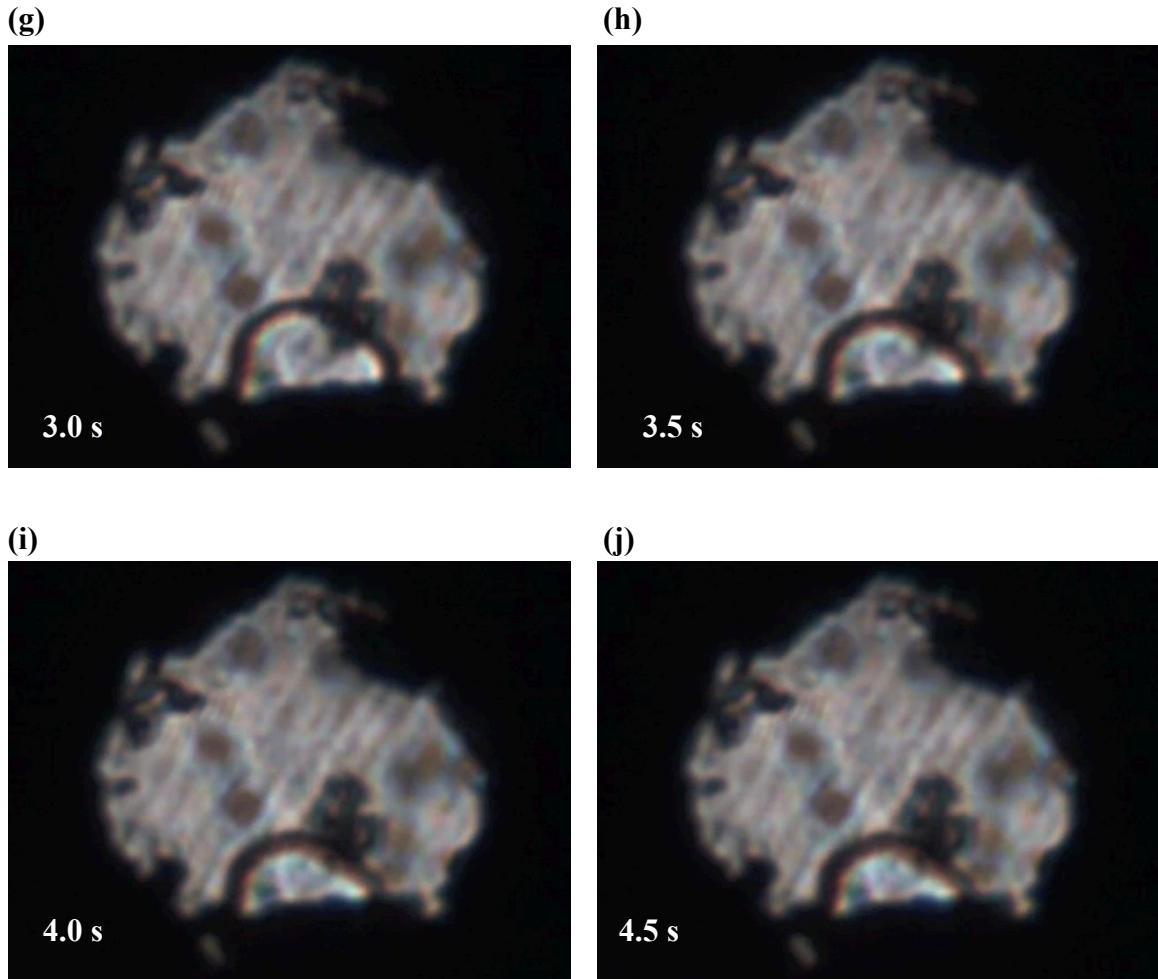


Figure 2.12: Video Images of Water/ Ice VI in Equilibrium in a DDAC Changing as Voltage (150 V) Was Instantly Removed from PE Actuators



Images extracted (at 2fps) from a section of video showing a change in the water/ Ice VI equilibrium ratio in a DDAC when a voltage was instantly removed from PE actuators. The voltage was removed by switching off the enable button on the Thorlabs control box. Original frame rate was 20 fps. The voltage was removed at frame (a). The removal of voltage (less compression) can be shown to favor the formation of liquid water over Ice VI since it has lesser density.

Figure 2.13: Video Images of Water/Ice VI in a DDAC Changing as Voltage (150 V) Was Instantly Applied to the PE Actuators

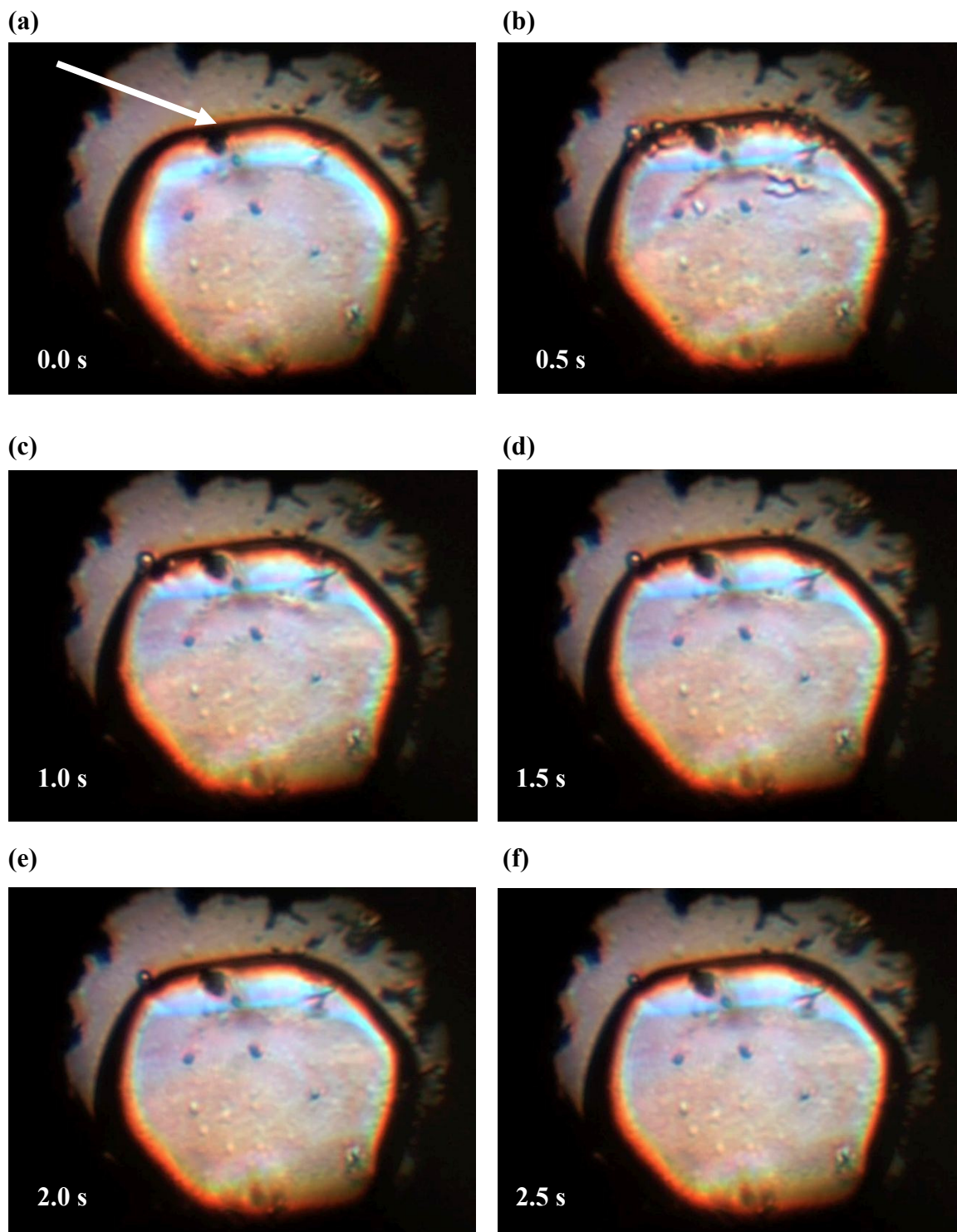
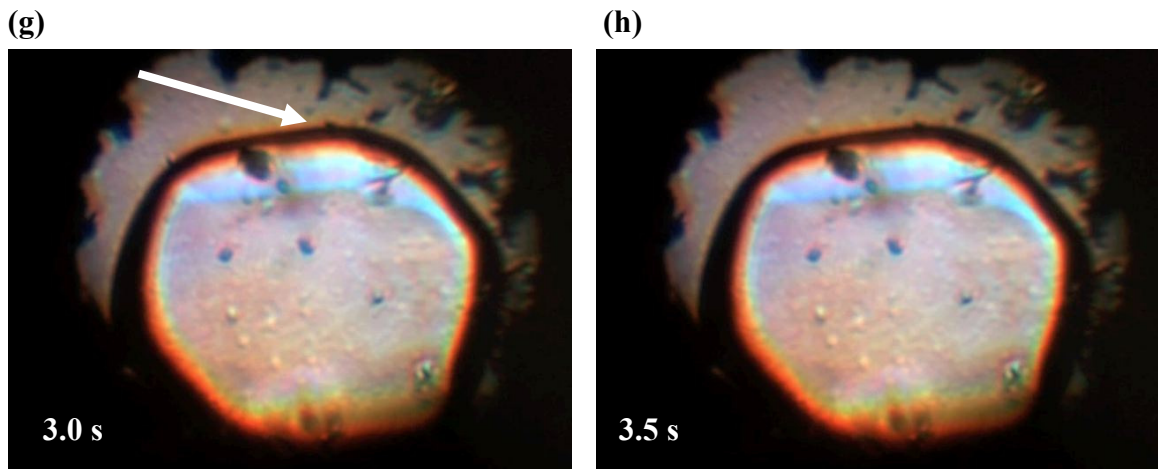


Figure 2.13: Video Images of Water/Ice VI in a DDAC Changing as Voltage (150 V) Was Instantly Applied to the PE Actuators



Images extracted (2 fps) from a section of a video showing the change in the water/Ice VI equilibrium ratio when full voltage (~ 150 V) was instantaneously applied to the PE actuators using a square wave with the Thorlabs PE actuator control software function generator. Original video frame rate of 20 fps. The changes are minute due to the limitations of the dynamic DAC at the time of the experiment (~ 1 kbar pressure change.) Arrows point to the area of noticeable change in size as the images progress. The crystal is growing due to the increase in the compression as the voltage is removed.

Figure 2.14: Video Images of Water/Ice VI in Equilibrium in a DDAC Changing as Voltage (150 V) Was Instantly Removed from the PE Actuators

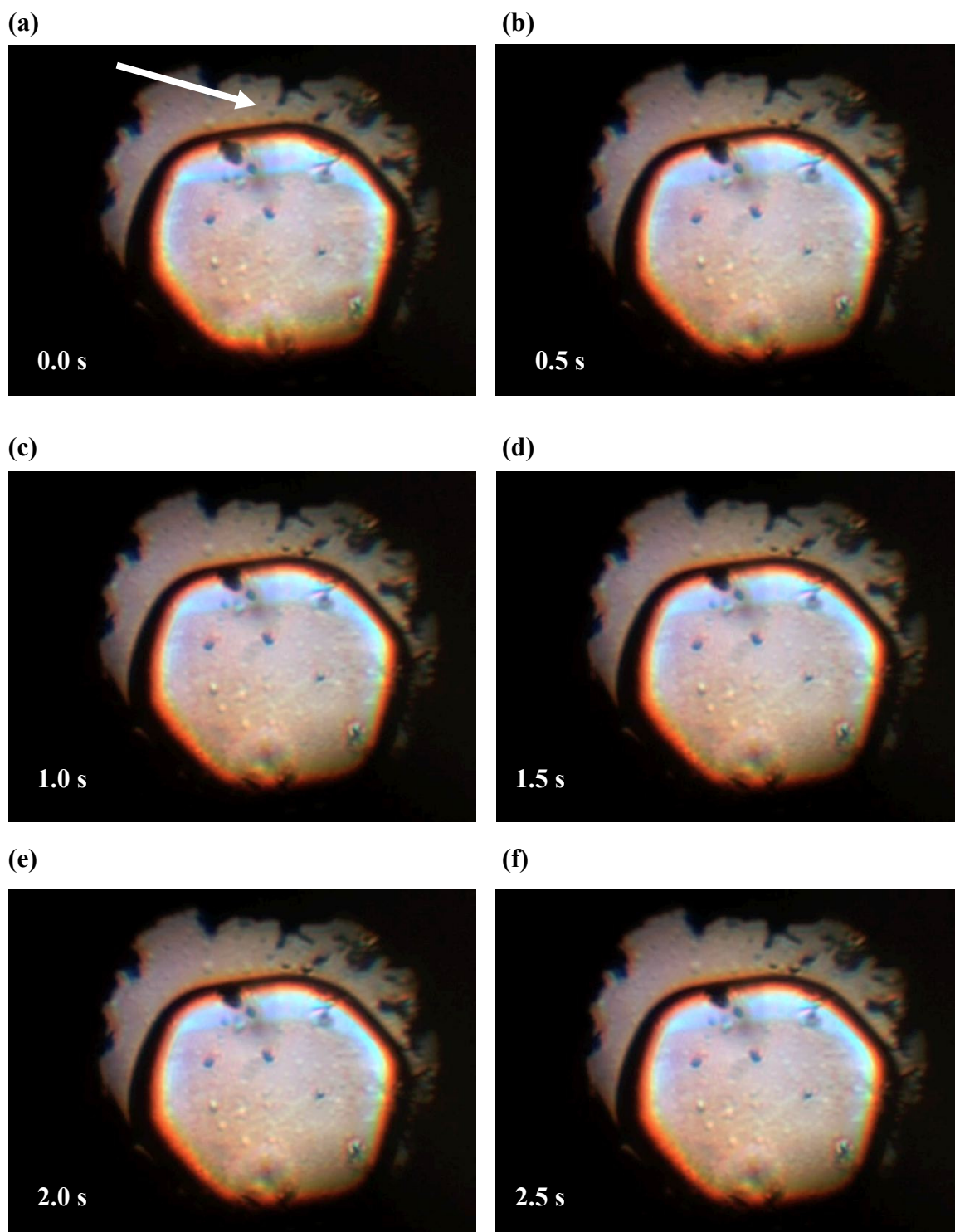
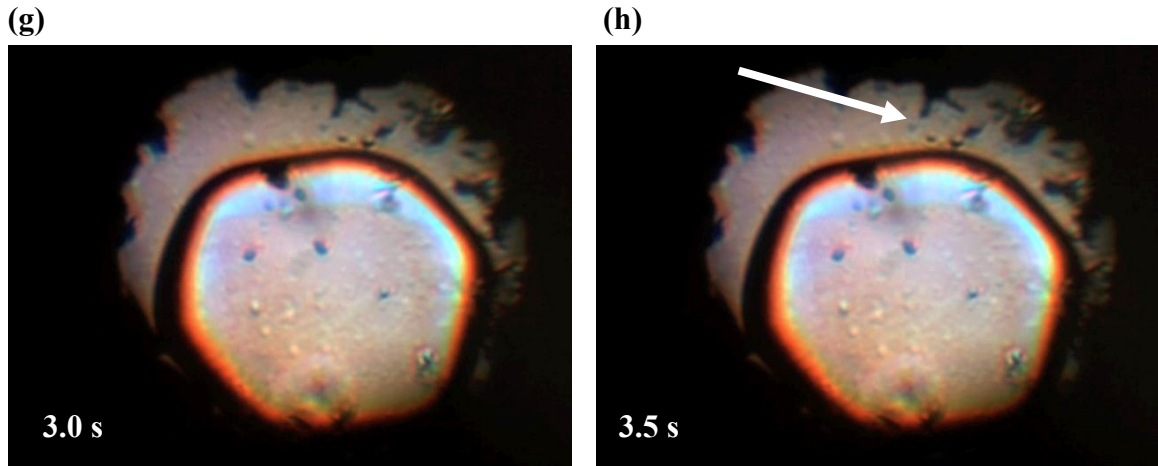


Figure 2.14: Video Images of Water/Ice VI in Equilibrium in a DDAC Changing as Voltage (150 V) Was Instantly Removed from the PE Actuators



Images extracted (2 fps) from a section of a video showing the change in the water/Ice VI equilibrium ratio when full voltage (~150 V) was instantaneously removed to the PE actuators using a square wave with the Thorlabs PE actuator control software function generator. Original video frame rate of 20 fps. The changes are minute due to the limitations of the dynamic DAC at the time of the experiment (~1 kbar pressure change.) Arrows point to the area of noticeable change in size as the images progress. The crystal is shrinking due to the decrease in the compression as the voltage is removed.

Figure 2.15: Video Images of Water/Ice VI in Equilibrium in the DDAC Change as a Triangle Wave (18 s, 0V to 150 V to 0 V) Was Applied to the PE Actuators

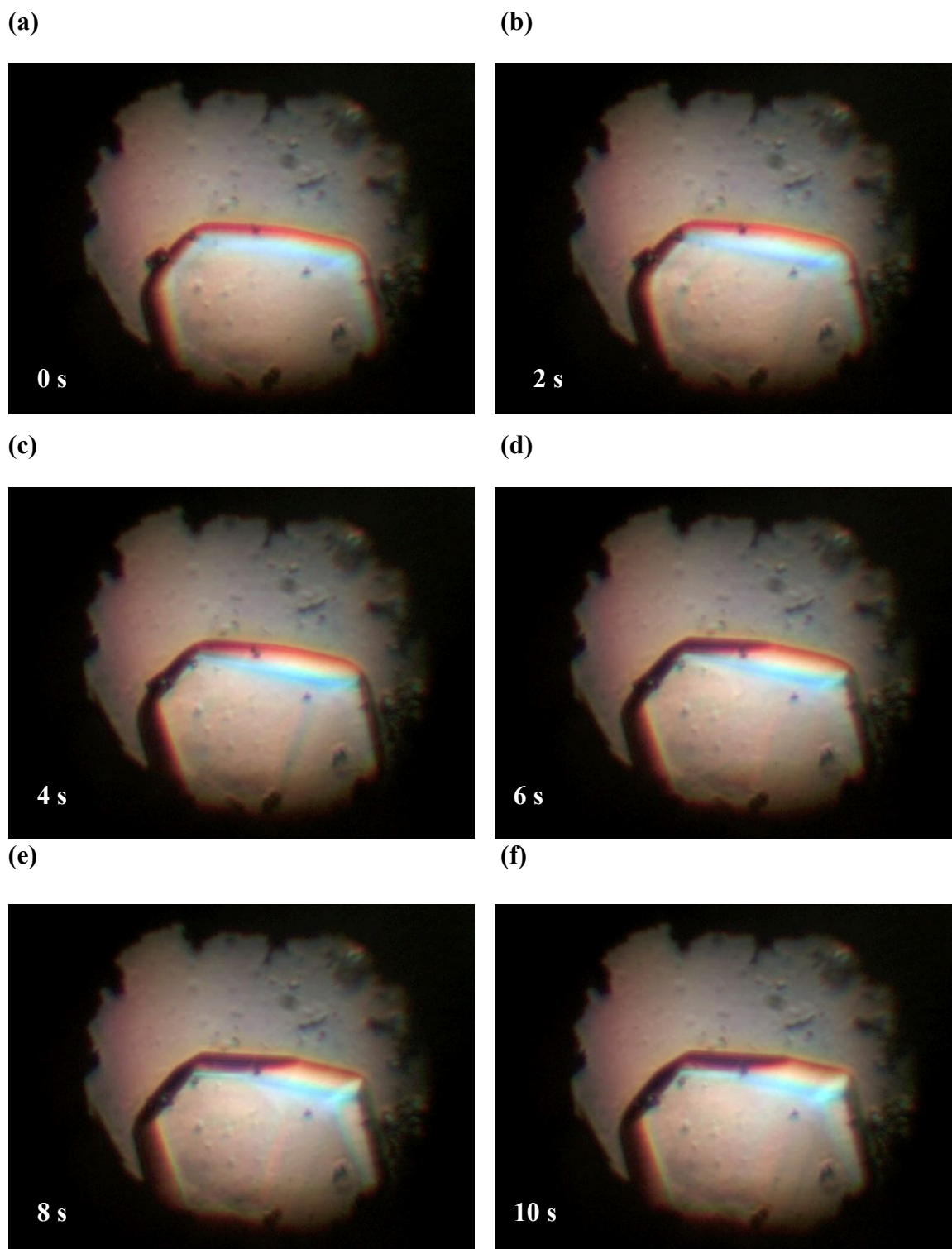
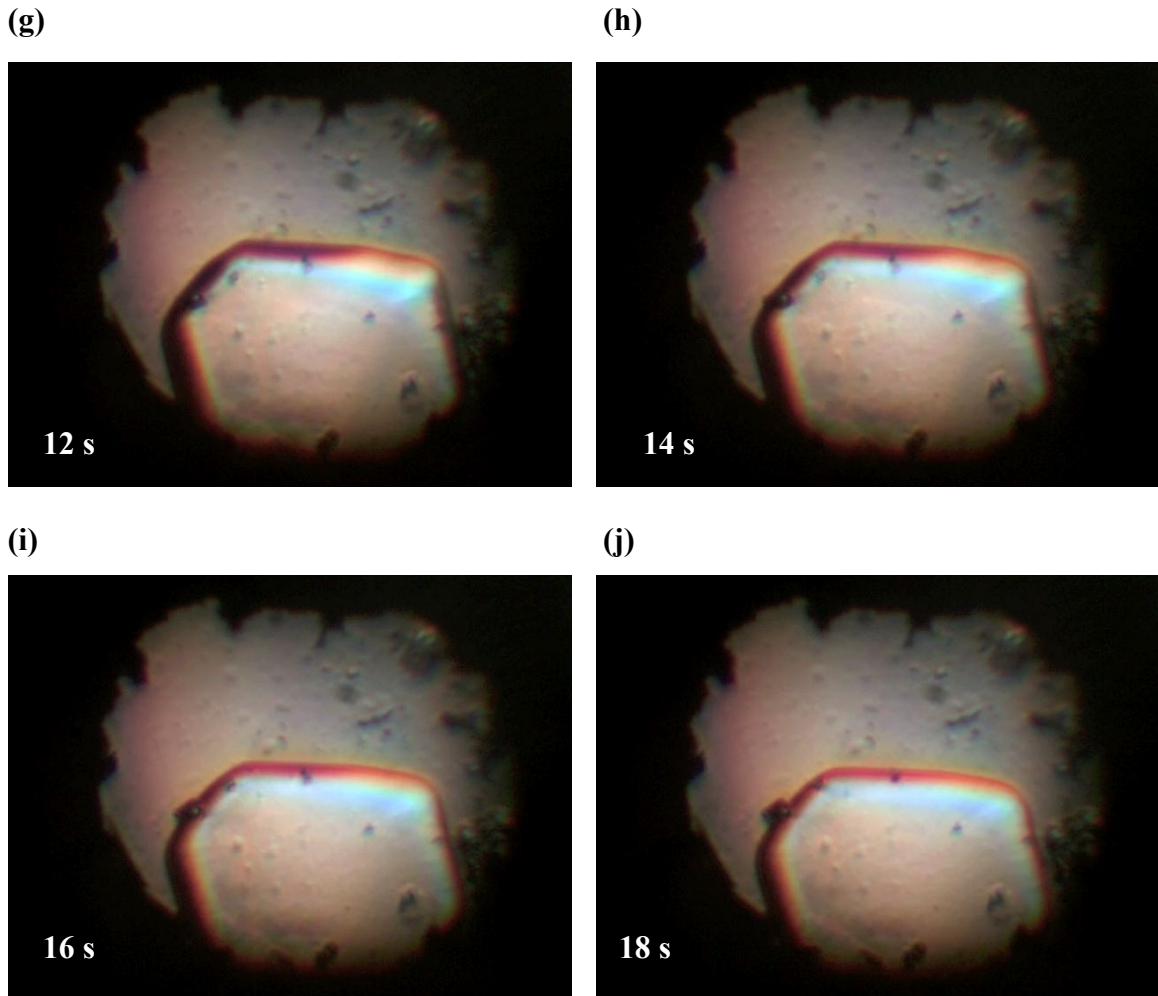


Figure 2.15: Video Images of Water/Ice VI in Equilibrium in the DDAC Change as a Triangle Wave (18 s, 0V to 150 V to 0 V) Was Applied to the PE Actuators



Images extracted (0.5 fps) from a section of a video showing the change in the water/Ice VI equilibrium ratio when an 18 s triangle wave is applied (0 V to 150 V to 0 V) to the PE actuators using a the Thorlabs PE actuator control software function generator. Original video frame rate of 20 fps. The changes are minute due to the limitations of the dynamic DAC at the time of the experiment (~1 kbar pressure change.) A change in the size of the Ice VI crystal can be observed in the center of the gasket hole where the barrier between the ice and water moves past the speck of gasket metal or ruby chip and back again as the voltage increases and decreases, respectively.

Figure 2.16: Video Images of Ice VI/Ice VII in Equilibrium in the DDAC Changing as a Triangle Wave (18 s, 0V to 150 V to 0 V) is Applied to PE Actuators

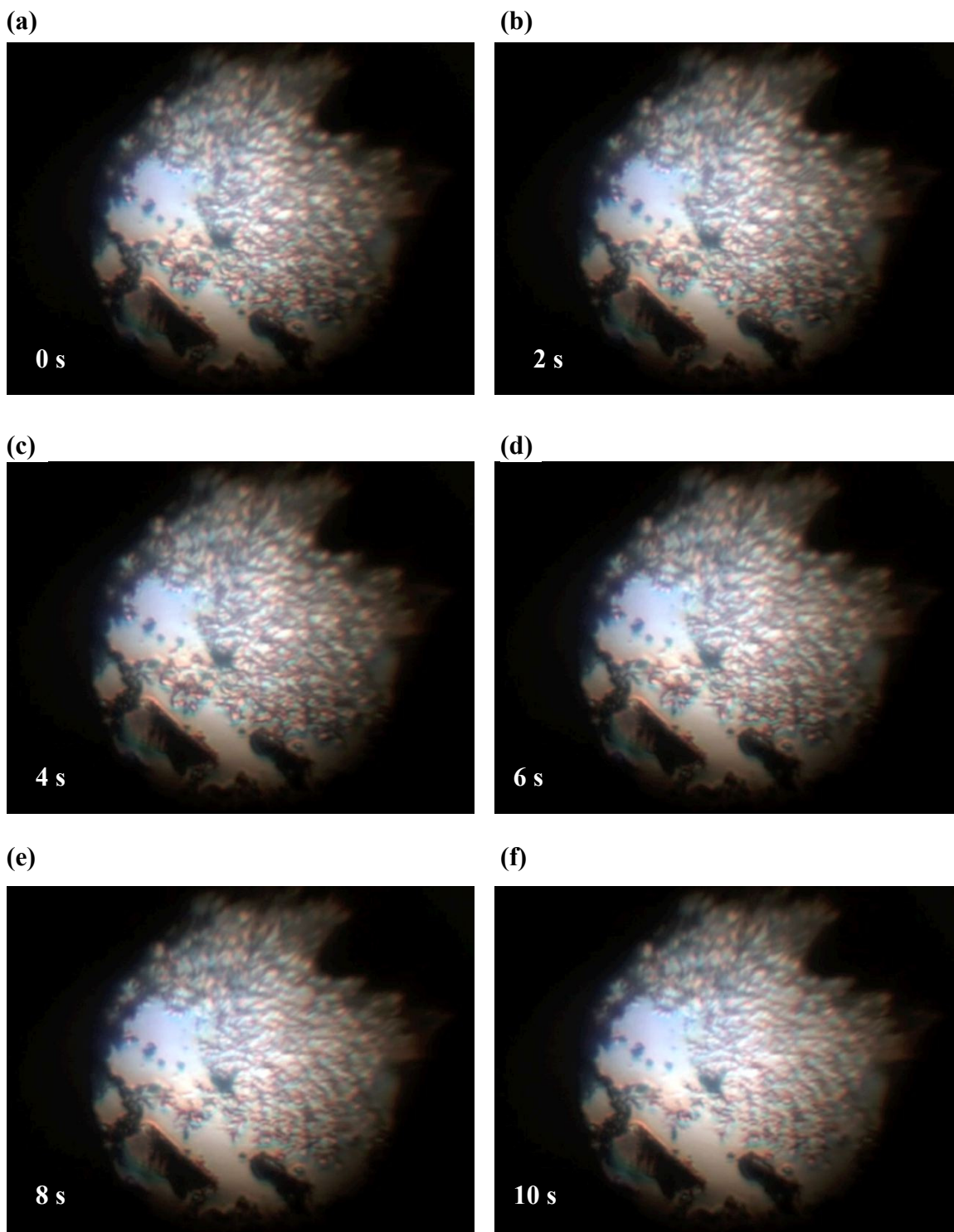
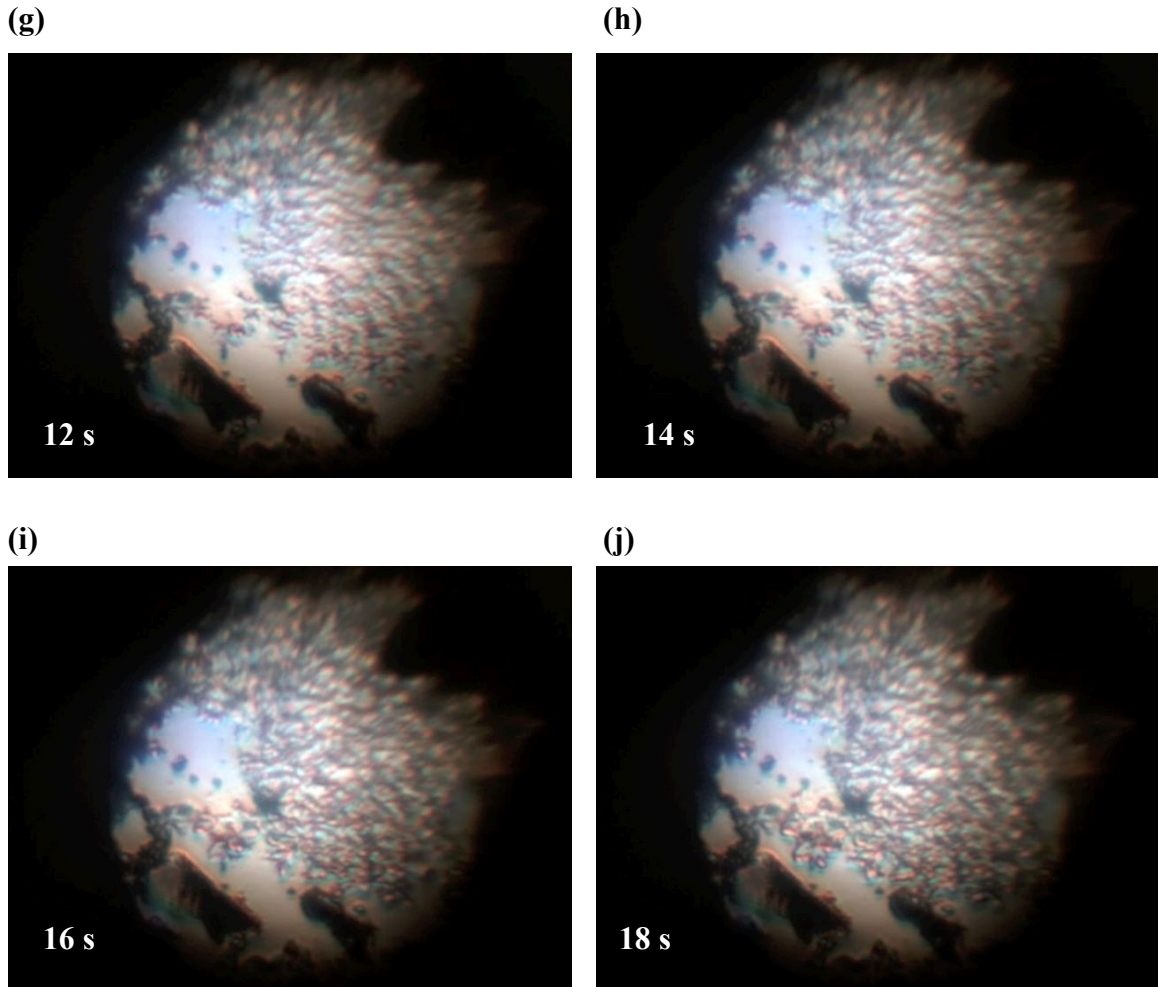


Figure 2.16: Video Images of Ice VI/Ice VII in Equilibrium in the DDAC Changing as a Triangle Wave (18 s, 0V to 150 V to 0 V) is Applied to PE Actuators



Images extracted (0.5 fps) from a section of a video showing the change in the Ice VI/Ice VII equilibrium ratio when an 18 s triangle wave is applied (0 V to 150 V to 0 V) to the PE actuators using the Thorlabs PE actuator control software function generator. Original video frame rate of 20 fps. The changes are minute due to the limitations of the dynamic DAC at the time of the experiment (~1 kbar pressure change.) The change in the density of a diffuse design is seen emanating from the upper right to the center and lessens and then reintensifies as the voltage is increased and then decreased.

In **Figures 2.15** and **2.16**, instead of an instantaneous change in voltage (as in **Figures 2.11-2.14**), a triangle waveform voltage (18 s, 0 V to 150 V to 0 V) was applied to the PE actuator ports using the Thorlabs software. In both figures, 0 s is the start of the triangle waveform (at 0 V.)

2.5: Conclusion

In this chapter, the development and characterization of a DDAC has been presented. Having developed a dynamic way of controlling pressure using a Diamond Anvil Cell, the DDAC was shown to produce a ~5 kbar pressure change with a time scale of ms time scale with a commercial voltage driver. A μ s time scale can be achieved with a custom voltage driver.

It was also demonstrated that the DDAC can control and alter the phase equilibrium ratio between two states of matter using the extension of the PE actuators. This provides an interesting tool for looking at the dynamics of phase transitions either by video or spectroscopic means. The Raman spectroscopy of water and its many solid phases has been studied before.^{10-12,14,18} It may be possible to measure the change in the Raman signal for water as it transforms to different states of matter. This would allow for the investigation of the kinetics of the phase transition and the determination of the energy of activation for the phase transitions of water \leftrightarrow Ice VI and Ice VI \leftrightarrow Ice VII.

Other possible systems which could be studied are molecular crystals with phase changes such HMX¹⁵ or 33HMCHBr, whose phase transition has been shown in the following chapter. Also, pressure induced bond breaking reactions in solid crystals have also been studied recently with bis- and dianthracene.²¹

References

- (1) Eisele, J. L.; Rosenbusch, J. P. *Journal of Biological Chemistry* **1990**, *265*, 10217.
- (2) Yang, W. Y.; Gruebele, M. *Nature* **2003**, *423*, 193.
- (3) Panick, G.; Winter, R. *Biochemistry* **2000**, *39*, 1862.
- (4) Panick, G.; Malessa, R.; Winter, R.; Rapp, G.; Frye, K. J.; Royer, C. A. *Journal of Molecular Biology* **1998**, *275*, 389.
- (5) Woenckhaus, J.; Kohling, R.; Winter, R.; Thiyagarajan, P.; Finet, S. *Review of Scientific Instruments* **2000**, *71*, 3895.
- (6) Woenckhaus, J.; Köhling, R.; Thiyagarajan, P.; Littrell, K. C.; Seifert, S.; Royer, C. A.; Winter, R. *Biophysical Journal* **2001**, *80*, 1518.
- (7) Vidugiris, G. J. A.; Markley, J. L.; Royer, C. A. *Biochemistry* **1995**, *34*, 4909.
- (8) Panick, G.; Vidugiris, G. J. A.; Malessa, R.; Rapp, G.; Winter, R.; Royer, C. A. *Biochemistry* **1999**, *38*, 4157.
- (9) Paladini, A. A.; Weber, G. *Review of Scientific Instruments* **1981**, *52*, 419.
- (10) Chou, I.-M.; Blank, J. G.; Goncharov, A. F.; Mao, H.-k.; Hemley, R. J. *Science* **1998**, *281*, 809.
- (11) Marckmann, J. P.; Whalley, E. *The Journal of Chemical Physics* **1964**, *41*, 1450.
- (12) Minceva-Sukarova, B.; et al. *Journal of Physics C: Solid State Physics* **1984**, *17*, 5833.
- (13) Petrenko, V. F.; Whitworth, R. W. *Physics of ice*; Oxford University Press: Oxford ; New York, 1999.
- (14) Walrafen, G. E. *Journal of Solution Chemistry* **1973**, *2*, 159.
- (15) Yoo, C.-S.; Cynn, H. *The Journal of Chemical Physics* **1999**, *111*, 10229.
- (16) Evans, W. J.; Yoo, C.-S.; Lee, G. W.; Cynn, H.; Lipp, M. J.; Visbeck, K. *Review of Scientific Instruments* **2007**, *78*, 073904.

- (17) Lee, G. W.; Evans, W. J.; Yoo, C.-S. *Proceedings of the National Academy of Sciences* **2007**, *104*, 9178.
- (18) Lee, G. W.; Evans, W. J.; Yoo, C.-S. *Phys Rev B* **2006**, *74*, 134112.
- (19) Mao, H. K.; Bell, P. M.; Shaner, J. W.; Steinberg, D. J. *J Appl Phys* **1978**, *49*, 3276.
- (20) Bassett, W. A. *High Pres. Res.* **2009**, *29*, 163
- (21) Jezowski, S.; Zhu, L.; Wang, Y.; Rice, A.; Scott, G.; Bardeen, C.; Chronister, E. L.; University of California, Riverside: to be Submitted.

Chapter III

High Pressure Raman Spectroscopy of Protonated and Deuterated Cyclic Aliphatic Tertiary Diamines

3.1: Low Barrier Hydrogen Bonds (LBHB)

The hydrogen bond has been actively researched for the past 90 years since it was first defined by Latimer and Rodebush.¹ So enigmatic is the hydrogen bond that there is currently a move to have its definition redefined.² An interesting and sometimes contentious aspect of hydrogen bond related research is the low-barrier hydrogen bond (LBHB) and its role in enzyme catalysis.³⁻⁹

A LBHB is defined as a hydrogen bond where the donor and acceptor atoms share similar pKa, are a relatively short distance from each other and the hydrogen is equally shared between the two (equidistant from each other).^{5,9} A hydrogen bond can be described by a double well potential in which the two minima represent the hydrogen located on one atom or the other. In a LBHB, the barrier in the double well potential is lowered as the donor and acceptor atoms are moved closer together such that the barrier height is below the zero point energy for the hydrogen atom wavefunction in the potential. The result of that is the hydrogen atom position maximum is located in the center of the well at the barrier maximum.^{5,10,11} This type of hydrogen bonding has been suggested to play a role in enzymatic catalysis by providing energy from the transformation of a hydrogen bond to a LBHB due to a change in the pKa of either the

donor or acceptor atoms such that they match, meeting the criteria for a LBHB; this would provide around 18 kcal mol⁻¹ of energy.⁹

These claims, however, have been disputed in a response⁸ to Science articles by Cleeland and Kreevoy⁶ and, Frey *et al.*⁷, to which the later authors counter respond. Warshell *et al.* argue that the effects, suggested by the aforementioned articles, are better explained by simple electrostatic calculations and it is argued that solvation in the active sites is important.⁸ Because of that, it is suggested that LBHB would actually have an anticatalytic effect by interfering in the solvation and electrostatics in the active site of the protein.⁸ The authors of the articles counter-argue that solvation is not an issue as the active sites tend to be desolvated upon activation and push out most water and that electrostatic calculations can be made to simulate the observed effects because of uncertainty in the variables of the dielectric constants and interatomic distances.⁸

Recently, evidence of a LBHB in the photoactive yellow protein (PYP) of the bacterium *Halorhodospira halophila* has been reported.¹² It was shown using x-ray and neutron diffraction that the position of the hydrogen in the short hydrogen bond between PYP and its chromophore, *p*-coumaric acid, is equidistant from the donor and acceptor atom suggesting that it is a LBHB. The LBHB is located between Glu46 and the phenolic oxygen of *p*-coumaric acid, which share similar pKa values in the protein system.¹² Upon excitation, the pKa of *p*-coumaric acid changes and the proton is shifted to Glu46 for the duration of the excited state, which is demonstrated in a change in the CO carbonyl stretching frequency in the IR.^{12,13}

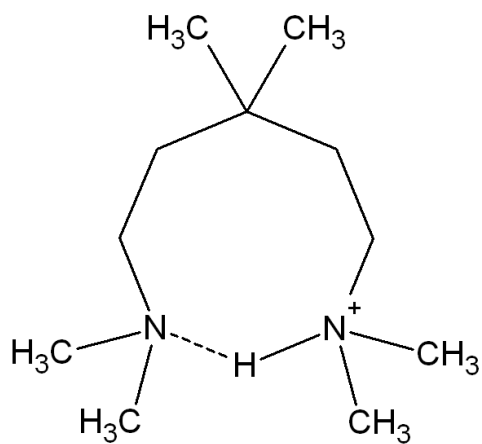
Interest in the LBHB is not restricted to its possible biochemical role. Small molecules with LBHBs have also been a subject of study. Recent studies have shown that aliphatic tertiary diamines, such as $N^1,N^1,N^5,N^5,3,3$ - hexamethylcadaverine and N,N,N',N' -tetramethylputrescine, can form a cyclic compound with an intermolecular hydrogen bond when protonated.¹⁴⁻¹⁶ Experimental and computational studies suggest that these compounds involve LBHB.¹⁴⁻¹⁶ Raman spectroscopy has been used in this chapter to study the effect of pressure on the vibrational modes of these compounds.

High pressure Raman spectroscopy has been used to study the effect of pressure on hydrogen bonded compounds.¹⁷ Red shifts (soft modes), where the wavenumber of the mode decreases with increased pressure, have been observed for hydrogen bonded $-OH$ in L-ascorbic acid crystals using Raman.¹⁷ In the same study, a phase change for the crystal was also seen at ~ 1.8 GPa and 4.0 GPa.¹⁷ High pressure Raman spectroscopy has also been used to study phase changes in Deuterated γ -Glycine.¹⁸ Evidence of a phase change in the Raman pressure series was seen as a discontinuity in the shift of the peak positions with pressure, as well as a change in the overall shape of the spectrum.¹⁸ In this Chapter, Raman spectroscopic evidence of a phase change in $N^1,N^1,N^5,N^5,3,3$ - hexamethylcadaverine HBr will be presented along with a possible soft mode of the apparent NHN asymmetric mode of the LBHB in N,N,N',N' -tetramethylputrescine HI.

Figure 3.1: Structures for Monoprotonated and Diprotonated N¹,N¹,N⁵,N⁵,3,3-Hexamethylcadaverine

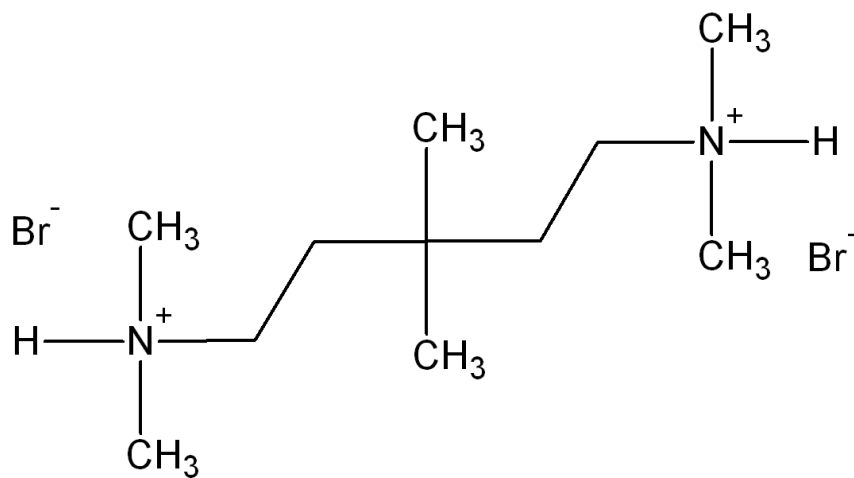
(a) N¹,N¹,N⁵,N⁵,3,3- hexamethylcadaverine monobromide

(b) N¹,N¹,N⁵,N⁵,3,3- hexamethylcadaverine dibromide



(a)

Br⁻



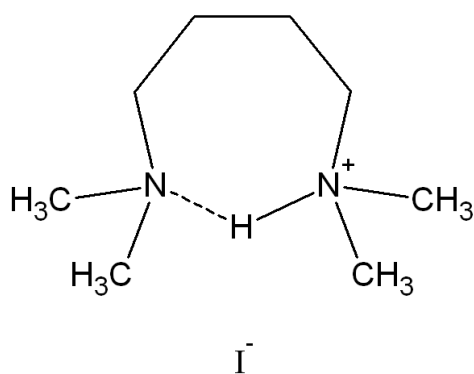
(b)

Figure 3.2: Structures for Monoprotonated, Diprotonated, and Deuterated N,N,N',N'-Tetramethylputrescine

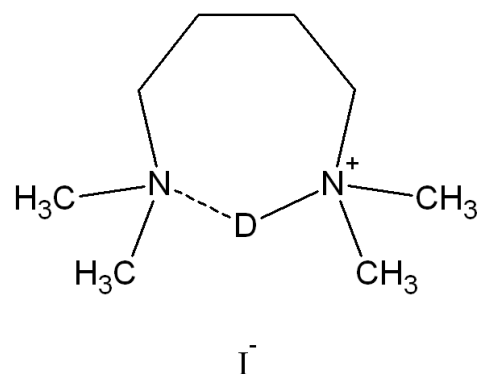
(a) N,N,N',N'-tetramethylputrescine monoiodide

(b) Singly deuterated N,N,N',N'-tetramethylputrescine monoiodide

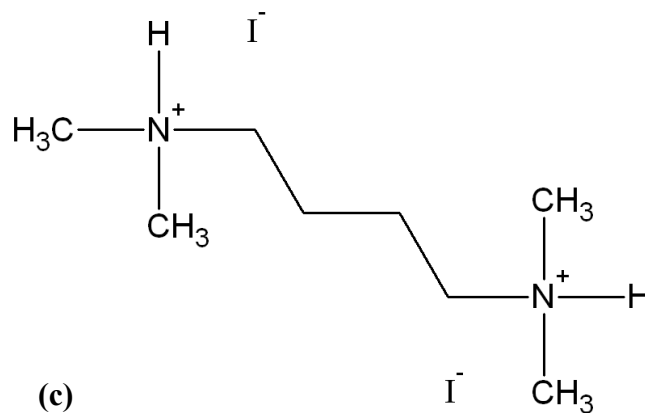
(c) N,N,N',N'-tetramethylputrescine diiodide



(a)



(b)



(c)

3.2: Raman Spectroscopy in a Diamond Anvil Cell (DAC)

3.2.1: Loading the DAC and Obtaining Spectra

A sample of monoprotonated (MP) and diprotonated (DP) $N^1, N^1, N^5, N^5, 3, 3$ -hexamethylcadaverine HBr (33HMCHBr MP and 33HMCHBr DP) and monoprotonated (MP) N, N, N', N' -tetramethylputrescine HI (TMPHI) and deuterated N, N, N', N' -tetramethylputrescine (TMPDI) were provided by a collaborator for pressure dependent Raman spectroscopic analysis. The structures of each set of compounds can be seen in **Figures 3.1** and **3.2**, respectively. Each sample was individually loaded into a Merrill-Basset DAC. A 0.010" thick Inconel gasket was pre-dented approximately 1% of the thickness before then drilling an initial hole diameter of 0.4 mm. The cell was then loaded first with a small chip of ruby (for use as a pressure indicator using a standard calibration formula developed by Mao et al¹⁹) then with small flakes of the sample. The cell was then loosely tightened and the bolts were tightened while immersed in liquid nitrogen, which is used as a pressure mediating fluid to ensure homogenous pressure distribution. The cell was then removed from the liquid nitrogen bath and allowed to return to room temperature.

Raman spectra of the sample were taken at varying pressures (including ambient before loading into a cell with liquid nitrogen) at room temperature using a Dilor XY Laser Raman Spectrometer with imaging microscope. Unless otherwise stated, the spectrometer was centered at 650 cm^{-1} and spectra was taken at 30 second intervals and

averaged over 120 acquisitions using the 10x microscope objective for all Raman spectra. A 200 mW DPSS 532 nm laser was used.

There is an intense Raman peak around 1300 cm^{-1} due to the carbon in the diamond anvils. For this reason, the majority of spectra were taken around the region centered at 650 cm^{-1} . Furthermore, calculations suggest a Raman peak for the NHN asymmetric stretch in the region.¹⁶ The spectra have been baseline corrected for the baseline noise either caused by the spurious and broad emissions in the laser or from the Raman shift at 1300 cm^{-1} for diamond.

3.2.2: Determining Peak Positions by Fitting a Sum of Gaussian Lineshapes

Each baseline corrected spectra were fitted to a sum of Gaussian lineshapes in order to determine the position of the peaks. This was done using Microsoft Excel by minimizing the sum of the squared difference between the the experimental spectrum and the value from the sum of the Gaussian lineshape functions. The minimization was done by first estimating the values of the position (x_0), Γ ($\Gamma = \text{FWHM} / \sqrt{2\text{Ln}(2)}$), and height, I of each Gaussian function such that the sum closely resembled the actual spectrum. The Gaussian lineshape function used is shown in **Equation 3.1**.

$$f_{\text{Gaussian}} = I\sqrt{2\pi}\left(\frac{1}{\Gamma}\right)e^{-2\left(\frac{x-x_0}{\Gamma}\right)^2} \quad 3.1$$

The parameters were then minimized for each peak followed by a simultaneous minimization of all the parameters. Occasional tweaks were made followed by further minimization runs when needed. Minimization was performed using the built-in solver feature of Excel 2003, with the sum of the squared differences being minimized. Each baseline corrected spectrum was further corrected with a constant vertical shift by either adding or subtracting a constant from the original spectrum so that the minimum was near the zero axis to better assist the minimization process.

3.2.3: Error Analysis of Peak Positions from a Fitted Sum of Gaussian Lineshapes

The error bars for the peak position were obtained from the error of the position parameter, a , for each peak from the minimized fit of the sum of the Gaussian lineshape functions to the experimental data. The formula²⁰ used to calculate this error is shown in **Equation 3.2** where the χ^2 values are defined as in **Equation 3.3**. The Δa value was chosen arbitrarily and the values for a_1 - a_3 were determined by **Equations 3.4-3.6**. Since the χ^2 value is defined as **Equation 3.7**, the value of the sum of squared differences for each a value (a_1 - a_3) was obtained and multiplied by the inverse of the error in the y_1 value (intensity of the spectra) which was assumed to be the standard deviation of a small flat portion of the respective baseline corrected spectrum.

$$\sigma = \Delta a \sqrt{2(\chi_1^2 - 2\chi_2^2 + \chi_3^2)^{-1}} \quad 3.2$$

$$\chi_i^2 = \chi^2(a_i) \quad 3.3$$

$$a_1 = a_2 - \Delta a \quad 3.4$$

$$a_2 = a_3 - \Delta a \quad 3.5$$

$$a_3 = a_{\min} + 0.5\Delta a \quad 3.6$$

$$\chi^2 = \frac{1}{\sigma_y^2} \sum (y_i - \bar{y}_i)^2 \quad 3.7$$

3.3: Results

3.3.1: 33HMCHBr Pressure Dependent Shift in Raman Frequencies

The results of Raman spectroscopy for the 33HMCHBr monoprotinated over a pressure series ranging from ambient pressure to around 26 kbar can be seen in **Figures 3.3 and 3.4**, which are the comparison of the baseline corrected spectra at each pressure. As pressure was increasingly applied, the peaks shifted to higher wavenumber while, upon release, the peaks shifted back down to lower wavenumbers. There appears to be no evidence of any soft modes in the observed region. This could be due to the absence of such modes or that any modes present are being obscured by the broad baseline peaks that appear in the spectra. Instead of a soft mode, evidence of a phase change was observed. This is seen clearly in **Figures 3.3 and 3.4**. Also, the change is evident in

Figure 3.5, where the Gaussian fitted peak positions are plotted versus the pressure obtained by subsequent increases in pressure; there appears to be a distinct discontinuity in the pressure induced shift between the 14.02 kbar and 16.24 kbar. This could be an indication of a solid/solid phase transition between those pressures.

Another interesting aspect of this phase change is the hysteresis, which is observed when comparing the shift in the Gaussian fitted peak positions of the Raman spectra when the pressure was increased and decreased (**Figure 3.6**). There were only two hours between the sets of points at 4.53 kbar and 14.02 kbar (pressure increasing) and at 15.58 kbar and 9.87 kbar (pressure decreasing) such that either the sample at 14.02 kbar or 9.87 kbar was in a metastable state that finally transitioned with further pressure change and time (1 day).

In **Figure 3.7**, a comparison of the protonated and diprotonated 33HMCHBr is shown. The similarities in the spectra are such that it is likely that they are the same material. It was later confirmed to be the case that these compounds were both a mixture of their respective compound with the other. For that reason, it is impossible to distinguish which compound contains the phase change.

Figure 3.3: Raman Pressure Series (Increasing Pressure) for 33HMCHBrMP

Pressure was increased to around 26 kbar in a diamond anvil cell with fluid nitrogen and ruby. As pressure increases, peaks can be shown shifting to higher wavenumbers. There is a discontinuity in the shift of the peaks with pressure between 14.02 kbar and 16.24 kbar indicative of a possible phase transition.

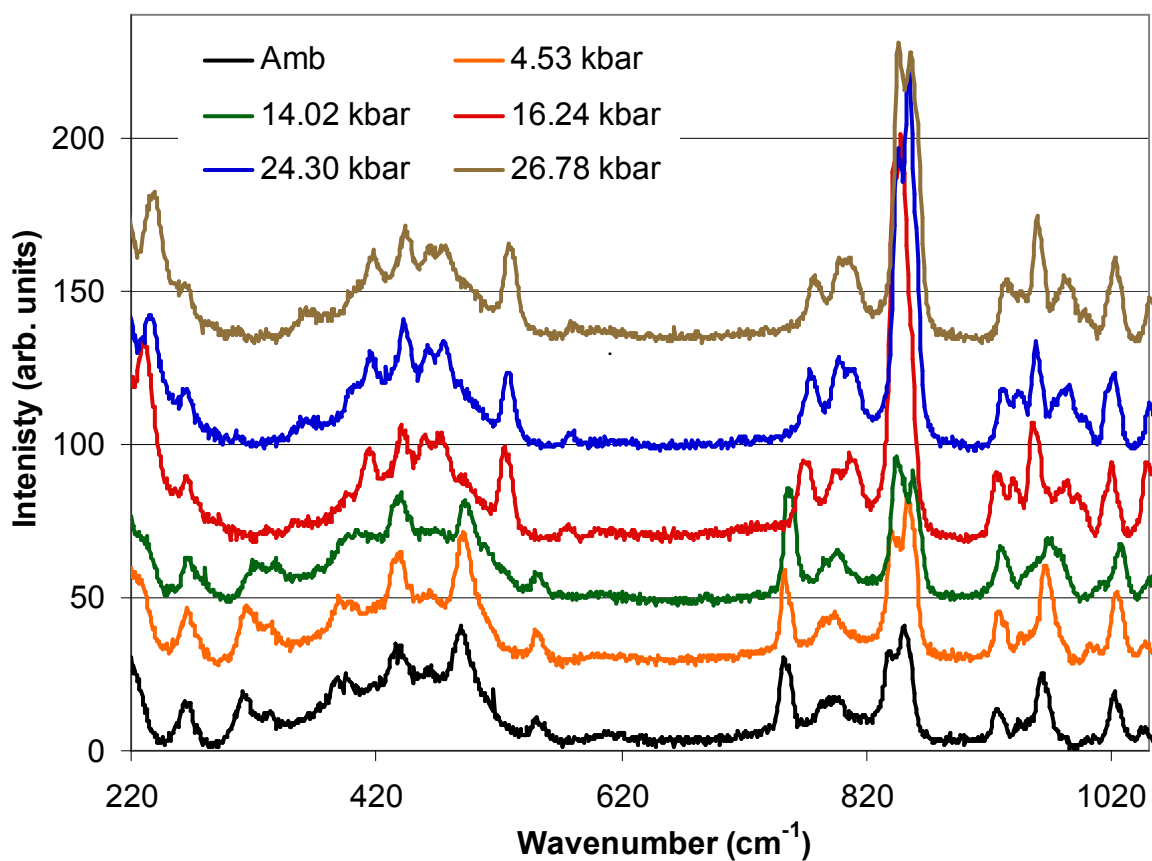


Figure 3.4: Raman Pressure Series (Decreasing Pressure) for 33HMCHBrMP
Pressure was decreased from ~26 kbar to ambient pressure in a diamond anvil cell with fluid nitrogen and ruby. As pressure decreases, peaks can be shown shifting to lower wavenumbers. There is a discontinuity in the shift of the peaks with pressure between 9.87 kbar and 15.58 kbar indicative of a phase transition.

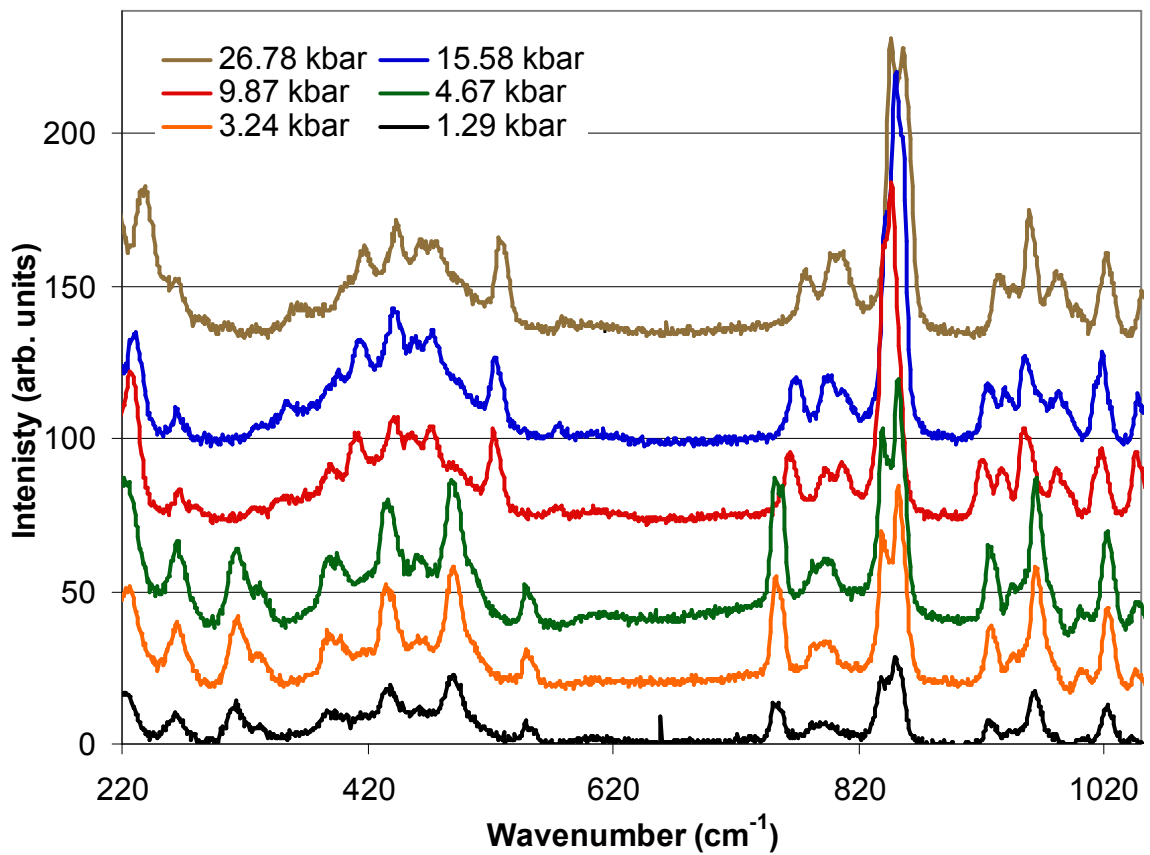


Figure 3.5: Pressure Induced Shift in Select Peaks for 33HMCHBr MP as Pressure is Increased

This shows that there is a break in the shift between 14.02 and 16.24 kbar indicating a phase change occurring around that pressure range.

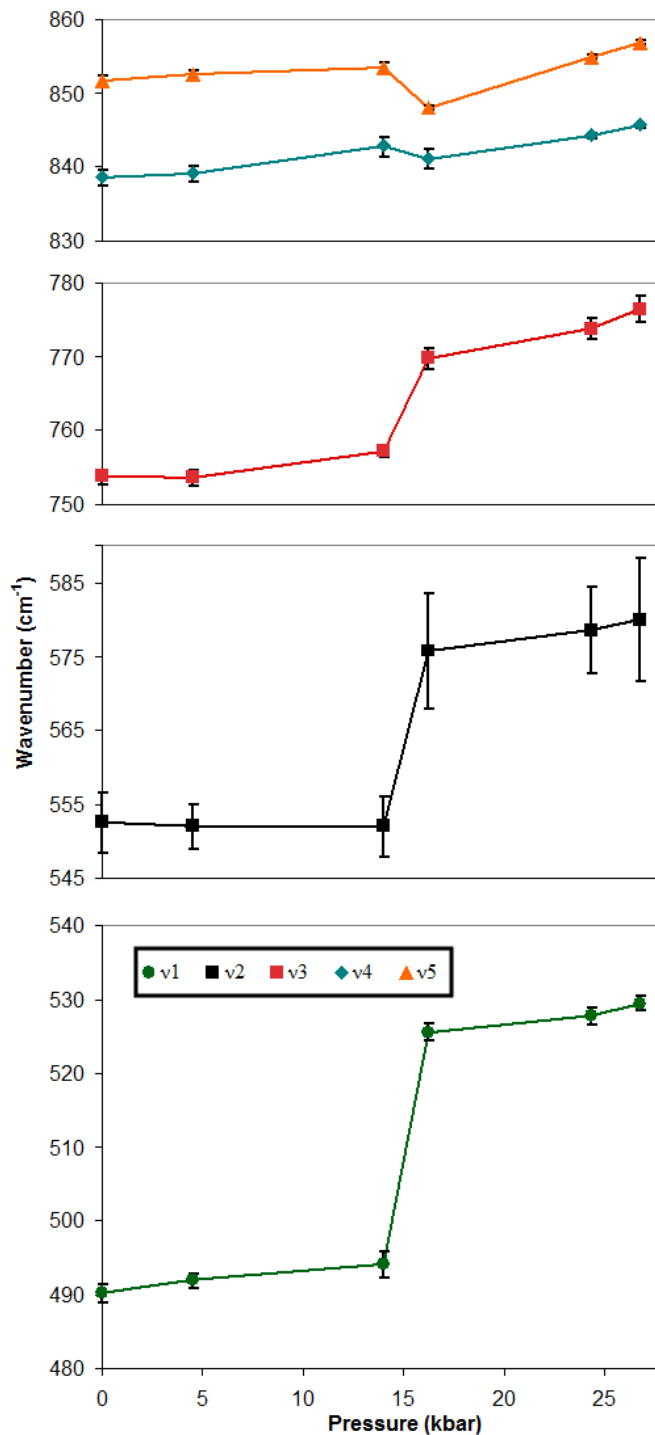


Figure 3.6: Apparent Hysteresis in Phase Change When Applying Pressure Versus Releasing Pressure at Different Days

There are typically ~2 hr between changing pressures, except for data taken on new days. A hysteresis appears which could be indicative of one of the pressure points being in a metastable state due to the limited time (2hr) between the spectra.

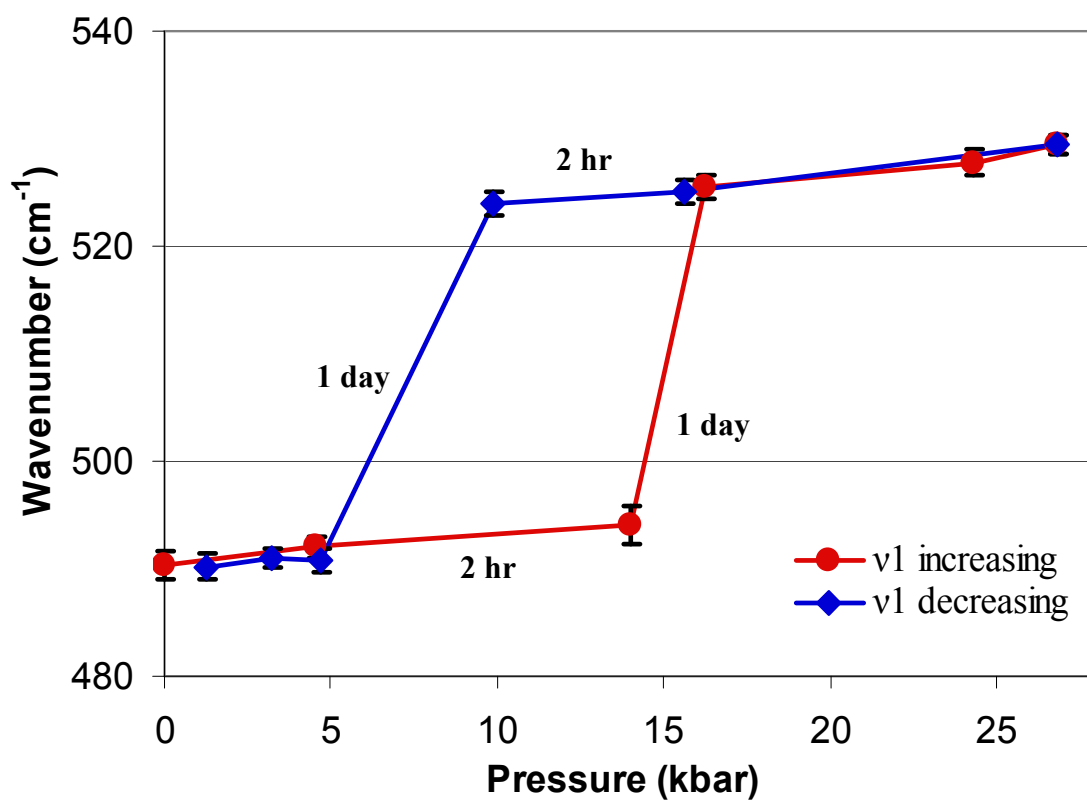
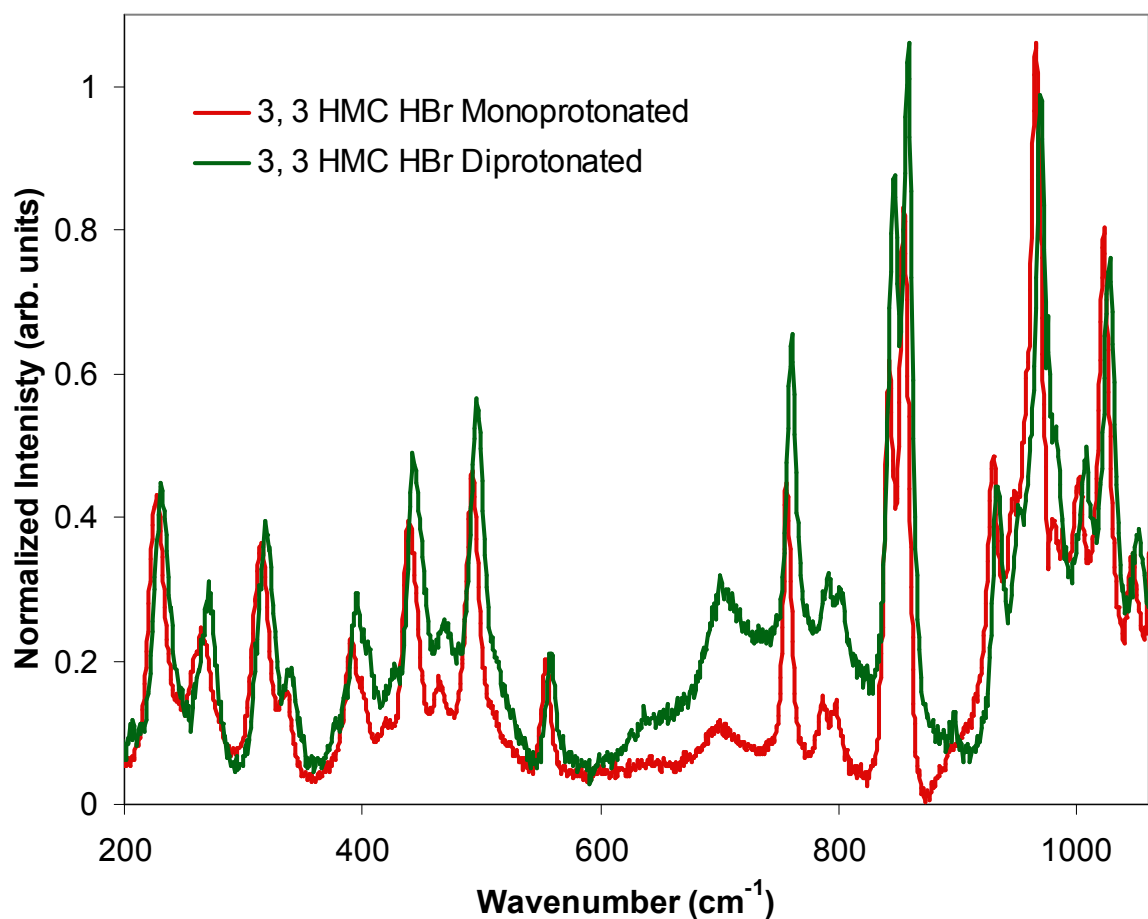


Figure 3.7: Raman Spectra of “Monoprotonated” and “Diprotonated” 33HMCHBr

The similarity in the spectra of 33HMCHBrMP and 33HMCHBrDP when compared suggests that the two samples are the same. They are likely a mixture of the mono- and diprotonated compounds.



3.3.2: TMPHI Pressure Dependent Shift in Raman Frequencies

The Raman pressure series for the second set of compounds, TMPHI (or TMPDI for the deuterated sample) also shows a shift in peak position with pressure change, which is shown in **Figure 3.8** (decreasing pressure) and **Figure 3.9** (increasing pressure); it can be seen that most of the peaks shift to higher wavenumber with increasing pressure (hard mode), similar to the 33HMCHBr. However, unlike 33HMCHBr, when a selection of Gaussian fitted peak positions were plotted with respect to pressure (**Figures 3.10 and 3.11**), a single peak (ν_2) appears to decrease in wave number initially before continuing with an increase in wavenumber. This peak happens to be located in the region where previous calculations and experimental studies have suggested a peak for the NHN asymmetric stretch.¹⁶ In order to further investigate the nature of this peak, the Raman pressure series for the singly deuterated TMP (TMPDI, **Figure 3.2b**) was obtained. A comparison of two similar pressures for the two compounds (TMPHI and TMPDI) suggests an absence of the ν_2 peak upon deuteration, **Figure 3.12**. The protonated spectrum was multiplied by a constant of 2.5 to better compare the two spectra. This seems to further suggest the presence of a soft mode peak related to the NHN asymmetric stretch.

Figure 3.8: Raman Pressure Series (Decreasing Pressure) for TMPHIMP

Pressure decreased from around 24 kbar to around 4.69 kbar (ambient shown for comparison) performed with fluid nitrogen and ruby in a diamond anvil cell. As pressure decreases, peaks can be shown shifting to lower wavenumbers. There does not appear to be a distinct discontinuity.

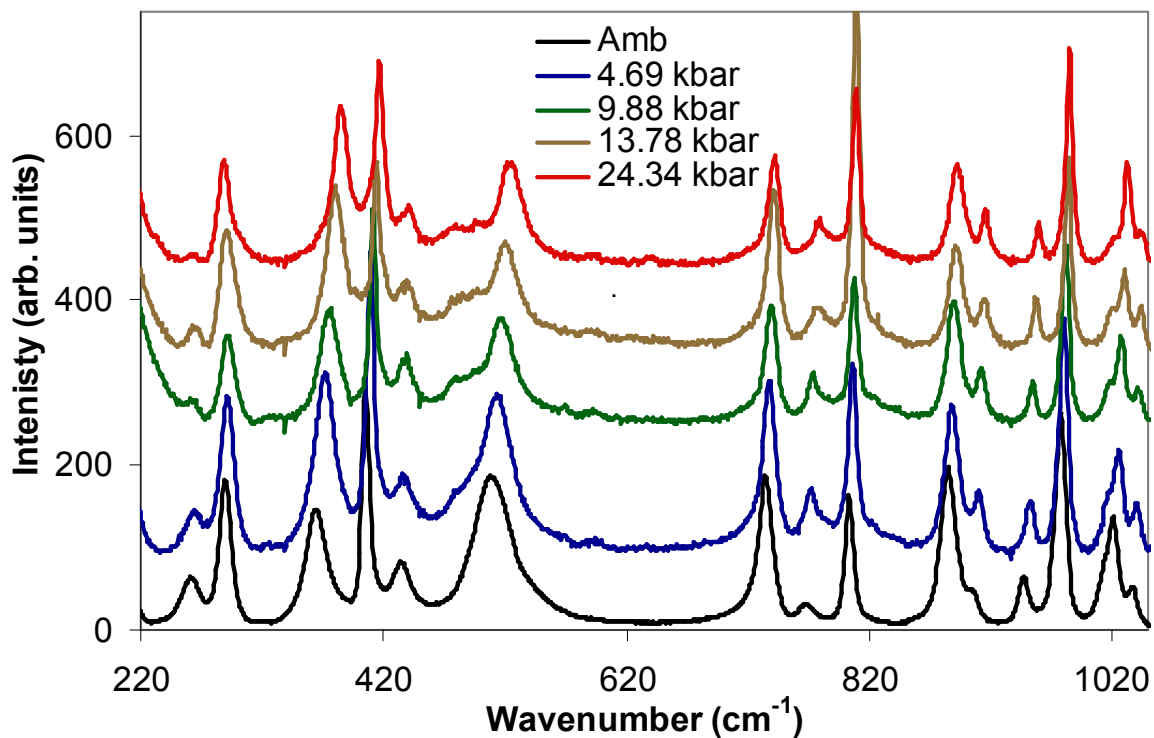


Figure 3.9: Raman Pressure Series (Increasing Pressure) for TMPHIMP

Pressure increased from around 4.69 kbar to 22.90 kbar performed with fluid nitrogen and ruby in a diamond anvil cell. As pressure decreases, peaks can be shown shifting to higher wavenumbers. There does not appear to be a distinct discontinuity.

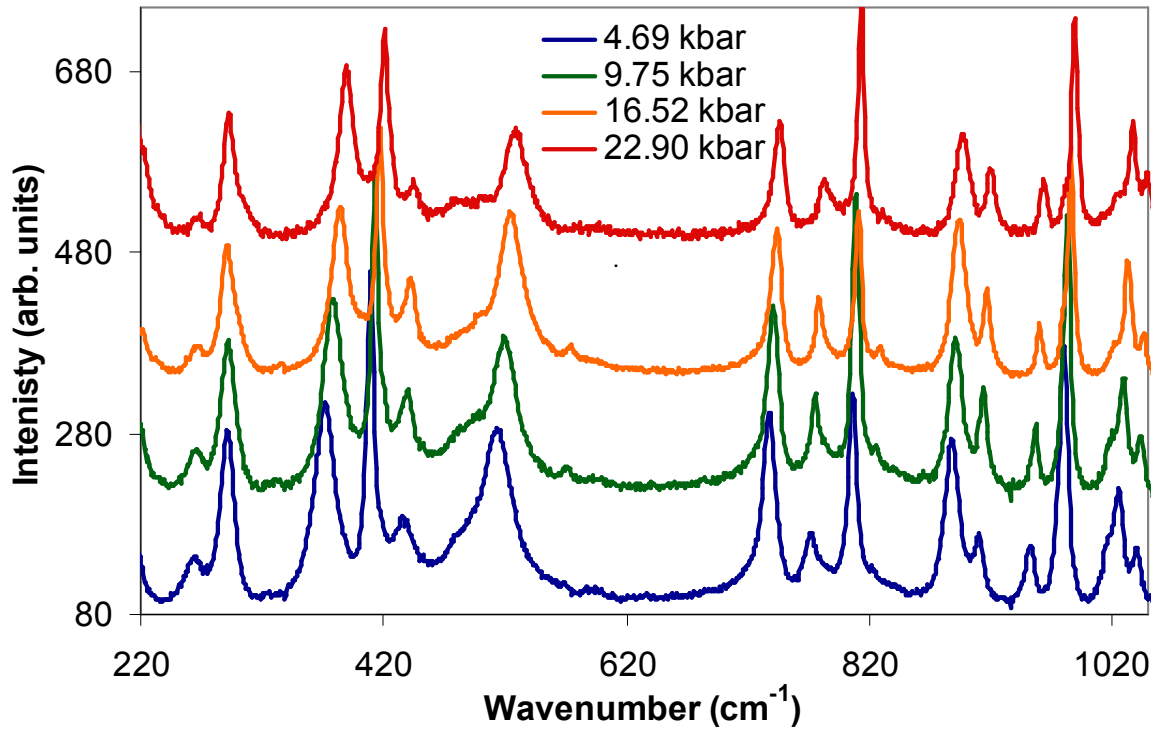


Figure 3.10: Pressure Induced Shift in the Raman Peak Position for TMPHIMP (v1-v4)

Select Raman peaks (v1-v4) of TMPHI in fluid nitrogen and ruby in a diamond anvil cell shows that the increase in the wavenumbers as pressure is increased. There appears to be no distinct phase change. There appears to be a soft mode for v2 from ambient pressure to ~4 kbar, after which it becomes a hard mode.

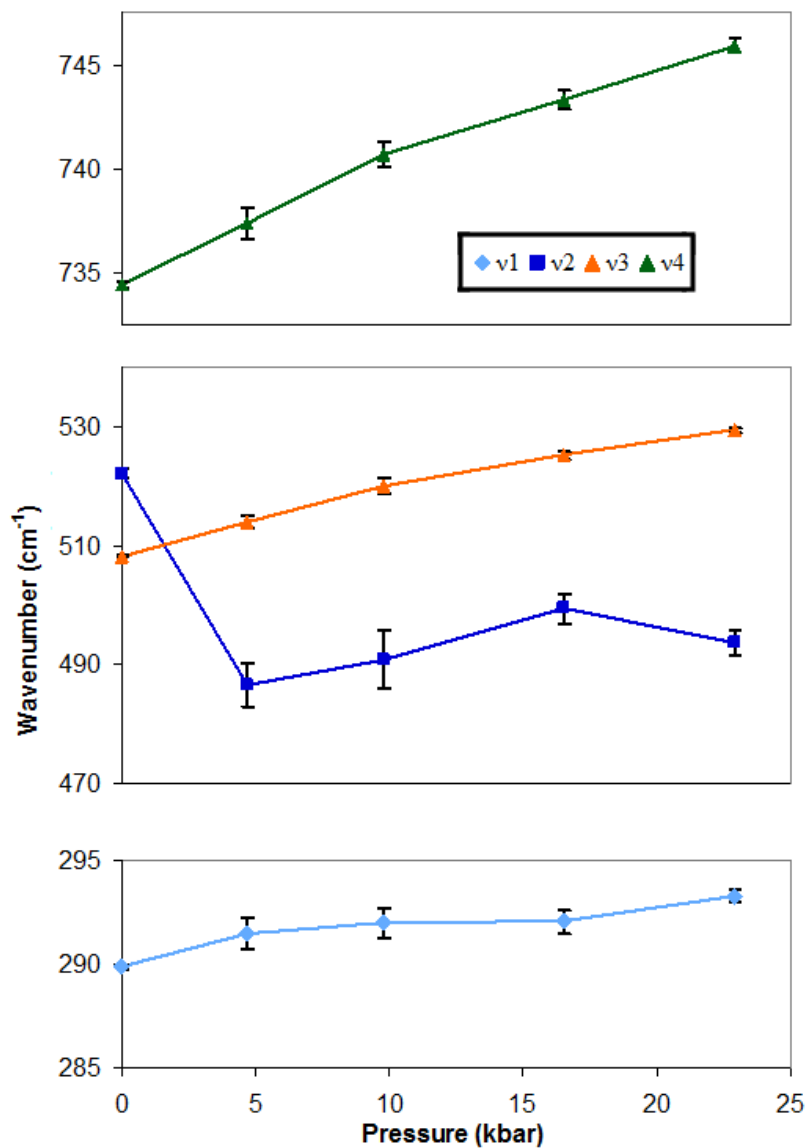


Figure 3.11: Pressure Induced Shift in the Raman Peak Position for TMPHIMP (v5-v8)

Select Raman peaks (v5-v8) of TMPHI in fluid nitrogen and ruby in a diamond anvil cell shows that the increase in the wavenumbers as pressure is increased. There appears to be no distinct phase change.

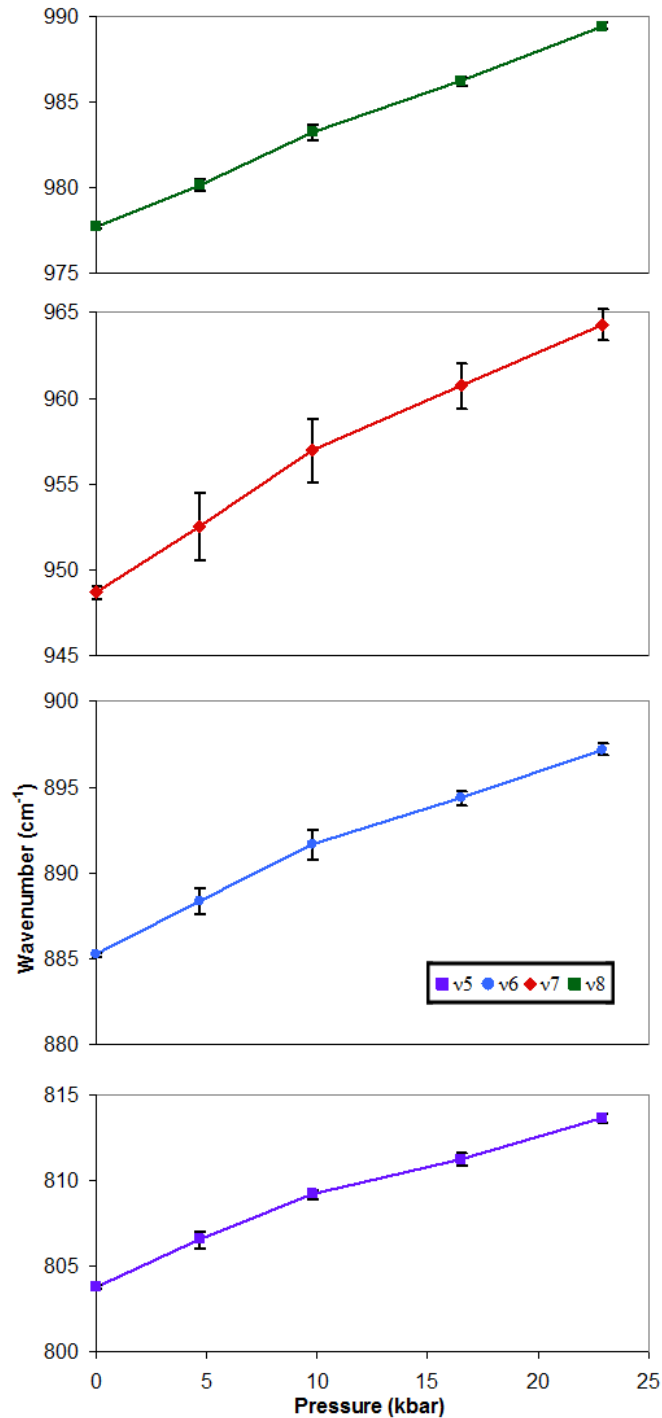
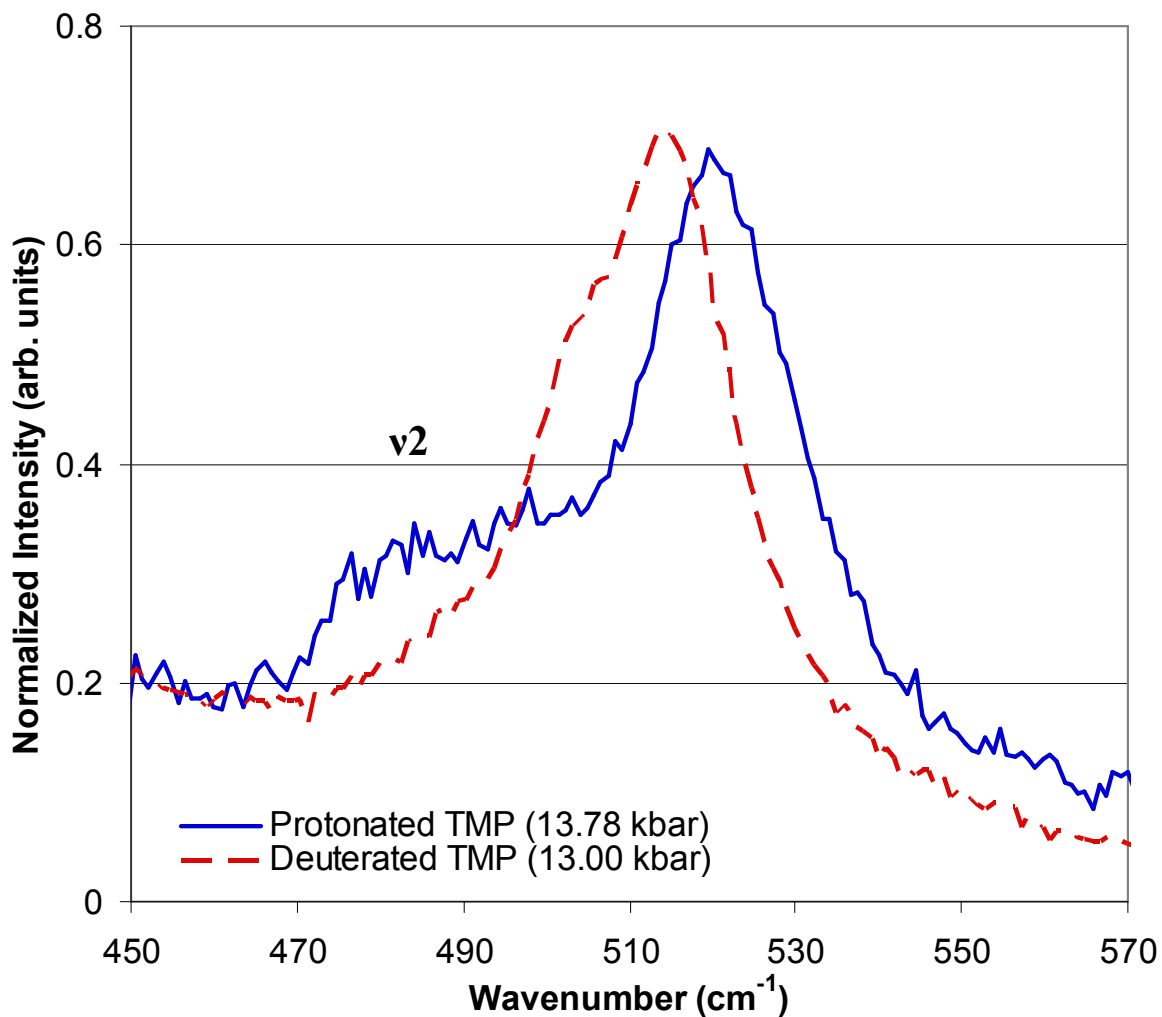


Figure 3.12: Evidence of ν_2 Peak Absence (Shift) Due to Deuteration

A comparison of the deuterated and protonated forms of TMP at similar pressures suggest an absence of the ν_2 peak, which is around the wavenumber of a mode suggested to be coupled to the symmetric NHN stretch of the LBHB in TMP.¹⁶



3.4: Conclusions

In this chapter, the results of the Raman spectroscopic studies of cyclic tertiary diamines have been reported. A phase transition has been observed for the compound 33HMCHBr, either monoprotonated or diprotonated as it was a mixture of the two. A study of a pure compound would identify the compound that undergoes the phase transition and determine more precisely the critical pressure of the transition. A soft vibrational mode has been observed for TMPHI at $\sim 520\text{ cm}^{-1}$, which has also been shown to shift (disappear from observed region) upon deuteration of the NHN proton.

In addition to Raman spectroscopy, X-ray crystallography can be used to study the effect of parameters of pressure, as well as temperature on the crystal structure of molecular crystals. In the following chapter, a temperature dependent single x-ray crystallographic study has elucidate the critical temperature of the temperature induced phase transition of p-terphenyl.

References

- (1) Latimer, W. M.; Rodebush, W. H. *J Am Chem Soc* **1920**, *42*, 1419.
- (2) Kemsley, J. *Chemical & Engineering News* **2010**, *88*, 32.
- (3) Gerlt, J. A.; Gassman, P. G. *Biochemistry* **1993**, *32*, 11943.
- (4) Gerlt, J. A.; Gassman, P. G. *J Am Chem Soc* **1993**, *115*, 11552.
- (5) Cleland, W. W. *Biochemistry* **1992**, *31*, 317.
- (6) Cleland, W. W.; Kreevoy, M. M. *Science* **1994**, *264*, 1887.
- (7) Frey, P. A.; Whitt, S. A.; Tobin, J. B. *Science* **1994**, *264*, 1927.
- (8) Warshel, A.; Papazyan, A.; Kollman, P. A.; Cleland, W. W.; Kreevoy, M. M.; Frey, P. A. *Science* **1995**, *269*, 102.
- (9) Cleland, W. W.; Frey, P. A.; Gerlt, J. A. *Journal of Biological Chemistry* **1998**, *273*, 25529.
- (10) Kreevoy, M. M.; Liang, T.-M.; Chang, K.-C. *J Am Chem Soc* **1977**, *99*, 5207.
- (11) Kreevoy, M. M.; Liang, T. M. *J Am Chem Soc* **1980**, *102*, 3315.
- (12) Yamaguchi, S.; Kamikubo, H.; Kurihara, K.; Kuroki, R.; Niimura, N.; Shimizu, N.; Yamazaki, Y.; Kataoka, M. *Proceedings of the National Academy of Sciences* **2009**, *106*, 440.
- (13) van Wilderen, L. J. G. W.; van der Horst, M. A.; van Stokkum, I. H. M.; Hellingwerf, K. J.; van Grondelle, R.; Groot, M. L. *Proceedings of the National Academy of Sciences* **2006**, *103*, 15050.
- (14) Yaghmaei, S., University of California, Riverside, 2008.
- (15) Yaghmaei, S.; Khodagholian, S.; Kaiser, J. M.; Tham, F. S.; Mueller, L. J.; Morton, T. H. *J Am Chem Soc* **2008**, *130*, 7836.
- (16) Khodagholian, S., University of California, Riverside, 2010.
- (17) Shimada, H.; Nibu, Y.; Shimada, R. *J Raman Spectrosc* **2008**, *39*, 32.
- (18) Mishra, A. K.; Murli, C.; Sharma, S. M. *The Journal of Physical Chemistry B* **2008**, *112*, 15867.

(19) Mao, H. K.; Bell, P. M.; Shaner, J. W.; Steinberg, D. J. *J Appl Phys* **1978**, *49*, 3276.

(20) Bevington, P. R.; Robinson, D. K. *Data reduction and error analysis for the physical sciences*; 3rd ed.; McGraw-Hill: Boston, 2003.

Chapter IV

An X-ray Crystallography Study of the Crystal Structure of p-Terphenyl at Varying Temperature

4.1: The Basics of X-ray Crystallography Structure Determination

A detailed explanation and description of the basics of X-ray crystallography can be found in several texts from which the following summary was based.¹⁻⁵

Because the wavelength of x-rays is on the same order of magnitude as the distances between atoms in crystals, x-rays undergo diffraction when passed through solid crystalline material. It is this property that is used in x-ray crystallography to determine the position, structure, and symmetry of the atoms in solid crystalline materials. In single crystal x-ray diffraction, a single crystal of the substance is prepared and mounted on the instrument. Computer software is then used to determine the orientation of the crystal on the instrument, as well as the crystal system, Bravais lattice and unit cell. Bragg's Law of Diffraction treats the diffracted x-rays as reflections of the radiation off of families of parallel planes that intersect the unit cell of the crystal at distinct points and separated by a spacing d_{hkl} .¹ The points of intersection are labeled by the reciprocal of the fraction along each of the three crystallographic axes (a, b, c) where the planes intersect, called Miller indices (hkl). For example, the Miller planes (210) would intersect $\frac{1}{2}$ distance along the a axis, one full distance along the b axis, and never intersect the c axis (the reciprocal of infinity is zero, therefore a zero Miller index represents an intersection

at infinity.)¹ According to Bragg's Law of Diffraction, for a given x-ray wavelength, the separation of the planes and the angle of the incoming x-ray beam, with respect to the Miller planes, must satisfy **Equation 4.1** so that the radiation reflected off each of the planes in the family, when it reaches the detector, is in phase.¹

The diffraction pattern from the sample represents a reciprocal lattice of the real space crystal lattice where each point in the reciprocal lattice represents the normal vectors for a family of Miller planes and so is labeled by a unique set of Miller Indices. Two types of data are obtained from the reflections of the reciprocal lattice: the position and symmetry of the reflection points provides information on the type of crystal lattice and its symmetry, while the intensity, I_{hkl} , is related to the electron density since the oscillation of the electrons is the cause for the diffraction of the x-rays.¹⁻⁴

$$n\lambda = 2d \sin(\theta) \quad 4.1$$

The location and indexing (assigning of Miller Indices to the points in reciprocal space, which is performed through the use of most modern software packages) of the reflection points in reciprocal space is what allows a crystallographer to begin to interpret the lattice geometry and symmetry of the structure in real space. First, there are fourteen Bravais lattices, which represent the fourteen unique ways you can create a repeating pattern of points in three-dimensional space.^{1,2,4} The lattice is defined by the lengths and angles of its three dimensional axes (lengths A, B, C and angles α , β , γ), as well as the location of points in the lattice which can represent either single atoms or molecules, depending on the type of solid. Further symmetry in the crystal is investigated by

determining the space group of the crystal from the possible 230 space groups; these space groups arise when the fourteen Bravais lattices are combined with further symmetry elements, such as glide planes and screw axes.^{2,4} Not all space groups have been seen in real crystal systems. According to Hammond, “over 60% of organic and inorganic crystals belong to space groups $P2_1/c$, $C2/c$, $P2_1$, $P\bar{1}$, P_{bca} and $P2_12_12_1$ and of these $P2_1/c$ ” is “the commonest.”²

After the initial determination of the lattice geometry and symmetry from the indexing of the reciprocal space reflections, the intensity of the reflections is then used in determining the positions of the atoms in the structure. The basis for this determination comes from the fact that the intensity, I_{hkl} , of the diffracted radiation is proportional to the square modulus of the structure factor. The structure factor, F_{hkl} , is a function of the atomic scattering factors and atomic positions of all the atoms. The scattering factors, f_j , are based on electron density and wavelength of scattered radiation. These relationships

$$I_{hkl} = F_{hkl}^* F_{hkl} \quad 4.2$$

$$F_{hkl} = \sum_j f_j e^{i\phi_{hkl}(j)} \quad \phi_{hkl}(j) = 2\pi(hx_j + ky_j + lz_j) \quad 4.3$$

$$f = 4\pi \int_0^\infty \rho(r) \frac{\sin(kr)}{kr} r^2 dr \quad k = \frac{4\pi}{\lambda} \sin(\theta) \quad 4.4$$

$$\rho(r) = \frac{1}{V} \sum_{hkl} F_{hkl} e^{-2\pi i(hx+ky+lz)} \quad 4.5$$

can be seen in **Equations 4.2-4.4**.¹ Due to this relationship between the structure factor and the electron density, $\rho(r)$, an electron density map can be constructed from a Fourier transformation of the structure factors as seen in **Equation 4.5**.¹

However, since the structure factor is not measured directly, but rather the intensity, there arises ambiguity in whether the root of the intensity should be taken to be either the positive or the negative of the structure factor. In other words, we can calculate the magnitude but we do not know the phase. In modern analyses, the direct methods are quite often used. Direct methods involve treating the phases as probabilistically determinable values, which allows for the initial phases to be determined.¹⁻⁴ From there, crystal structure refinement is then employed.

$$M = \sum w(F_o^2 - F_c^2)^2 \quad 4.6$$

$$M = \sum w(|F_o| - |F_c|)^2 \quad 4.7$$

The purpose of crystal structure refinement can be threefold: to improve the phasing for a more accurate electron density map; to check the structure for “correctness”; and to improve the parameters of the structure model.³ An example of some of the parameters refined for the structure model are the three position coordinates for each atom, usually in fractional coordinates with respect to the length and geometry of the determined crystal lattice axes, and displacement parameters for each atom, which can either be one isotropic parameter (representing a sphere) or six anisotropic parameters (representing an ellipsoid.)³⁻⁵ The displacement parameters can be interpreted as either dynamic disorder, which is movement due to the temperature and vibrations of

the molecules, or static disorder, which is caused by atoms occupying different positions in different lattice cells in the real crystal structure.⁴

In crystal refinement, the parameters are changed to minimize the function M. Depending on the crystallographer, M can be defined as either **Equation 4.6** or **Equation 4.7**, where F_o and F_c are the experimental and model calculated values of the structure factor, F_{hkl} , and w are weighting factors based on the uncertainty of the experimental values. The quality of the model is often based on two values R1 and wR2, defined in **Equations 4.8** and **4.9**, where w is the weighting factors based on the uncertainty of the observed measurements.

$$R1 = \frac{\sum ||F_o| - |F_c||}{\sum |F_o|} \quad 4.8$$

$$wR2 = \left[\frac{\sum w(F_o^2 - F_c^2)^2}{\sum wF_o^2} \right]^{1/2} \quad 4.9$$

4.2: Optical Studies of p-Terphenyl Crystal Structure Using Pentacene Guest

Molecule as Probe

It has been seen for the mixed frystal pentacene in p-terphenyl that when the temperature is lowered below the transition point for p-terphenyl (PTP), $T_c=193$ K, four distinct pentacene photosites (O1-O4) are seen, which are due to pentacene substitution into the four unique PTP molecules in the low temperature triclinic $P\bar{1}$ crystal structure.⁶⁻⁸

The use of these four unique photosites has allowed for the study of the local crystal

structure of PTP around these four photosites as well as study the pressure induced phase transition between triclinic $P\bar{1}$ (four unique photosites) to monoclinic $P2_1/a$ crystal structure (one photosite.)⁹⁻¹³

The first vibronic transition of each origin band has been observed and the V4 vibronic peak was shown to be much narrower than the other three peaks.⁸ It was suggested that both V2 and V4 are coupled to lattice modes whose two quantum excitation is degenerate in energy to the vibronic transitions.⁸ This leads to motional averaging for the V2 and V4 lines and is evidence that slight differences in the local structure of the host lattice can significantly alter the vibrational relaxation and dephasing of guest molecules.⁸

Using time resolved fluorescence spectroscopy, the fluorescence lifetimes for the four photosites were studied.¹⁰ It was observed that the fluorescence lifetime for two of the photosites (O1 and O2) is insensitive to pressure, whereas the lifetimes for photosites O3 and O4 increase as pressure is increased.¹⁰ This occurs due to the different amount of shifting the triplet and singlet states for the O3 and O4 photosites undergo with pressure. As pressure increases, the triplet state energy decreases at a rate less than that of the singlet state so that the difference in energy decreases till the singlet state drops below the triplet state, which decreases the intersystem crossing.¹⁰ A third distinct crystal region is postulated due to a unique set of absorption peaks, and distinct fluorescence lifetimes for those peaks.¹⁰

In Baer and Chronister¹³, photon echo measurements of pentacene doped PTP were made at varying temperatures and pressures. It was shown that below the phase

transition (triclinic phase) there appears to be a mode softening effect in the pseudolocal phonon of the pentacene molecule as PTP approaches the transition pressure (increasing pressure).¹³ Above the phase transition (monoclinic phase) there appears to be strong mode hardening as pressure moves away from the transition pressure (increasing pressure). This could also be looked at as mode softening if going in the direction towards the phase transition from the monoclinic side of the boundary (decreasing pressure).¹³ It was suggested that the presence of the phase boundary at 5.5 kbar causes a mode softening of the pseudolocal phonon which would indicate a correlation between a change in the crystal coordinate related to the phase transition and the coordinate of the pseudolocal phonon.¹³ Such an effect will be considered computationally in **Chapter 5**.

4.3: Low and Room Temperature Crystal Structures for PTP

Rietveld *et al.* has shown that room temperature PTP has a monoclinic $P2_1/a$ crystal structure, with geometry $a=8.10 \text{ \AA}$, $b=5.61 \text{ \AA}$, $c=13.61 \text{ \AA}$, and $\beta=92^\circ$.¹⁴ The diffraction data suggested that the three rings of PTP were parallel with each other with a slight deviation of $\sim 0.4^\circ$.¹⁴ However, it was later shown that the planarity was an average of the middle ring moving between two states being above and below the plane of the outer rings, with an angle of $\varphi=\pm 13.3^\circ$ out of the average molecular plane.¹⁵⁻¹⁷ At low temperatures (below $T_c=193 \text{ K}$), PTP was shown to have a triclinic $P\bar{1}$ crystal structure where the movement of the inner ring locks into four distinct conformations with four unique torsion angles between the inner and outer rings.¹⁸

In Reitseveld *et al.*, x-ray and neutron diffraction studies were performed on PTP in order to determine a more accurate determination of the molecular geometry found in the x-ray structure determined by Pickett¹⁹. One crystal was prepared from the melt and another was prepared from solution. The one from the melt showed a smaller temperature factor indicating less disorder and a more perfect crystal compared to the one made from solution.¹⁴ The difference in the temperature factor was found to be 0.88 \AA^2 .¹⁴ It was observed that the principal axes of libration coincided with the molecular axes closely.¹⁴ Results suggested that center and outer rings do not deviate significantly from planarity but that they are not co planer either.¹⁴ The results of the hydrogen position analysis indicated steric strain between the ortho hydrogens.¹⁴

Baudour, et al. performed x-ray diffraction on PTP at low temperature below a previously demonstrated temperature induced phase change.¹⁸ The crystal structure was initially reasoned, by implication of the known double well potential of the ring torsion, to be in a unit cell where the relative position of the central ring and outer rings alternate position every $\frac{1}{2}$ translation along the **a** or **b** axes. The structure factors for the crystal structure were calculated for sixty of the most intense super structure Bragg peaks and seven intense Bragg peaks ($k=\text{even}$) giving an R value of 0.25 followed by refinement.¹⁸ The unit cell was determined to be $P\bar{1}$ with four molecules in the unit cell. Using software developed by the group, which allowed for the refinement of atomic coordinates and molecular libration and translation tensors, a new R-value of 0.16 was obtained but with distorted benzene ring bond lengths of 1.3-1.5 \AA .¹⁸

The structure was then refined again with the bond lengths between the carbons (both connecting the rings and in the rings) set to 1.5 Å and 1.4 Å, respectively; the position of the molecules were based on the high temperature data, while the orientation in space for the molecules were left as variables; this gave a new R-value of 0.15.¹⁸ Nine thermal parameters were assumed isotropic and similar for equivalent atoms. The R-value was then lowered to 0.109 with the addition of hydrogen atoms.¹⁸ The software, WAGG, was then used to refine the molecular librations and translational tensors with the four unique molecules having the same thermal parameters, which lowered the R-value to 0.103.¹⁸ The final structure shows that the middle ring rotates opposite that of the outer ring and there are four unique torsions which can be grouped into two categories, $\sim 16^\circ$ and $\sim 25^\circ$.¹⁸ It is suggested that larger thermal disorder in the torsion between the benzene rings at room temperature is changed into four distinct torsion angles representing one side of the double well potential.¹⁸

Using neutron (at 200 K) and x-ray diffraction (at room temperature) of PTP, the double well potential energy for the libration of the middle ring about the long molecular axis was studied by Baudour et al.¹⁵ It was determined that the barrier height is approximately 0.6 kcal/mol and that the internal g mode is sufficient to bring the ring libration over the barrier.¹⁵ The combination of the double peak distribution of the central ring torsion angle and the low barrier height suggests that the low temperature phase transition is an order-disorder transition but that it is close to the boundary that separates it from the displace transition.¹⁵

In classical forcefield calculations by Schatschneider et al., it was shown that neither the PCFF nor COMPASS forcefields could accurately simulate the known temperature and pressure phase transitions for PTP.²⁰ A new forcefield was developed from the PCFF model using nonbonding terms from COMPASS. The forcefield was optimized for the torsion angle values of the four unique molecules in the low temperature phase by adjusting the V2 constant in the potential energy 2nd order term.²⁰ It was observed that the dynamics are sensitive to the initial velocities used in the calculations causing fluctuations in each run but was found to average out over multiple runs.²⁰ The resulting temperature and pressure series calculations accurately determined the room pressure transition temperature and low temperature transition pressure. In the temperature series, it was shown that the unique torsion angles begin to converge and average out to zero as the transition temperature was reached.²⁰

4.4: X-ray Diffraction Data Collection for PTP at Varying Temperatures

Two colorless prism crystals grown from toluene were used for the single crystal x-ray diffraction study of PTP, C₁₈H₁₄. Each crystal was glued on to a glass fiber with epoxy resin and mounted on to the goniometer head. A sphere of reflections was collected at 100K, 175K, 200K, and 296K using one crystal (size 0.21 x 0.45 x 0.50 mm). A second crystal (size 0.12 x 0.44 x 0.47 mm) was used to collect two full data sets at 188K and 193K and 100 frames of partial data set at 100K, 175K, 183-196K, 200K, and

296K to examine the reciprocal lattice diffraction patterns before and after the phase transition temperature (ca.193K).

A Bruker APEX2 (version 2010.9-1)²¹ platform-CCD x-ray diffractometer system (Mo-radiation, $\lambda = 0.71073 \text{ \AA}$) was used for data collection. A total of 3600 frames were collected for a sphere of reflections (with scan width of 0.3° in ω , starting ω and 2θ angles at -30° , and ϕ angles of 0° , 90° , 120° , 180° , 240° , and 270° for every 600 frames, 10 sec/frame exposure time) for 100K, 175K, 188K, 193K, 200K and 296K temperatures. The angle ϕ was set at 0° for the 100 frames of partial data sets collected using omega scan (0.30° scan width). The frames were integrated using the Bruker SAINT software package (version V7.68A)²² and using a narrow-frame integration algorithm. Absorption corrections were applied to each full data set using the Bruker SADABS software program (version 2008/1).²³

4.5: Structure Refinement for PTP at Varying Temperatures

Structure solutions and refinements were done using the Bruker SHELXTL software (version 2008/1)²⁴. Dual space method of phase determination followed by two cycles of Fourier refinement led to an electron density map from which most of the non-hydrogen atoms were identified in the asymmetry unit of the unit cell for both the triclinic “C-centered”, “ $C\bar{1}$ ” space group, and the monoclinic P-primitive, $P2_1/a$ space group. With subsequent isotropic refinement, all of the non-hydrogen atoms were identified. There were four different conformers of the half-PTP-molecules present in the

asymmetry unit of the triclinic system. There were two different conformers of the disordered-half-PTP-molecules present in the asymmetry unit of the monoclinic system where the disordered were model as 50%/50% disorder. At 188K triclinic data, all four conformers were modeled with disorder (87%/13% disordered site occupancy ratio). No disorder was observed for the triclinic structure at 175K and 100K.

The established pseudo-merohedral triclinic C-centered twin law was TWIN (1 0 0 | 0 -1 0 | 0 0 1). The minor/major components pseudo-merohedral twin ratios at 188K, 175K and 100K were 33%/67%, 43%/57%, and 50%/50%, respectively. In both the triclinic and monoclinic crystal systems, all the half-PTP-molecules were located at the inversion symmetry. Atomic coordinates, isotropic and anisotropic displacement parameters of all the non-hydrogen atoms were refined by means of a full matrix least-squares procedure on F^2 . The H-atoms were included in the refinement in calculated positions riding on the atoms to which they were attached. A summary of the results are given in **Tables 4.1-4.3**. **Tables 4.4 and 4.5** show the selected torsion angles between the terminal and middle rings for 100K, 175K, 188K, 193K, 200K, and 296K structures. An example of the angles can be seen in **Figure 4.3** (torsion angle C2-C1-C7-C8). **Table 4.6** shows the final R1-values of the PTP molecule modeled with disordered-middle-ring (296K, 200K, 193K, 188K), modeled with no-disordered-middle-ring (175K, 100K), and the pseudo-merohedral twinning ratios for the triclinic system (188K, 175K, 100K).

Using the first crystal (size 0.21 x 0.45 x 0.50 mm) at 100K as an example, 200 frames of data were harvested for reflections with I/σ greater than 20. The reflections were then indexed to give a reduced triclinic unit cell parameters of $\mathbf{a} = 9.72 \text{ \AA}$, $\mathbf{b} = 9.72 \text{ \AA}$, $\mathbf{c} = 13.56 \text{ \AA}$, $\alpha = 88.11^\circ$, $\beta = 88.07^\circ$, $\gamma = 69.33^\circ$. This reduced triclinic unit cell was transformed to a triclinic C-centered cell with $\mathbf{a} = 15.99 \text{ \AA}$, $\mathbf{b} = 11.06 \text{ \AA}$, $\mathbf{c} = 13.56 \text{ \AA}$, $\alpha = 90.03^\circ$, $\beta = 92.32^\circ$, $\gamma = 90.00^\circ$ using the transformation matrix $(1 \ 1 \ 0 \ | \ 1 \ -1 \ 0 \ | \ 0 \ 0 \ -1)$ (similar to the previous study¹⁸). This cell transformation procedure was similarly applied to the 175K and 188K data before data integration. All the 100K, 175K, and 188K data frames were then integrated using the unconstrained triclinic C-centered cell parameters instead of the constrained monoclinic C-centered cell parameters (where angle $\alpha = \gamma = 90^\circ$). The final unit cell parameters are summarized in **Tables 4.1 and 4.2**. No special unit cell transformation was required for the monoclinic cell (296K, 200K 193K) before the phase transition where the harvested reflections indexed to the correct monoclinic primitive cell. The final monoclinic unit cell parameters at 193K, 200K, and 296K are summarized in **Tables 4.2 and 4.3**.

Table 4.1: Crystal data and Structure Refinement for PTP at 100K and 175K

Empirical formula	C18 H14	C18 H14
Formula weight	230.29	230.29
Temperature	100(2) K	175(2) K
Wavelength	0.71073 Å	0.71073 Å
Crystal system	Triclinic	Triclinic
Space group	C $\bar{1}$	C $\bar{1}$
Unit cell dimensions	a = 15.9750(13) Å b = 11.0451(9) Å c = 13.5426(11) Å α = 89.9966(11)° β = 92.3329(11)° γ = 89.9982(11)°	a = 16.0588(10) Å b = 11.0980(7) Å c = 13.5651(8) Å α = 89.9593(9)° β = 92.2215(9)° γ = 89.9994(9)°
Volume	2387.5(3) Å ³	2415.8(3) Å ³
Z	8	8
Density (calculated)	1.281 Mg/m ³	1.266 Mg/m ³
Absorption coefficient	0.072 mm ⁻¹	0.071 mm ⁻¹
F(000)	976	976
Crystal size	0.50 x 0.45 x 0.20 mm ³	0.50 x 0.45 x 0.20 mm ³
Theta range for data collection	1.50 to 29.13° -21 ≤ h ≤ 21	1.50 to 29.13° -21 ≤ h ≤ 21
Index ranges	-15 ≤ k ≤ 15 -18 ≤ l ≤ 18	-15 ≤ k ≤ 15 -18 ≤ l ≤ 18
Reflections collected	25816	26185
Independent reflections	6411 [R(int) = 0.0197]	6486 [R(int) = 0.0208]
Completeness to theta = 29.13°	99.70%	99.70%
Absorption correction	Semi-empirical from equivalents	Semi-empirical from equivalents
Max. and min. transmission	0.9853 and 0.9650	0.9855 and 0.9654
Refinement method	Full-matrix least-squares on F ²	Full-matrix least-squares on F ²
Data / restraints / parameters	6411 / 0 / 326	6486 / 0 / 326
Goodness-of-fit on F ²	1.047	1.053
Final R indices [I > 2σ(I)]	R1 = 0.0393, wR2 = 0.1201	R1 = 0.0492, wR2 = 0.1472
R indices (all data)	R1 = 0.0455, wR2 = 0.1288	R1 = 0.0605, wR2 = 0.1631

Table 4.2: Crystal data and Structure Refinement for PTP at 188K and 193K

Empirical formula	C18 H14	C18 H14
Formula weight	230.29	230.29
Temperature	188(2) K	193(2) K
Wavelength	0.71073 Å	0.71073 Å
Crystal system	Triclinic	Monoclinic
Space group	$C\bar{1}$	$P2_1/a$
Unit cell dimensions	a = 16.0585(5) Å b = 11.1159(4) Å c = 13.5743(5) Å α = 89.9354(5)° β = 92.2285(5)° γ = 90.0011(5)°	a = 8.0210(2) Å b = 5.5639(2) Å c = 13.5775(4) Å α = 90° β = 92.2370(4)° γ = 90°
Volume	2421.24(15) Å ³	605.48(3) Å ³
Z	8	2
Density (calculated)	1.264 Mg/m ³	1.263 Mg/m ³
Absorption coefficient	0.071 mm ⁻¹	0.071 mm ⁻¹
F(000)	976	244
Crystal size	0.47 x 0.44 x 0.12 mm ³	0.47 x 0.44 x 0.12 mm ³
Theta range for data collection	1.50 to 29.13° -21 ≤ h ≤ 21	3.00 to 29.13° -10 ≤ h ≤ 10
Index ranges	-15 ≤ k ≤ 15 -18 ≤ l ≤ 18	-7 ≤ k ≤ 7 -18 ≤ l ≤ 18
Reflections collected	32346	12577
Independent reflections	6501 [R(int) = 0.0232]	1633 [R(int) = 0.0172]
Completeness to theta = 29.13°	99.60%	99.90%
Absorption correction	Semi-empirical from equivalents	Semi-empirical from equivalents
Max. and min. transmission	0.9918 and 0.9675	0.9918 and 0.9675
Refinement method	Full-matrix least-squares on F ²	Full-matrix least-squares on F ²
Data / restraints / parameters	6501 / 24 / 351	1633 / 0 / 101
Goodness-of-fit on F ²	1.052	1.075
Final R indices [I > 2σ(I)]	R1 = 0.0468, wR2 = 0.1427	R1 = 0.0466, wR2 = 0.1427
R indices (all data)	R1 = 0.0585, wR2 = 0.1597	R1 = 0.0497, wR2 = 0.1487
Largest diff. peak and hole	0.250 and -0.304 e.Å ⁻³	0.281 and -0.198 e.Å ⁻³
Pseudo-merohedral twin law	1 0 0, 0 -1 0, 0 0 1	none

Table 4.3: Crystal data and Structure Refinement for PTP at 200K and 296K

Empirical formula	C18 H14	C18 H14
Formula weight	230.29	230.29
Temperature	200(2) K	296(2) K
Wavelength	0.71073 Å	0.71073 Å
Crystal system	Monoclinic	Monoclinic
Space group	P2 ₁ /a	P2 ₁ /a
Unit cell dimensions	a = 8.0230(3) Å b = 5.5669(2) Å c = 13.5755(5) Å α = 90°. β = 92.2226(5)°. γ = 90°.	a = 8.0985(5) Å b = 5.6067(3) Å c = 13.6041(8) Å α = 90°. β = 92.0329(9)°. γ = 90°.
Volume	605.87(4) Å ³	617.32(6) Å ³
Z	2	2
Density (calculated)	1.262 Mg/m ³	1.239 Mg/m ³
Absorption coefficient	0.071 mm ⁻¹	0.070 mm ⁻¹
F(000)	244	244
Crystal size	0.50 x 0.45 x 0.20 mm ³	0.50 x 0.45 x 0.20 mm ³
Theta range for data collection	3.00 to 29.13°. -10 ≤ h ≤ 10	3.00 to 29.13°. -11 ≤ h ≤ 11
Index ranges	-7 ≤ k ≤ 7 -18 ≤ l ≤ 18	-7 ≤ k ≤ 7 -18 ≤ l ≤ 18
Reflections collected	12564	12807
Independent reflections	1633 [R(int) = 0.0176]	1664 [R(int) = 0.0211]
Completeness to theta = 29.13°	99.80%	99.80%
Absorption correction	Semi-empirical from equivalents	Semi-empirical from equivalents
Max. and min. transmission	0.9855 and 0.9655	0.9858 and 0.9662
Refinement method	Full-matrix least-squares on F ²	Full-matrix least-squares on F ²
Data / restraints / parameters	1633 / 0 / 100	1664 / 2 / 100
Goodness-of-fit on F ²	1.094	1.108
Final R indices [I > 2σ(I)]	R1 = 0.0471, wR2 = 0.1439	R1 = 0.0504, wR2 = 0.1562
R indices (all data)	R1 = 0.0514, wR2 = 0.1509	R1 = 0.0580, wR2 = 0.1658
Largest diff. peak and hole	0.324 and -0.170 e.Å ⁻³	0.237 and -0.176 e.Å ⁻³
Pseudo-merohedral twin law	none	none

Table 4.4: Torsion Angles of PTP Molecules in Monoclinic P₂/a Space Group at 296K, 200K, and 193K

Space Group	P ₂ /a	P ₂ /a	P ₂ /a
Atoms/Temp.	296K	200K	193K
Middle Ring Torsion Angle			
C2-C1-C7-C8	-14.0(2)	-15.23(18)	-15.42(17)
C6-C1-C7-C9	-13.3(2)	-14.82(18)	-15.16(17)
C2-C1-C7-C8D	11.1(2)	11.99(17)	12.36(16)
C6-C1-C7-C9D	11.4(2)	11.88(17)	12.13(16)

Table 4.5: Torsion Angles of PTP Molecules in Triclinic $C\bar{1}$ Space Group at 188K, 175K, and 100K

Space Group Atoms/Temp.	$C\bar{1}$ 188K	$C\bar{1}$ 175K	$C\bar{1}$ 100K
C2A-C1A-C7A-C8A	-19.1(2)	-20.8(2)	-22.85(19)
C6A-C1A-C7A-C9A	-19.1(2)	-20.4(2)	-22.82(19)
C2B-C1B-C7B-C8B	17.1(2)	17.2(2)	18.48(18)
C6B-C1B-C7B-C9B	16.9(2)	17.1(2)	18.45(19)
C2C-C1C-C7C-C8C	-22.84(19)	-24.8(2)	-26.46(16)
C6C-C1C-C7C-C9C	-23.23(19)	-24.5(2)	-26.01(16)
C2D-C1D-C7D-C8D	15.7(2)	16.3(2)	17.06(19)
C6D-C1D-C7D-C9D	15.4(2)	16.3(2)	17.02(18)
C2A-C1A-C7A-C8E	14.6(6)		
C6A-C1A-C7A-C9E	15.4(6)		
C2B-C1B-C7B-C8F	-4.9(7)		
C6B-C1B-C7B-C9F	-4.2(7)		
C2C-C1C-C7C-C8G	10.2(7)		
C6C-C1C-C7C-C9G	10.5(7)		
C2D-C1D-C7D-C8H	-5.8(6)		
C6D-C1D-C7D-C9H	-6.4(6)		

Table 4.6: Comparison of Final R1 values for Crystal Structure at Varying Temperatures (with and without twinning or middle ring disorder)

Temperature	296K	200K	193K	188K	175K	100K
Space group	$P2_1/a$	$P2_1/a$	$P2_1/a$	$C\bar{1}$	$C\bar{1}$	$C\bar{1}$
No-disordered R1 values	6.43%	6.73%	6.90%	7.69%	4.92%	3.93%
Disordered R1 values	5.04%	4.71%	4.66%	4.68%		
Disordered Ratios	50%/50%	50%/50%	50%/50%	87%/13%		
Pseudo-merohedral twin ratios				Ratios	Ratios	Ratios
				33%/67%	43%/57%	50%/50%

4.6: Determining the Phase Transition Temperature from X-ray Diffraction

Using the second crystal (size 0.12 x 0.44 x 0.47 mm,) 100 frames of data were collected at 100K-296K. The reflections were harvested (reflection intensity, I/σ , greater than 20) and indexed accordingly; monoclinic P-primitive cell before phase transition, and triclinic C-centered cell after phase transition. **Figure 4.1** shows the indexed reciprocal lattice reflections harvested from 100 frames of data, projected parallel to the c -axis (001 plane). **Figures 4.1 a-f** show the reciprocal lattice of the monoclinic primitive cell, with \mathbf{a} and \mathbf{b} axes, labeled as red-reflections. The c -axis is pointing out towards the viewer. A few grey labeled reflections (1-14 reflections), which are part of the triclinic C-centered, $\mathbf{a}^*=2\mathbf{a}$ and $\mathbf{b}^*=2\mathbf{b}$ axes, lattice were observed in room temperature measurements (298K - 193K) and not used for the monoclinic-P unit cell determination (considered as outliers). **Figures 4.1 g-r** show the reciprocal lattices of the triclinic C-centered cell, with $\mathbf{a}^*=2\mathbf{a}$ and $\mathbf{b}^*=2\mathbf{b}$ axes, with both red labeled reflections and grey labeled reflections present. By themselves, either the red-reflections or the grey-reflections lattice are identical to a monoclinic-P cell with \mathbf{a} and \mathbf{b} axes. Combined, the red and grey reflections show “monoclinic C-centering”; either the red-lattice has grey-reflections centering or the grey-lattice has red-reflections centering.

Table 4.7 shows the total number of reflections (harvested from **Figures 4.1 a-r**, I/σ greater than 20), the number of red reflections, the number of grey reflections, and the ratios of the red reflections to grey reflections. As the crystal was cooled from 193K to 192K, there is a phase transition between these temperatures, indicated by the

sudden drop in the red reflections to grey reflections ratio, seen in **Table 4.7** and **Figure 4.2**. The number of grey-reflections to red-reflections ratios was closed to zero (0.07) before the phase transition temperature (ca. 193K-192K) and increased significantly after the phase transition temperature (0.23 at 192K). **Figure 4.2** clearly indicates that the phase transition is between 193K and 192K. This is in agreement with calorimetric data that also indicates a transition temperature of around 193K.²⁵

Tables 4.1 and 4.2 show the final results for the triclinic C-centered system after phase transition (i.e. $h+k = 2n$, similar to previous studies¹⁸) where the pseudo-merohedral triclinic twin emulate the monoclinic C-centered system). Instead of the standard triclinic “ $P\bar{1}$ ” space group, we decided to name the space group as “ $C\bar{1}$ ”. **Tables 4.2 and 4.3** show the final results of the monoclinic-P system with $P2_1/a$ space group before phase transition (including 193K data). The non-standard monoclinic $P2_1/a$ space group was chosen instead of the standard $P2_1/c$ for easier packing arrangement comparison of the PTP-molecule before and after the phase transition (where the monoclinic-P **a** and **b** axes were doubled after phase transition to give the triclinic C-centered $\mathbf{a}^*=2\mathbf{a}$ and $\mathbf{b}^*=2\mathbf{b}$ axes). The **c**-axis and \mathbf{c}^* -axis are basically identical for both the monoclinic-P cell (before phase transition) and the triclinic C-centered cell (after phase transition), respectively, when thermal contraction was taken into account (temperature lowered from 296K to 100K).

Figure 4.1: Indexed Reciprocal Lattice Reflections Plots Projected Parallel to the c-Axis

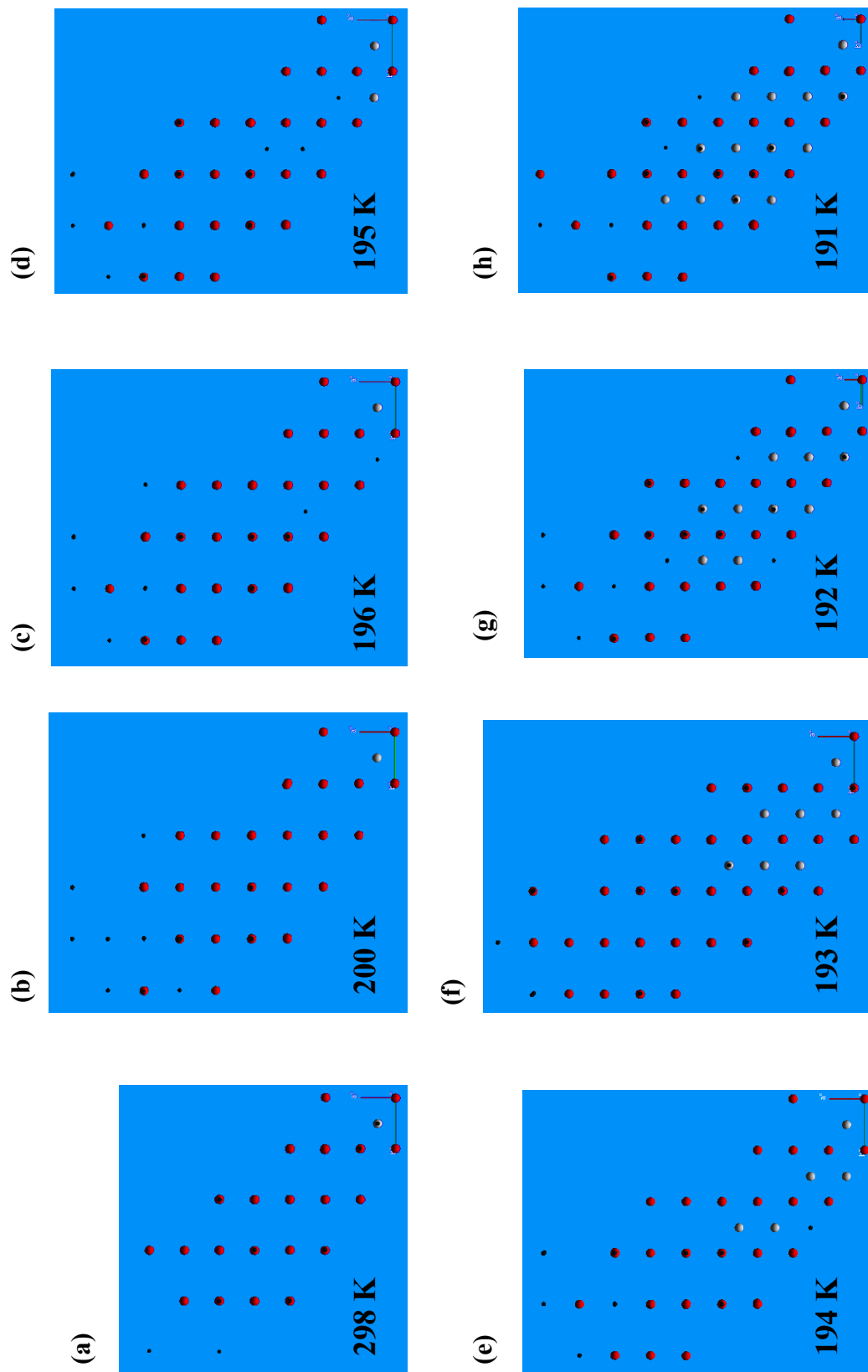


Figure 4.1: Indexed Reciprocal Lattice Reflections Plots Projected Parallel to the c-Axis

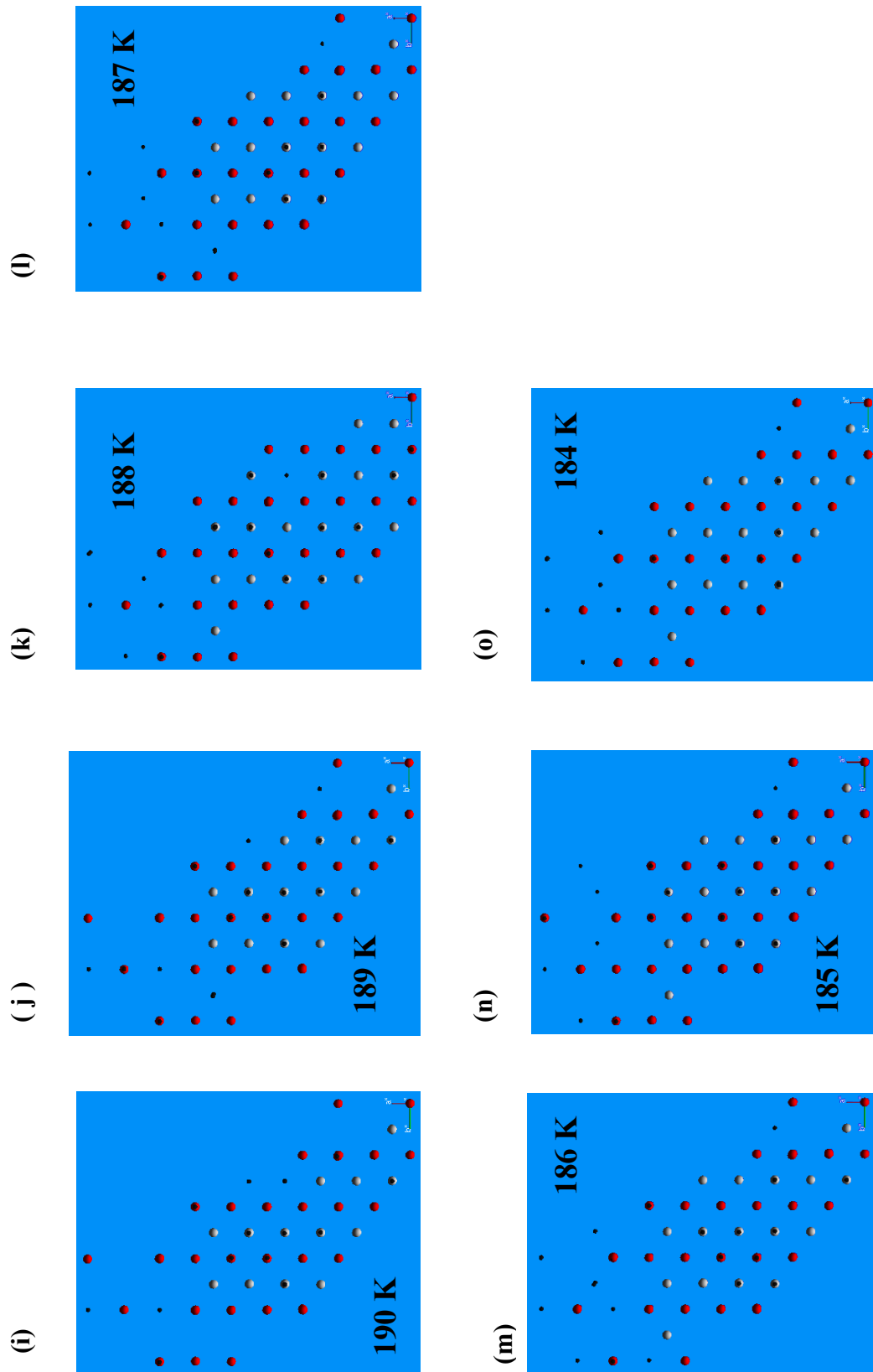
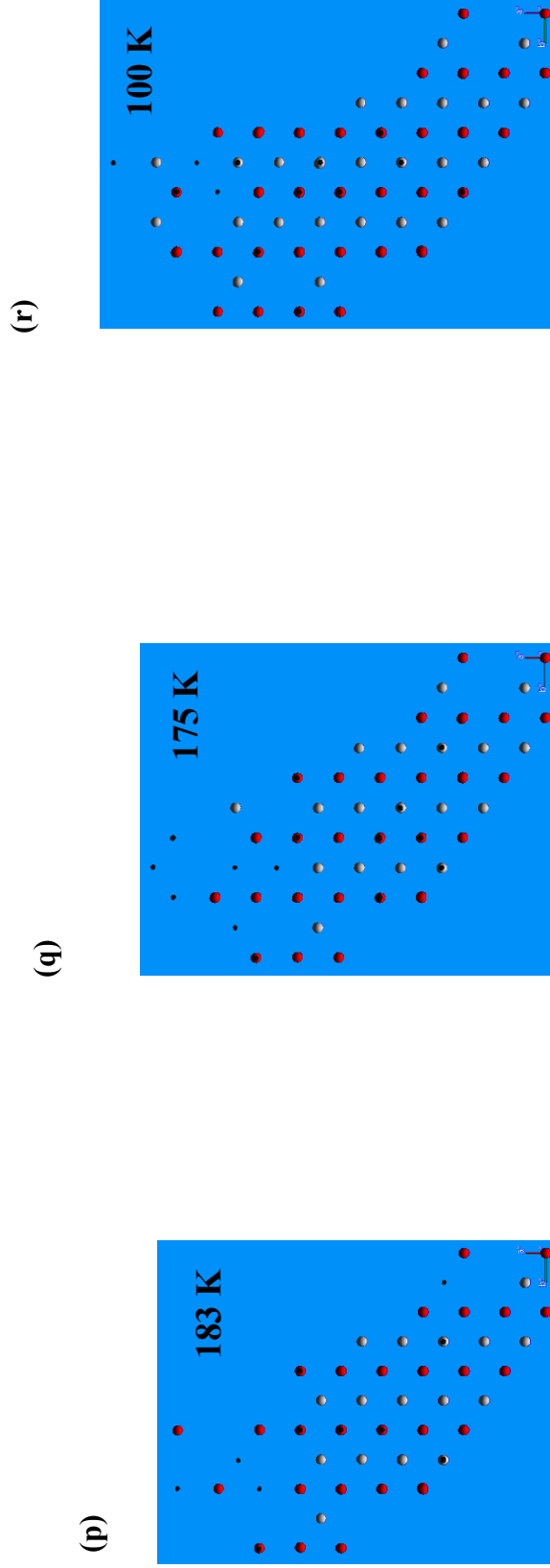


Figure 4.1: Indexed Reciprocal Lattice Reflections Plots Projected Parallel to the c-Axis



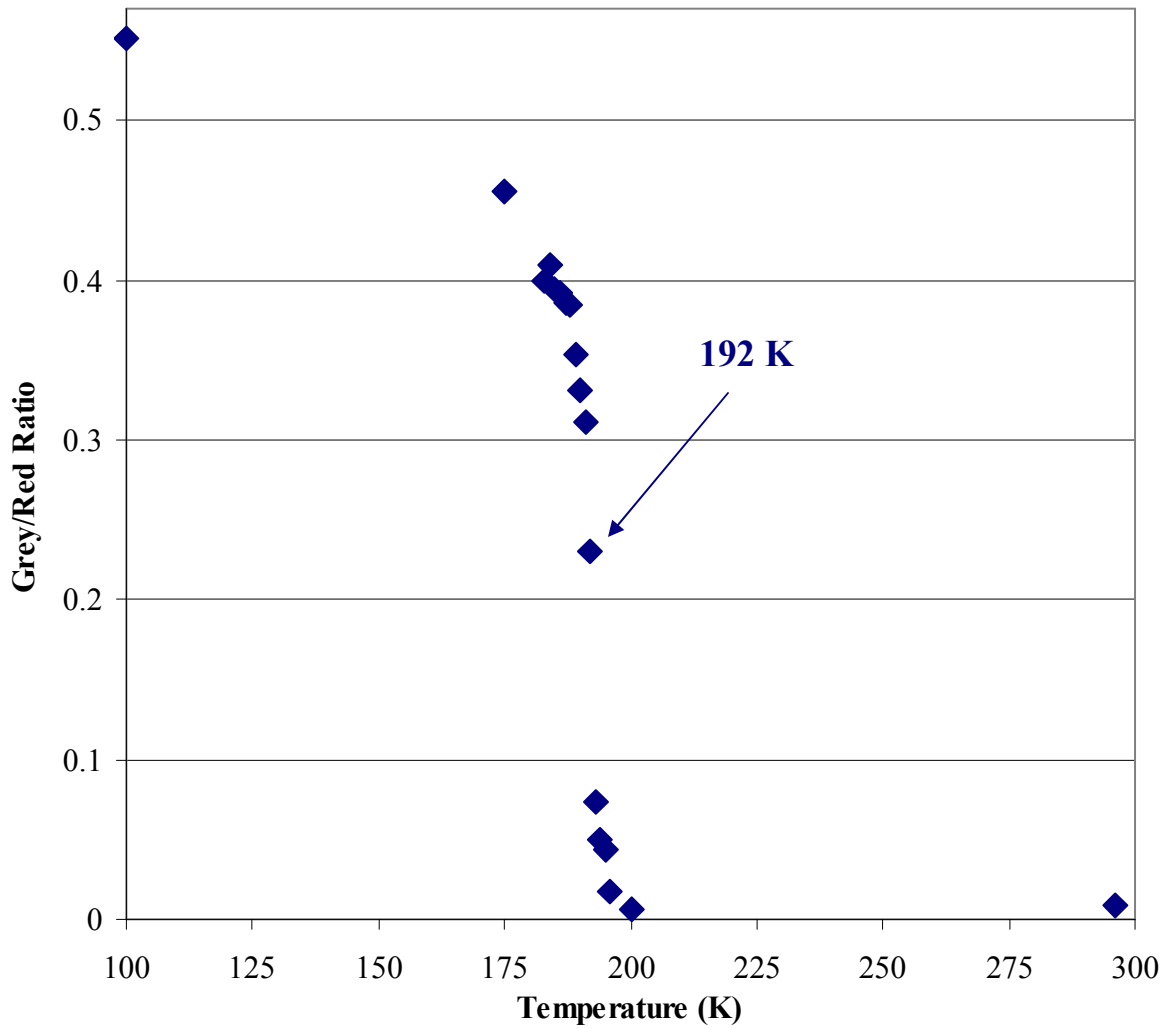
The indexed reciprocal lattice reflections harvested from 100 frames of data, projected parallel to the **c**-axis (001 plane) at varying temperatures. Grey reflections are part of the triclinic C-centered crystal lattice (low temperature phase). Red reflections are found in both the monoclinic P (Room Temperature) and the triclinic C-centered crystal lattice. Since the lattice is three dimensional, there are reflections which are behind those seen . Black reflections are weaker intensity, and so the graphing program has trouble labeling them with color.

Table 4.7: Total Number of Reflections Harvested from 100 Frames of Partial Data Set and Their Grey/Red reflection ratios at Varying Temperatures

Temperature	Total No. of refl. (red+grey refl.)	No. red-refl. P-primitive cell (a-b axes)	No. grey-refl. C-centered cell (2a-2b axes)	Refl. grey/red Ratios
100K	318	205	113	0.551
175K	243	167	76	0.455
183K	228	163	65	0.399
184K	231	164	67	0.409
185K	233	167	66	0.395
186K	231	166	65	0.392
187K	230	166	64	0.386
188K	220	159	61	0.384
189K	218	161	57	0.354
190K	217	163	54	0.331
191K	211	161	50	0.311
192K	198	161	37	0.23
193K	205	191	14	0.073
194K	168	160	8	0.05
195K	167	160	7	0.044
196K	166	163	3	0.018
200K	162	161	1	0.006
296K	118	117	1	0.009

Figure 4.2: Temperature Dependent Change in Ratio of Grey Reflections to Red Reflections

Demonstrates the evidence of the temperature dependent phase change using x-ray crystallography. Grey reflections are from the low temperature crystal lattice. The red reflections are found in both the room temperature and low temperature crystal structures. The inflection point lies around 192 K.



4.7: Modeling Disorder in the PTP Crystal Structure

The PTP molecule models used at various temperature, 296K, 200K, 193K, 188K, 175K, and 100K were examined. **Figure 4.3** shows the PTP molecule (50% probability thermal ellipsoid) with no disorder in the middle-ring before phase transition, viewed along the edge of the terminal phenyl rings and perpendicular to the long-axis of the PTP-molecule at 296K, 200K, and 193K, respectively. The middle ring thermal ellipsoids indicated that the PTP molecule models without middle ring disorder were inadequate models. Once the middle ring disorder (disordered site occupancy ratio of 50%/50%) was modeled into the final refinement, the final R1 values dropped significantly from 6.43% to 5.04%, 6.73% to 4.71%, and 6.90% to 4.66% at 296K, 200K, and 193K, respectively, **Table 4.6**. **Figures 4.4-4.6** shows the two disordered molecules (50% probability thermal ellipsoid) separately for the 296K, 200K, and 193K structures. **Figure 4.7** shows the relation of the two disordered half middle rings at 193K, viewed parallel to the long-axis of the half PTP molecule (terminal rings were removed for clarity). There are two different conformers in the asymmetry unit of the unit cell at 296K, 200K, and 193K. As the temperature was lowered from 296K to 193K, the torsion angles increased slightly as given in **Tables 4.4 and 4.5**.

The PTP molecule transition from a disordered PTP molecule (monoclinic $P2_1/a$) phase to an ordered PTP molecule phase (triclinic C-centered $C\bar{1}$) seems to occur continuously (after the initial phase transition at ca. 193K-192K) as the temperature was lowered from 192K to 100K. The results at 188K support this theory. At 188K, the

minor/major components pseudo-merohedral triclinic C-centered twinning ratio remained constant at 33%/67% whether the four conformers half PTP molecule were modeled with or without middle ring disorder. With the no-disorder middle ring model, the residual electron density peaks next to the atoms of the middle ring were much higher than expected (0.50-0.88 e.Å⁻³). **Figure 4.8** (50% probability thermal ellipsoid) shows the Q-peaks (residual electron density peaks) located next to atoms of the middle ring, clearly indicating possible middle ring disorder. **Figure 4.9** (50% probability thermal ellipsoid) shows the middle ring modeled with disorder (when the Q-peaks were replaced as carbon atoms). The terminal phenyl rings in **Figures 4.8 and 4.9** were removed for clarity. The final R1 value at 188K changed significantly from 7.69% (no middle-ring disorder) to 4.68% (maximum residual electron density peak 0.25 e.Å⁻³, middle ring disorder, **Tables 4.2-4.4 and 4.7**).

Figures 4.10 and 4.11 (193K structure, 50% probability thermal ellipsoid) show the packing arrangement of PTP molecules in the monoclinic P2₁/a space group (unit cell dimension extended to 2a and 2b.) projected along the c-axis (001 plane) to the plane of the paper. **Figure 4.11** shows both disordered middle ring, while **Figures 4.10a and 4.10b** show one half of the disordered middle ring, separately. **Figures 4.12 and 4.13** (50% probability thermal ellipsoid) shows the middle ring viewed parallel to the long axis of the PTP molecule (terminal rings removed for clarity). **Figure 4.14** shows the packing of the whole disordered PTP molecule projected along the b-axis (010 plane) to the plane of the paper. The disordered red and green atoms of the middle ring show their orientations related to each other in the packing arrangement. The 2-fold screw axes

parallel to the **b**-axis (located at $\frac{1}{4}\mathbf{a}$ and $\frac{3}{4}\mathbf{a}$) and the **a**-glide mirror planes (located at $\frac{1}{4}\mathbf{b}$ and $\frac{3}{4}\mathbf{b}$) perpendicular to the **b**-axis are clearly indicated by the PTP molecule positions in **Figures 4.10-4.13**. After the phase transition, these two symmetry elements (2-fold screw axis and **a**-glide mirror plane) were lost as the PTP molecules transformed from the middle ring disordered arrangement to the fully ordered middle-ring arrangement at 100K.

Figure 4.3: PTP molecule at 298 K with 50% Thermal Ellipsoids Without Modeling Middle Ring Disorder
 This figure shows the PTP molecule at 296K (a), 200K (b), and 193K (c) with 50% thermal ellipsoids. This model assumes no disorder in the middle ring. The elongation of the middle ring thermal ellipsoids suggests that a model with disorder in the middle ring would provide a more accurate model.

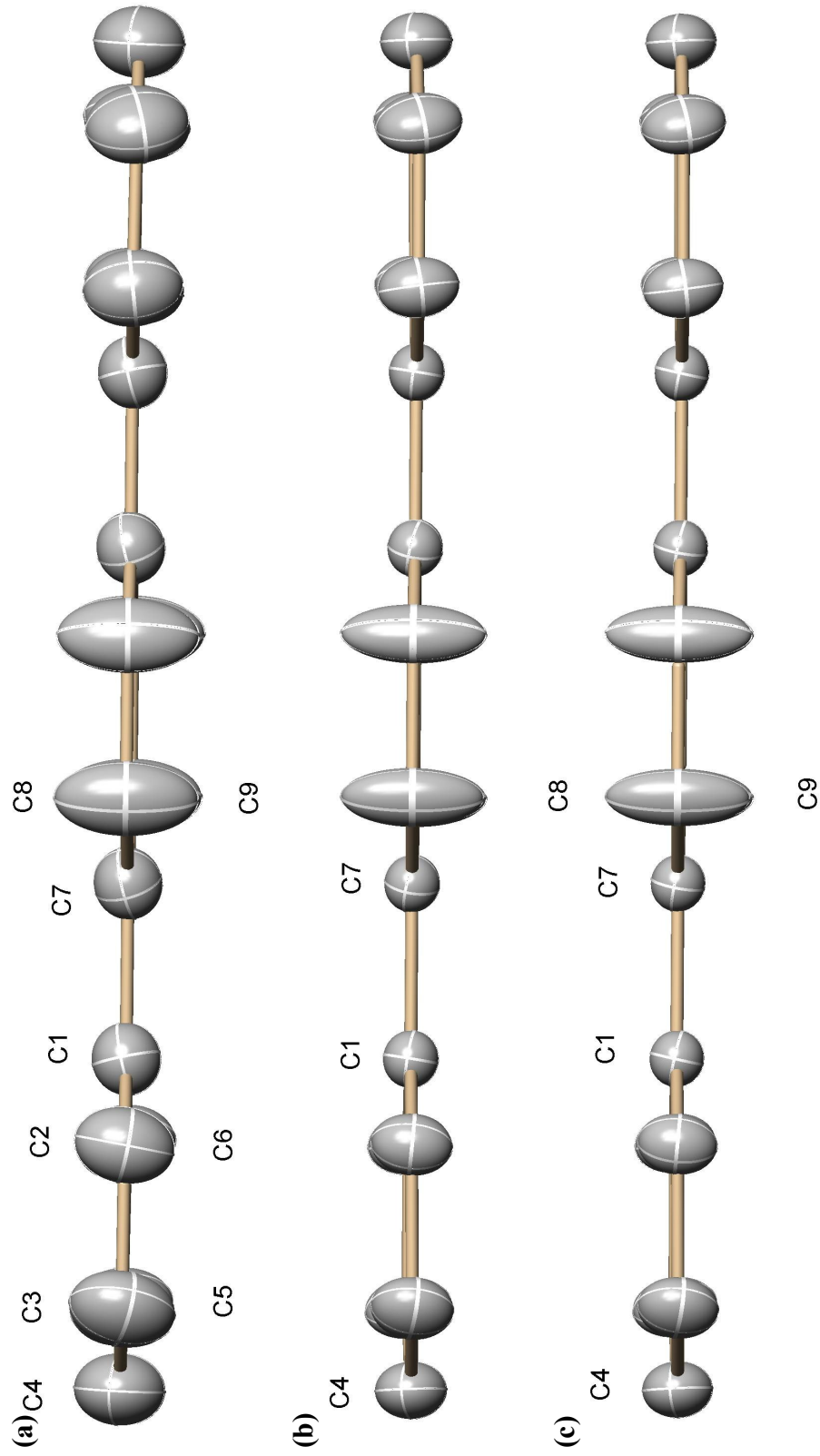


Figure 4.4: PTP Molecule at 298 K with 50%/50% Middle Ring Disorder
The two forms of the PTP molecule at 298 K with a 50%/50% disordered site occupancy ratio, which lowered the R1 value from 6.43% to 5.04%.

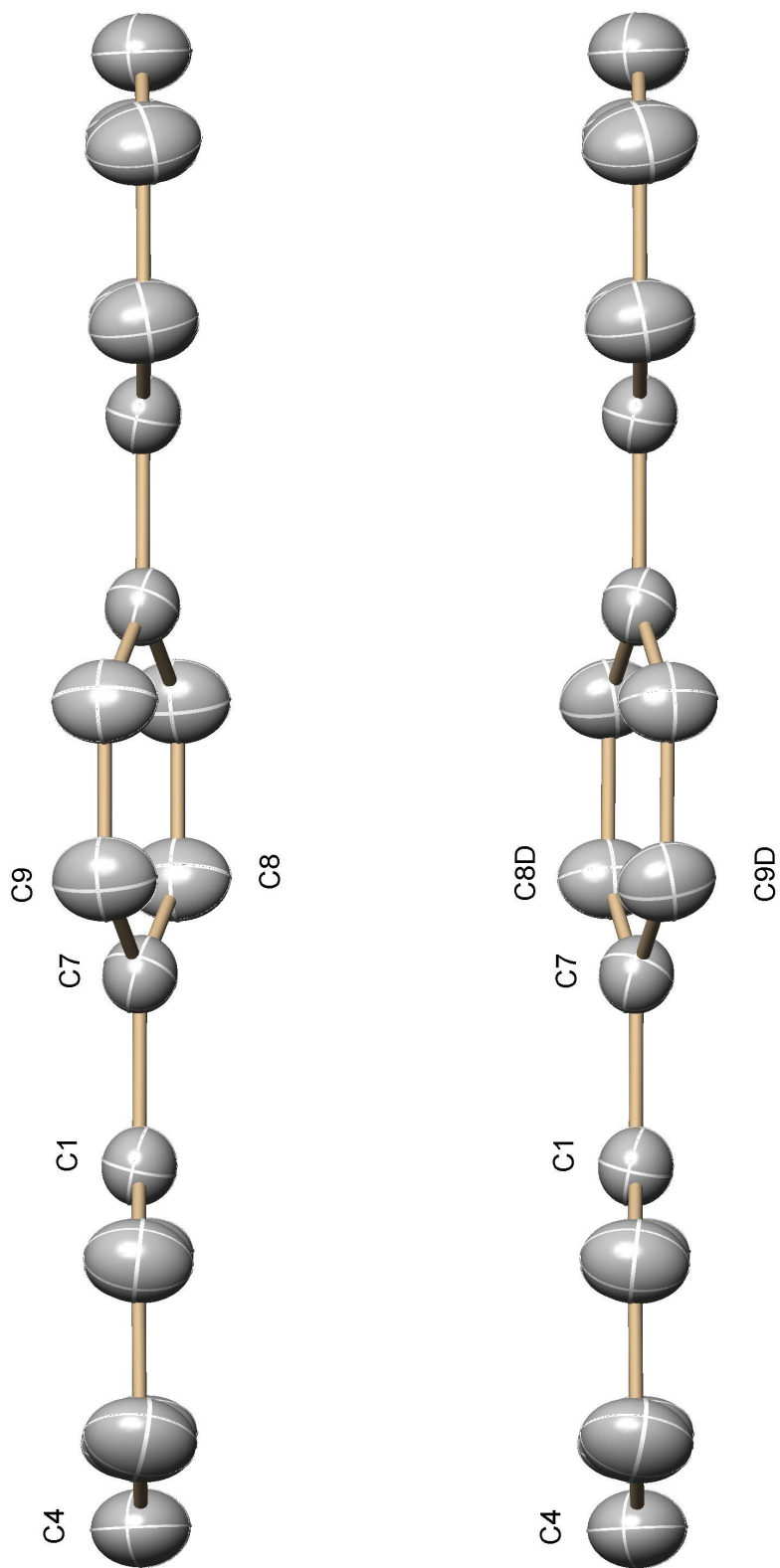


Figure 4.5: PTP Molecule at 200 K with 50%/50% Middle Ring Disorder
The two forms of the PTP molecule at 200 K with a 50%/50% disordered site occupancy ratio, which lowered the R1 value from 6.73% to 4.71%.

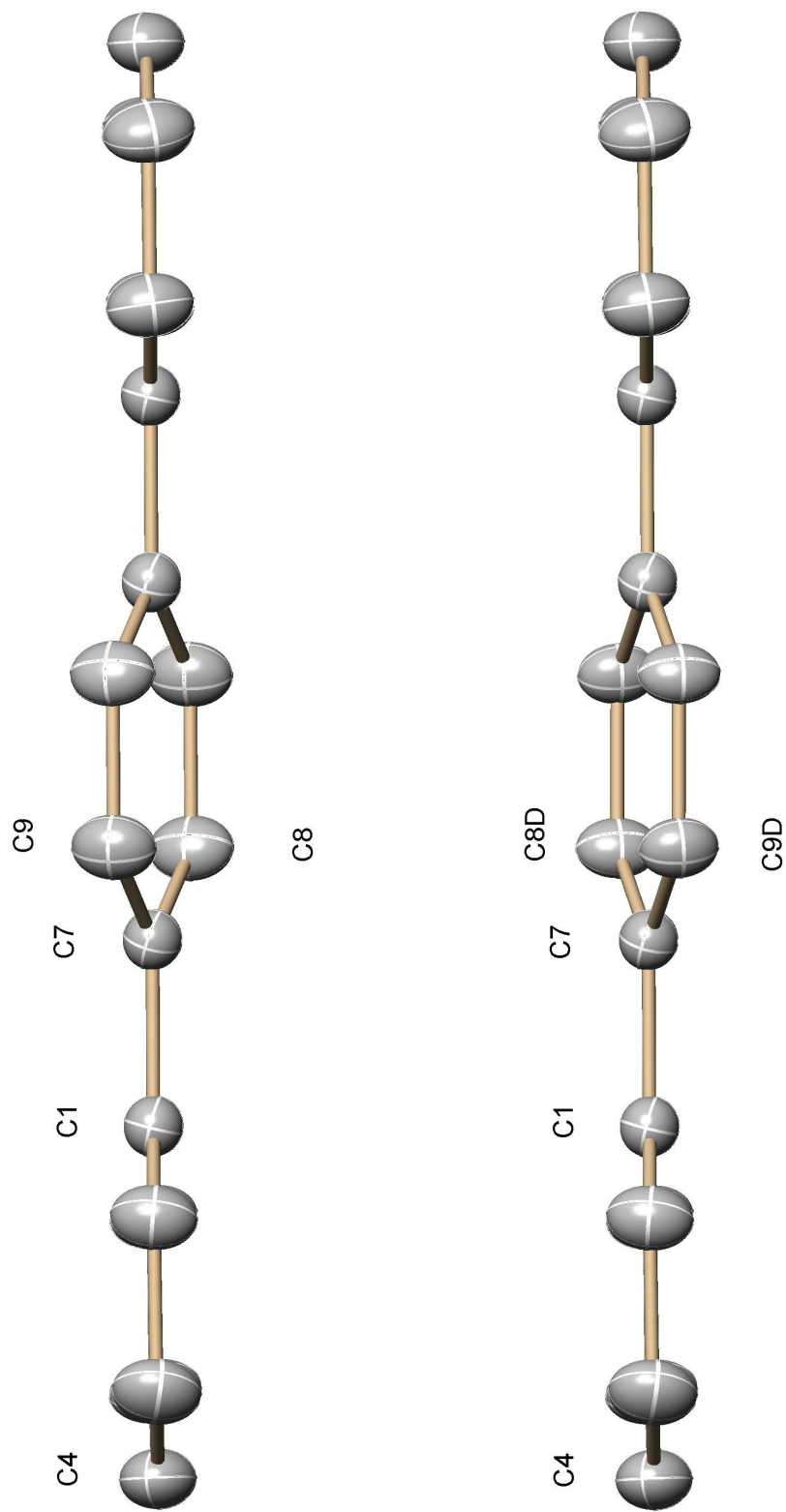


Figure 4.6: PTP Molecule at 193 K with 50%/50% Middle Ring Disorder
The two forms of the PTP molecule at 193 K with a 50%/50% disordered site occupancy ratio, which lowered the R1 value from 6.90% to 4.66%.

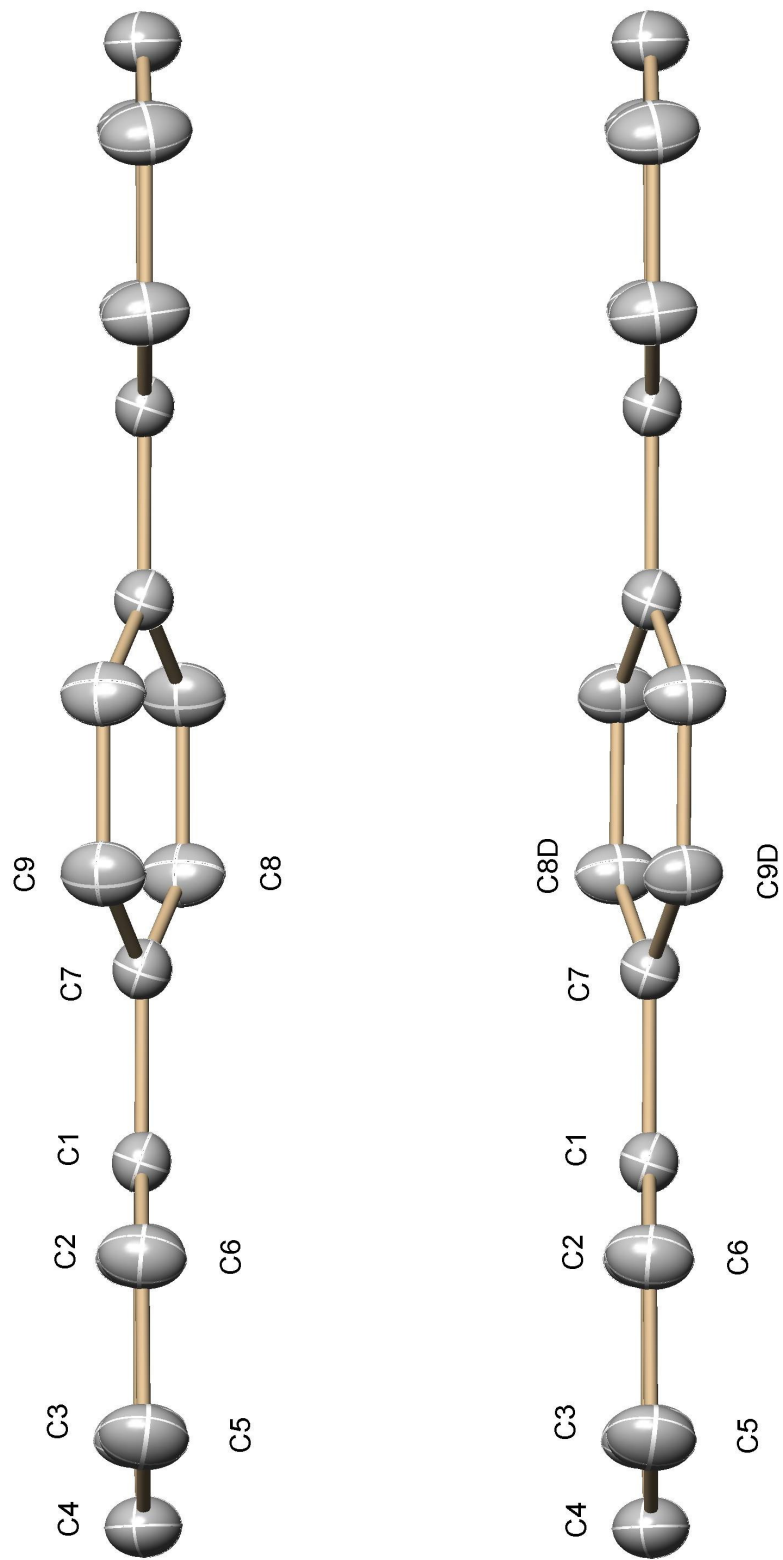


Figure 4.7: Relative Position of Carbon Atoms in the Disordered Sites at 193K.
The relative position of two disordered sites for the carbons in the middle ring (terminal rings absent for clarity) at 193K. This is viewed along the long axis of the molecule.

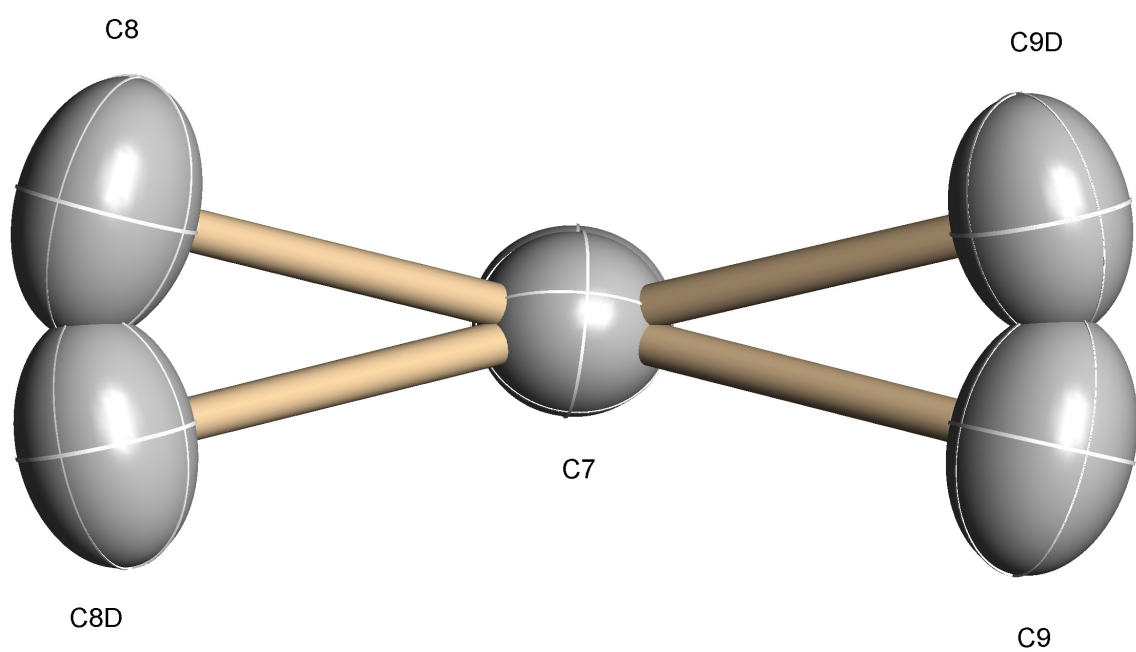


Figure 4.8: Four Unique PTP Molecules in the Low Temperature Pseudo Merohedral Triclinic “ $C\bar{1}$ ” Space Group (188 K) without Middle Ring Disorder
The Q-peaks (residual electron density peaks) located next to the atoms in the middle ring indicate possible middle ring disorder. (Terminal rings absent for clarity.)

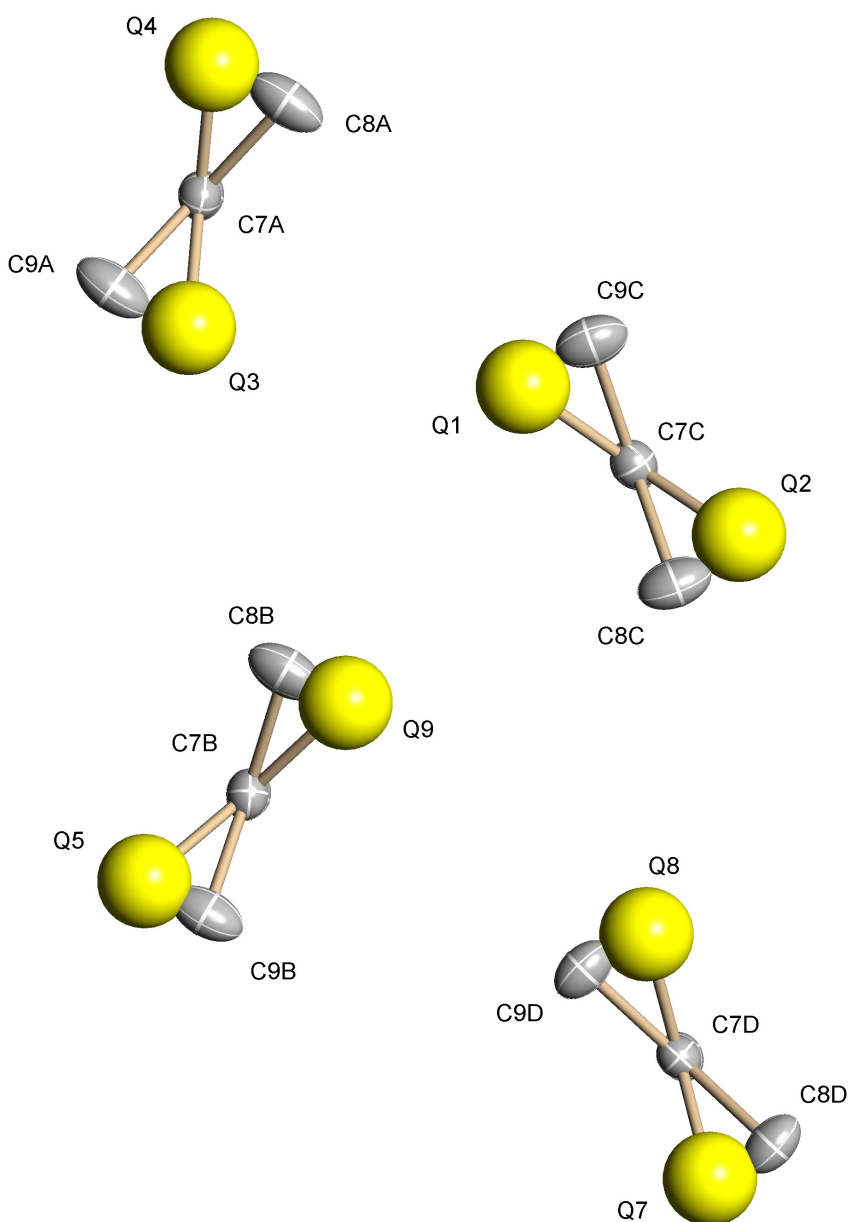


Figure 4.9: Four Unique PTP Molecules in the Low Temperature Pseudo Merohedral Triclinic “ $C\bar{1}$ ” Space Group (188 K) with Middle Ring Disorder
The Q-peaks (residual electron density peaks) are replaced with carbon atoms modeling middle ring disorder. (Terminal rings absent for clarity.)

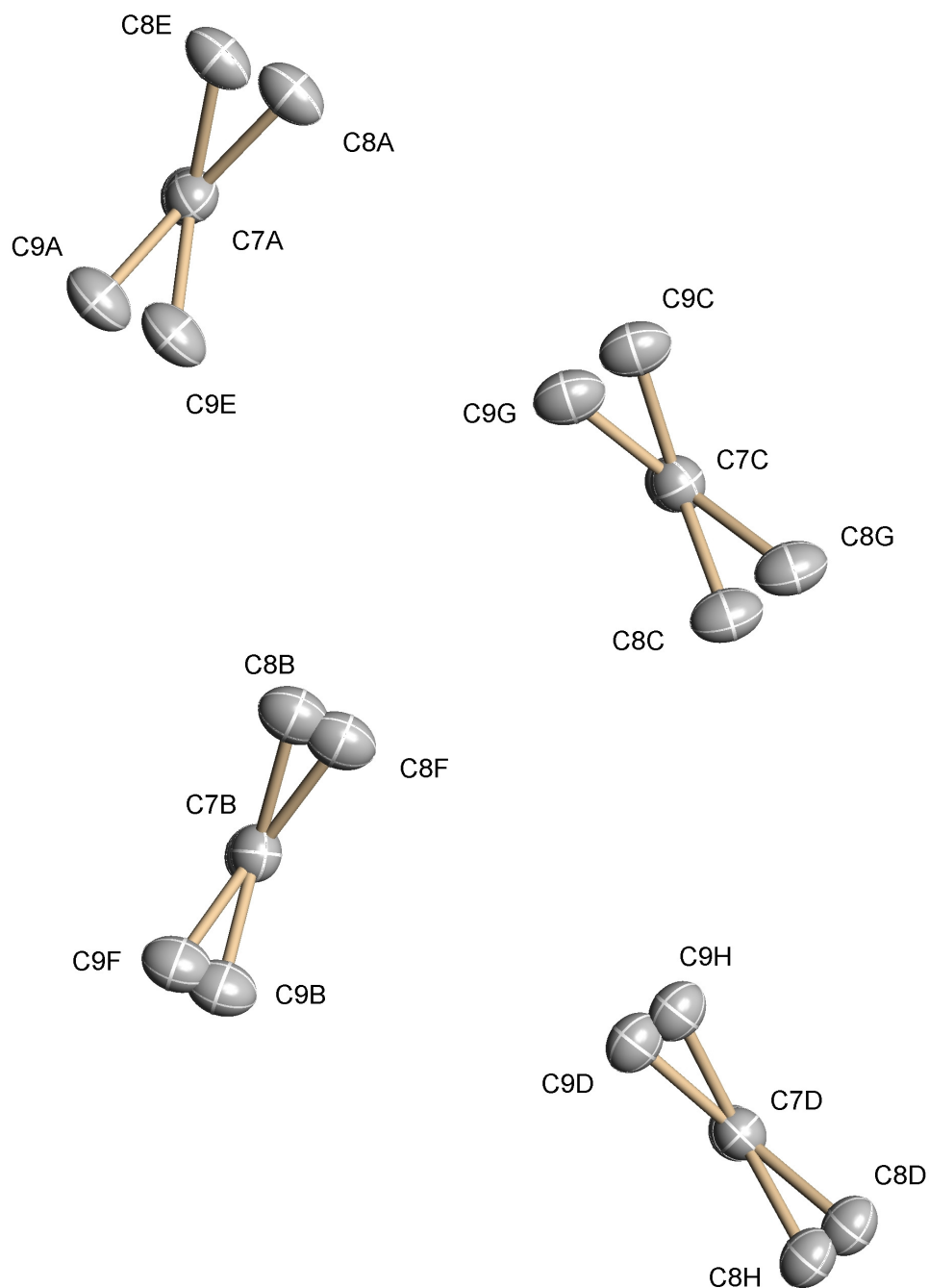


Figure 4.15 (100K structure, 50% probability thermal ellipsoid) shows the packing arrangement of PTP-molecules in the pseudo-merohedral triclinic C-centered, “ $C\bar{1}$ ” space group, projected along the **c**-axis (001 plane) and **b**-axis (010 plane), respectively, to the plane of the paper. The four different conformers in the unit cell are shown in green, red, blue and orange color. Initially space group determination of the intensity data collected at 100K indicated a monoclinic C-centering lattice exception; i.e. $h+k=2n$ (similar Baudour¹⁸). However, none of the monoclinic C-centered space groups ($C2$, Cm , $C2/m$, Cc and $C2/c$) could provide a structure solution to the experimental data. Further examination of the unit cell axes indicated that the **a*** and **b***-axes were doubled that of the monoclinic-P **a** and **b** axes (**a***=2**a** and **b***=2**b**) and the **c***-axis was identical to **c**-axis (when thermal contraction was taken into account). The exceptionally high mean intensity statistics, $|E^2-1| = 1.476$, indicated a possible pseudo-merohedral twinning problem (expected normal centro-symmetry mean intensities, $|E^2-1| = 0.968$).

Using the standard triclinic space group $P\bar{1}$ and lattice centering exceptions (LATT 7 instruction), the dual space method of phase determination was used to obtain initially the four different conformers of the half-PTP-molecules. Although one could clearly see the four different conformers, the R1 value anisotropic atomic coordinates refinement convergence was high, ca. 11%-13%. This clearly indicates that the calculated theoretical intensities from the structure-model used do not match the observed measured intensities. The pseudo-merohedral triclinic C-centered twin law was then determined, TWIN (1 0 0 | 0 -1 0 | 0 0 1), and applied to the final refinement where a scaling factor

(BASF) of the minor/major twin components ratio was used and refined. In pseudo-merohedral triclinic twinning, the reciprocal reflections of the minor and major twin components have identical overlapping indices. The BASF scale factor was refined to determine the percentage of each twin component relative to the other. The minor/major components pseudo-merohedral triclinic C-centered twinning ratio was affected when the temperature was lowered from 188K (33%/67% ratio) to 175K (43%/57% ratio) to 100K (50%/50% ratio.) **Table 4.6** shows the final twin component ratios. These results were also reflected in **Figures 4.1 k, q, r** with more grey-reflections, and **Table 4.7**. The pseudo-merohedral twinning occurred at a mirror-plane perpendicular to the **2b**-axis of the triclinic C-centered cell. **Figure 4.15a** shows the C-centering of the blue-PTP-molecule. Once the pseudo-merohedral twin law, twin components scaling factors, and the C-centering lattice parameters were correctly introduced, the final atomic coordinate least-squares refinement converged to $R1 = 3.93\%$. **Figure 4.16** shows the 50% probability thermal ellipsoid drawing of the asymmetry unit of the four different conformers projected parallel to the **c**-axis. Unlike previous studies¹⁸, the atomic coordinates of each conformer were refined without applying any rigid model restraints or constraints once the twin law was determined. The thermal and libration problems found discussed in Baudour¹⁸ completely disappeared when the twin law was applied. The torsion angles between the terminal and middle rings for the four ordered conformers (at 175K and 100K) are given in **Tables 4.4 and 4.5**.

Figure 4.10: Packing of the PTP Molecules in the $P2_1/a$ Unit Cell at 193K (ab plane)
The unit cell dimensions have been extended to $2a$ and $2b$. The two disordered occupation sites are shown separately in (a) and (b) projected along the c -axis (001 plane) to the plane of the paper. Terminal rings absent for clarity.

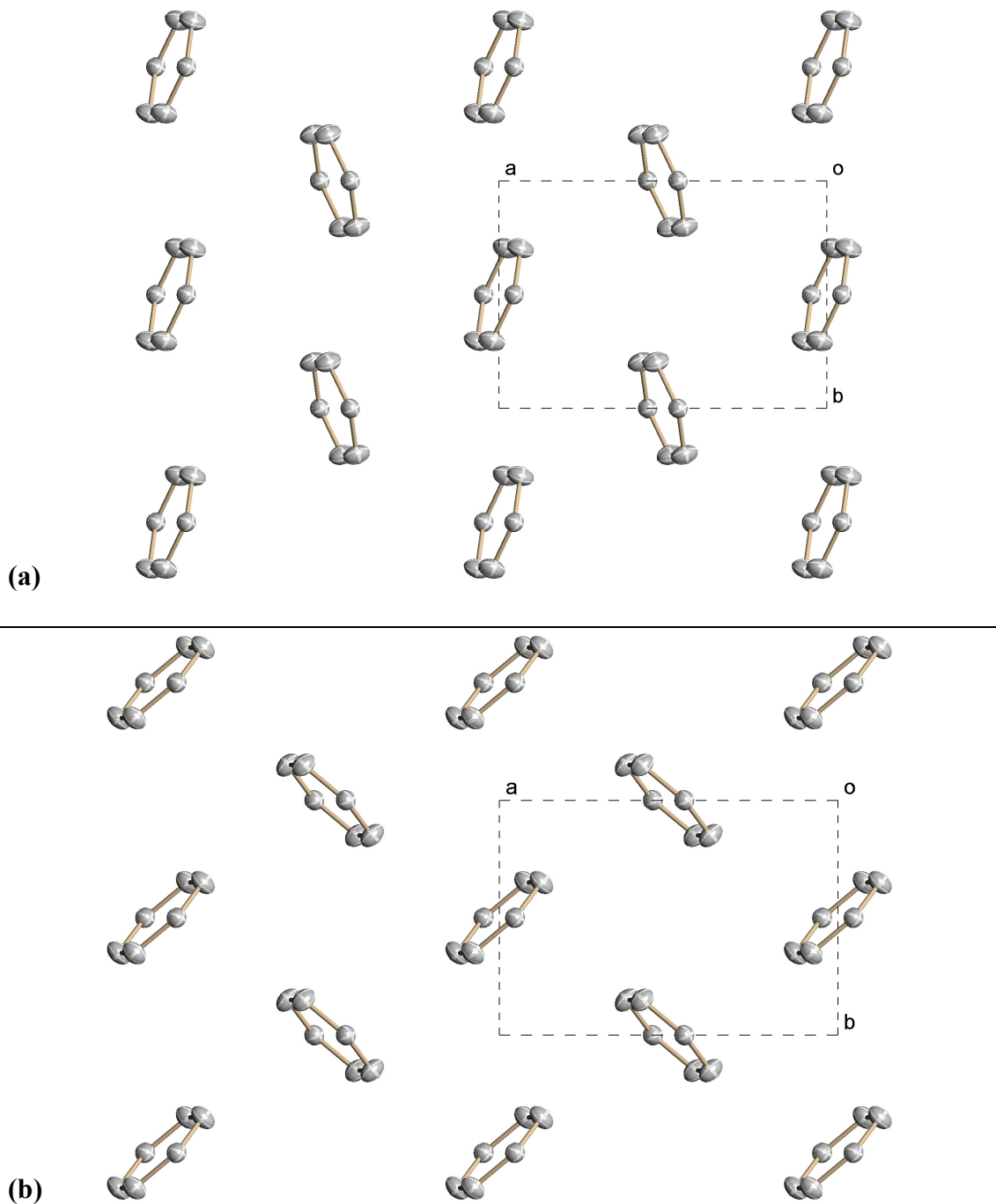


Figure 4.11: Packing of the PTP Molecules in the $P2_1/a$ Unit Cell at 193K (Projected Along c-Axis (001 plane))

The unit cell dimensions have been extended to **2a** and **2b**. The two disordered occupation sites are shown together projected along the **c**-axis (001 plane) to the plane of the paper. Terminal rings absent for clarity.

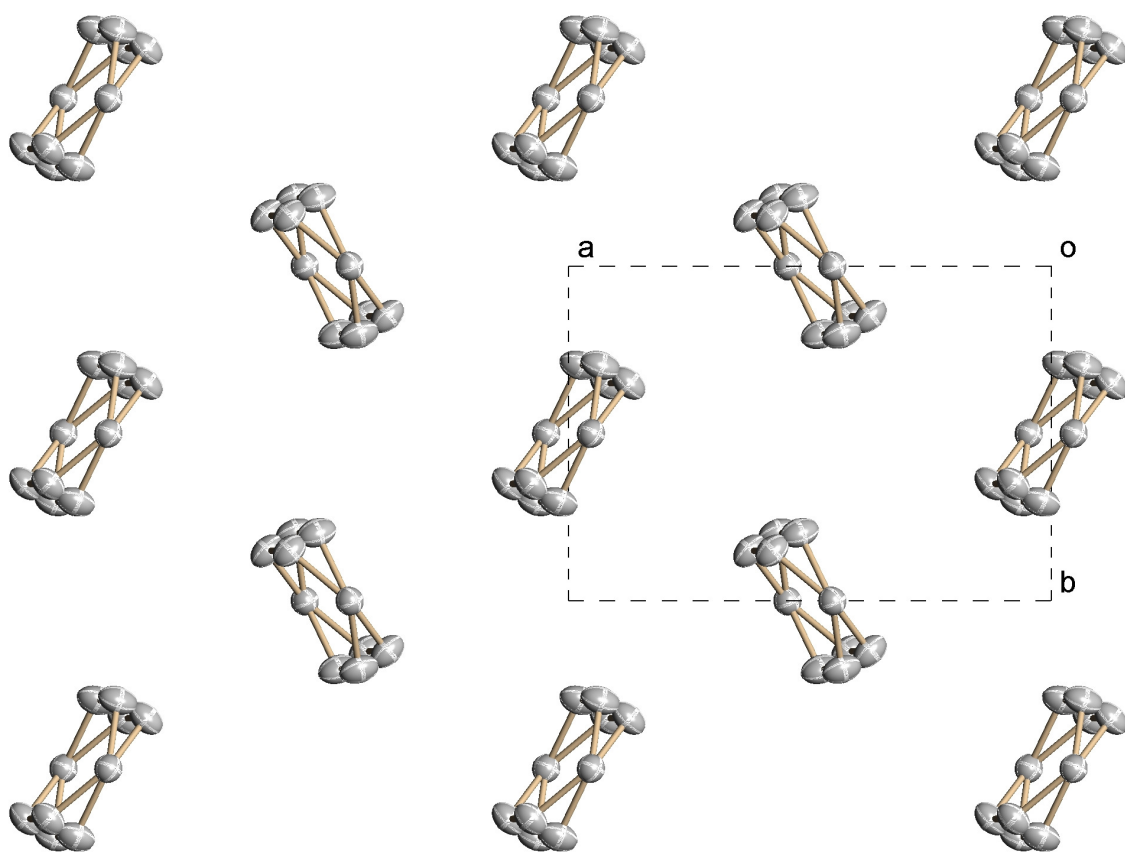


Figure 4.12: Packing of the PTP Molecules in the $P2_1/a$ Unit Cell at 193K (Projected Along Long Molecular Axis)

The unit cell dimensions have been extended to **2a** and **2b**. The two disordered occupation sites are shown separately in **(a)** and **(b)** projected down the long molecular axis. Terminal rings absent for clarity.

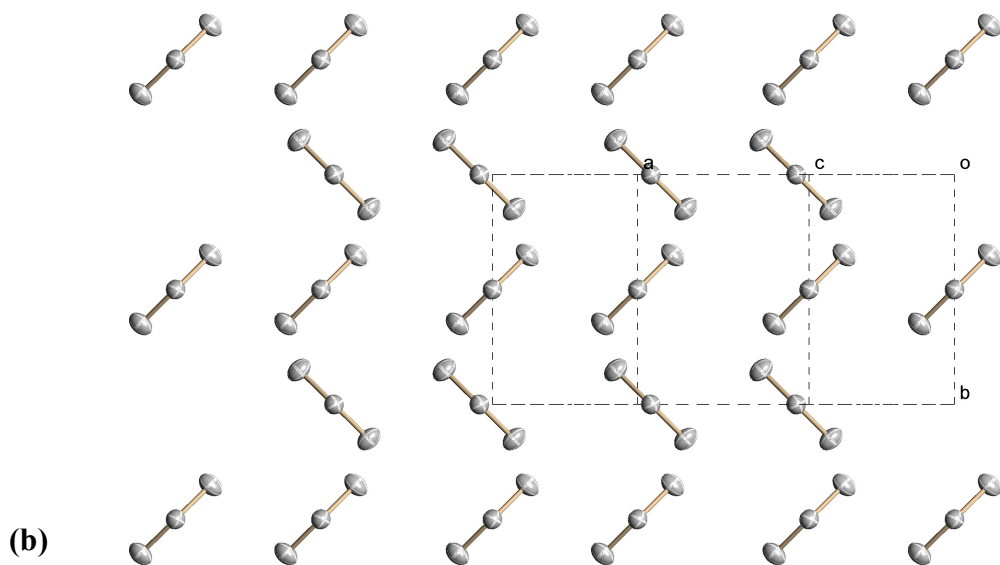
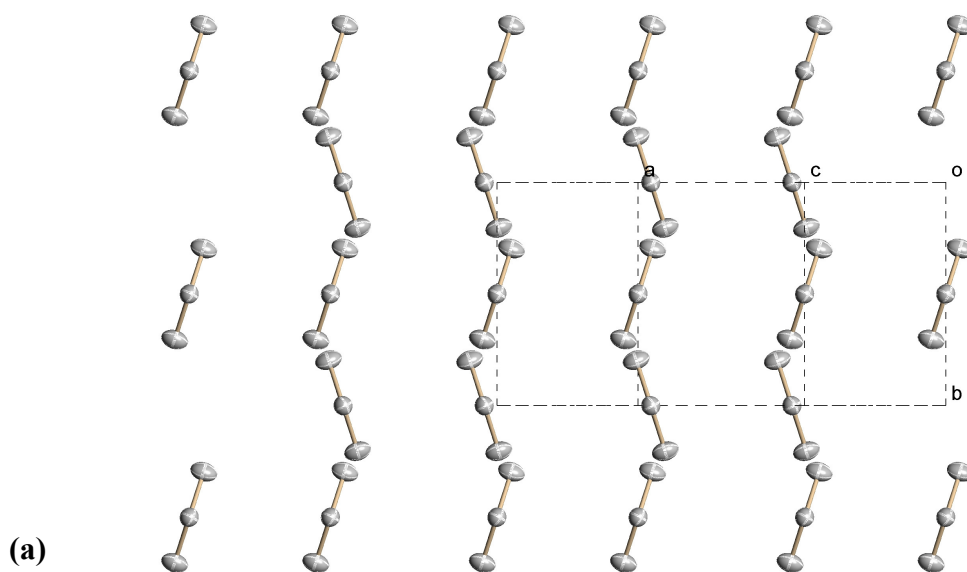


Figure 4.13: Packing of the PTP Molecules in the $P2_1/a$ Unit Cell at 193K (Projected Along Long Molecular Axis)

The unit cell dimensions have been extended to **2a** and **2b**. The two disordered occupation sites are shown together projected down the long molecular axis. Terminal rings absent for clarity.

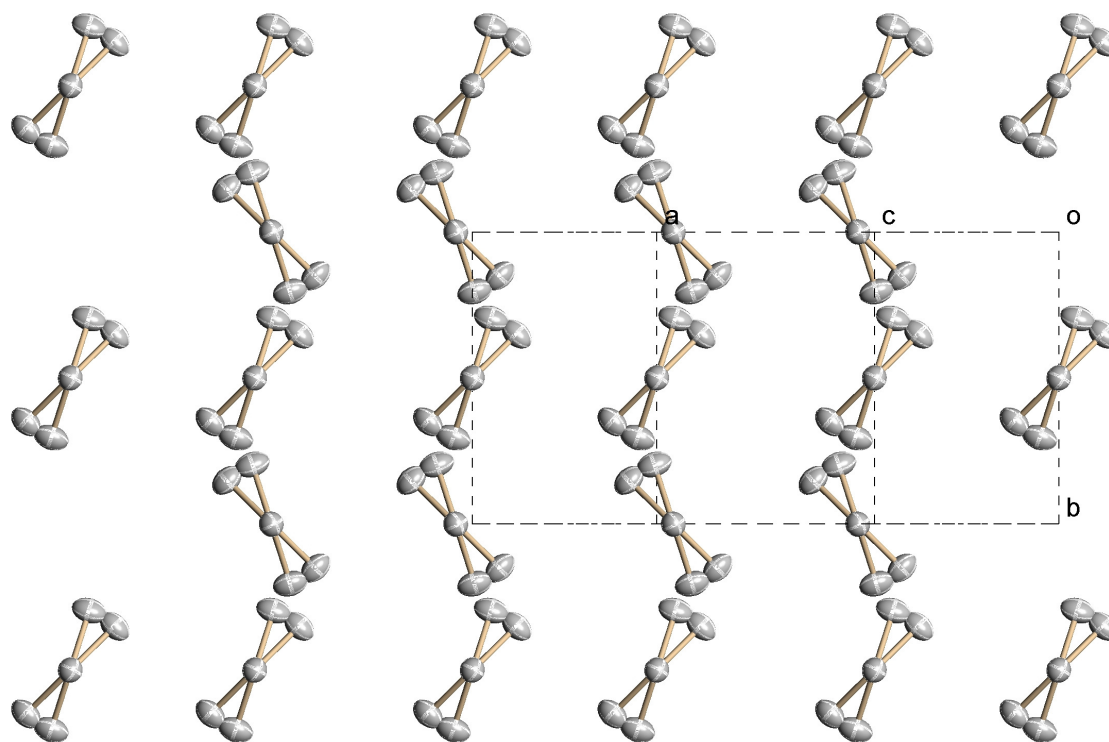


Figure 4.14: Packing of the PTP Molecules in the $P2_1/a$ Unit Cell at 193K (Projected Along b-Axis (010 plane))

The unit cell dimensions have been extended to $2a$ and $2c$ and projected along the **b**-axis (010 plane) to the plane of the paper. The middle ring disorder is shown with red and green atoms representing the two positions of the middle ring.

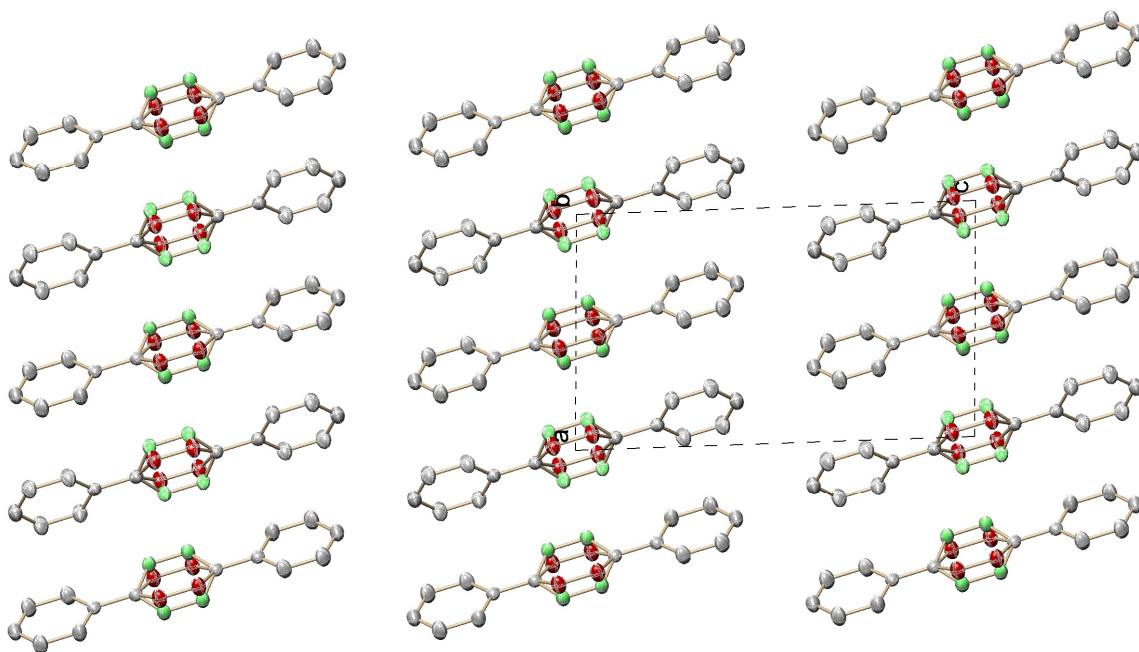


Figure 4.15: Packing of the PTP Molecules in the Low Temperature Pseudo Merohedral Triclinic “ $C\bar{1}$ ” Space Group at 100K

Projected along the (a) c-axis (001 plane) and (b) b-axis (010 plane). The four different unique conformers of the PTP molecule are labeled separately (i.e. green, red, blue, and orange.) Notice the blue molecule, which is the C-centered molecule.

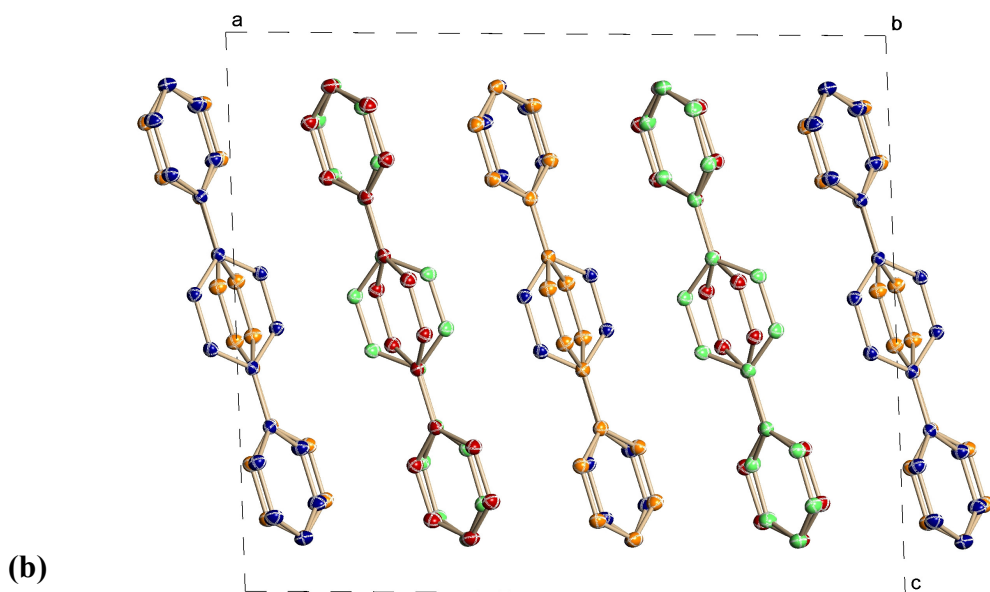
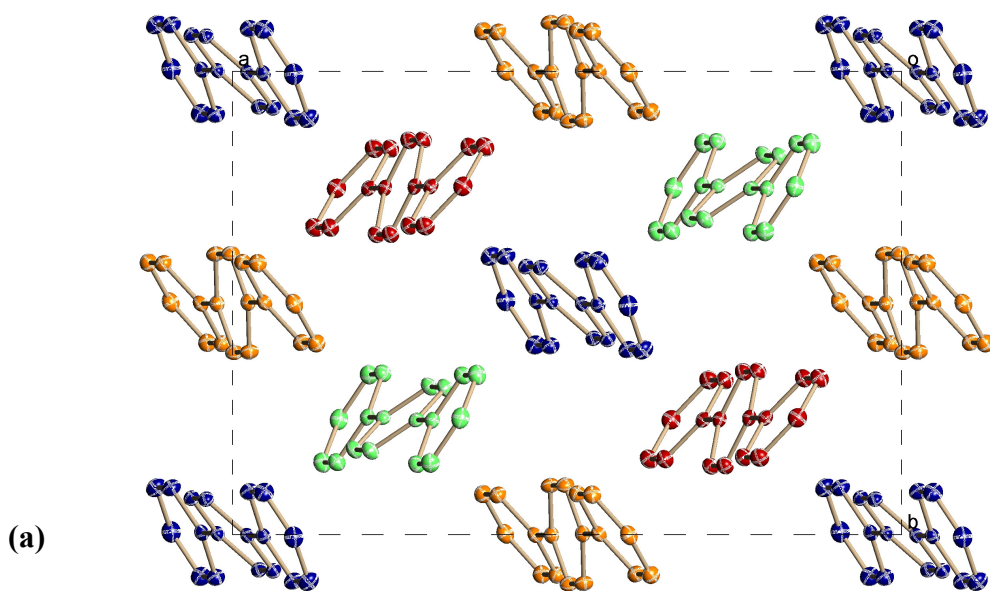
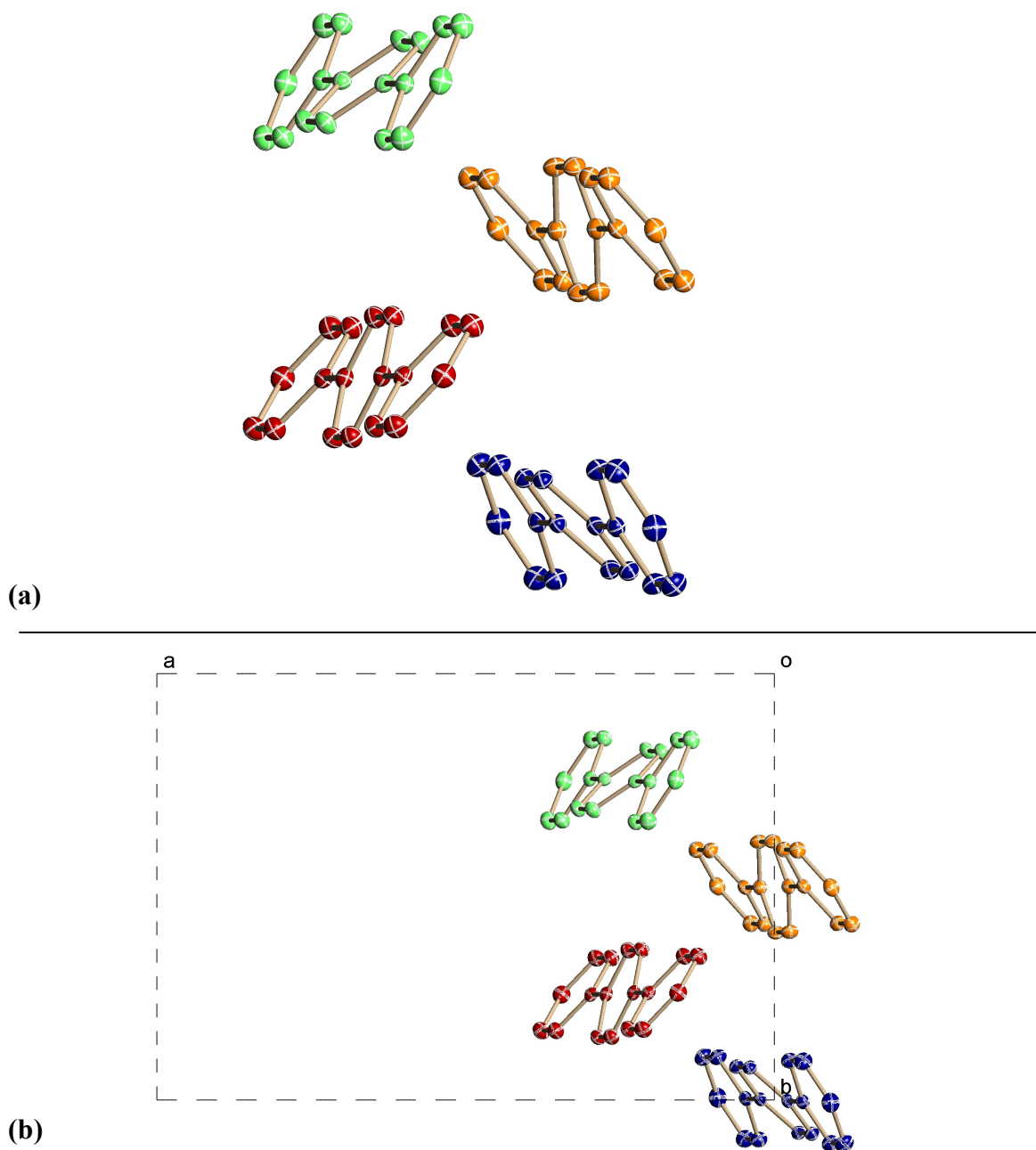


Figure 4.16: Packing of the Asymmetrical Unit of PTP Molecules in the Low Temperature Pseudo Merohedral Triclinic “ $C\bar{1}$ ” Space Group at 100K
With **(a)** and without **(b)** the unit cell outline projected along the **c**-axis (001 plane). The four distinct molecules which are present in the low temperature phase.



4.8: Conclusion

At temperatures before phase transition (296K, 200K, and 193K,) the PTP-molecule packing arrangement in the solid state was clearly identified as being a disordered phase. The final R1 values given in **Table 4.6** indicated a significant difference when a disordered atomic coordinate refinement model (R1 values of 5.04%, 4.72%, 4.66%) was used compared to the no-disordered model (R1 values of 6.43%, 6.73%, 6.90%). The torsion angles given in **Tables 4.4 and 4.5** of the disordered model seem to show two distinct conformers present in the asymmetric unit of the unit cell. However, it is possible that the disorder present in the structure at room temperature is due to the thermal motion of the middle ring as it alternates between the two sides of the double well potential.

The first crystallographic evidence of the temperature induced phase transition for PTP was demonstrated to be between 193K and 192K. Using x-ray crystallography, temperature was lowered one degree at a time from 196K to 183K and the grey-reflections/red-reflections ratios (**Table 4.7**) were observed to change from 0.07 and 0.23 at 193K and 192K, respectively. This was shown more clearly in **Figure 4.2**.

It was shown that the conversion of the disordered PTP-molecule to ordered PTP-molecule after phase transition was temperature dependent. At 188 K (**Table 4.6**), the disordered site occupancy ratio was 87%/13% for all four conformers. The pseudo-merohedral triclinic C-centered minor/major components twin ratios were also temperature dependent (**Table 4.6**). The twin ratios were 33%/67%, 43%/57%, and

50%/50% at 188K, 175K and 100K, respectively. At 188K, switching from no-disordered middle-ring model to disordered middle-ring model does not affect the minor/major components twin ratio.

At 100K, there were four ordered conformers of the PTP-molecule present in the unit cell (**Figure 4.15a**). Once the pseudo-merohedral twin law was established, the atomic coordinates final least-squares refinement converged to $R1 = 3.93\%$ (**Table 4.1**). The torsion angles of the four conformers are 17.0° , 18.5° , 22.8° and 26.2° , with s.u. of 0.2° (**Table 4.5**). Previous analysis¹⁸ obtained a large value of 1° s.u., which is likely due to the lack of the correct twinning model. It was shown that the PTP went from the disordered phase (two different conformers in solid crystalline state) at 296K-193K to an ordered phase (four different conformers in solid crystalline state) at 188K-100K where the phase transition between these phases occurred between 193K-192K.

Finally, while we determined a new crystal structure for the low temperature PTP crystal structure, the fact that we still measure four unique crystallographic site is still in agreement with the previous experimental results of the optical absorption of the pentacene doped p-terphenyl. In the next chapter computational results for the mixed crystal system will be presented.

References

- (1) Atkins, P. W.; De Paula, J. *Atkins' Physical chemistry*; 7th ed.; Oxford University Press: Oxford; New York, 2002.
- (2) Hammond, C. *The Basics of Crystallography and Diffraction*; 3rd ed.; Oxford University Press: Oxford; New York, 2009.
- (3) Blake, A. J.; Clegg, W.; Cole, J. M.; Evans, J. S. O.; Main, P.; Parsons, S.; Watkin, D. J. *Crystal Structure Analysis : Principles and Practice*; 2nd ed.; Oxford University Press: Oxford; New York, 2009.
- (4) Glusker, J. P.; Lewis, M.; Rossi, M. *Crystal structure analysis for chemists and biologists*; VCH Publishers, Inc.: New York, 1994.
- (5) Müller, P.; Herbst-Irmer, R.; Spek, A. L.; Schneider, T. R.; Sawaya, M. R. *Crystal Structure Refinement : A Crystallographer's Guide to SHELXL*; Oxford University Press: Oxford; New York, 2006.
- (6) Marchetti, A. P.; McColgin, W. C.; Eberly, J. H. *Phys Rev Lett* **1975**, *35*, 387.
- (7) Orłowski, T. E.; Zewail, A. H. *The Journal of Chemical Physics* **1979**, *70*, 1390.
- (8) Olson, R. W.; Fayer, M. D. *The Journal of Physical Chemistry* **1980**, *84*, 2001.
- (9) Baer, B. J.; Chronister, E. L. *The Journal of Chemical Physics* **1993**, *99*, 3137.
- (10) Baer, B. J.; Chronister, E. L. *The Journal of Chemical Physics* **1994**, *100*, 23.
- (11) Baer, B. J.; Chronister, E. L. *Chem Phys* **1994**, *185*, 385.
- (12) Baer, B. J.; Chronister, E. L. *High Pres. Res.* **1994**, *12*, 101
- (13) Baer, B. J.; Chronister, E. L. *The Journal of Physical Chemistry* **1995**, *99*, 7324.
- (14) Rietveld, H. M.; Maslen, E. N.; Clews, C. J. B. *Acta Crystallographica Section B* **1970**, *B 26*, 693.
- (15) Baudour, J. L.; Cailleau, H.; Yelon, W. B. *Acta Crystallographica Section B* **1977**, *33*, 1773.

- (16) Baudour, J. *Acta Crystallographica Section B* **1991**, *47*, 935.
- (17) Baudour, J. L.; Toupet, L.; Delugeard, Y.; Ghemid, S. *Acta Crystallographica Section C* **1986**, *42*, 1211.
- (18) Baudour, J. L.; Delugeard, Y.; Cailleau, H. *Acta Crystallographica Section B* **1976**, *32*, 150.
- (19) Pickett, L. W. *Proceedings of the Royal Society of London. Series A, Containing Papers of a Mathematical and Physical Character* **1933**, *142*, 333.
- (20) Schatschneider, B.; Chronister, E. L. *Mol Simulat* **2008**, *34*, 1159.
- (21) Bruker; 2010.9-1 ed.; Bruker AXS Inc.: Madison, Wisconsin, USA, 2010.
- (22) Bruker; V7.68A ed.; Bruker AXS Inc.: Madison, Wisconsin, USA, 2008.
- (23) Bruker; 2008/1 ed.; Bruker AXS Inc.: Madison, Wisconsin, USA, 2008.
- (24) Bruker; 2008/4 ed.; Bruker AXS Inc.: Madison, Wisconsin, USA, 2008.
- (25) Cailleau, H.; Dworkin, A. *Mol Cryst Liq Cryst* **1979**, *50*, 217

Chapter V

Molecular Dynamics of Mixed Molecular Crystals under High Pressure and Low Temperature

5.1: Introduction

5.1.1: Experimental Studies of Ideal Mixed Molecular Crystals

Pressure and temperature are useful tools for studying the vibrational and electronic properties of condensed matter. The pentacene in p-terphenyl mixed crystal has been often studied¹⁻⁷ because it is considered an ideal mixed crystal due to the size similarities between the pentacene and p-terphenyl molecules, as can be seen in **Figure 5.1**. When pentacene is mixed into p-terphenyl it will be found to substitute into each of the four unique crystallographic sites of p-terphenyl when in its low temperature triclinic state,⁸ which gives rise to four unique electronic origin bands in the absorption spectrum.⁹ However, in the monoclinic structure there is only one unique site, which is seen as only one absorption band for pentacene in monoclinic p-terphenyl.^{1,3} The low temperature, high pressure phase of p-terphenyl was diagramed using Raman spectroscopic data, along with the evidence of the change in the absorption bands of the doped pentacene.^{1,3} The phase diagram constructed by Baer and Chronister is reprinted with permission in **Figure 5.2**.¹

Studies of the photon echo measurements of the pentacene in p-terphenyl mixed crystal system at carrying temperatures and pressures determined the optical dephasing

time for pentacene. and it was shown that the phase transition induces a mode softening (decreased frequency of vibration with increased pressure) on the pseudolocal phonons coupled to the dephasing of the electronic excitation of the pentacene molecule (**Figure 5.3**).⁴ In order to elucidate the nature of the vibrational modes of the pentacene molecule in the p-terphenyl crystal lattice, a computational study was performed and will be presented in this chapter.

5.1.2: Refined Classical Forcefield for p-Terphenyl Molecular Dynamics

Simulations

Previous studies have been done on p-terphenyl using classical forcefield molecular dynamics in order to develop an accurate forcefield that simulates the phase transitions of p-terphenyl. A study by Bordat and Brown developed a forcefield that modeled the phases of p-terphenyl at room pressure from low temperature to room temperature.⁵ This study, however, did not simulate the low temperature, pressure induced phase transition. Schatschneider and Chronister, using a forcefield which consisted of a mixture of the COMPASS and PCFF forcefields, refined the forcefield to accurately describe both the temperature induced and pressure induced phase transitions of p-terphenyl.⁷ By measuring the distribution of the torsion angle between the inner and outer rings, it was shown that the modeled transition temperature at room pressure was near the experimental value of 193 K. When looking at a pressure series at 20 K the transition pressure was modeled to be at 0.4 GPa, only 0.1 GPa less than the expected

value of 0.5 GPa.⁷ Using this optimized forcefield, mixed crystals of p-terphenyl can be studied using classical forcefield MD.

5.1.3: Fourier Transform Analysis of Molecular Dynamics Trajectories Used for Investigating Molecular Motions

In order to study the vibrational modes of pentacene in p-terphenyl, it was determined that a Fourier transform of the data from the trajectory files, such as the center of mass of the pentacene molecule, would provide a way to investigate the vibrational motions of the pentacene molecule. A similar method has been employed by Osguthorpe in studies of protein dynamics.¹⁰⁻¹² In Sessions *et al.*, a Fast Fourier Transform was used on the time domain data of the position of all atoms in the trajectory and summed together to create a spectrum.¹² This could then be filtered and reversed FT back to the time domain to investigate the low frequency motions of Phospholipase A₂. A simpler method, focusing on particular measured values such as the center of mass and vectors representing the rotations of the molecule, will be employed for the investigation of the vibrational modes of the pentacene molecule in p-terphenyl in this chapter.

Figure 5.1: Comparison of the Pentacene Molecule and p-Terphenyl Molecule
Demonstrates the size comparison between the molecules of (a) p-terphenyl and (b) pentacene.

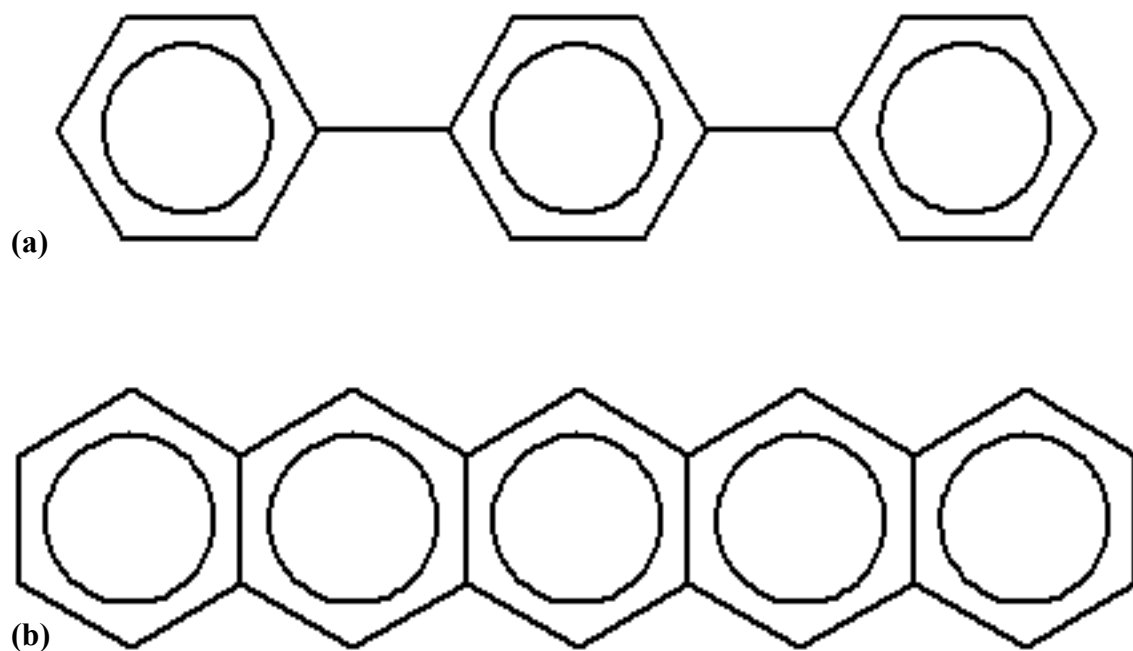


Figure 5.2: Phase Diagram of p-Terphenyl Determined from Mixed Crystal Studies

The phase diagram of p-terphenyl determined from Raman spectroscopic data and optical studies of the mixed crystal of pentacene in p-terphenyl. Reprinted with Permission from Ref 1.

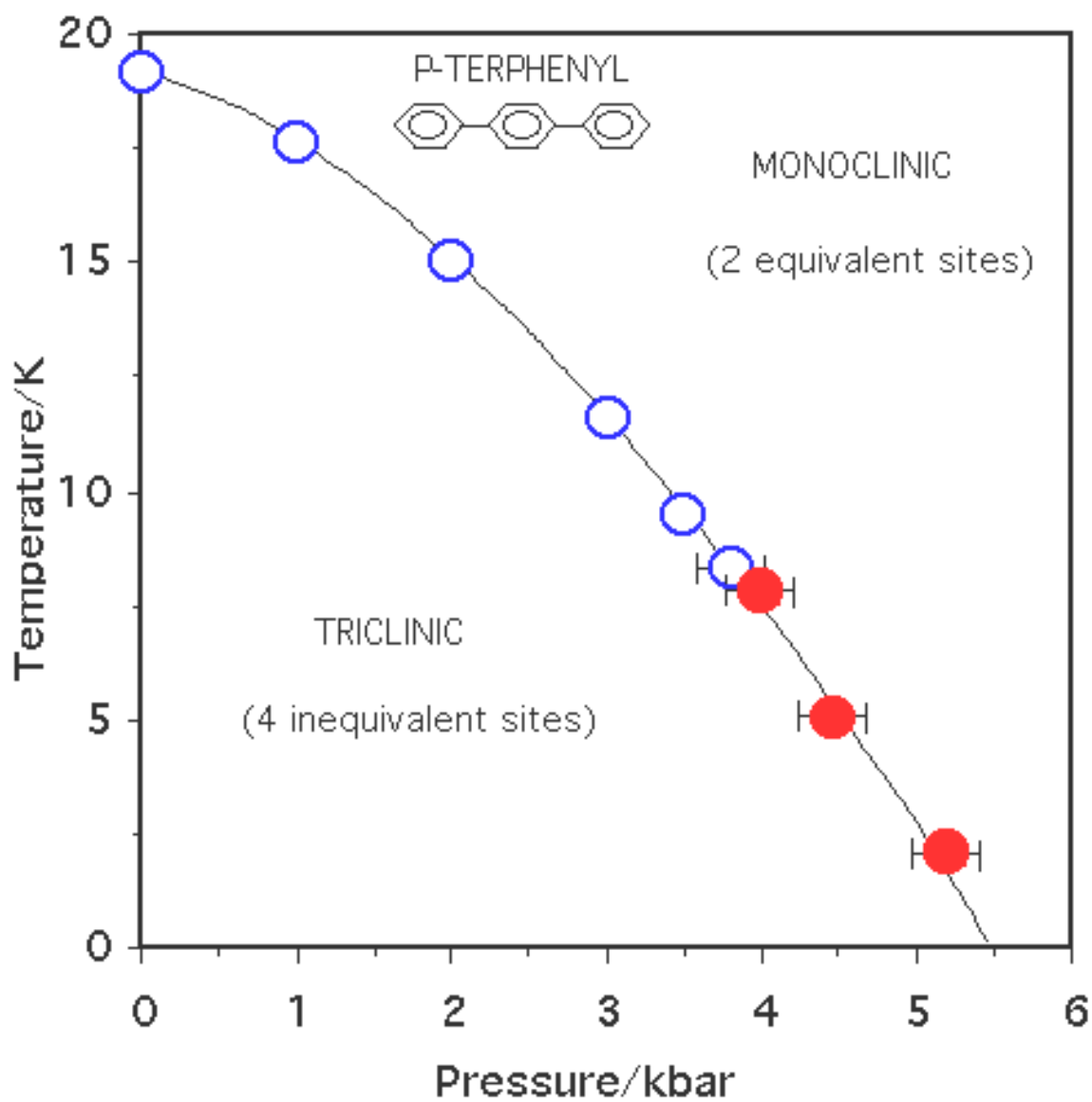
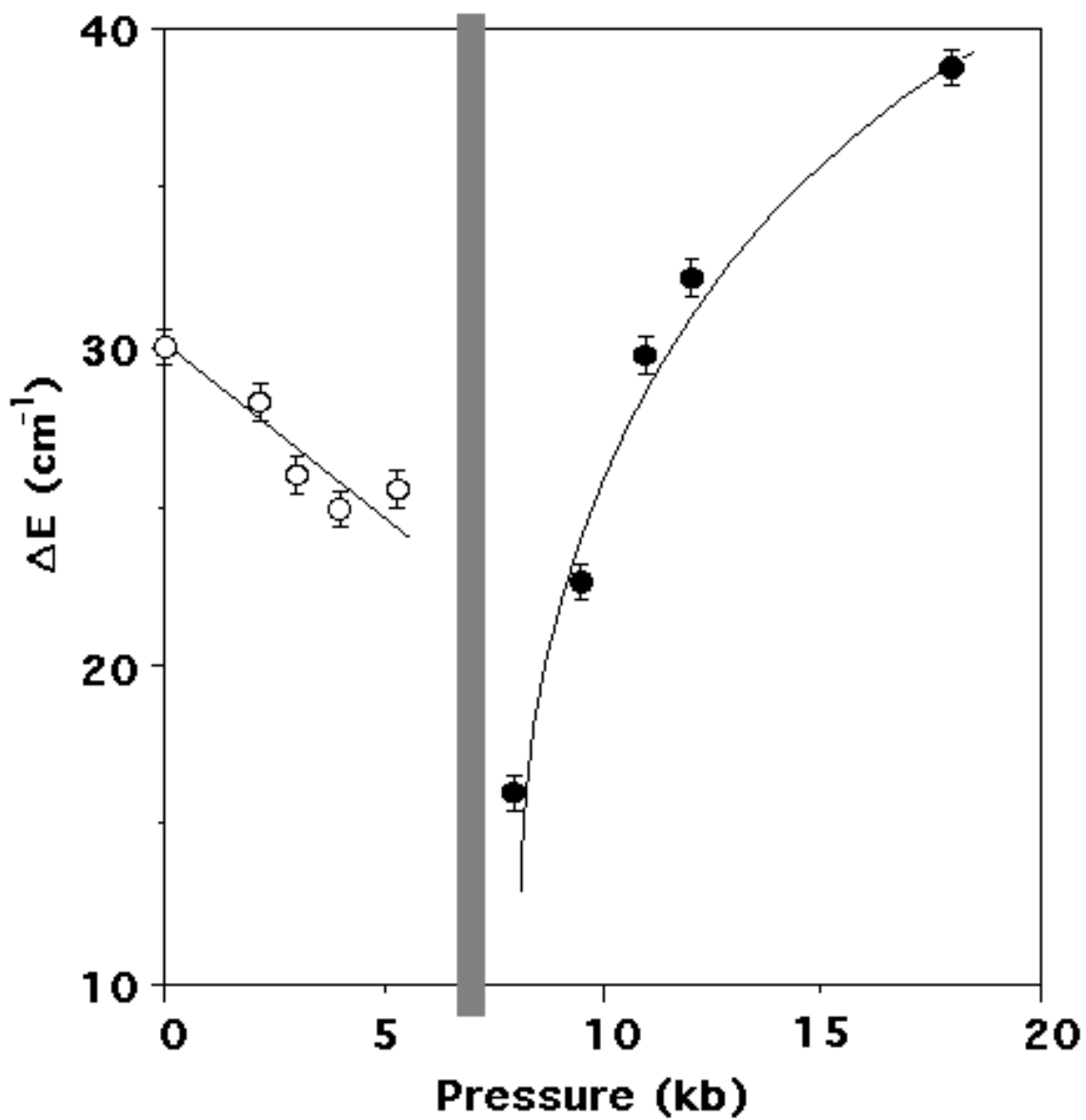


Figure 5.3: The Effect of the Phase Transition on the Optical Dephasing of Pentacene in p-Terphenyl

The presence of the phase transition, drawn as a grey line, appears to have a mode softening effect on the pseudolocal phonon of pentacene in p-terphenyl. Reprinted with Permission Ref. 4.



5.2: Method for Obtaining Hindered Vibrational Modes from Classical Molecular Dynamic Calculation of Pentacene in p-terphenyl

5.2.1: Classical Molecular Dynamics Calculations Settings

Using the coordinates from the low temperature triclinic P $\bar{1}$ crystal structure from literature⁸, a 2x2x2 crystal lattice (that is to say 2 unit cells by 2 unit cells by 2 unit cells) was drawn in Accelrys® Materials Studio. A pentacene molecule was then substituted for one of the p-terphenyl molecules near the center of a 2x2x2 crystal lattice.

The system was then minimized using the Accelrys® Discover Minimizer package set to Smart Minimizer, which uses an algorithm to perform an optimum combination of the Steepest Decent, Conjugate Gradient and Newton methods of minimization, with default settings. The forcefield used was a PCFF modified in a previous study to best model the p-terphenyl solid/solid phase change.^{6,7} All calculations were performed using periodic boundary conditions. The non-bonding settings used for both van der Waals and Columbic non-bonding energies were E-wald method with the default settings for Medium (Accuracy= 0.01 kcal/mol, and Update Width= 1.00 Å.)

For each pressure and temperature, an initial molecular dynamics calculation to equilibrate the system was performed on the minimized structure using a NPT ensemble in the Accelrys® Discover Molecular Dynamics package. The temperature and pressure were controlled using the Berendsen¹³ thermometer and the Berendsen¹³ barometer. The Parrinello¹⁴ barometer was attempted, however the energy exponentially increased till the calculation failed. The settings for this initial equilibration calculation are the following:

20000 steps at 0.5 fs per step, recording only the 20000 step as a frame. After that, the main calculation was performed by restarting from that last frame (the 20000 step) of the trajectory from the equilibration calculation using similar settings, except for 200000 steps and recording a frame every twenty steps. [Note: *As recent as Version 4.4, Accelrys® Discover package has a bug, that when you use 0.5 fs time steps and choose to restart from a previous trajectory, it outputs frames at half the rate you tell it. (i.e. telling it to collect every ten steps causes it to collect every 20 steps.)*] Molecular Dynamic trajectories were calculated at varying pressures between 0-20 kbar (inclusive).

5.2.2: Method for Extracting Translation and Rotation Data for Pentacene from the MD Trajectories

From these trajectories, the position of the center of mass (CoM) for the pentacene molecule was extracted at each frame which is represented as X, Y, and Z coordinates with respect to the arbitrary coordinate axis of the software. This data can then be used to explore the hindered translations of the pentacene molecule in the p-terphenyl host lattice. First, the data was used to explore the movement of the molecule in general by looking at the overall magnitude of the CoM vector formed by the coordinates and the origin of the arbitrary axis.

Second, the CoM vector was projected onto two separate set of axes. The first set of axes was based on the A, B, and C edges of the crystal cell, which are described in **Table 5.1**. Using trigonometry, these values were used to determine the vectors values of

the A, B, and C axes of the crystal lattice **Table 5.2**. The second set of axes was a set of “molecular” axes whose directions were along the long and short lengths of the pentacene molecule, with the third coming out of the plane of the molecule (**Figure 5.4**). The molecular axes were calculated from the original minimized structure using the vector between the CoM and C11-C12 bond midpoint coordinates for the “x-vector”; using the vector between the CoM and the C6 carbon coordinates for the “y-vector”; the cross product of the above two vectors was used as the “z-vector”. Since the minimized structure was used, the “x-vector” and the “y-vector” are not orthogonal to each other. Since the “z-vector” is a cross product it is orthogonal to the two other vectors. (See **Table 5.3**)

Data to investigate the hindered rotations of the pentacene in p-terphenyl was obtained in two ways. A single vector method was developed in which vectors, similar to the X- and Y-axes of the defined molecular axes, were extracted at each step of MD trajectories. Each vector was used to determine the amount of rotation about each axis of the molecular axes as defined in **Table 5.4** as the cross product of the current vector by the initial vector projected along the desired axis of rotation. A current vector (labeled with a subscript t) was the vectors calculated at each step of a trajectory, while an initial vector (labeled with subscript the 0) was defined as the vectors of the molecular axes of pentacene (**Table 5.3**). These two vectors can be seen in **Figure 5.5** as the blue vectors.

However, the vectors were susceptible to fluctuations from intramolecular vibrations of the pentacene molecule. In order to correct for this, a multivector method was developed, in which additional vectors were defined on the molecule and value of

the rotation, as defined in a similar way as earlier, were summed up in order to average out the effect of the intramolecular vibrations. These additional vectors can be seen in **Figure 5.5** as the red and green vectors. There are a total of 6 x-vectors and 10 y-vectors. All the vectors were made similar to the x- and y- vectors in the molecular axes definition. For the y-vectors on the four outer benzene rings, the CoM of the 6 carbon atoms was used in place of the CoM of the molecule used for the two center y-vectors (yatom and yatom2.) The formula for each rotation can be seen in **Table 5.5**, where the vectors X_{1_t} - X_{6_t} represent x_{bond} - x_{bond6} , respectively, and Y_{1_t} - Y_{10_t} represent y_{atom} - y_{atom10} , respectively. The prime represents the negative vector used so that the sign of the cross product magnitude would match. The scripts used to extract the data from the trajectories can be seen in **Appendix A.1**.

Figure 5.4: Diagram of the Defined Molecular Axes of the Pentacene Molecule

The X-axis was an x-vector that went from the CoM of the Molecule to the midpoint of the bond between Carbon 11 and Carbon 12. The Y-axis was a y-vector that went from the CoM of the molecule to the Carbon 6 atom, while the Z-axis was defined as the cross product of the two vectors. The axes are in blue and the Z-axis is coming out of the plane of the molecule.

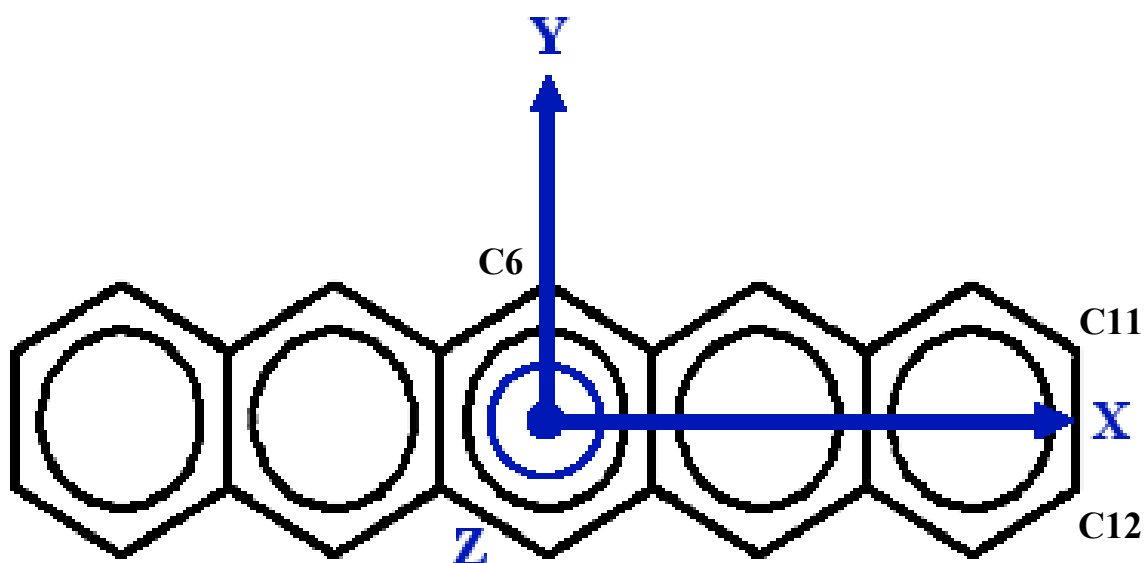


Table 5.1: 2x2x2 Crystal Lattice Parameters for p-Terphenyl	
Length A	33.2077 Å
Length B	21.3515 Å
Length C	26.7925 Å
Angle α	89.9369 °
Angle β	95.7873 °
Angle γ	90.6357 °

Table 5.2: Normalized Crystal Lattice Axes			
A axis	0.994841	-0.0111293	-0.100836
B axis	0	0.9999994	0.001101
C axis	0	0	1

Table 5.3: Normalized Molecular Axes of Pentacene			
X axis	-0.3039	-0.13954	0.942433
Y axis	-0.50726	-0.86007	-0.05451
Z axis	0.83926	-0.50737	0.19551

Figure 5.5: Diagram of Molecular Vectors for Rotation Determination

The diagram shows the vectors used for the determination of the rotation of the pentacene molecule about its molecular axes. The single vector method used the same vectors as those used to determine the molecular axes (shown in blue). A multivector approach was used by creating additional vectors shown in the diagram in red and green which were used to average out the effects of the intramolecular motions of the molecule in the MD simulation. The bonds along the long axis of the molecule are labeled $xbond\#$, while the vectors along the short axis of the molecule are labeled $yatom\#$.

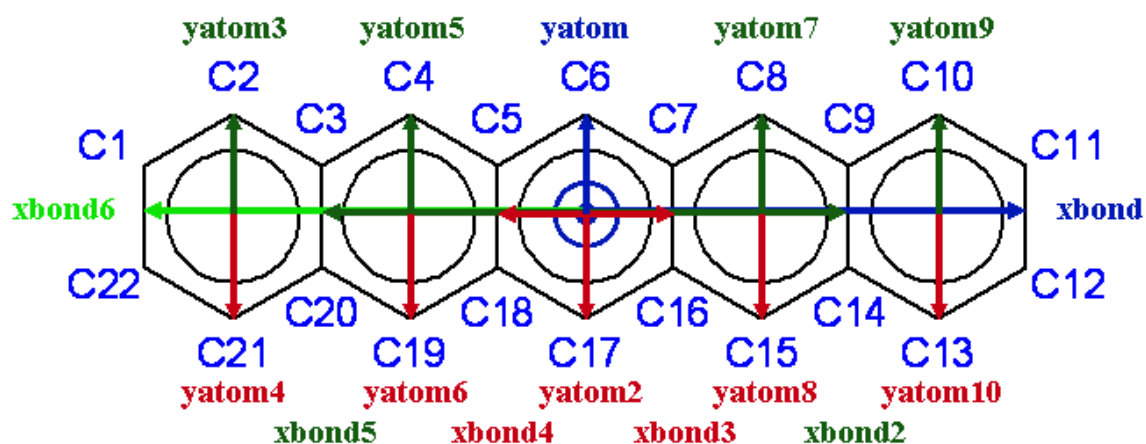


Table 5.4: Single Vector Definitions of the Rotations of the Pentacene Molecule about Molecular Axes	
Rotation about Z axis	$\vec{X}_t \times \vec{X}_0 \bullet \vec{Z}_0$
Rotation about Y axis	$\vec{X}_t \times \vec{X}_0 \bullet \vec{Y}_0$
Rotation about X axis	$\vec{Y}_t \times \vec{Y}_0 \bullet \vec{X}_0$

Table 5.5: Multivector Definitions of the Rotations of the Pentacene Molecule about the Molecular Axes	
Rotation about Z axis	$\vec{X}1_t \times \vec{X}_0 \bullet \vec{Z}_0 + \vec{X}2_t \times \vec{X}_0 \bullet \vec{Z}_0 + \vec{X}3_t \times \vec{X}_0 \bullet \vec{Z}_0$ $+ \vec{X}4_t \times \vec{X}'_0 \bullet \vec{Z}_0 + \vec{X}5_t \times \vec{X}'_0 \bullet \vec{Z}_0 + \vec{X}6_t \times \vec{X}'_0 \bullet \vec{Z}_0$
Rotation about Y axis	$\vec{X}1_t \times \vec{X}_0 \bullet \vec{Y}_0 + \vec{X}2_t \times \vec{X}_0 \bullet \vec{Y}_0 + \vec{X}3_t \times \vec{X}_0 \bullet \vec{Y}_0$ $+ \vec{X}4_t \times \vec{X}'_0 \bullet \vec{Y}_0 + \vec{X}5_t \times \vec{X}'_0 \bullet \vec{Y}_0 + \vec{X}6_t \times \vec{X}'_0 \bullet \vec{Y}_0$
Rotation about X axis	$\vec{Y}1_t \times \vec{Y}_0 \bullet \vec{X}_0 + \vec{Y}2_t \times \vec{Y}_0 \bullet \vec{X}'_0 + \vec{Y}3_t \times \vec{Y}_0 \bullet \vec{X}_0$ $+ \vec{Y}4_t \times \vec{Y}_0 \bullet \vec{X}'_0 + \vec{Y}5_t \times \vec{Y}_0 \bullet \vec{X}_0 + \vec{Y}6_t \times \vec{Y}_0 \bullet \vec{X}'_0$ $+ \vec{Y}7_t \times \vec{Y}_0 \bullet \vec{X}_0 + \vec{Y}8_t \times \vec{Y}_0 \bullet \vec{X}'_0 + \vec{Y}9_t \times \vec{Y}_0 \bullet \vec{X}_0$ $+ \vec{Y}10_t \times \vec{Y}_0 \bullet \vec{X}'_0 +$

5.2.3: Fourier Transform Analysis of Extracted Translation and Rotation Data

The Fourier transform was taken for each data set (translations and rotations) extracted from the trajectories. The FT was performed using Mathematica's built-in FT function by way of a notebook written to import and export the data from two dummy .csv files (labeled `timedata.csv` for the data to be transformed and `freq.csv` for the outputted FT of the data). The notebook can be seen in **Appendix A.2**.

In order to better interpret the effect of pressure on the frequencies of the hindered translations and rotations of the pentacene molecule in p-terphenyl, a Gaussian lineshape functions were fit to the calculated "spectra" (the FT of the time data) using the same minimization procedure mentioned in **Chapter 3**. Using data provided by additional calculations (beyond the first 5 calculated for all points) performed at 0 kbar (at 298K and 50K), error analysis was performed by grouping the data into unique and random averages of 5 sets of data. These groupings were then used to provide values for peak positions from the Gaussian lineshape fit. Standard statistical analysis was performed to obtain the standard deviations for the peak positions. The relative error was used for error was at the other pressures.

5.3: Results of the Hindered Translations and Rotations of Pentacene in p-Terphenyl at 298K and 50K

5.3.1: Improved FT Spectrum Using Additional MD Calculations

When repeating a second 200,000 step calculation using the results of a former calculation's equilibration step (20,000 steps), the exact set of data was obtained (**Figure 5.6 a**). Although repeatability is often desired in experimental studies, when performing calculations, results as identical as this indicated that restarting the calculation using the same equilibration step was using the same initial velocities for the atoms and so this would always give the same result. Performing a completely new set of calculations, including the equilibration set, from the initial minimized structure would create new distinct sets of data (starting the calculation fresh would use a new random seed for the initial velocities). The next set of calculations using a new equilibration calculation at the same pressure, showed that the data was not exactly reproducible, which demonstrated that new initial velocities provide a distinct subset of data which is likely a sampling of the frequency space for the system at the given conditions (**Figure 5.6 b**). Averaging the data would provide a more accurate and distinct data for each data point (the frequency spectrum at a given temperature and pressure).

The results of multiple calculations at the same pressure averaged in different sized sets demonstrated the amount of averaging required to obtain an accurate and repeatable result. When several different combinations of 3 out of six sets of FT data at 8 kbar were averaged, the results appeared to converge and take shape (**Figure 5.7**). The

effect of successive averaging beyond the first 5 calculations is shown in **Figure 5.8** for data at 298 K and 0 kbar, and demonstrates that even further averaging provides further clarity to the FT spectra. Because of computational cost of the calculations, most of the data points were limited to an averaging of five sets of data.

5.3.2: Effect of Non-bonding Method on the Hindered Translations of Pentacene in p-Terphenyl

$$S_m = \frac{1}{2} \sum_{L,i,j} \frac{A_{ij}}{|r_i - r_j - R_L|^m} \quad 5.1$$

$$S_m = \frac{1}{2} \sum_{L,i,j} \frac{A_{ij} \phi_m(|r_i - r_j - R_L|)}{|r_i - r_j - R_L|^m} + \frac{1}{2} \sum_{L,i,j} \frac{A_{ij} [1 - \phi_m(|r_i - r_j - R_L|)]}{|r_i - r_j - R_L|^m} \quad 5.2$$

As can be seen in **Figure 5.9**, there is a difference in the results between atoms based and Ewald summation methods of non-bonding interaction. The atoms-based method is the simplest method of considering the non-bonding energy of the system. In this method the energy for all the atoms pairs are calculated and summed up, limited by a defined cutoff distance between atoms. In order to avoid an unreal jump in energy when an atom goes past the cutoff boundary, Materials Studio uses a switching function that gradually lowers the potential energy of the bonding interactions as the cutoff distance is reached. The settings used for the atom-based method were the default settings.

The Ewald summation method is a technique for calculating the non-bonding energy in a periodic system proposed initially by Ewald¹⁵. The technique, as used by

Materials Studio, has been explained in detail in literature^{16,17}. Essentially, the non-bonding energies are solved using a general lattice sum (**Equation 5.1**), which is multiplied by a convergence function ϕ_m and $1-\phi_m$. This is done because the second part of the resulting lattice sum can be solved quicker in reciprocal space. The convergence function used for electrostatic energy is **Equation 5.3** and the convergence function used for dispersive energy is **Equation 5.4**. The value of η controls how fast the real space and reciprocal space sums convergence. The larger η is the more quickly the real space sum converges and the slower the reciprocal space sum converges and vice versa. For that reason a balance is needed for optimum performance, which Materials Studio determines on its own. For the most part, since the use of a cutoff point is avoided, the Ewald summation method tends to be more accurate for periodic structures. The effect of this can be seen in **Figure 5.9**, where the choice of non-bonding method affects the resulting frequencies of the hindered translations of the pentacene in p-terphenyl. The use of atoms based method seems to make the frequencies from 0-50 cm^{-1} disappear that are present using the Ewald method.

$$\phi_1 = 1 - \text{erf}(r/\eta) \quad 5.3$$

$$\phi_6 = \left[1 + (r/\eta)^2 + \frac{1}{2}(r/\eta)^4 \right] e^{-(r/\eta)^2} \quad 5.4$$

Figure 5.6: The Effect of Unique and Identical Initial Velocities on Molecular Dynamics Calculations

In (a) it is shown that repeated calculations using the same equilibration calculation result produce identical results in the second (200000 step) calculation. One spectrum is a thick blue line and the second is a thin red line overlapping it. In (b) a unique result was produced for the same temperature and pressure when using a new equilibration step.

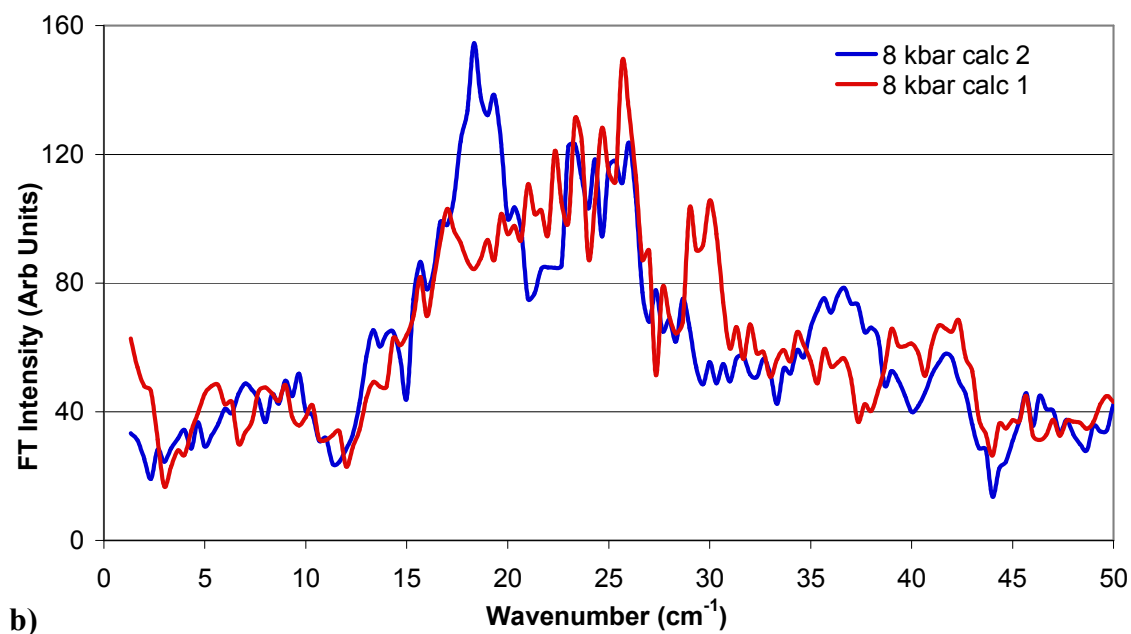
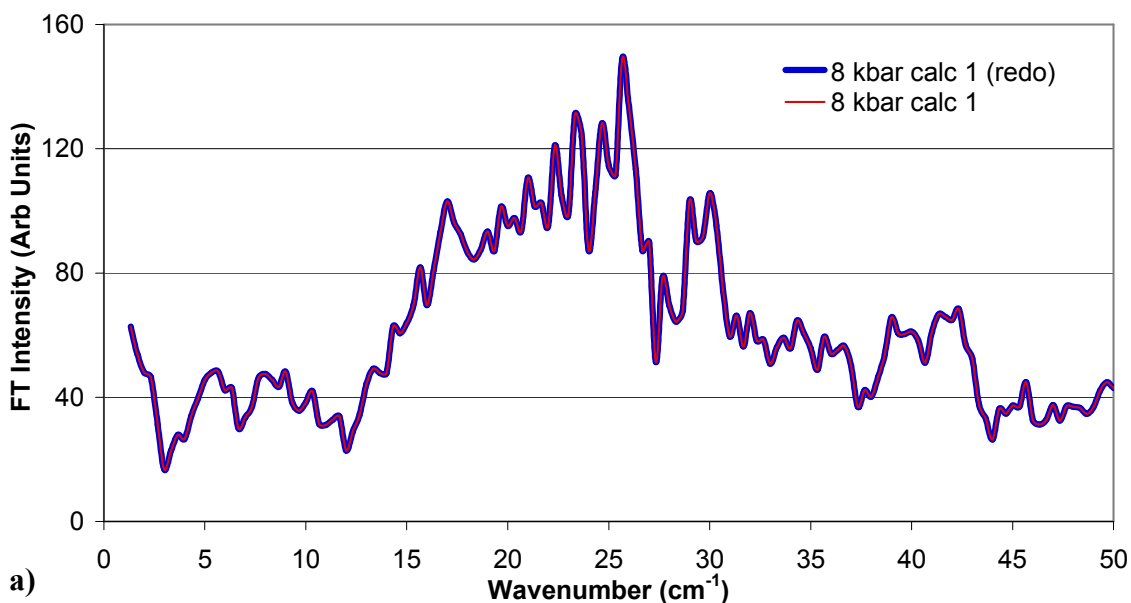


Figure 5.7: Effect of Averaging 3 Unique Sets on the Hindered Translations Spectrum

A comparison of the averages of different combinations of 3 sets of FT of the hindered translations at 298K and 8 kbar showing that the data seems to be converging to a unique form. A 5-point smoothing was used for each plot. Five data sets each were taken as a standard average for the majority of the calculations.

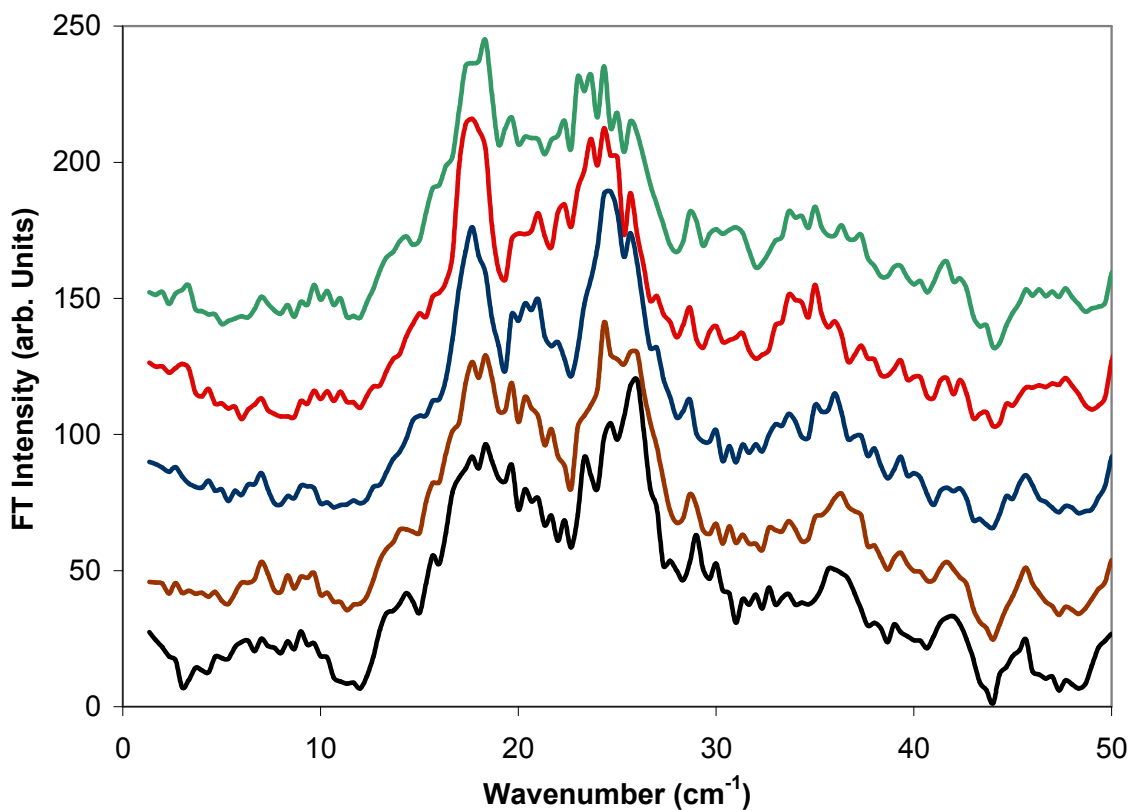


Figure 5.8: Successive Averaging of the Hindered Translations for Pentacene in p-Terphenyl at 298 K and 0 kbar

This further demonstrates the data converging to a unique form by averaging.

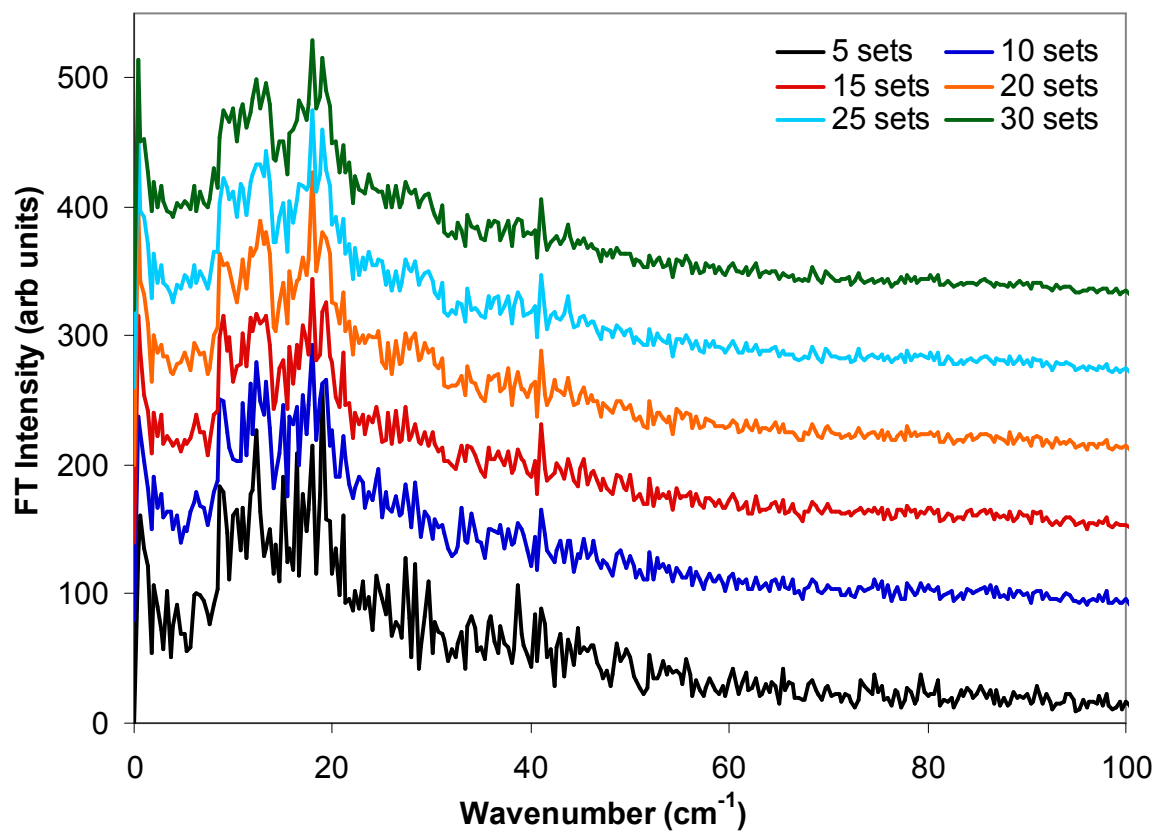
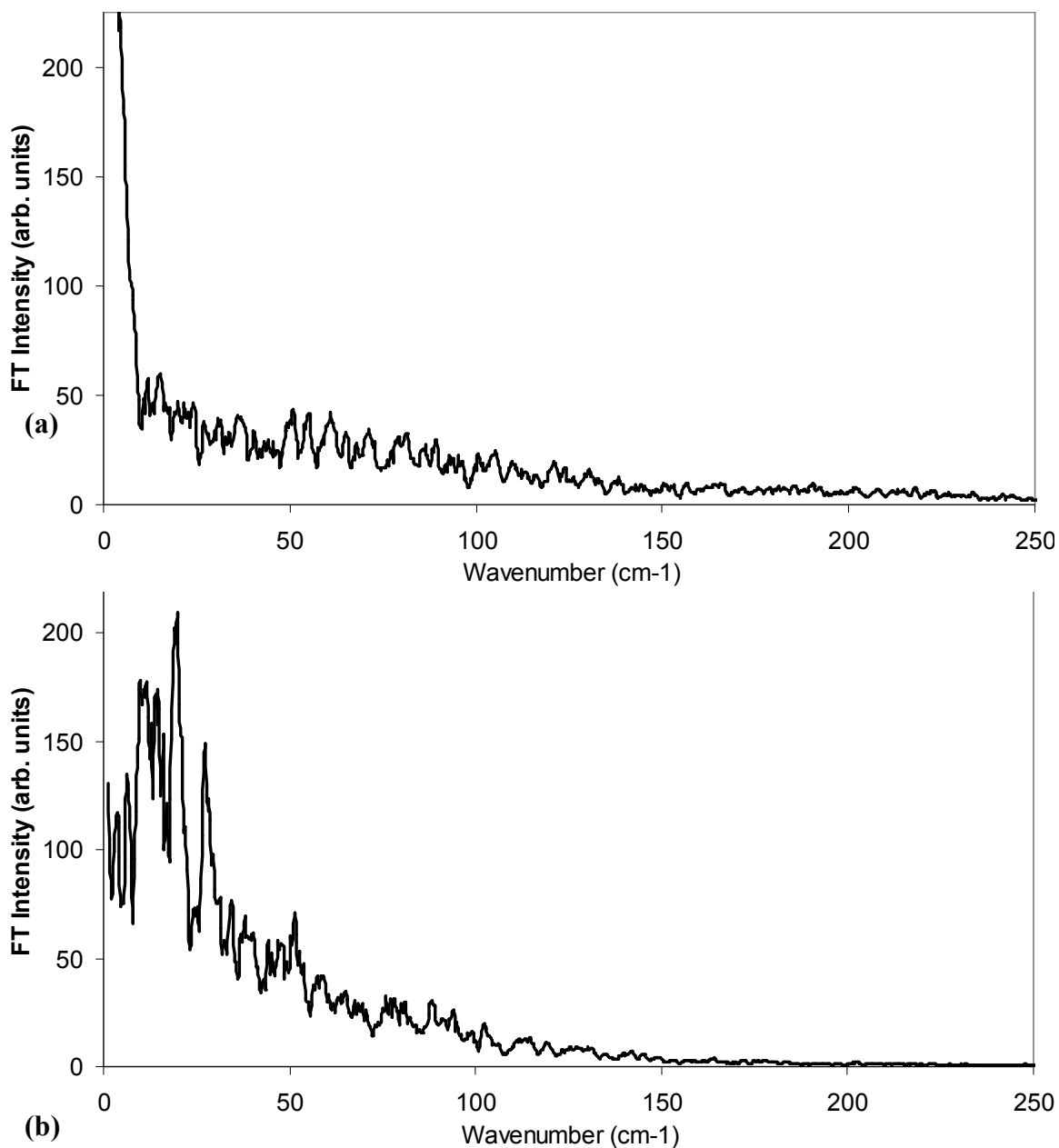


Figure 5.9: Effect of Atoms Based versus Ewald Methods for Non Bonding Interactions on the Hindered Translations for Pentacene in p-Terphenyl

(a) The data obtained using the atom base method of non-bonding interaction. (b) The data obtained previously, using Ewald summation. There is an obvious change in the frequencies in the hindered translations of pentacene, signified by a decrease in the intensity of the frequencies between 0-50 cm^{-1} .



5.3.3: Determining the Polarization of the Hindered Translations modes at 298 K and 50 K along the Molecular and Crystallographic Axes

The FT of the change in the CoM position magnitude shows several modes which can be seen in **Figure 5.10**. It is possible that these four modes could be polarized along a certain direction. Often the polarization can occur either along the axes of the crystallographic lattice or along the molecular axes. By comparing the FT of the CoM with the FT of the projections of the CoM movement onto the crystal axes and molecular axes, the polarization of the modes was investigated.

In **Figure 5.11**, the projections along the molecular axes were compared with the CoM for pentacene in p-terphenyl at 298K and 0 kbar. It can be seen that ν_1 loses intensity in both the Y-axis and Z-axis projections but increases in intensity along the X-axis. It can be said that the mode ν_1 is polarized along the X-axis. The mode ν_2 also appears to be polarized along the X-axis, but less so than ν_1 since it doesn't decrease much in intensity along the Y-axis and Z-axis. The mode ν_3 seems to be slightly polarized along the X-axis and Z-axis since it appears to increase in intensity in both the X-axis and Z-axis projections. The mode ν_4 appears to be polarized along the Y-axis as it has a dramatic increase in intensity in the Y-axis projection, while it remains relatively unchanged in the X-axis and Z-axis projections.

In **Figure 5.12**, the projections along the crystallographic axes were compared with the CoM for pentacene in p-terphenyl at 298K and 0 kbar. The ν_1 mode appears to have polarization along the C-axis as does the ν_2 mode. The mode ν_3 appears to be

polarized along the A-axis, while the v4 mode is polarized along the B-axis. As can be seen in **Tables 5.2 and 5.3**, there is a correlation between the A/Z, B/Y and C/X axes of the crystallographic and molecular axes. This would explain the related polarization of the modes along those corresponding axes. A summary of the polarization of the modes at 298 K can be seen in **Table 5.6**.

Table 5.6: Polarization of the Vibrational Modes of the Hindered Translations of Pentacene in p-Terphenyl at 298 K			
Molecular Axes		Crystallographic Axes	
v1	X-axis Polarized	v1	C-axis Polarized
v2	X-axis Polarized	v2	C-axis Polarized
v3	X- and Z- axes Polarized	v3	A- axis Polarized
v4	Y-axis Polarized	v4	B-axis Polarized

The same analysis was done for the data at 50 K. In **Figure 5.13 a**, the modes, v2-v5, at 0 kbar are shown, while in **Figure 5.13 b**, the modes, v1- v5, at 20 kbar are shown since mode v1 does not appear until ~10 kbar. In **Figure 5.14**, the projections along the molecular axes were compared with the CoM for pentacene in p-terphenyl at 50 K and 0 kbar. It can be seen that the mode v4 is polarized along the X-axis, while the mode v5 appears to be polarized along the Y-axis. In **Figure 5.15**, the projections along the crystallographic axes were compared with the CoM for pentacene in p-terphenyl at 50 K and 0 kbar. It appears that v4 is polarized along the C-axis, while v5 is polarized along the A-axis and B-axis. In the region around 20 and 30 cm^{-1} , two single Gaussians were used to describe the modes, labeled v2 and v3, respectively. However, in the projections

along the molecular and crystallographic axes, pieces of the mode v2 disappear suggesting the possibility of multiple overlapped modes in that region.

In **Figure 5.16**, the projections along the molecular axes were compared with the CoM for pentacene in p-terphenyl at 50 K and 20 kbar, while, in **Figure 5.17**, the projections along the crystallographic axes were compared with the CoM for pentacene in p-terphenyl at 50 K and 20 kbar in order to look at the mode v1. It can be seen in **Figure 5.16** that the mode v1 is polarized along the X-axis, while in **Figure 5.17** it can be seen that v1 is polarized along the C-axis. A summary of the polarization of the modes at 50 K can be seen in **Table 5.7**.

Table 5.7: Polarization of the Vibrational Modes of the Hindered Translations of Pentacene in p-Terphenyl at 50 K			
Molecular Axes		Crystallographic Axes	
v1	X-axis Polarized	v1	C-axis Polarized
v4	X-axis Polarized	v4	C-axis Polarized
v5	Y-axis Polarized	v5	A- and B-axes Polarized

Figure 5.10: Labeled Vibrations from the Fitted Gaussian Peaks for the Hindered Translations of Pentacene in p-Terphenyl at 298 K and 0 kbar

The four Gaussian peaks fit to the hindered translations of pentacene in p-terphenyl at 298 K and 0 kbar labeled v 1-v4.

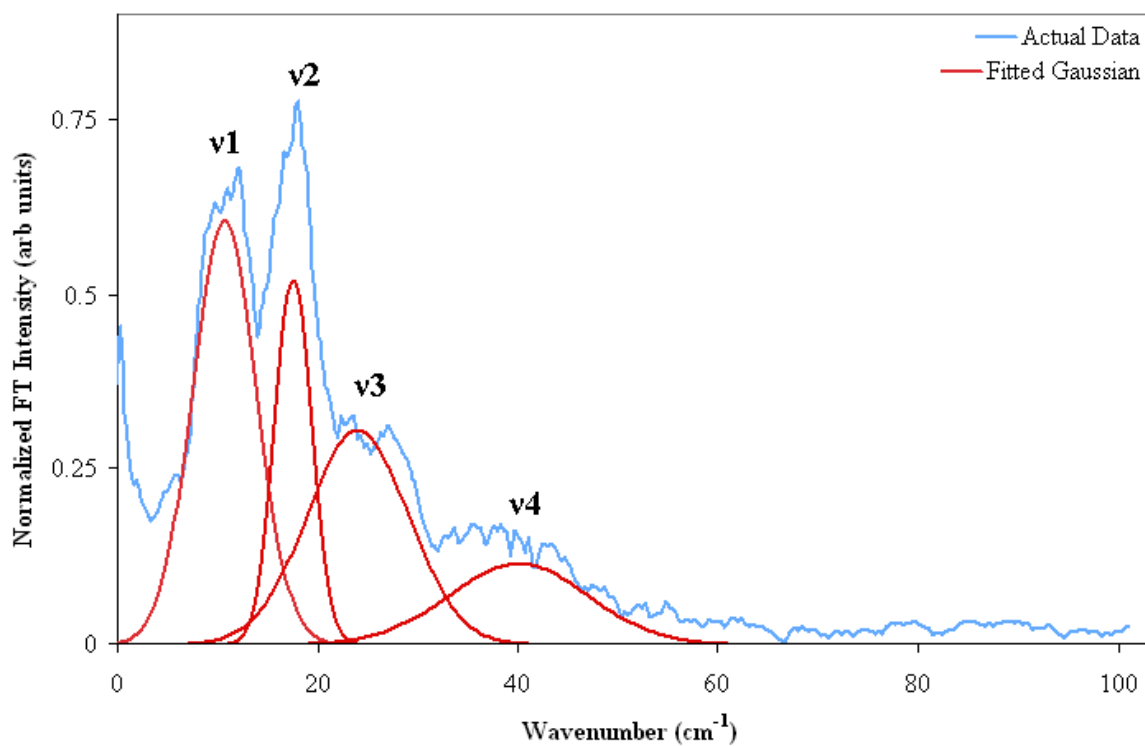


Figure 5.11: Polarization of the Hindered Translations of Pentacene in p-Terphenyl at 298 K and 0 kbar Along Molecular Axes

Based on the comparative intensities of the modes, it appears that v1 is polarized along the X-axis; v2 is polarized along the X-axis; v3 is polarized along the X- and Z-axes; v4 is polarized along the Y-axis.

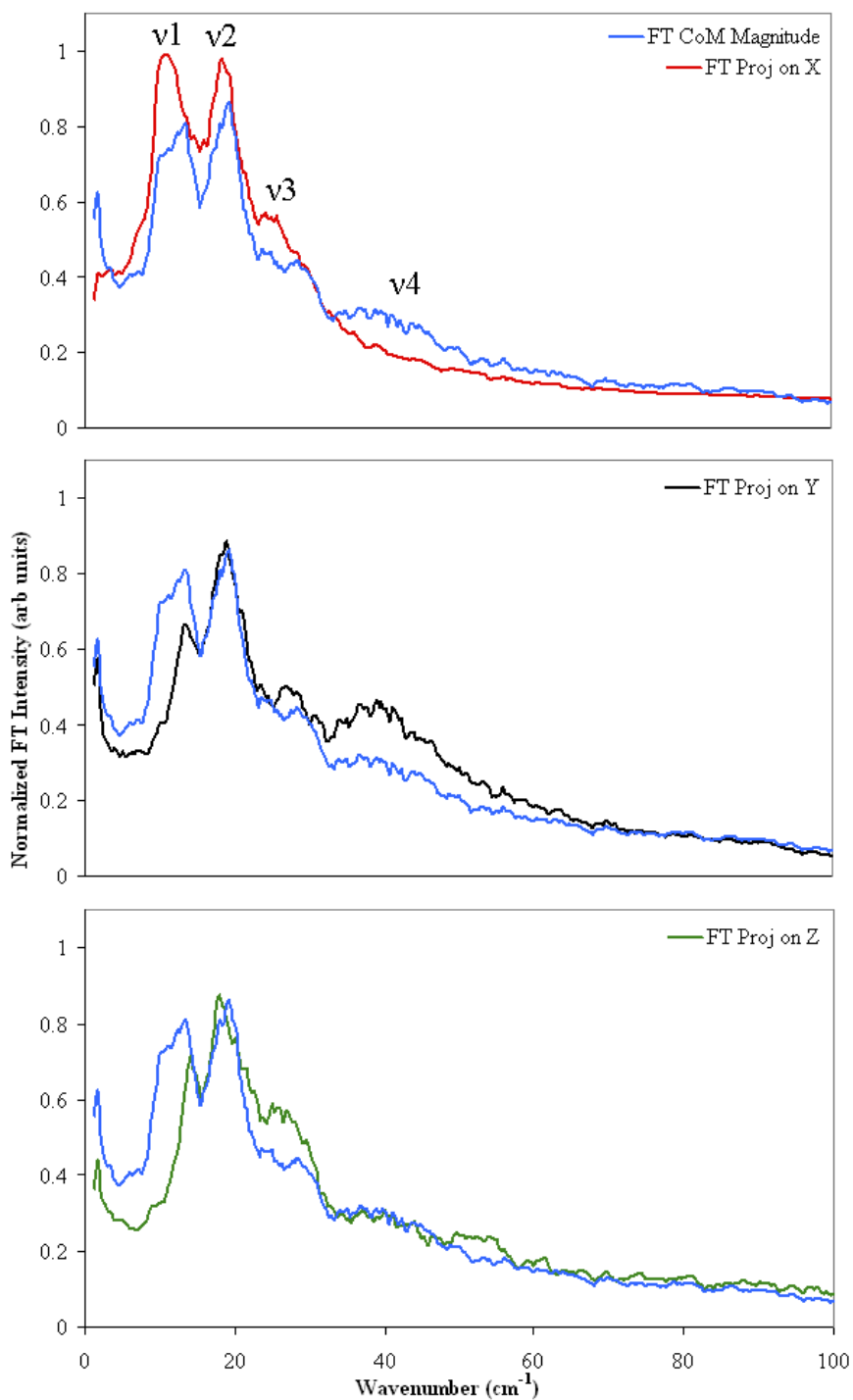


Figure 5.12: Polarization of the Hindered Translations of Pentacene in p-Terphenyl at 298 K and 0 kbar Along Crystal Lattice Axes

Based on the comparative intensities of the modes, it appears that v1 is polarized along the C-axis; v2 is polarized along the C-axis; v3 is polarized along the A-axis; v4 is polarized along the B-axis.

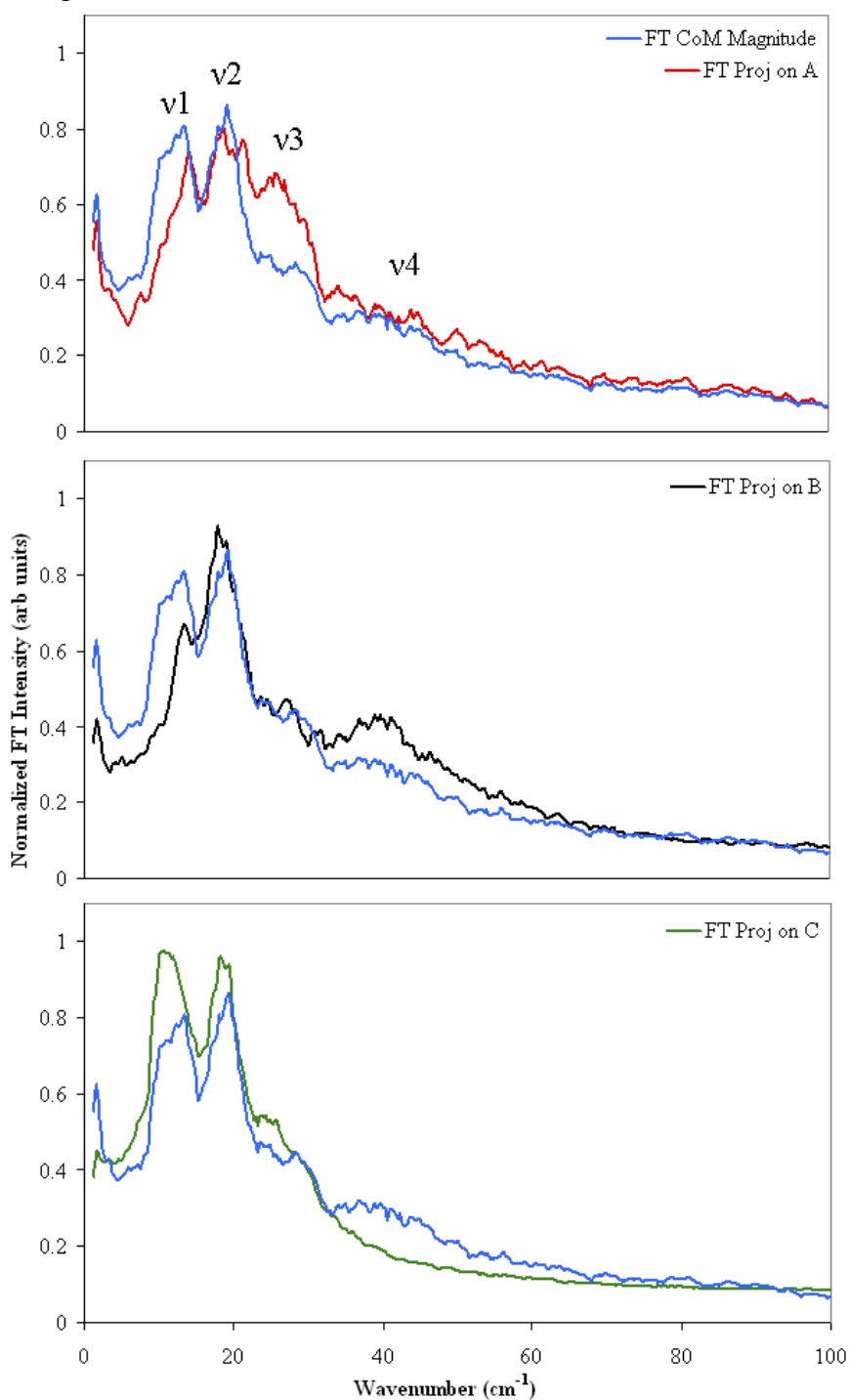


Figure 5.13: Labeled Vibrations from the Fitted Gaussian Peaks for the Hindered Translations of Pentacene in p-Terphenyl at 50 K

The four Gaussian peaks fit to the hindered translations of pentacene in p-terphenyl at 50 K and 0 kbar labeled v2-v5 (a). The mode v1 is found at 10 kbar and above and is demonstrated in them hindered translations at 20 kbar (b).

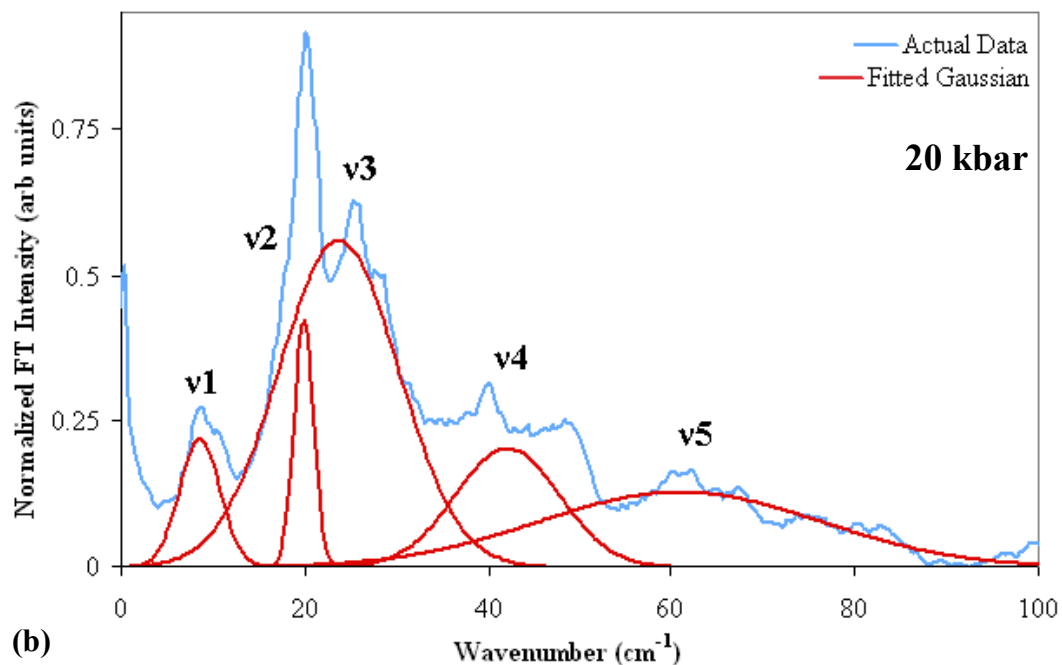
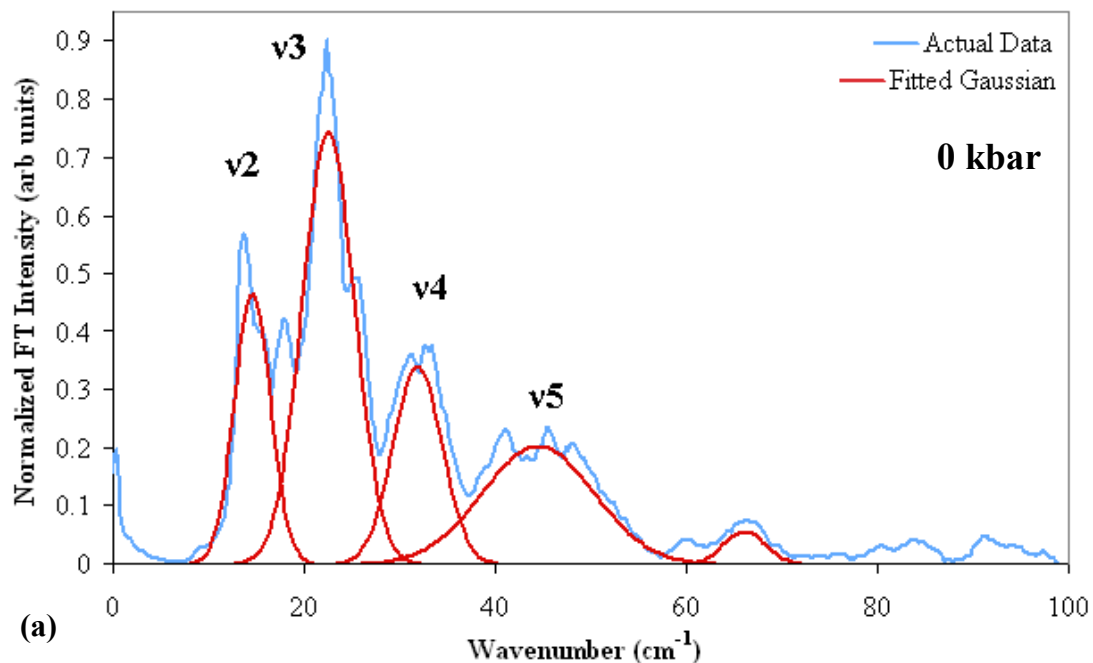


Figure 5.14: Polarization of the Hindered Translations of Pentacene in p-Terphenyl at 50 K and 0 kbar Along Molecular Axes

The mode v4 appears to be polarized along the X-axis while v5 appears to be polarized along the Y-axis.

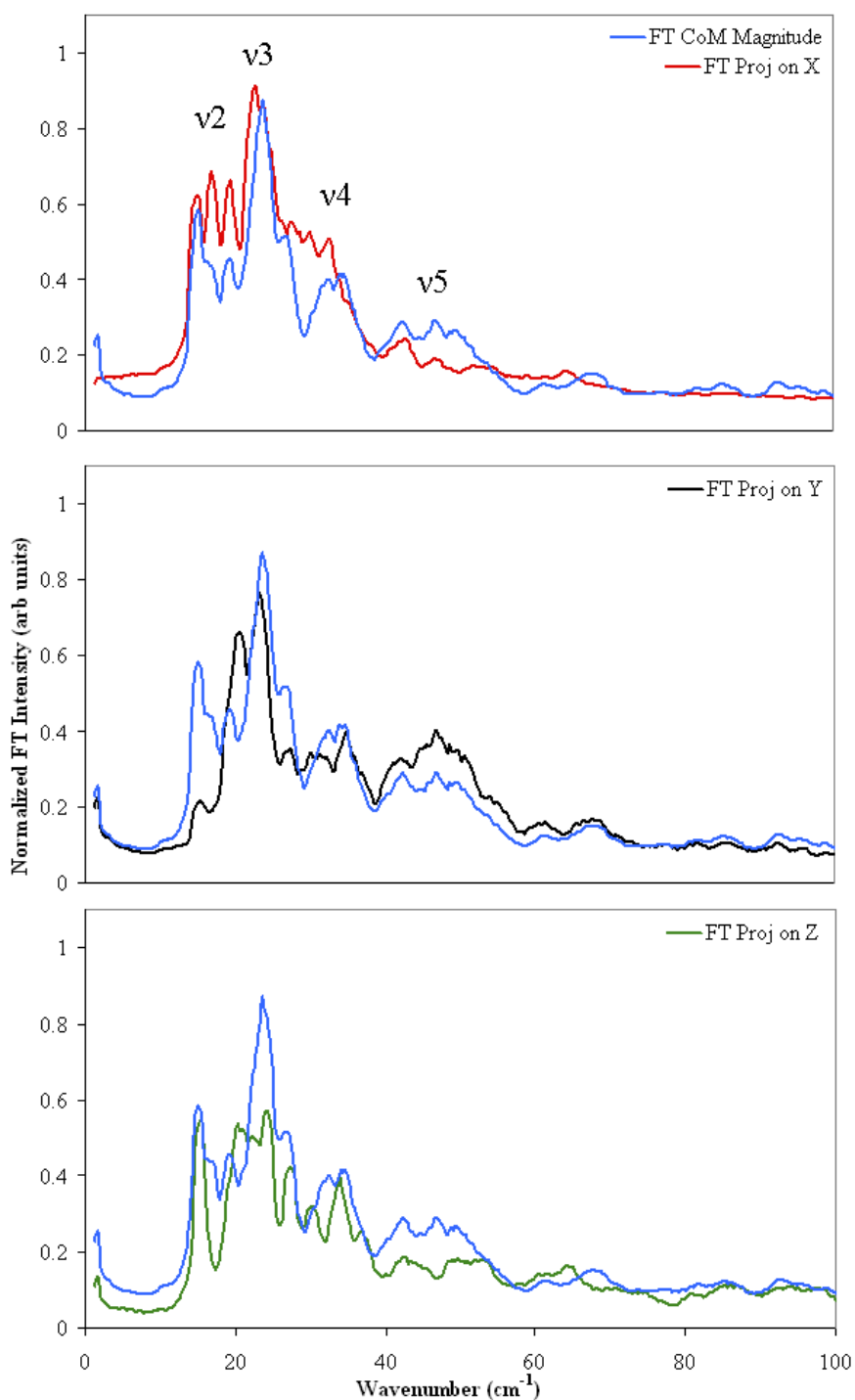


Figure 5.15: Polarization of the Hindered Translations of Pentacene in p-Terphenyl at 50 K and 0 kbar Along Crystal Axes

The mode v4 appears to be polarized along the C-axis while v5 appears to be polarized along both the A and B axes.

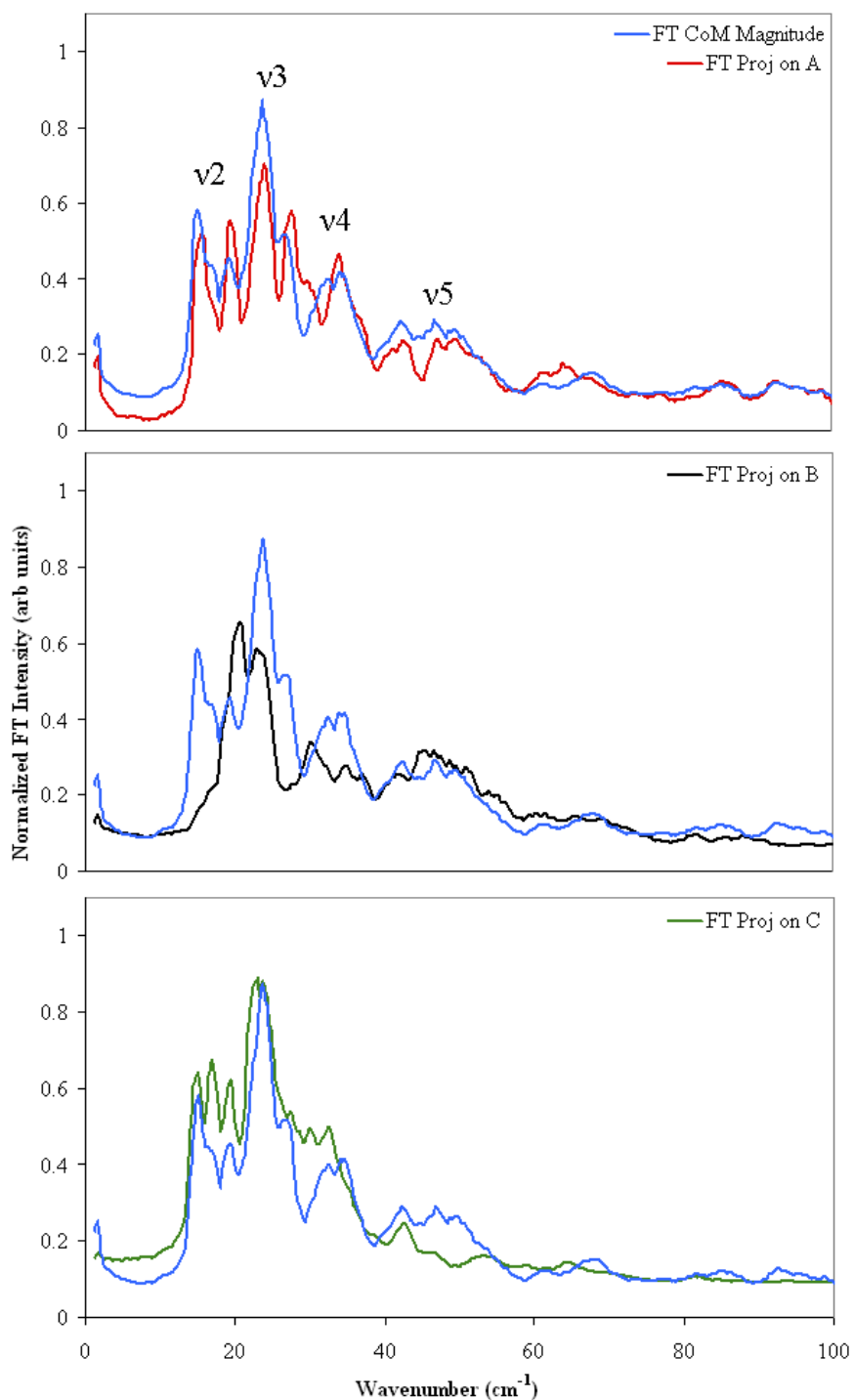


Figure 5.16: Polarization of the Hindered Translations of Pentacene in p-Terphenyl at 50 K and 20 kbar Along Molecular Axes (Focus on ν_1)

The comparison of the projections of the hindered translations onto the molecular axes of the pentacene at 50 K (20 kbar, focusing on the mode ν_1). The mode ν_1 appears to be polarized along the X-axis.

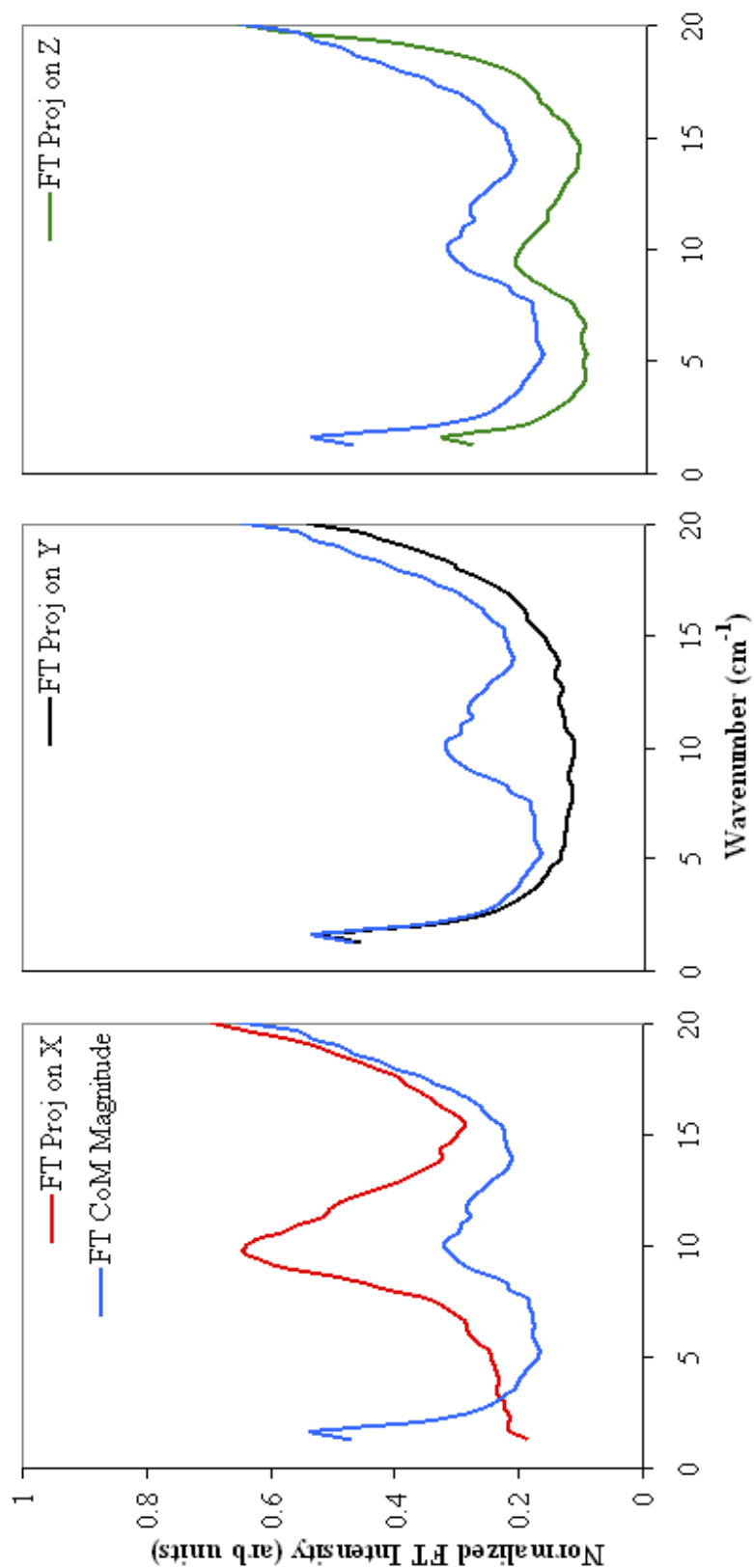
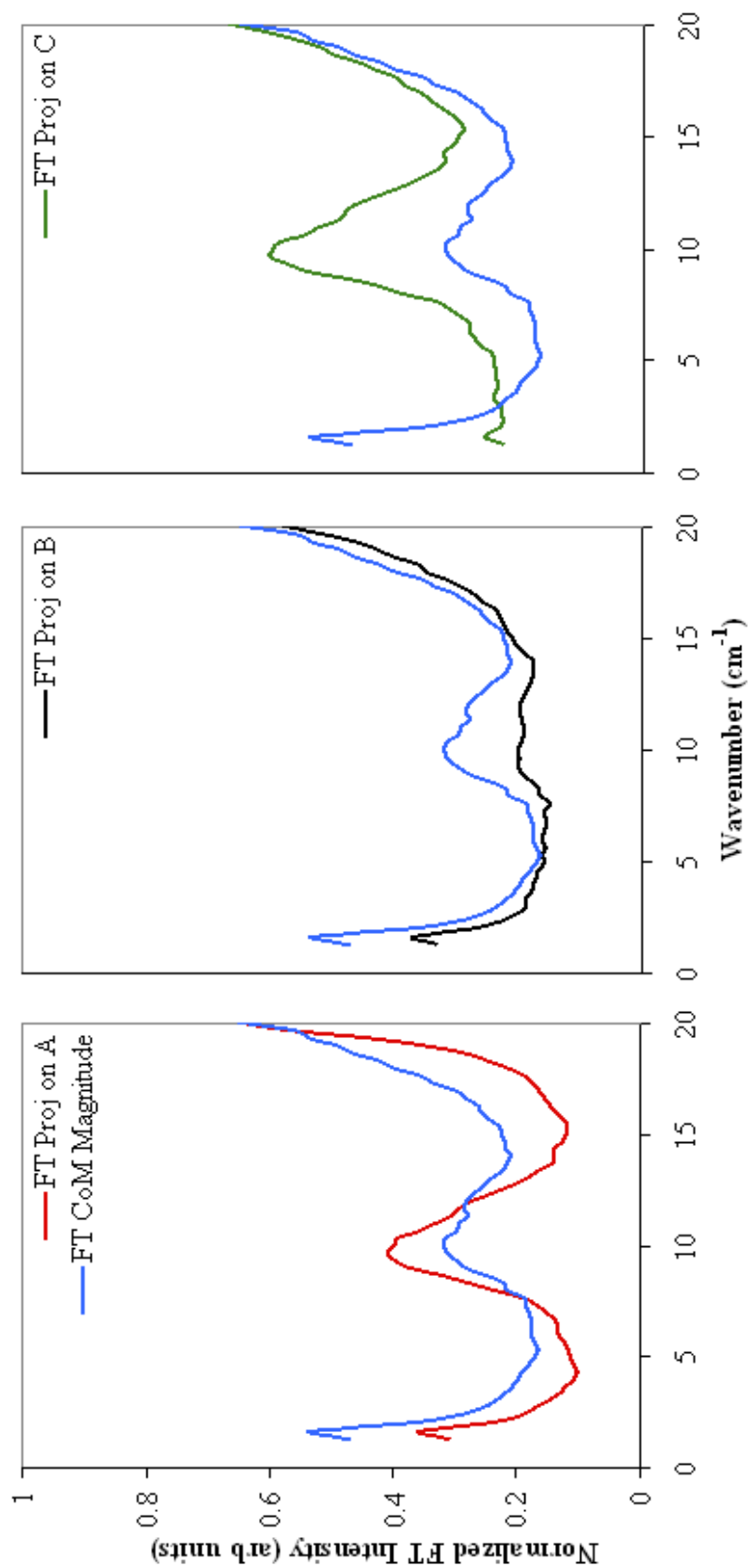


Figure 5.17: Polarization of the Hindered Translations of Pentacene in p-Terphenyl at 50 K and 20 kbar Along Crystallographic Axes (Focus on ν_1)

The comparison of the projections of the hindered translations onto the crystallographic axes of the pentacene at 50 K (20 kbar, focusing on the mode ν_1). The mode ν_1 appears to be polarized along the C-axis.



5.3.4: Effect of Pressure on the Frequency of the Calculated Vibrational Modes of the Hindered Translations at 298 K

Using Gaussian fitted peak positions, the effect of pressure on the frequency of the vibrational modes was studied. In **Figure 5.18**, the FT spectra of the hindered translations of pentacene in p-terphenyl at 298 K, from an average of 5 calculations, are plotted as a pressure series from 0 kbar (room pressure) to 20 kbar. It can be seen that the modes shift to higher wavenumber with an increase in pressure. There appears to be a slight anomaly around 18 kbar but that could be corrected by additional averaging.

In **Figure 5.19**, the wavenumber of the four vibrational modes fitted by Gaussians are plotted with respect to pressure. It can be seen that the error bars for the two modes ν_3 , and ν_4 are quite large, which is due to the broad and overlapping nature of the two modes. For the most part the modes appear to increase in wavenumber rather steadily, which is to be expected as there is no known phase transition at room temperature for p-terphenyl.¹

In **Figure 5.20**, the mode Grüneisen parameters were obtained for each mode as the slope of the plot of $\ln[\nu(P)/\nu(0)]$ versus $\ln[V(0)/V(P)]$, according to **Equation 5.5**.¹⁸ The mode Grüneisen parameter is a measure of the anharmonicity of the mode^{18,19} and the effect that the compression has on the mode. The largest value is 4.395

$$\frac{\nu_i(P)}{\nu_i(0)} = \left[\frac{V(0)}{V(P)} \right]^{\gamma_i} \quad 5.5$$

for the mode at 10.8 cm^{-1} (ν_1). Since the ν_1 mode was shown to be polarized along the C-axis of the crystal lattice and X-axis of the molecule, it would seem that the greatest anharmonicity of the pentacene hindered translations is along those axes. The next highest constant is 3.365 for the mode at 23.8 cm^{-1} (ν_3). The mode ν_3 was shown to be polarized along the A-axis of the crystal lattice and the X- and Z-axis of the molecule. The anharmonicity of this mode may be due to the movement along the Z- and A-axis, but may also be contributed by the motion of the mode along the X-axis. The mode Grüneisen parameters for ν_2 and ν_4 (2.419 and 2.549, respectively) are similar. Though the parameter is less for the mode ν_2 than for ν_1 , the polarization of the mode at 17.8 cm^{-1} (ν_2) was shown to be along the X- and C- axes, similar to ν_1 . However, as can be seen in **Figures 5.11 and 5.12**, the polarization effect was less intense than that of the mode ν_1 so it is likely, given their mode Grüneisen parameters, that ν_2 is not as polarized along the coordinates as much as ν_1 . The mode at 37.0 cm^{-1} (ν_4) is polarized along the B-axis of the crystal lattice and the Y-axis of the molecule. Being the lowest values, these vibrational coordinates (Y- and B-axes) appear to be the least anharmonic.

Figure 5.18: Pressure Induced Shift in the Averaged (5 data sets) Hindered Translations Spectra at 298 K

Averaged over five calculations, it shows an increase in the wavenumbers of the vibrational frequencies as pressure was increased. Since there is no distinct phase change at this temperature, this was reasonable.

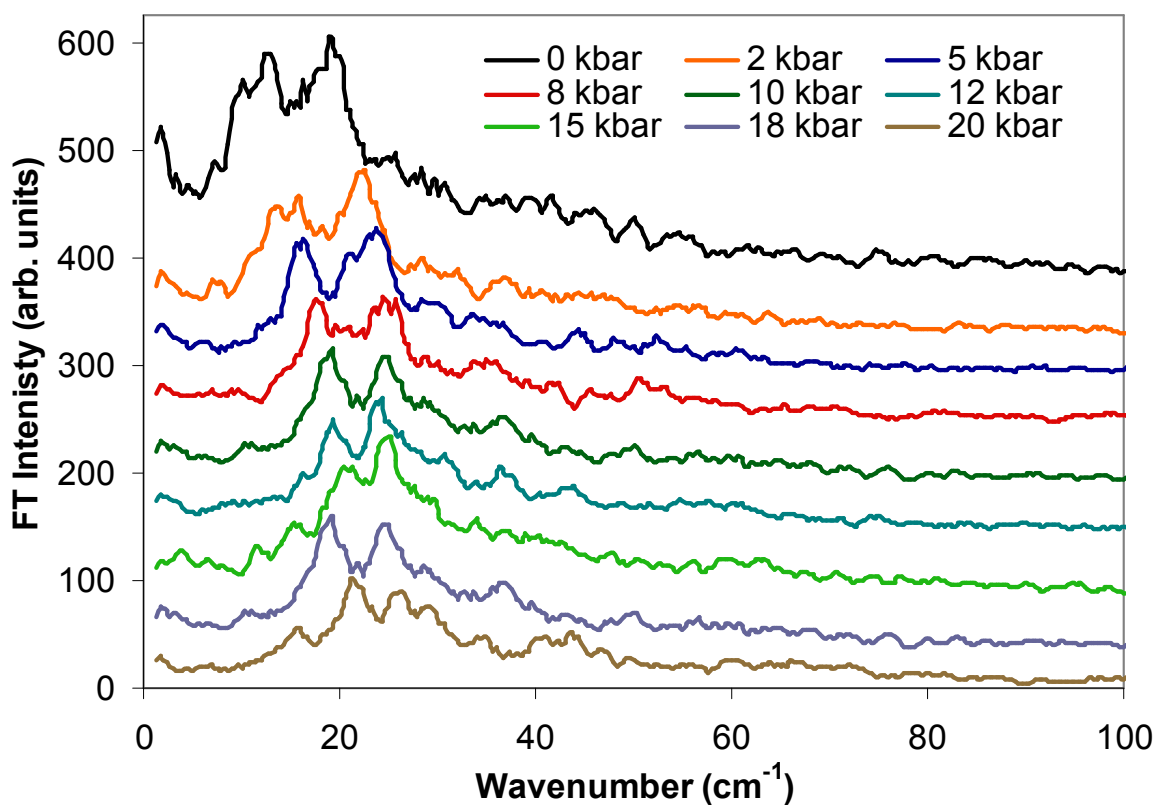


Figure 5.19: Shift of Vibrational Modes of the Hindered Translations at 298 K

The frequencies of the vibrational modes of the hindered translations increased as pressure increased. This make sense since there should be no distinct phase change for p-terphenyl at this temperature.

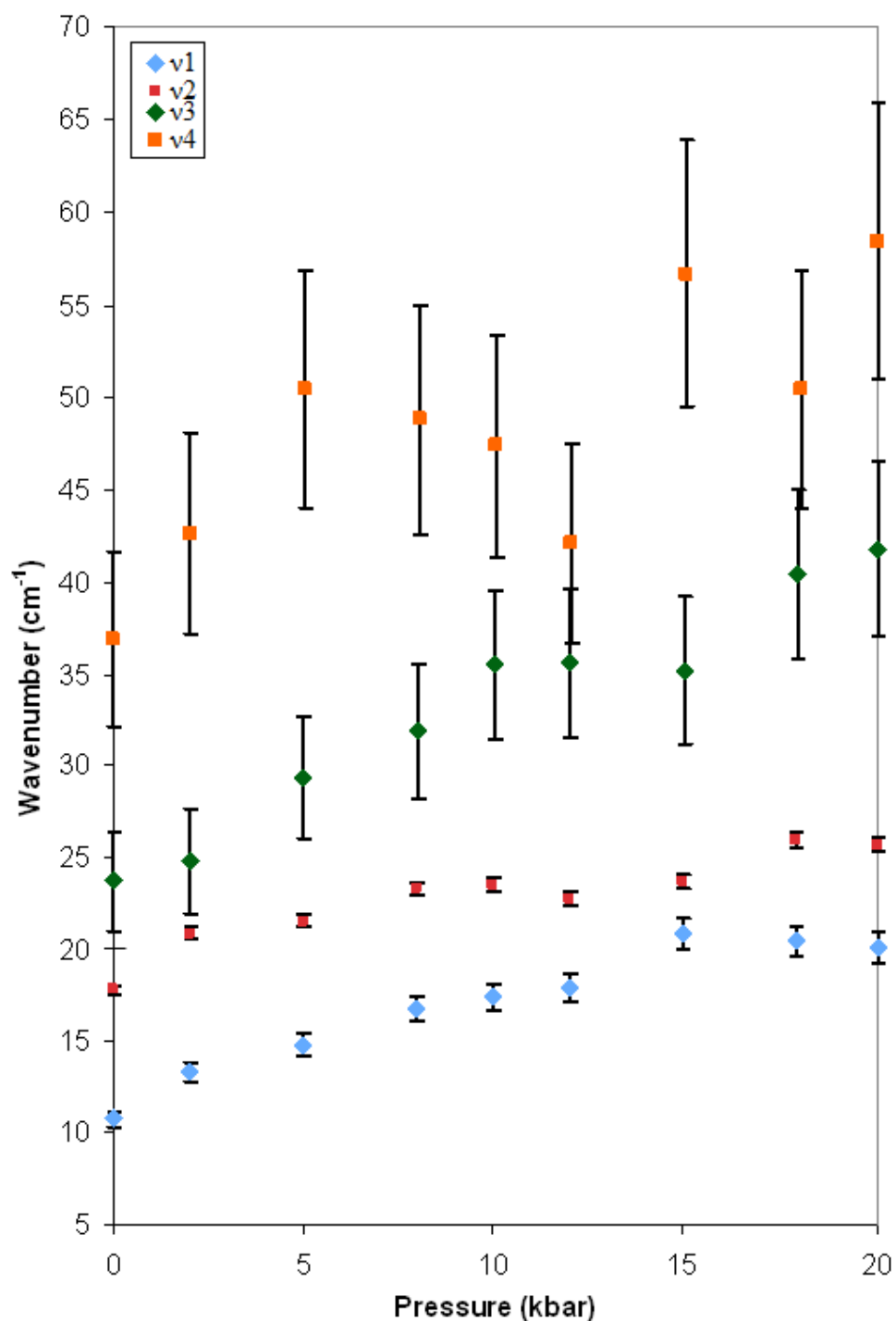
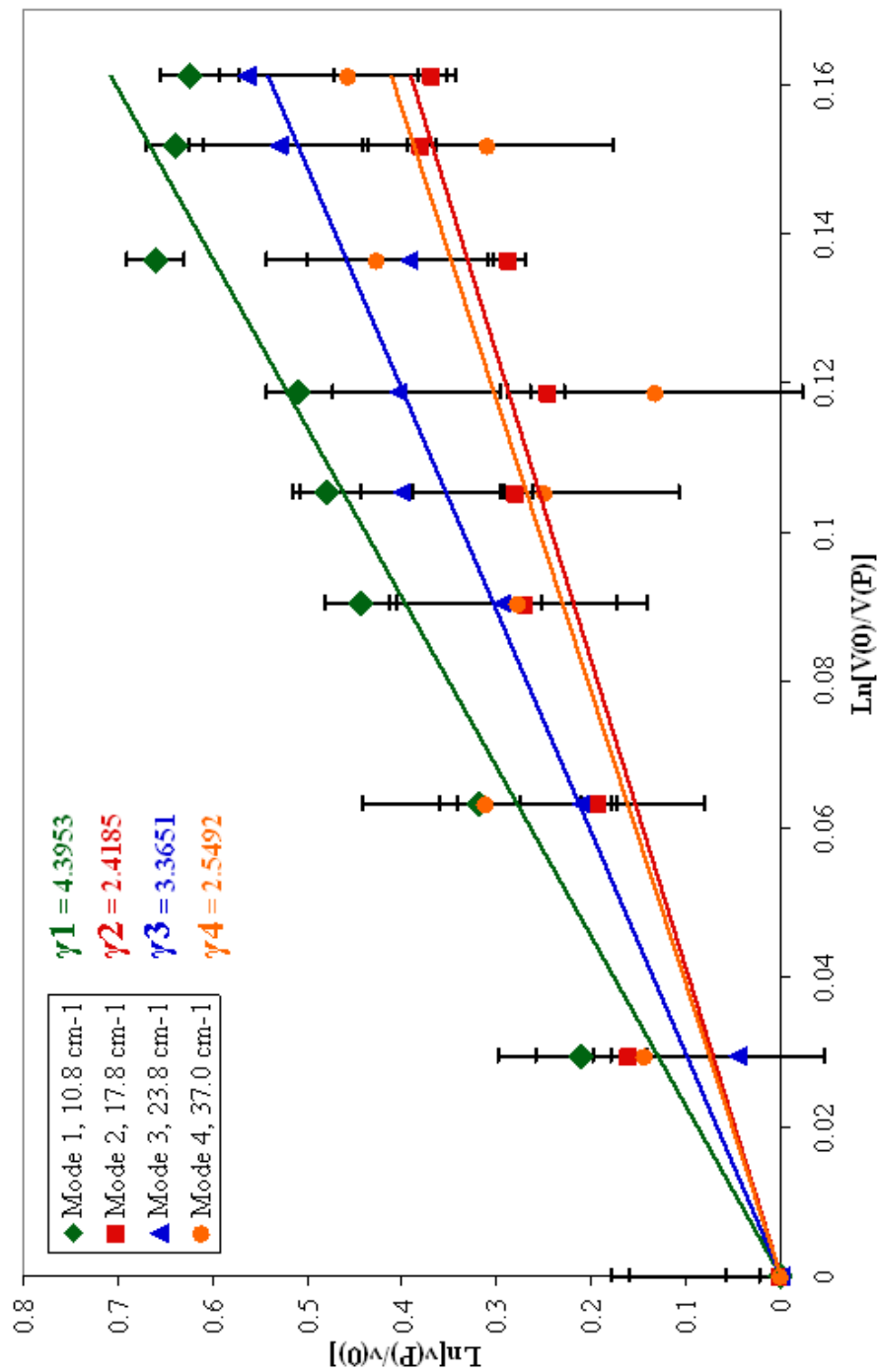


Figure 5.20: The Mode Grüneisen Parameter Plot for the Hindered Translations of Pentacene in p-Terphenyl at 298 K

This further demonstrates the effect of pressure on the frequency of the modes. The mode with the largest mode Grüneisen parameter is ν_1 (10.8 cm^{-1}) indicating a large anharmonicity in the vibration energy.



5.3.5: Effect of Pressure and a Phase Transition on the Frequency of the Calculated Vibrational Modes of the Hindered Translations at 50 K

In **Figure 5.21**, the FT spectra of the hindered translations of pentacene in p-terphenyl at 50 K, from an average of 5 calculations, are plotted as a pressure series from 0 kbar (room pressure) to 20 kbar. It can be seen that for the most part the modes appear to be increasing in wavenumber (hard modes) with pressure. However, around 10 kbar a new peak appears, which is decreasing in wavenumber (soft mode) with increased pressure. This could be a new peak appearing after the p-terphenyl phase transition around 6 kbar or a mode that was mixed in with other modes (ν_2 and ν_3) at lower pressures.

In **Figure 5.22**, the wavenumber of the five modes fitted by Gaussians were plotted with respect to pressure. A line was drawn in the region where the phase change for p-terphenyl occurs at 50 K. It can be seen that the new peak at around 10 cm^{-1} appears, after the phase transition, shifting down in frequency with pressure.

In **Figure 5.23**, the mode Grüneisen parameters were obtained for the modes (ν_2 – ν_5) from the slope of the $\text{Ln}[\nu(P)/\nu(0)]$ versus $\text{Ln}[V(0)/V(P)]$ plot. The modes at 32 and 45 cm^{-1} (ν_4 and ν_5 , respectively) have the largest mode Grüneisen parameters. Looking at the polarizations of ν_4 and ν_5 , the anharmonicity at low temperature and triclinic phase appears to be located along the Y- and X- molecular axes and the B- and C- crystallographic axes, different than the room temperature phase in which the

anharmonicity appears to be along the X- and Z- molecular axes and the A- and C-crystallographic axes.

In **Figure 5.23**, a line is drawn representing the location of the ~6 kbar phase transition for p-terphenyl at 50 K, after which the shifting of the frequency of the modes behaves differently, an effect not seen in the room temperature data where there is no phase change. The most evident effect is an apparent mode softening (decrease in frequency with pressure) of the mode at 45.0 cm^{-1} (ν_5) immediately after the phase transition. This is then followed by an immediate mode hardening (increase in frequency with pressure). This is similar to the experimental results from the photon echo measurements in which mode softening induced by the presence of the phase transition was seen in the electronic dephasing of the pentacene molecule in p-terphenyl.⁴ The mode ν_5 could be coupled to this effect, although it is at a higher frequency than measured in the experiment. The soft mode at 10 cm^{-1} (ν_1), which appears after the phase transition (**Figure 5.22**), may also have an effect on the observed experimental mode softening.

Figure 5.21: Pressure Induced Shift in the Averaged (5 data sets) Hindered Translations Spectra at 50 K

This seemed to show an increase in the frequencies of the vibrations as pressure was increased for some modes. After 5kbar, a new soft mode appears at around 10 cm^{-1} .

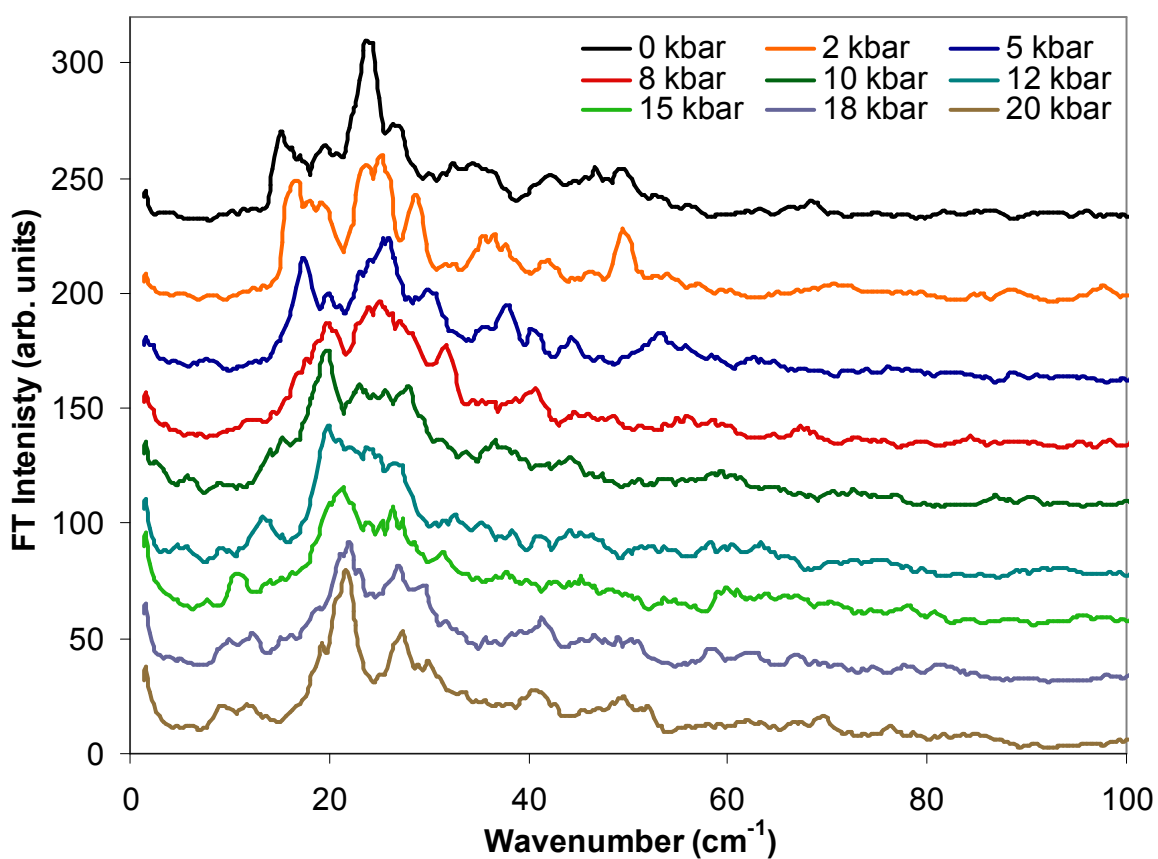


Figure 5.22: Shift of Vibrational Modes in the Hindered Translations at 50 K

The frequencies of the hindered translational motion at 50 K for pentacene in the p-terphenyl increased up to 5 kbar. The grey line represents the 6 kbar phase transition of p-terphenyl at 50K. Above $P > 6$ kbar, the shifts in the vibrational modes of the hindered translations behave differently. Also, a new soft mode appears $\sim 10 \text{ cm}^{-1}$ for $P > 6$ kbar.

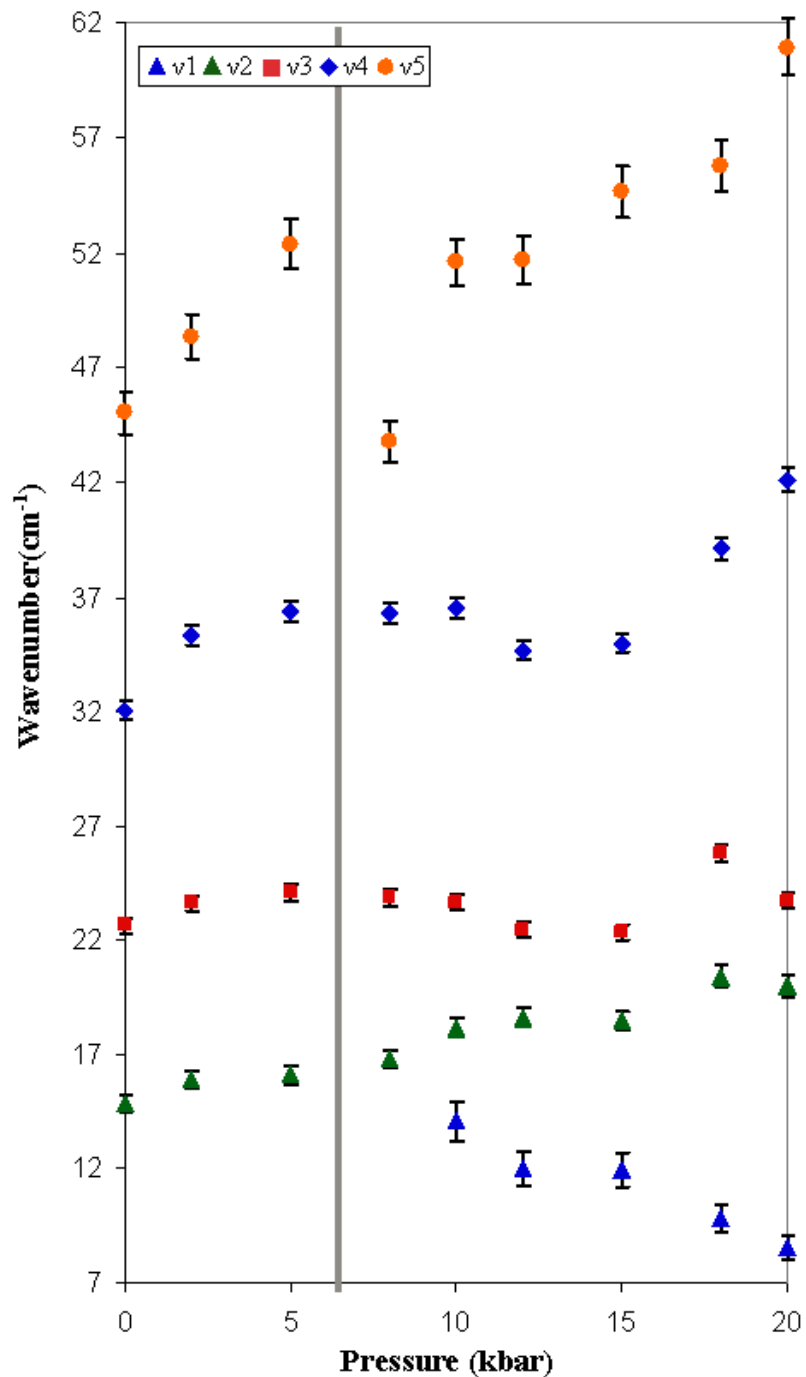
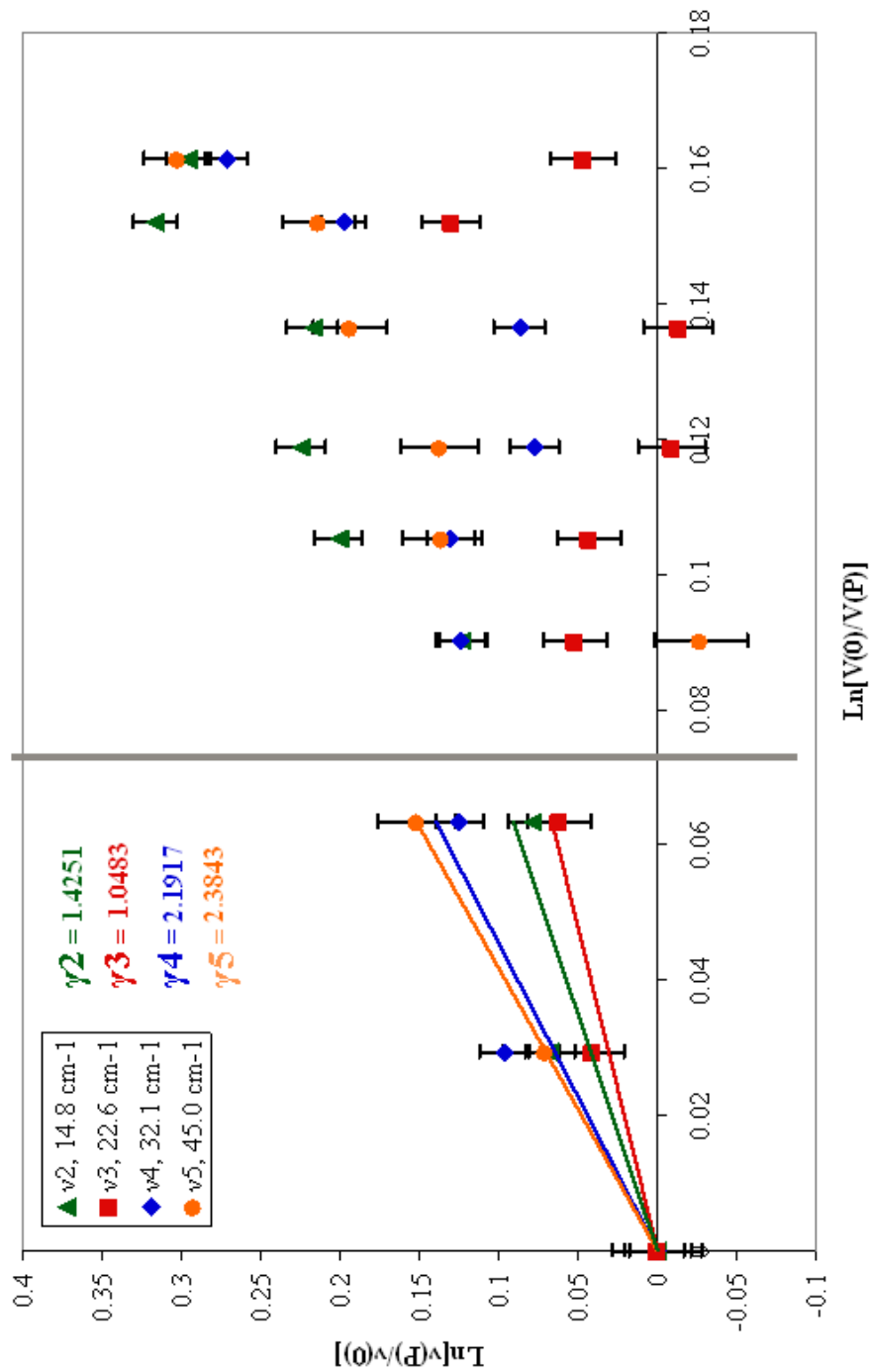


Figure 5.23: The Grüneisen Parameter Plot for the Hindered Translations of Pentacene in p-Terphenyl at 50 K
 Further demonstrates the effect of pressure on the frequency of the modes. The grey line represents the 6 kbar phase transition of p-terphenyl at 50 K. The mode Grüneisen parameters were determined from the first three points before the phase transition. After the phase transition, the data behaves differently, including an apparent mode softening (decrease in frequency) in v5, after the phase transition, followed by an immediate mode hardening (increase in frequency).



5.3.6: Identification and Removal of Intramolecular Modes from the FT of the Hindered Rotations of the Pentacene in p-Terphenyl at 50 K

Having investigated the hindered translations of pentacene in p-terphenyl, the next step was to investigate the hindered rotations of the pentacene molecule. At first a single vector approach was used to measure the rotation about each of the molecular axis, described previously. However, it was later determined that intramolecular vibrations were coupled into the movement of the vectors and that a multiple vector (multivector) approach would be required to cancel out the effect of the intramolecular movements and emphasize the rigid, concerted rotations of the pentacene molecule. The resulting comparison of the single vector and multivector approach can be seen in **Figure 5.24**.

In the spectrum for the rotations about the Z-axis (**Figure 5.24 a**), a peak at around 160 cm^{-1} was shown to disappear with the multivector method and a peak at around 270 cm^{-1} appeared to increase. The peak at 160 cm^{-1} appears to be an intramolecular mode, while the peak at 270 cm^{-1} appears to be a rotation about the Z-axis of the molecule. In the spectrum of the rotations about the Y-axis (**Figure 5.24 b**), many intramolecular modes in the regions of $100\text{-}200\text{ cm}^{-1}$ and $230\text{-}270\text{ cm}^{-1}$ decreased or disappeared entirely, while a peak around 210 cm^{-1} intensified. The mode at 210 cm^{-1} appears to be a rotation about the Y-axis. In the spectrum of the rotations about X-axis (**Figure 5.24 c**) similar intramolecular modes present in the single vector Y-axis rotations spectrum disappeared or decreased in intensity. A peak at around 145 cm^{-1} remained and

is likely a rotation about the X-axis. Another peak around 210 cm^{-1} also remained, but this could be the rotation about the Y-axis leaking into the X-axis rotation spectrum.

In **Figure 5.25**, the five-point smoothed spectra of the hindered rotations of pentacene in p-terphenyl at 50 K are shown for 0, 5, and 20 kbar. Several of the discernable peaks appear to shift to higher frequency with increased pressure. However, it is difficult to follow the trend in going from 5 kbar to 20 kbar. Some changes may be caused by the phase transition at 6 kbar but additional pressure points will be needed to elucidate.

Figure 5.24: Reduction of Intramolecular Modes in the Hindered Rotations Spectrum for Pentacene in p-Terphenyl

By using additional vectors to represent the rotations of the pentacene molecule, the effect of the intramolecular motions on the original vectors was canceled out. Several peaks disappeared or were reduced, identifying them as likely intramolecular modes. Also peaks remained and intensified revealing them as true rotations about the axes.

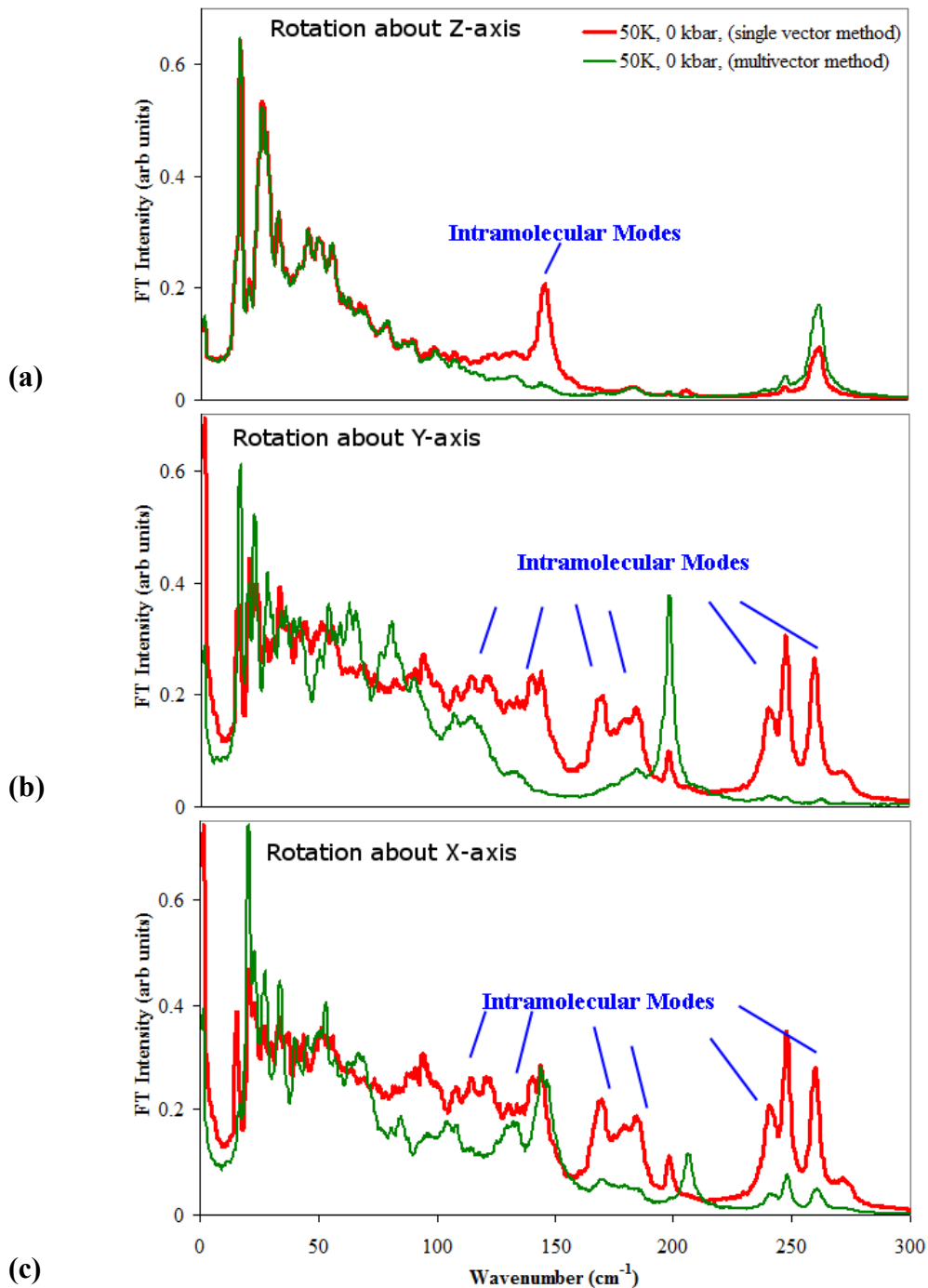
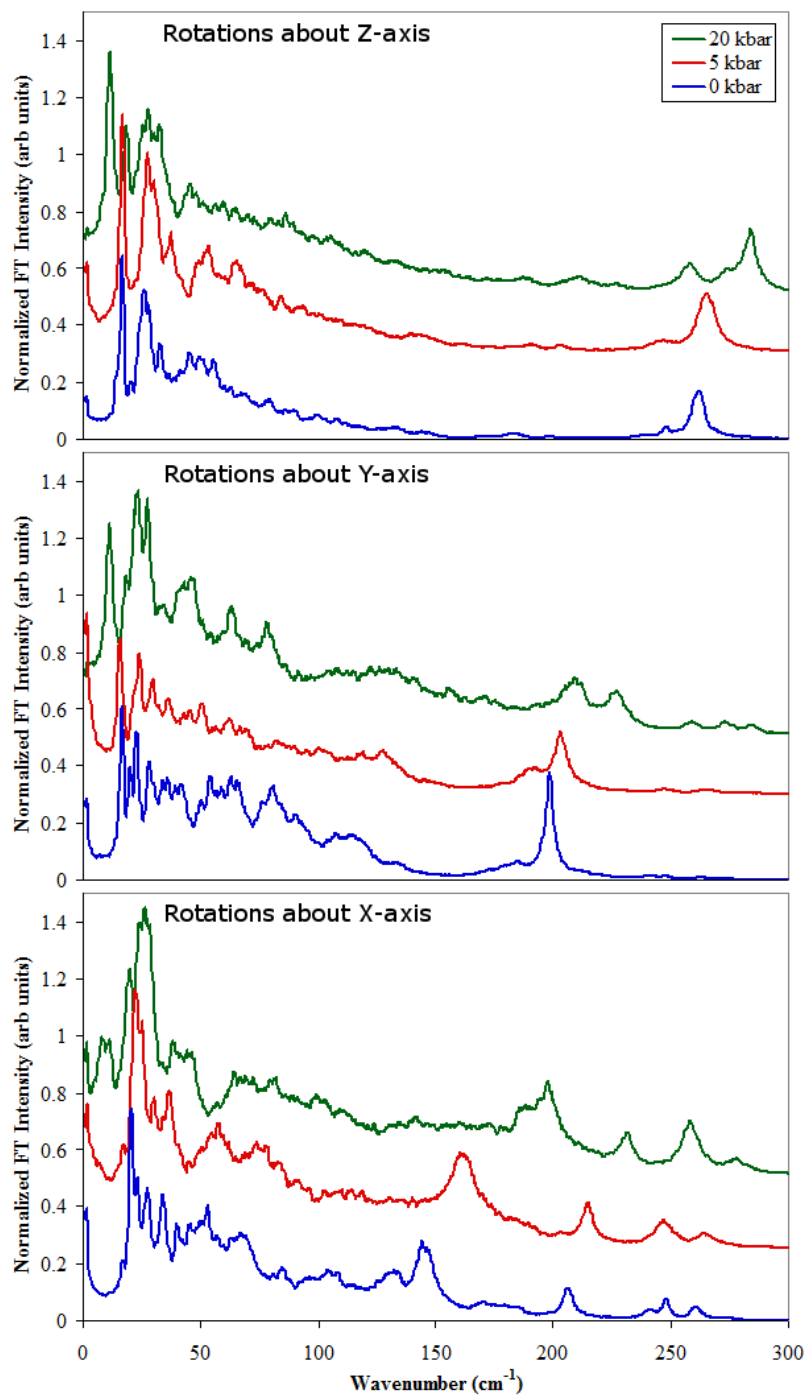


Figure 5.25: Pressure Series of the Hindered Rotations of Pentacene in p-Terphenyl at 50 K About the Molecular Axes

The five-point smoothed plots of the hindered rotations of pentacene in p-terphenyl at 50 K, averaged over 32 calculations. The peaks appear to shift to higher frequency with increased pressure. Any effect by the presence of the phase transition will require additional pressure points.



5.4: Conclusions and Future Work

The use of Fourier transform analysis of classical forcefield molecular dynamics trajectories has been used to study the vibrational modes (hindered translations and rotations) of the pentacene molecule in the p-terphenyl crystal lattice. It was shown that this method can provide information about the frequency of vibrations and local translations in crystal lattice. It was demonstrated that multiple calculations were required to fully sample the vibrational spectra because of the effect of the choice of initial velocities as well as noise reduction provided from averaging data. It was shown that the Ewald method of summation over the periodic crystal lattice was necessary to observe the vibrations in the phonon region, and this would make sense since it is likely that the summation is better able to handle the periodic crystal lattice, than the atom based method.

The hindered translations were shown to demonstrate polarization along certain molecular and crystallographic axes. The effect of pressure on the frequency of the modes was also elucidated by the FT spectra. At room temperature, the effect was generally linear with several modes shown to possess a large mode Gruneisen parameter (anharmonicity along the vibrational coordinates). The low temperature calculations appeared to show an effect from both the low temperature (being in the triclinic phase of p-terphenyl) and the phase transition back to monoclinic at around six kilobar. It was shown that the hindered rotations of the pentacene molecule required a

method that would average out the effect of intramolecular vibrations on the vectors used to measure the rotations of the molecule.

Further study of this system will require additional calculations at additional pressure points, as well as additional calculations for averaging at each pressure. Also, an investigation of the surrounding p-terphenyl structure similar to that of Schatschneider and Chronister^{6,7} may elucidate whether or not the employed forcefield still induces a phase transition at the correct pressure and temperature with the pentacene replacement. The barometer algorithm used in that study was Parrinello,¹⁴ which failed for the mixed crystal structure. Determining how to get the Parrinello¹⁴ barometer to work on this system could also create new data and further insights.

References

- (1) Baer, B. J.; Chronister, E. L. *The Journal of Chemical Physics* **1993**, *99*, 3137.
- (2) Baer, B. J.; Chronister, E. L. *Chem Phys* **1994**, *185*, 385.
- (3) Baer, B. J.; Chronister, E. L. *High Pres. Res.* **1994**, *12*, 101
- (4) Baer, B. J.; Chronister, E. L. *The Journal of Physical Chemistry* **1995**, *99*, 7324.
- (5) Bordat, P.; Brown, R. *Chem Phys* **1999**, *246*, 323.
- (6) Schatschneider, B. 3332637, University of California, Riverside, 2008.
- (7) Schatschneider, B.; Chronister, E. L. *Mol Simulat* **2008**, *34*, 1159.
- (8) Baudour, J. L.; Delugeard, Y.; Cailleau, H. *Acta Crystallographica Section B* **1976**, *32*, 150.
- (9) Marchetti, A. P.; McColgin, W. C.; Eberly, J. H. *Phys Rev Lett* **1975**, *35*, 387.
- (10) Dauber-Osguthorpe, P.; Osguthorpe, D. J. *J Am Chem Soc* **1990**, *112*, 7921.
- (11) Dauber-Osguthorpe, P.; Osguthorpe, D. J.; Stern, P. S.; Moulton, J. *Journal of Computational Physics* **1999**, *151*, 169.
- (12) Sessions, R. B.; Dauber-Osguthorpe, P.; Osguthorpe, D. J. *Journal of Molecular Biology* **1989**, *210*, 617.
- (13) Berendsen, H. J. C.; Postma, J. P. M.; van Gunsteren, W. F.; DiNola, A.; Haak, J. R. *The Journal of Chemical Physics* **1984**, *81*, 3684.
- (14) Parrinello, M.; Rahman, A. *J Appl Phys* **1981**, *52*, 7182.
- (15) Ewald, P. P. *Annalen der Physik* **1921**, *369*, 253.
- (16) Deem, M. W.; Newsam, J. M.; Sinha, S. K. *The Journal of Physical Chemistry* **1990**, *94*, 8356.
- (17) Karasawa, N.; Goddard, W. A. *The Journal of Physical Chemistry* **1989**, *93*, 7320.

- (18) Born, M.; Huang, K. *Dynamical Theory of Crystal Lattices*; Oxford University Press: Oxford, 1985.
- (19) Flores, J. J.; Chronister, E. L. *J Raman Spectrosc* **1996**, 27, 149.

Appendix

A.1: Extraction Scripts

The following are the scripts used for extracting the data from the pentacene in p-terphenyl MD trajectory files in Materials Studio. The file names given in the scripts were often renamed with the number of the calculation from which they were extracted. Names for atoms, bonds and centroids defined in the trajectory files either after the calculation or in the Minimized file before the calculation.

A.1.1: Center of Mass

```
#!/perl

use strict;
use Cwd;
use MaterialsScript qw(:all);

my $cwd = getcwd;
open my $out, '>', "Penta_Position.txt";
print $out "Frame Num Position X Position Y Position Z", "\n";

my $trajectory = $Documents{"Min_Penta_in_PTP.xtd"}->Trajectory;
for (my $i=1; $i<=$trajectory->NumFrames; ++$i) {
    $trajectory->CurrentFrame=$i;

    my $doc = $Documents{"Min_Penta_in_PTP.xtd"};
    my $system = $doc->DisplayRange;
    my $pentamolec = $system->Molecules("Sketch 1");
    my $center = $pentamolec->Center;
    printf $out "$i %f %f %f". "\n", $center->X, $center->Y, $center->Z;
}
close ($out);
Documents->Import("$cwd/Penta_Position.txt");
```

A.1.2: Single Vector Rotations

```
#!/perl

use strict;
use Cwd;
use MaterialsScript qw(:all);

my $cwd = getcwd;
open my $out, '>', "Penta_Rot.txt";
print $out "FrameNumber      Xx      Xy      Xz      Yx      Yy      Yz"."\\n";

my $doc = $Documents{"Min_Penta_in_PTP.xtd"};
my $trajectory = $Documents{"Min_Penta_in_PTP.xtd"}->Trajectory;
for (my $i=1; $i<=$trajectory->NumFrames; ++$i) {

    $trajectory->CurrentFrame=$i;
    my $pentamolec = $doc->DisplayRange->Molecules("Sketch 1");
    my $center=$pentamolec->Center;
    my $xbond = $pentamolec->Bonds("xbond")->MidPoint;

    my $Cx=$center->X;
    my $Cy=$center->Y;
    my $Cz=$center->Z;
    my $x1x=$xbond->X;
    my $x1y=$xbond->Y;
    my $x1z=$xbond->Z;

    my $Xx=$x1x-$Cx;
    my $Xy=$x1y-$Cy;
    my $Xz=$x1z-$Cz;

    my $yatom = $pentamolec->Atoms("yatom");
    my $y1x= $yatom->X;
    my $y1y= $yatom->Y;
    my $y1z= $yatom->Z;

    my $Yx=$y1x-$Cx;
    my $Yy=$y1y-$Cy;
    my $Yz=$y1z-$Cz;

    print $out "$i      $Xx      $Xy      $Xz      $Yx      $Yy      $Yz"."\\n";}

close ($out);
Documents->Import("$cwd/Penta_Rot.txt");
```

A.1.3: Multivector Rotations

```
#!/perl

use strict;
use Cwd;
use MaterialsScript qw(:all);

my $cwd = getcwd;
open my $out, '>', "Penta_Rot_Y_EXT.txt";
print $out "FrameNumber   Xx   Xy   Xz   Xx2   Xy2   Xz2   Xx3
           Xy3   Xz3   Xx4   Xy4   Xz4   Xx5   Xy5   Xz5   Xx6   Xy6   Xz6
           Yx   Yy   Yz   Yx2   Yy2   Yz2   Yx3   Yy3   Yz3   Yx4   Yy4
           Yz4   Yx5   Yy5   Yz5   Yx6   Yy6   Yz6   Yx7   Yy7   Yz7   Yx8
           Yy8   Yz8   Yx9   Yy9   Yz9   Yx10  Yy10  Yz10". "\n";

my $cwd = getcwd;
my $doc = $Documents{"Min_Penta_in_PTP.xtd"};
my $trajectory = $Documents{"Min_Penta_in_PTP.xtd"}->Trajectory;
for (my $i=1; $i<=$trajectory->NumFrames; ++$i) {

    $trajectory->CurrentFrame=$i;
    my $pentamolec = $doc->DisplayRange->Molecules("Sketch 1");
    my $center=$pentamolec->Center;
    my $center1=$pentamolec->Centroids("center1")->CentroidXYZ;
    my $center2=$pentamolec->Centroids("center2")->CentroidXYZ;
    my $center3=$pentamolec->Centroids("center3")->CentroidXYZ;
    my $center4=$pentamolec->Centroids("center4")->CentroidXYZ;

    my $xbond = $pentamolec->Bonds("xbond")->MidPoint;
    my $xbond2 = $pentamolec->Bonds("xbond2")->MidPoint;
    my $xbond3 = $pentamolec->Bonds("xbond3")->MidPoint;
    my $xbond4 = $pentamolec->Bonds("xbond4")->MidPoint;
    my $xbond5 = $pentamolec->Bonds("xbond5")->MidPoint;
    my $xbond6 = $pentamolec->Bonds("xbond6")->MidPoint;

    my $Cx=$center->X;
    my $Cy=$center->Y;
    my $Cz=$center->Z;
    my $Cx1=$center1->X;
    my $Cy1=$center1->Y;
    my $Cz1=$center1->Z;
    my $Cx2=$center2->X;
    my $Cy2=$center2->Y;
    my $Cz2=$center2->Z;
    my $Cx3=$center3->X;
    my $Cy3=$center3->Y;
    my $Cz3=$center3->Z;
```

```
my $Cx4=$center4->X;
my $Cy4=$center4->Y;
my $Cz4=$center4->Z;
```

```
my $x1x=$xbond->X;
my $x1y=$xbond->Y;
my $x1z=$xbond->Z;
my $x2x=$xbond2->X;
my $x2y=$xbond2->Y;
my $x2z=$xbond2->Z;
my $x3x=$xbond3->X;
my $x3y=$xbond3->Y;
my $x3z=$xbond3->Z;
my $x4x=$xbond4->X;
my $x4y=$xbond4->Y;
my $x4z=$xbond4->Z;
my $x5x=$xbond5->X;
my $x5y=$xbond5->Y;
my $x5z=$xbond5->Z;
my $x6x=$xbond6->X;
my $x6y=$xbond6->Y;
my $x6z=$xbond6->Z;
```

```
my $Xx=$x1x-$Cx;
my $Xy=$x1y-$Cy;
my $Xz=$x1z-$Cz;
my $Xx2=$x2x-$Cx;
my $Xy2=$x2y-$Cy;
my $Xz2=$x2z-$Cz;
my $Xx3=$x3x-$Cx;
my $Xy3=$x3y-$Cy;
my $Xz3=$x3z-$Cz;
my $Xx4=$x4x-$Cx;
my $Xy4=$x4y-$Cy;
my $Xz4=$x4z-$Cz;
my $Xx5=$x5x-$Cx;
my $Xy5=$x5y-$Cy;
my $Xz5=$x5z-$Cz;
my $Xx6=$x6x-$Cx;
my $Xy6=$x6y-$Cy;
my $Xz6=$x6z-$Cz;
```

```
my $yatom = $pentamolec->Atoms("yatom");
my $yatom2 = $pentamolec->Atoms("yatom2");
my $yatom3 = $pentamolec->Atoms("yatom3");
my $yatom4 = $pentamolec->Atoms("yatom4");
my $yatom5 = $pentamolec->Atoms("yatom5");
my $yatom6 = $pentamolec->Atoms("yatom6");
my $yatom7 = $pentamolec->Atoms("yatom7");
```

```

my $yatom8 = $pentamolec->Atoms("yatom8");
my $yatom9 = $pentamolec->Atoms("yatom9");
my $yatom10 = $pentamolec->Atoms("yatom10");

my $y1x= $yatom->X;
my $y1y= $yatom->Y;
my $y1z= $yatom->Z;
my $y2x= $yatom2->X;
my $y2y= $yatom2->Y;
my $y2z= $yatom2->Z;

my $Yx=$y1x-$Cx;
my $Yy=$y1y-$Cy;
my $Yz=$y1z-$Cz;
my $Yx2=$y2x-$Cx;
my $Yy2=$y2y-$Cy;
my $Yz2=$y2z-$Cz;

my $y3x= $yatom3->X;
my $y3y= $yatom3->Y;
my $y3z= $yatom3->Z;
my $y4x= $yatom4->X;
my $y4y= $yatom4->Y;
my $y4z= $yatom4->Z;

my $Yx3=$y3x-$Cx1;
my $Yy3=$y3y-$Cy1;
my $Yz3=$y3z-$Cz1;
my $Yx4=$y4x-$Cx1;
my $Yy4=$y4y-$Cy1;
my $Yz4=$y4z-$Cz1;

my $y5x= $yatom5->X;
my $y5y= $yatom5->Y;
my $y5z= $yatom5->Z;
my $y6x= $yatom6->X;
my $y6y= $yatom6->Y;
my $y6z= $yatom6->Z;

my $Yx5=$y5x-$Cx2;
my $Yy5=$y5y-$Cy2;
my $Yz5=$y5z-$Cz2;
my $Yx6=$y6x-$Cx2;
my $Yy6=$y6y-$Cy2;
my $Yz6=$y6z-$Cz2;

my $y7x= $yatom7->X;
my $y7y= $yatom7->Y;
my $y7z= $yatom7->Z;

```

```
my $y8x= $yatom8->X;
my $y8y= $yatom8->Y;
my $y8z= $yatom8->Z;
```

```
my $Yx7=$y7x-$Cx3;
my $Yy7=$y7y-$Cy3;
my $Yz7=$y7z-$Cz3;
my $Yx8=$y8x-$Cx3;
my $Yy8=$y8y-$Cy3;
my $Yz8=$y8z-$Cz3;
```

```
my $y9x= $yatom9->X;
my $y9y= $yatom9->Y;
my $y9z= $yatom9->Z;
my $y10x= $yatom10->X;
my $y10y= $yatom10->Y;
my $y10z= $yatom10->Z;
```

```
my $Yx9=$y9x-$Cx4;
my $Yy9=$y9y-$Cy4;
my $Yz9=$y9z-$Cz4;
my $Yx10=$y10x-$Cx4;
my $Yy10=$y10y-$Cy4;
my $Yz10=$y10z-$Cz4;
```

```
print $out "$i  $Xx  $Xy  $Xz  $Xx2  $Xy2  $Xz2  $Xx3  $Xy3
$Xz3  $Xx4  $Xy4  $Xz4  $Xx5  $Xy5  $Xz5  $Xx6  $Xy6  $Xz6  $Yx
$Yy  $Yz  $Yx2  $Yy2  $Yz2  $Yx3  $Yy3  $Yz3  $Yx4  $Yy4  $Yz4
$Yx5  $Yy5  $Yz5  $Yx6  $Yy6  $Yz6  $Yx7  $Yy7  $Yz7  $Yx8  $Yy8
$Yz8  $Yx9  $Yy9  $Yz9  $Yx10  $Yy10  $Yz10"."\\n";}
```

```
close ($out);
Documents->Import("$cwd/Penta_Rot_Y_EXT.txt");
```

A.2: Fourier Transform Mathematica Notebook

The following is the Mathematica notebook used to obtain the Fourier transform of all data in this thesis. Timedata.csv and freq.csv are temporary files used to import and export the data within Mathematica. The data must be manually copied and pasted from Excel worksheets to and from those files.

```
timedata=Import["C:/Documents and Settings/Administrator/My
Documents/Andrew/Research/New Files/timedata.csv"];
freqamp=timedata;
dim=Last[Dimensions[timedata]];
For[i=1, i<dim+1,i++,
  t=timedata[[All,i]];
  f=Abs[Fourier[t, FourierParameters->{1,-1}]];
  freqamp[[All,i]]=f;]
Export["C:/Documents and Settings/Administrator/My
Documents/Andrew/Research/New Files/freq.csv", freqamp];
```